Prediction of the static modulus of elasticity in concrete cylinders using resonant tests

by

Cristóbal Abraham Lara

A thesis
presented to the University of Waterloo
in fulfillment of the
thesis requirement for the degree of
Master of Applied Science
in
Civil Engineering

Waterloo, Ontario, Canada, 2019

AUTHOR'S DECLARATION

I hereby declare that I am the sole author of this thesis. This is a true copy of the thesis, including any required final revisions, as accepted by my examiners.

I understand that my thesis may be made electronically available to the public.

Abstract

Concrete is widely used in construction nowadays, and it is crucial that its behaviour conforms to the original design. In every construction site, standard concrete cylinders are cast for quality control. Concrete cylinders are routinely tested to validate their design requirements. Concrete cylinders are traditionally tested for their compressive strength, disregarding the modulus of elasticity. Mostly because the evaluation of the modulus of elasticity is more time consuming and costly than the evaluation of the compressive strength

Non-destructive test (NDT) are often used to estimate the properties of concrete. The use of NDT methods allows the continuous monitoring of specimens; the required equipment is portable. Hence NDT methods are affordable and fast than traditional destructive tests. Nevertheless, the elastic properties obtained from non-destructive tests (e.g. dynamic tests) differ from traditional tests (e.g. static tests); Mostly because the strain levels used in the dynamic tests are more than three orders of magnitude lower than in the static tests.

This work has two main objectives: 1) To develop a simpler, more affordable and faster methodology for testing the concrete cylinders using a cellphone. 2) To develop a reliable forecasting methodology for the static modulus using the methodology from the first point.

To achieve the main objectives, a comprehensive experimental program was undertaken. Over 100 cylinders from four different concrete mixes were tested. Their resonant frequencies were evaluated using the standard microphone of a smartphone. To validate the methodology, the results obtained using the cell microphone were compared with the ones obtained with an accelerometer. Different supports, impact locations, impulse hammers and sensor positions were tested to find the optimal test setup.

The signal processing algorithm for extracting the resonant frequencies from the microphone signal is presented. Using this algorithm along with the optimal test setup, it was possible to find the right frequencies in all cases.

The methodology developed for forecasting the static modulus is based on the linearity between static and dynamic moduli, and the linear development of concrete stiffness with the logarithm of time. An example of forecasting the static modulus is presented. The example given yielded a 95% confidence interval within the ±15% of the expected value, although the actual estimation error was less than 2%.

Acknowledgements

First I would like to express my gratitude to my supervisor Dr. Giovanni Cascante, who give me the opportunity to pursue this degree under his guidance. His patience and knowledge were key for me to conclude this work successfully. His enthusiasm for creating a better and more enjoyable work environment was very welcomed. I want to extend my gratitude to my thesis readers, Professors Trevor Hrynyk and Mahesh Pandey, who took the time for reviewing my work and helped me in polish the final results.

I would also like to acknowledge my former supervisor Dr. Francisco De la Mora Galvez who inspired the idea for developing this work. His insights were a key part of the ideas presented. Besides of his encouragement for pursuing a degree with Dr. Cascante

Thanks to the structure lab team, who provide me with training, guidance and support for the experimental part of my work. Especially to Peter Volcic who personally trained me in the usage of the structure lab equipment. To Colin Van Niejenhuis who share me of his precious time and helped me with the concrete design and casting of my cylinders.

My warmest thanks to my colleagues on the NDT group who not only introduced me to the lab equipment but also provided me with guidance through my degree. To Maria José Rodriguez, who was like a lighthouse in the dark, guiding me step by step to what I should do as a newcomer in UW, and introducing me to the lunch group. Thanks to Piotr Wiciak for setting an example to me for achieving a balanced life, always encouraging me to go beyond my limits by enduring long bike rides with me. Similarly, I'm thankful to Fredy Diaz, Mohammed Irfan, Sabah Fartosy for sharing their knowledge and insights with me. And finally, but not least, thanks to Edward Ginzel who was like another supervisor to me, sharing all his vast knowledge and resources to aid on my project.

I am grateful also to all the friends I made here at the University of Waterloo, especially to the members of the lunch group, who constantly provide motivation to keep moving forward by creating joyful life experiences outside the research.

Finally, I would like to thanks the financial support given by the Mexican National Council of Science and Technology (CONACYT) and the Mexican Foundation for Education, Technology and Science (FUNED). Likewise, I want to thank the Natural Sciences and Engineering Research Council of Canada (NSERC) for partially funding my degree. Without their sponsorship and support studying a master wouldn't have been possible.

Dedication

To my family who supported me along the way, is always close to me despite the distance. Especially to my parents who taught me and raised me, without them, I wouldn't be here today.

Table of Contents

List of Figures

List of Tables

List of Symbols

A	The amplitude of a signal or sinusoidal wave
b	half-thickness of the plate. (Rayleigh waves)
c	General wave velocity
D	Cylinder diameter
d_s	The diameter of a steel sphere
E	Elasticity modulus or Young's modulus (GPa)
E_d	Dynamic modulus of elasticity
E_{df}	Dynamic modulus of elasticity computed by the flexural resonant frequency
E_{dl}	Dynamic modulus of elasticity computed by the longitudinal resonant frequency
E_{it}	The initial tangent slope or Young's modulus at strain close to 0.
E_s	Static modulus of elasticity
f	Frequency in cycles per unit time (Hz)
f_c	Compressive strength of concrete
f'_c	Specified compressive strength of concrete determined using cylinder specimens
f'_{cu}	Specified compressive strength of concrete determined using cubic specimens
f_f	Flexural or transversal natural frequency
f_l	Longitudinal natural frequency
f_s	Sampling Frequency
G	Shear modulus (GPa), Second Lamé parameter
G_{dt}	Dynamic Shear Modulus computed by the torsional resonant frequency
I	Identity Matrix
k	Wavenumber
K_{RP}	The ratio between V_R and V_P
K_{RS}	The ratio between V_R and V_S
L	Length of the cylinder/rod/bar
N	Total number of receivers/traces in MASW array
P_h	Phase velocity dispersion image matrix
q	Body force by unit length or volume accordingly
r	The radius of the cylinder/rod
R_i	Receiver sensor at position *i*
t	Time variable
T	Period of vibration (s)
t_p	The thickness of the plate (Rayleigh wave)
T_r	The transmitter of the input signal/Trigger

u	Displacement
V_P	Longitudinal or P-wave velocity
V_{Pr}	Longitudinal wave velocity in a thin rod
V_R	Rayleigh or R-wave velocity
V_{Rmin}	Minimum expected Rayleigh wave velocity
V_S	Transversal or S-wave velocity
x_i	The distance of Receiver *i* from the source in MASW array
X_L	Spread length on MASW array (x_N - x1)
α	The square root of the squared difference of wavenumber with Vp
$\alpha^\wedge$	Minus α

Chapter 1
Introduction

1.1 Background & Significance

Concrete is a material widely used for civil infrastructure around the world due to its versatility of being cast in diverse shapes for construction and the availability of their main ingredients (sand, aggregates, pozzolanic materials, and water) (Nilson, Darwin et al., 2004). Due to its importance in construction, it is crucial to know if the concrete poured satisfy the structural design requirements to guarantee structural safety.

Therefore, in every construction site quality control of concrete is typically performed. The quality control can be done in two methods: 1) By casting a certain amount of standard concrete cylinders for every batch of concrete poured. 2) By extracting concrete cores from the structure. Being the first one the most common practice, given the destructive nature of the second one. However, regardless of the method chosen, the standard concrete cylinders or the cores need to be tested for their compressive strength and its modulus of elasticity. Nevertheless, typically only the compressive strength of the cylinders is evaluated.

The modulus of elasticity is disregarded from the test because it requires a longer specimen preparation and the test itself is at least 3 times longer than the compressive test alone. Additionally, it is typically assumed in the practice that the modulus of elasticity of concrete can be estimated by the concrete strength. However, there is extensive research stating the opposite, that the elastic modulus and compressive strength relationship depends on many factors including the admixtures used and the testing methodology (Neville, 1996; Noguchi, Tomosawa et al., 2009).

Building codes propose different empirical equations to estimate the elasticity modulus of concrete based on its compressive strength. The equations change between regions to account for the most common admixtures used in the zone. Nevertheless, they are not reliable enough, as it is shown in Figure 1.1. This figure shows the modulus of elasticity and compressive strength for cylinders all cast in the same region. Yet, the building code from the zone (GDL Building Code) fails to accurately estimate the elasticity moduli with an estimation error of 4.69 GPa (more than 25% error).

The modulus of elasticity is a crucial parameter for estimating the deformations in a structure, failure in estimating it can cause serviceability and safety problems. Hence the need for verifying on

the field if the concrete meets the elasticity requirements given by the structural designer. Both, overestimating it and sub estimating it can cause problems to the structure.

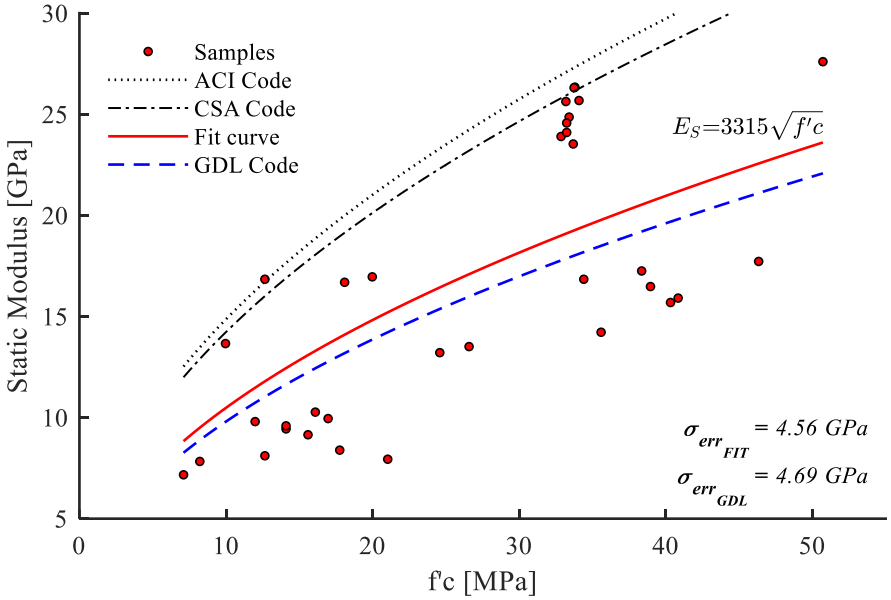

Figure 1.1 E-f'c relationship for concrete cylinder tested by (Lara, 2015) along with three different building code relationships (ACI, CSA and GDL building codes). The curve fitting results for the data is also shown.

The quality control of concrete is also affected by a time factor. Concrete develops its strength and stiffness over time, and it's usually specified as their values on the 28th day. This can critically affect the construction process. If the concrete assessment is delayed until the 28th day after casting, and it shows the concrete lack the stiffness of strength required, it could impact negatively to the time schedule and budget of the project by needing to reinforce the existing structure or even demolishing the structure. However, it is allowed by standards to use concrete cylinders/cores at an early age to estimate the final concrete strength at its 28th day provided there is enough information for the estimation to be reliable enough.

With early testing for quality control, there are huge savings both in time and moneywise. Detecting problems in concrete strength and stiffness at an early age can provide in-situ engineers with information to take corrective measures such as improve the curing methods used in situ or taking the decision to stop the construction for demolishing the deficient elements before more elements are being placed over them. It can save time as well by assessing if removing the formwork is possible or to open the structure to transit. This is especially true for roads and bridges.

However, testing concrete cylinders or cores at an early age with conventional methods has some challenges. For the specimens to be representatives of the concrete cast in-situ, the specimens need to be kept near the structure under the same curing conditions. The tests need to be done in a specialized compressive machine capable of reaching up to 400 kN, therefore the specimens need to be taken to a testing laboratory. The transportation cannot be longer than 4 hrs and the specimens need to be protected against impact and moisture loss. Besides, the destructive nature of the test makes the tested cylinders not longer useful for further testing. So if monitoring of the concrete would be required, several concrete cylinders would need to be cast and also several trips between the construction site and testing lab would be required. This proves almost impossible for projects far from cities, such as dams, bridges.

Because of all these reasons, non-destructive tests are commonly used to asses the concrete properties in situ. Typically the non-destructive testing equipment is significantly more portable than the conventional testing techniques. This allows the equipment to move to the site, rather than the specimens moving to the lab. Non-destructive tests, as their name implies, do not destroy the specimens, this allows them to perform the same test in the same cylinder countless times. Therefore, being able to monitor the concrete batch with less amount of cylinders.

Values obtained using the conventional methods are called “static”, while the results from non-destructive testing are referred to as dynamic. Unfortunately, in concrete, these two values do not agree with each other. The static tests use relatively large strains ($\sim 1 \times 10^{-3}$) to compute the properties, while the dynamic tests measure low strains ($\sim 1 \times 10^{-6}$). There is no unique relationship between these two values, just as there is no unique relationship between the modulus of elasticity and the compressive strength.

A structure during its lifetime is exposed to large forces and its deformations can reach several centimetres. Therefore, the modulus of elasticity that represents best the structure behaviour is the static one. As a result, when dynamic tests are performed in the concrete they need to be correlated with their static values, so the results can be useful in the field.

1.2 Research Objectives

The intention of this work is to propose a methodology for predicting the concrete static modulus on the 28^{th} day using early age dynamic measurements. The forecasting methodology proposed in this study would fully exploit the advantages of the resonant test methodology using the built-in

microphone of a smartphone (Figure 1.2), instead of the specialized equipment required by the standards and the ones used by other researchers. The methodology proposed does not require any special or complex support for the cylinder, besides placing it vertically over a piece of foam. The test just requires a small impact hammer with a tip of a certain diameter and place the smartphone close of the cylinder at a specific location.

Figure 1.2 Sketch of final dynamic test methodology proposed, in order to make the test more affordable, time-efficient, and portable.

The main idea of this methodology is to spread out and normalize the static modulus testing by proposing this portable, affordable and quick test methodology. This would aid monitor the concrete stiffness from early ages (1, 2, 3… days), not only for projects of high importance with testing level A, such as high-rise constructions, dams or power plants but also to structures with inspection and testing level B and C, like residential constructions (ACI_311.4R, 2000).

The work presented in this thesis address the following goals:

- Determine if daily use microphones such as the ones found in laptops or smartphones have a flat response in the frequency range of interest for testing of standard concrete cylinders.
- Investigate the importance of the impulse hammer used for exciting the concrete cylinder and the best location for hitting the cylinder with it.
- Find the best test setup that optimizes the detection of the resonant frequencies with the microphone. Among the test setup parameters are the impulse hammer, the support used, the location of the impact, and the position to hold the smartphone around the cylinder.

- Compare the results of performing the same test using an accelerometer and the microphone. Assessing how reliable is the methodology proposed when compared to traditional sensors.
- Propose a signal processing algorithm to detect the resonant frequencies of the cylinder from an audio signal recorded under a low noisy environment.
- Compare the dynamic modulus of elasticity obtained by the resonant test using the microphone, with other NDT techniques.
- Develop a forecasting methodology that could allow predicting the static modulus on the 28th day by monitoring the dynamic modulus measured with the test methodology proposed using the first 3 days after casting.

1.3 Literature Review

This section summarizes previous research and work done directly related to the objectives of this thesis. Although there are further comments regarding related research on each one of the chapters, sections and subsections regarding the topics discussed there.

The relative portability and non-destructive nature of the dynamic tests make them very attractive for material evaluations. However dynamic properties measured at very low strains differ from their counterpart static properties that are measured at larger strains. Therefore, plenty of research has been done trying to correlate these two values, starting with Powers in 1938 (Powers, 1938). Not only correlations in concrete have been attempted (Nilsen & Aitcin, 1992), but also in other stabilized materials (Kolias & Williams, 1980) and even with rocks (Christaras, Auger et al., 1994). Among concrete research, many relationships have been proposed, some of them will be further discussed in section 2.8. Some of these research focuses on different aspects such as early age development (Carette & Staquet, 2016) or the nonlinear behaviour of concrete involving temperature and interatomic connections (Shkolnik, 2005)[1].

One of the simplest non-destructive techniques is UPV tests. It is just natural researchers who have taken this approach for evaluating the dynamic properties in concrete cylinders, with interesting

[1] This equation is expressed in MPa. σ is the stress at which the static elastic modulus is being measured as the tangent slope of the stress-strain curve. And $\dot{\sigma}$ is the stress rate in MPa/s. The equation assumes the tests are done at 20° C.

results. Comparing the Poisson's ratio computed based on the UPV and the resonant frequencies, (Simmons, 1955) found that when the inertial lateral correction factors, the Poisson's ratio obtained through the Vp and longitudinal resonant frequency was higher than when using the ratio between the longitudinal and torsional resonant frequencies. Later on (J. S. Popovics, Zemajtis et al., 2008) found that the dynamic modulus of elasticity computed from the resonant test is more reliable than using the UPV tests, provided the lateral inertia correction factors are included in the calculations.

The main struggle with using UPV to asses the dynamic modulus of cylinders is that the results are dependable of the cylinder size (B. J. Lee, Kee et al., 2015). The P-wave velocity measured in concrete cylinders will be higher for pulses with short wavelengths compared with the cylinder diameter (Wiciak, Cascante et al., 2019).

The other popular technique for testing concrete cylinders is the resonant test method, which sometimes is also called the Impact-Echo method. The methodology has been already standardized by the ASTM. Similarly as in the research presented in this thesis, (K.-M. Lee, Kim et al., 1997)tried to used early ages dynamic measurements but they used solely accelerometers following the standard methodology, they tried to correlate the values obtained to the concrete strength.

Attempts for optimizing or improving the standard methodology has been done. An example of this is (Boileau, Greiner et al., 1981) research, which also used microphones as sensors, and described one of the disadvantages of using traditional accelerometers for this kind of test, due to possible changes in frequencies caused by the coupling of the sensor.

Different setups and methodologies are still being tested, with far excentric ones, using magnetic excitation of steel rods and measuring the response with a stereo-phonogram (Davis & Opat, 1983). Perhaps the closest setup to the one proposed in this work is the one used by(Han & Kim, 2004). They also placed the cylinder vertically and impacted the top surface with a steel sphere of 8 mm while measuring the response with an accelerometer. They also proposed a different static-dynamic moduli relationship that is not linear.

Among the main innovations intended in this research is the usage of a conventional microphone for measuring the resonant frequencies. Using air-coupled sensors for performing resonant tests in concrete cylinders has tried before (Boileau et al., 1981). Nevertheless, they used specialized condenser microphones to measure the resonant frequencies, these microphones were reported to have a flat response in the frequency range between 5Hz to 160 kHz. They also require a power

supply to provide amplification. The cost of these microphones (around 3500 USD) along with the requirement for a power supply that provides amplification, sets a limitation for their usage in the field (Jinying & Popovics John, 2007).

Most of the research in the usage of microphones with the impact-echo or resonant test is focused on detecting voids or cavities on flat surfaces. For example to measure surface waves in pavements (Bjurstrom, Ryden et al., 2016) with air-coupled sensors and comparing them with accelerometers. Another popular application of microphones is in concrete slabs to detect delamination (Diógenes, Cossolino et al., 2011).

Measuring the wave propagation of the Rayleigh wave within a plate has also ben done through microphones (Groschup & Grosse, 2015). However, the main problem when microphones have been used is environmental noise. Therefore, these techniques provide insulation around the microphone that blocks any undesired noises but allowing the sounds coming from the slab to go through the sensor (Ye, Kobayashi et al., 2018). These insulations could become bulky reducing the portability of the equipment used (Guthrie, Larsen et al., 2019).

It was mentioned before, that one of the main disadvantages of the microphones besides picking up vibrations coming from other sources easily, was their cost. However, using low budget microphones has also been attempted for measuring wave propagation in slabs (Groschup & Grosse, 2015). These low-cost microphones have a reduced frequency range around 50Hz and 15kHz and their cost is around 150 USD (Shin, Popovics et al., 2019).

Using the resonant frequencies in combination with the Rayleigh wave velocity for finding the dynamic elastic constants in a plate was also implemented by(Medina & Bayón, 2010). Nevertheless, their approach required the previous knowledge of the plate thickness.

The most common technique for processing the resonant and impact-echo signals is the Fourier Transform. The Fourier analysis allows knowing the frequency content within a signal. However, for vibration monitoring, the signal will normally contain several reflections or frequencies due to different wave propagation modes (Ni & Li, 2019). For this reason, especially for the impact echo in plates, different techniques have been tried. One approach taken is using the wavelet transform in combination with the Fourier Transform to enhanced the Fourier spectra for easily detecting the impact-echo peaks (Yeh & Liu, 2008). The Choi-Williams transformations is another tool used for impact-echo signals that allow visualized the data in both time and frequency, similar to a short

Fourier transform (Groschup & Grosse, 2015). The Hilbert-Huang transformation based on different empirical mode decompositions (C.-C. Lin, Liu et al., 2009) has also been used to distinguish different features from the Impact-Echo signals, making them easier to interpret (Y. Zhang & Xie, 2012).

Forecasting future concrete property values based on early age measurements it's not a new concept. Different approaches have been taken to extrapolate the data from static tests on the 7th day or earlier to values on the 28th day (Mostofinejad & Nozhati, 2005). It has even been standardized the procedure for estimating the compressive strength (ASTM_C918, 2013).

Nevertheless, the non-destructive nature of the dynamic tests allows monitoring the same specimen several times. Besides dynamic tests can be performed on the specimens as soon as 10 hours after casting (Carette & Staquet, 2016). Therefore, it has become relevant to forecast the static values using early age dynamic measurements. Back in 1952 (Erickson, 1952) there was already research trying to accomplish this feature. The equation proposed to forecast the elastic modulus was a hyperbola with two-parameter coefficients.

The Young's modulus can be monitored with dynamic methods, due to a dependency between these two values. However, the compressive strength in concrete not necessarily is a function of the stiffness, so the f'c can not be monitored with dynamic tests (Nilsen & Aitcin, 1992).

1.4 Research Methodology

The methodology followed during this research will be summarized in this section:

First, the different microphones were tested under the same conditions, to asses their capabilities in recording sounds on the frequency range of interest. For this, different pitch sounds of different frequencies were generated.

The first step was to asses the microphone capabilities for recording sounds with frequencies on the frequency range of interest. For this, the same test setup was followed in different microphones recording pitch sounds at different frequencies from 1 kHz to up to 20 kHz. The frequency spectrum was then compared and analyzed to see which microphone had the flattest response in the range of 5 to 13 kHz.

Next, different setups were tested in order to find the best position for the impact and the place for placing the microphone around the cylinder, such that the frequency spectral amplitudes for the

flexural and longitudinal resonant frequencies were maximized. For this set of tests, professional microphones were used, instead of the conventional ones. The results were then validated with a Finite Element Analysis,

Once the position for the impact and the place for placing the microphone were defined, as well as the microphone to be used. Then different impulse hammers were tested looking to maximize the excitation of the cylinder in the frequency range of interest. During these tests, different support materials were also tested in combination with different hammers, again looking to maximize the resonant of the modes of interest.

Finally, once the final setup was defined, different alternatives and techniques for cleaning the audio signals were tried. The algorithm meant to highlight the resonant frequencies from the spectrum to make it easier to identify. Then, all cylinders available at the moment (batch 000, and batch 300) were tested with the methodology. And then they were tested under compression to obtain their compressive strength and static modulus of elasticity.

Two batches of concrete were made specifically for this work, (batch 200 and 400) in order to test the cylinders through their development with age. For batch 200, 21 cylinders were cast, while for batch 400, a total of 48 cylinders were cast. These cylinders were tested dynamically at different ages with the methodology proposed, and once every certain day, a number of cylinders were taken to test them for its compressive strength and modulus of elasticity. Afterward, the cylinders were taken out of the study.

For the last 6 cylinders in batch 400, additional non-destructive tests were performed to them, just before being tested under compression. The non-destructive test performed were ultrasonic pulse velocity (UPV) test and multichannel analysis of surface waves (MASW). The goal was to use this additional data to verify the results obtained from the resonant tests.

Once all test data was gathered, the signals were processed with the algorithm previously developed. Nevertheless, the algorithm needed to be fine-tuned improving its efficiency for detecting the right resonant frequencies in all cases.

Finally, with the data processed the analysis of the results was the final step to take, in order to propose a forecasting methodology using the dynamic results obtained from the new test methodology proposed. For this, related research available was taken into account for formulating the forecasting approach.

1.5 Thesis Organization

This work starts with an introductory chapter that provides the outline of the research presented, along with its motivations and relevance. It also offers a brief literature review of available research related to this project.

Chapter 2 introduces the basic concepts needed for developing the current work. Among the topics discussed are the main mechanical properties that define a material behaviour such as the modulus of elasticity, Poisson's ratio, and shear modulus. It also provides with wave propagation background, presenting the derivation of the wave equations for the axial and flexural free vibration in rods. It describes how particle motions are transmitted within a solid body as body waves and surface waves. Later on, the chapter introduces the concrete as a material, highlighting its importance in the modern world and describing its behaviour. Finally, the chapters end discussing the difference between static and dynamic results, introducing research done trying to relate these two values.

Chapter 3 describes what a signal is and introduce different signal processing techniques used to analyze such signals. The techniques are divided into 3 sections depending on the domain they analyze the signal, either by its time domain, the frequency domain or a combination of the two. Cross-correlation, Fourier Transform, Short Fourier Transform and Phase Velocity Dispersion.

Chapter 4 present the different testing methods available for evaluating concrete properties such as compressive strength and modulus of elasticity. The test methods presented include revisions done by different researchers to each of them, introducing valuable information for the appropriate interpretation of the test results. The testing methods discussed are the compressive strength test, elastic modulus and Poisson ratio test, UPV, Resonant method or Impact-Echo and MASW. They have been divided into static and dynamic methods.

Chapter 5 describes the experimental methodology followed during this work. It starts by presenting the specimens used, its material and basic properties such as dimensions and densities. Then it summarizes the testing methodology for the different tests performed on the cylinders, such as the resonant method, MASW, UPV and the static compressive test to obtain the compressive strength and modulus of elasticity. The data processing techniques used on each test methodology are also presented along with examples of the raw data and the processed data. However, in the case of the Resonant Method, a more comprehensive discussion is presented due to being the main focus of this research. It includes the methodology followed to identify the best test setup regarding the impulse

hammer, the microphone used, the locations for both of them and the signal processing technique that best captures the resonant frequency of the cylinder.

Chapter 6 provides the final results obtained from the different tests presented in the previous chapter. The results are divided into three sections: the results from the dynamic tests, results from the static tests, and a third section fusing the results from both sets of tests. The dynamic test results include the results for each step of the process to define the final test setup. In the concluding section, the relationships for both elastic moduli and compressive strength are made, as well as an overview of the forecasting methodology proposed, including a practical example with further explanation of how to be placed on practice.

Finally, in chapter 7 the main conclusions of this research are summarized, presenting the advantages, disadvantages of the methodology proposed. It includes recommendations regarding the application of the test methodology on the field and suggestions for future work regarding this research.

Chapter 2
Mechanical Properties

2.1 Introduction

This chapter will review some mechanical properties of solid bodies related to this project. First, it will discuss the properties as a concept in a general way. Later on, the chapter will introduce concrete as a material to be able to put the properties reviewed in context with it.

2.2 Elastic Modulus

When a solid body is subject to a force applied over a certain area (stress), the body will suffer some deformation over its length (strain). This relationship can be expressed better by the sum of the following statements: 1) When the load increases, the measured strain increase in the same ratio; 2) When the load diminishes, the measured diminished in the same ratio; and 3) When the load is reduced to zero, no strain can be measured. These statements hold true within a certain load range. Although some exception exists (i.e. cast metals) (Love, 1944). The relationship between stress and strain is called Hooke's law which can be shown in the equation (2.1).

$$\sigma = E\varepsilon \tag{2.1}$$

The elastic modulus or Young's modulus (E) is the proportionality factor between stress and strain. From the equation (2.1), it can be shown that the factor E can be also described as the ratio between the stress and the strain. Figure 2.1 shows a graphical representation of stress and strain applied to a rectangular solid body, where tension stress is applied at both ends causing an axial strain in the same direction.

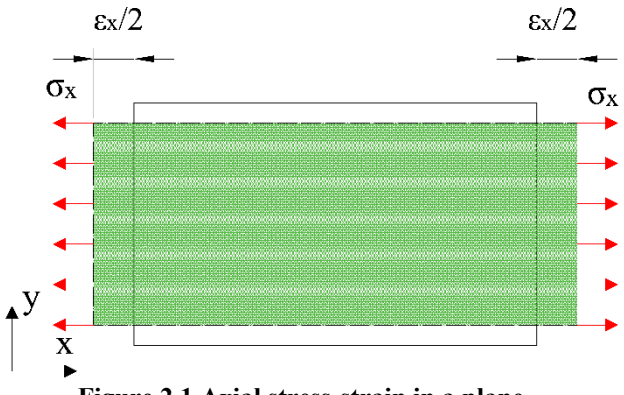

Figure 2.1 Axial stress-strain in a plane

The modulus of elasticity has the same value for tension and compression, however, the range on which this statement holds true may be different for tension and compression. The modulus of elasticity E is a constant depending on the material stiffness (Gross, Hauger et al., 2011). The higher the modulus of elasticity the stiffer the material (More force will be required to produce the same strain). Some typical values for the elastic modulus of different materials are shown in Table 2.1

Table 2.1 Typical values for the modulus of elasticity of different materials. (Gross et al., 2011) p. 17.

Material	E (GPa)
Steel	210
Aluminum	70
Concrete	25-35
Wood (in fibre direction)	7-20
Cast iron	100
Copper	120
Brass	100

2.3 Poisson's ratio

The previous section talked about the Elastic Modul as a one-dimensional problem, where only axial stress and strain were considered. However, the stress in 'x' direction will not only cause a deformation in the 'x' direction but it will also produce a reduction of width in the 'y' direction (Figure 2.1). This phenomenon is known as the Poisson effect. The relationship between the 'x' and 'y' strain can be expressed as:

$$\varepsilon_y = -\nu \cdot \varepsilon_x \tag{2.2}$$

The parameter 'ν' is called Poisson's ratio, which is also a material constant. The Poisson's ratio can take values from -1 to 0.5. When the Poisson's ratio is 0, the body will not experience any cross-sectional contraction (and therefore the volume will increase), and with a value of ν=0.5, the cross-sectional area will be reduced, keeping the same volume. Cork and rubber are two material examples of materials on both ends of this range, with a Poisson's ratio near to zero and 0.5 respectively. Negative values are theoretically possible, but they are found typically in artificial materials (Lakes, 1987). Negative Poisson's ratios are out of the scope of this research.

Merging equation (2.2) with (2.1), we can found the strains using the stress in both directions (Equation (2.3)).

$$\varepsilon_y = \frac{1}{E}\left(\sigma_y - \nu \cdot \sigma_x\right) \tag{2.3}$$

Expanding these definitions into a 3-dimensional space we can generalize Hooke's law with the Poisson's ratio in the following equations:

$$\begin{aligned} \varepsilon_x &= \frac{1}{E}\left(\sigma_x - \nu\left(\sigma_y + \sigma_z\right)\right) \\ \varepsilon_y &= \frac{1}{E}\left(\sigma_y - \nu\left(\sigma_x + \sigma_z\right)\right) \\ \varepsilon_z &= \frac{1}{E}\left(\sigma_z - \nu\left(\sigma_x + \sigma_y\right)\right) \end{aligned} \tag{2.4}$$

2.4 Shear Modulus

Solid bodies can experience two types of forces: Forces normal to the surface as they were discussed in section 2.2; and forces parallel to the surface. When the latest forces are applied over a certain area, they are called shear stresses. Similarly, when a solid body is subjected to shear stress, the body will experience a rotational deformation with angle γ_{xy} (Figure 2.2). The relationship between shear stress τ_{xy} and the angle change γ_{xy} is linear can be represented with the equation (2.5) (Gross et al., 2011).

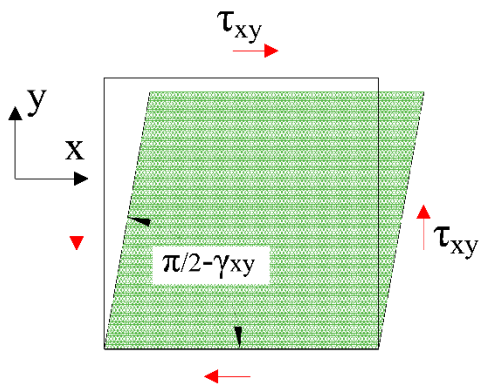

Figure 2.2 Shear stress-strain in a 2-dimensional plane. (Gross et al., 2011) p. 85

The constant G in the equation (2.5) is the proportionality factor between the shear stress and the angle change. It is called 'shear modulus'. Just as the elastic modulus, it is also a material constant that can be obtained using shear or torsion tests (Gross et al., 2011).

$$\tau_{xy} = G \cdot \gamma_{xy} \tag{2.5}$$

All three constants, G, E, and ν hold a relationship with each other in the form of the equation (2.6).

$$G = \frac{E}{2(1+\nu)} \tag{2.6}$$

2.5 General Hooke's Law

In the previous sections the Elastic Modulus, Poisson's ratio, and Shear Modulus were discussed in a plane stress context. They were introduced this way since sometimes is more practical to reduce a model to 1 or 2 dimensions for approaching the problem. Although the world we move in is a 3-dimensional space, hence Hooke's law in a general 3D form will be now introduced. For this, one additional elastic constant will be introduced in this section: The Lamé moduli. This constant is particularly useful and is extensively used in continuous mechanics. This section will define the Lamé moduli based on the previous elastic constants introduced before in the following formula:

$$\lambda_p = \frac{E \cdot \nu}{(1+\nu)(1-2\nu)} \tag{2.7}$$

Then it is possible to introduce the Hooke's law for isotropic bodies as in equation (2.8), where the stress (**σ**), strain (**ε**) are tensors, **I** the identity matrix, and tr() is the trace function (Kang & Zhong-Ci, 1996).

$$\sigma_{ij} = 2G\varepsilon_{ij} + \lambda_p \delta_{ij} \varepsilon_{kk} = 2 \cdot G \cdot \boldsymbol{\varepsilon} + \lambda_p \cdot tr(\boldsymbol{\varepsilon}) \cdot \mathbf{I} \tag{2.8}$$

In expanded matrix form:

$$\begin{bmatrix} \sigma_{11} & \sigma_{12} & \sigma_{13} \\ \sigma_{21} & \sigma_{22} & \sigma_{23} \\ \sigma_{31} & \sigma_{32} & \sigma_{33} \end{bmatrix} = 2G \begin{bmatrix} \varepsilon_{11} & \varepsilon_{12} & \varepsilon_{13} \\ \varepsilon_{21} & \varepsilon_{22} & \varepsilon_{23} \\ \varepsilon_{31} & \varepsilon_{32} & \varepsilon_{33} \end{bmatrix} + \lambda_p \begin{bmatrix} \varepsilon_{11} & 0 & 0 \\ 0 & \varepsilon_{22} & 0 \\ 0 & 0 & \varepsilon_{33} \end{bmatrix} \tag{2.9}$$

2.6 Wave Propagation Theory

2.6.1 Background

In the previous sections of this chapter, the loads were discussed as long-lasting loads. In comparison, this section will talk about the effects of a sharply applied localized disturbance in a solid body. The

effect of this sharp disturbance transmits fast to other parts of the solid body. This phenomenon is called wave propagation (Graff, 1975).

2.6.1.1 Vibrational Motion

The simplest form of vibration motion is harmonic or sinusoidal, which can be described by the equation (2.10) (Richart, Hall et al., 1970). The simplicity of the equation is an important feature because due to the Fourier's Theorem it is possible to decompose a complex signal into a sum of sinusoidal waves (Rayleigh & Strutt, 1877). This section will introduce different characteristics of the harmonic motion.

$$y = A \cdot \sin\left(\omega t - \varphi\right) \tag{2.10}$$

Figure 2.3 shows the equation (2.10) plotted as a function of time, showing the graphical representation of the main quantities in the basic harmonic equation. *'A'* represents the amplitude of the wave. The amplitude is typically measured from the mean value of the wave (zero) to the maximum value. Although sometimes the term *peak-to-peak amplitude* is used, to make reference to the displacement from the minimum amplitude to the maximum amplitude (*2A*). The circular frequency (ω) is the oscillation rate in radians per time unit, with 2π rad describing one full cycle of oscillation. Although, sometimes it is useful to express the frequency of oscillation in Hz (cycles per second). The equation (2.11) relates the frequency in cycles per second with the circular frequency.

$$f = \frac{\omega}{2\pi} \tag{2.11}$$

The time it takes to the wave motion to start repeating itself is called the *period of vibration* (T). This quantity is also represented clearly in Figure 2.3. The relationship between the period and the frequency is given by the equation (2.12), in which is possible to see the period has units of time, describing the time required by one cycle.

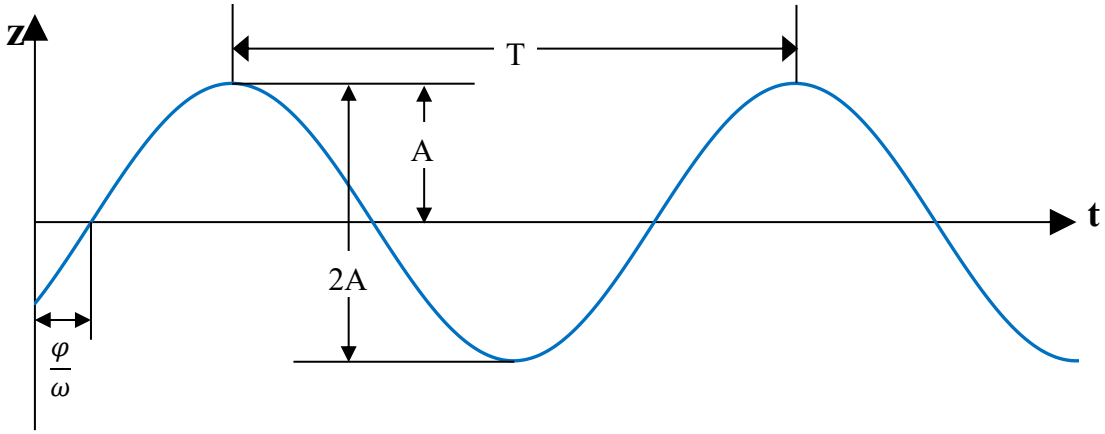

Figure 2.3 Harmonic motion equation characteristics

$$T = \frac{1}{f} = \frac{2\pi}{\omega} \tag{2.12}$$

Finally, the other quantity left to introduce is the phase angle (φ), which represents the shifting of the wave in time. It's useful to show the time relationship between two waves with the same frequency. The phase angle can take values between -π and π. Outside this range, the values are redundant since they would be equivalent to values inside this range.

2.6.1.1.1 Travelling wave

The sinusoidal wave defined before describes the vibration of the coordinate 'x' in time. In this section, the formulation for a wave moving in space and time will be defined along with other useful wave quantities that are going to be discussed during this work. The sinusoidal motion of any point along the axis 'x' can be described with the equation (2.13), where "A" is an amplitude coefficient with length units, and λ is the *wavelength* of the wave. The wavelength of a wave is the spatial dimension between one cycle and the next one, similar to frequency but in space. Therefore, by dividing x by λ, the distance "x" is converted in the number of cycles, since $\lambda = \text{distance/cycle}$. Then the 2π factor transforms the value in circular "frequency" (Physclips, 2019).

$$y = A\sin\left(2\pi\frac{x}{\lambda}\right) \tag{2.13}$$

In a similar way, If the wave velocity parameter is added to the equation (2.13), the travelling wave equation is obtained. Then it is possible to compute the vibrational motion at coordinate 'x' by using

the equation (2.14), which is as a function of the wave velocity *'c'*, the time *'t'*, and the wavelength *'λ'*. This equation introduces the spatial variable *'x'* and the time variable *'t'* in the harmonic motion equation. In Figure 2.4, the equation (2.14) was plotted at two different times; the initial displacement at time zero is shown with a continuous blue line, and the displacement at time *'t_1'* is shown with a dashed red line. In this figure, *Δx* is the spatial displacement of the wave, and it is computed by multiplying the wave velocity by their travelling time (Physclips, 2019).

$$y = A\sin\left(2\pi\frac{x - c\cdot t}{\lambda}\right) \tag{2.14}$$

If the wavelength is the distance travelled by the wave in one cycle, and the period of the wave is the time required to complete one cycle, we can define the wave velocity as:

$$c = \frac{\lambda}{T} = \lambda\cdot f \tag{2.15}$$

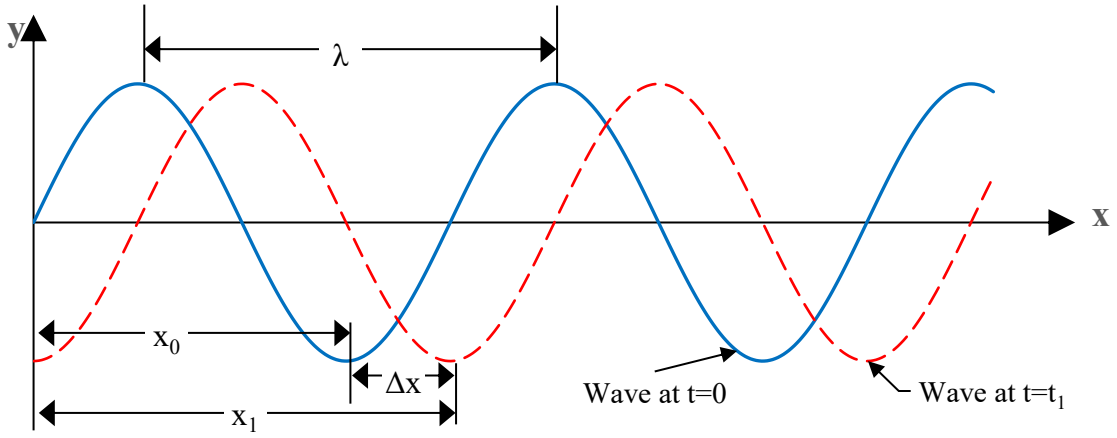

Figure 2.4 Graphic representation of the travelling wave

Substitution of (2.15) into (2.14) yields the equation (2.16). Each one of the variables had a similar coefficient: *2π/λ* for x and *2π/T* for time. The last is equal to the angular frequency (ω), which represents the number of cycles per unit time. The first term is an analogous expression in space, defining the number of cycles per unit length, this is called *wavenumber* (k).

$$y = A\sin\left(\frac{2\pi}{\lambda}x - \frac{2\pi}{T}t\right) \tag{2.16}$$

Therefore it is possible to write the equation (2.16) in a simpler way:

$$y = A\sin\left(kx - \omega t\right) \tag{2.17}$$

In the above equation, the wave velocity is indirectly expressed by the ratio between the angular frequency and the wavenumber.

$$\frac{\omega}{k} = \frac{2\pi/T}{2\pi/\lambda} = \frac{\lambda}{T} = c \tag{2.18}$$

Finally, for the general case of the travelling wave, it is needed to add the phase angle of the harmonic motions as in the previous section.

$$y = A\sin\left(kx - \omega t + \varphi\right) \tag{2.19}$$

2.6.2 Wave Equation

This section will review the mathematical background for the wave equation, starting from the derivation of the wave equation in a thin rod neglecting the lateral motion or Poisson effect for simplicity. Then the general form of the wave equation will be introduced along with their solution, discussing the origin and significance of the squared coefficient on it. And finally, the section will show the longitudinal and shear wave velocities with their proper equations.

2.6.2.1 Wave equation for long-thin rods

The forces applied to a small portion of the thin rod will be reviewed, using the second Newton's law *F=ma.* For this, the rod will be considered under dynamically varying stress along its length *σ(x, t)*. In Figure 2.5, the *'x'* coordinate refers to point along the rod while the displacements will be taken as *u(x, t).* A body force *q(x, t)* per unit volume is also being considered. The sum of all forces is shown in the equation (2.20), where ρ is the density of the material and A is the area of the cross-sectional area of the rod (Graff, 1975).

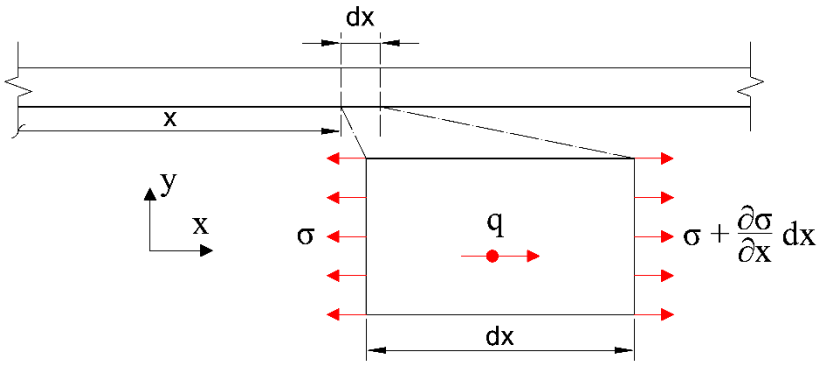

Figure 2.5 Stress and displacement diagram in a thin rod

$$-\sigma A+\left(\sigma+\frac{\partial\sigma}{\partial x}dx\right)A+q\cdot Adx=\rho Adx\cdot\frac{\partial^2 u}{\partial t^2} \tag{2.20}$$

Reducing terms of (2.20), the equation becomes the differential equation (2.21). Substituting Hooke's law in one direction (2.1) knowing the strain is defined by $\partial u/\partial x$. Equation (2.21) becomes (2.22). Assuming a homogeneous and isotropic material, therefore E and ρ can be considered as constants. Disregarding the body forces, and rearranging terms, the wave equation for thin rods results in (2.23)

$$\frac{\partial\sigma}{\partial x}+q=\rho\frac{\partial^2 u}{\partial t^2} \tag{2.21}$$

$$\frac{\partial}{\partial x}\left(E\frac{\partial u}{\partial x}\right)+q=\rho\frac{\partial^2 u}{\partial t^2} \tag{2.22}$$

$$\frac{E}{\rho}\frac{\partial^2 u}{\partial x}=\frac{\partial^2 u}{\partial t^2} \tag{2.23}$$

During the development of (2.23) some assumptions were done. The homogeneity of the material, a prismatic shape with a constant cross-sectional area, and the absence of body forces were mentioned. Although there are some other implicit assumptions: Plane sections remain plane, a uniform distribution of stress and as mentioned before the lateral expansions and contractions due to the Poisson effect were not considered (Graff, 1975).

2.6.2.2 General wave equation and its solution

The wave equation is typically represented as (2.24). By comparing it with the previous wave equation derived for a thin rod in (2.23), it is possible to see the resemblance quite easily. This form of wave equation holds not only for thin rods but for systems in general.

$$\frac{\partial^2 u}{\partial t^2} = c^2 \frac{\partial^2 u}{\partial x^2} \tag{2.24}$$

The solution of the wave equation looks like (2.25), where f_1 and f_2 are any arbitrary functions that describe the movement in the '*x'* coordinate (spatial variable) with a certain velocity '*c'* (time-variable), with both functions moving in opposite directions.

$$u(x,t) = f_1(x - ct) + f_2(x + ct) \tag{2.25}$$

Computing the derivatives of the moving forward part of *u(x, t)* the following equations are obtained:

$$\frac{\partial u}{\partial t} = -c \cdot f_1'(x - ct) \qquad \frac{\partial u}{\partial x} = f_1'(x - ct)$$

$$\frac{\partial^2 u}{\partial t^2} = c^2 \cdot f_1''(x - ct) \qquad \frac{\partial^2 u}{\partial x^2} = f_1''(x - ct)$$

Substituting the second partial derivatives of *u(x, t)* into (2.24). It becomes evident that the constant '*c'* corresponds to the wave velocity.

The travelling wave equation (2.17) has the same structure as the wave equation solution (2.25). It's not hard to prove the travelling equation (2.17) is a solution for the wave equation by following the same procedure as in this section.

2.6.2.3 Wave Velocity

The wave velocity refers to the speed at which the vibrational oscillations move through the medium. The observed wave movement is the result of the phase relationship between oscillations. There are three wave velocities in wave motion, distinct to each other but at the same time mathematically connected (Pain, 2005):

- Particle velocity: simple harmonic velocity of the oscillation at each point in space.

- Phase velocity: Velocity of planes with the same phase/crest moves through the medium.
- Group velocity: The overall velocity of a group of waves of different frequencies, wavelengths and velocities that are superposed. With time the group would disperse due to their individual velocities (phase velocities) would vary in different mediums.

2.6.2.3.1 Wave velocity equations

Recalling the wave equation for a thin rod (2.23), and comparing it with the general wave equation structure (2.24), and knowing the constant 'c' represent the wave velocity. It becomes evident the wave velocity for a thin rod is (2.26). Although, several assumptions were made when obtaining (2.23), the most critical being the absence of lateral contractions or expansions due to Poisson's effect, and therefore assuming a Poisson's ratio equal to zero.

$$c = V_{\mathrm{Pr}} = \sqrt{\frac{E}{\rho}} \tag{2.26}$$

To consider the Poisson's effect, the generalized Hooke's law equation (2.8) needs to be used instead of the one-dimensional equation (2.1). Knowing the infinitesimal strain tensor ε_{ij} (Cauchy's Strain Tensor) is defined as (2.27) (Pain, 2005).

$$\varepsilon_{ij} = \frac{1}{2}\left(u_{j,i} + u_{i,j}\right) = \frac{1}{2}\begin{bmatrix} 2u_{1,1} & u_{2,1}+u_{1,2} & u_{3,1}+u_{1,3} \\ u_{1,2}+u_{2,1} & 2u_{2,2} & u_{3,2}+u_{2,3} \\ u_{1,3}+u_{3,1} & u_{2,3}+u_{3,2} & 2u_{2,2} \end{bmatrix} \tag{2.27}$$

Then by substituting (2.27) into the expanded matrix form of the general Hooke's Law (2.9).

$$\sigma_{ij} = G\begin{bmatrix} 2u_{1,1} & u_{2,1}+u_{1,2} & u_{3,1}+u_{1,3} \\ u_{1,2}+u_{2,1} & 2u_{2,2} & u_{3,2}+u_{2,3} \\ u_{1,3}+u_{3,1} & u_{2,3}+u_{3,2} & 2u_{3,3} \end{bmatrix} + \lambda_p \begin{bmatrix} u_{1,1} & 0 & 0 \\ 0 & u_{2,2} & 0 \\ 0 & 0 & u_{3,3} \end{bmatrix} \tag{2.28}$$

And substituting now (2.28) into the second Newton's law (2.21), but without considering any external forces, and assuming the medium is isotropic and homogeneous, the wave equation becomes:

$$G\begin{bmatrix} 2u_{1,11} & u_{2,12}+u_{1,21} & u_{3,13}+u_{1,31} \\ u_{1,21}+u_{2,12} & 2u_{2,22} & u_{3,23}+u_{2,32} \\ u_{1,31}+u_{3,13} & u_{2,32}+u_{3,23} & 2u_{3,33} \end{bmatrix} + \lambda_p \begin{bmatrix} u_{1,11} & 0 & 0 \\ 0 & u_{2,22} & 0 \\ 0 & 0 & u_{3,33} \end{bmatrix} = \rho \frac{\partial^2}{\partial t^2} u_{ij} \tag{2.29}$$

Based on the principle of superposition for differential equations. The wave equation for homogeneous isotropic solids (2.29) can be treated as each one of their parts. The equation (2.29) can be decomposed into two groups:

$$\frac{\left(2G+\lambda_p\right)}{\rho}u_{i,ii}=\frac{\partial^2}{\partial t^2}u_{ii} \quad i=\{1,2,3\} \tag{2.30}$$

$$\frac{G}{\rho}u_{i,ji}=\frac{\partial^2}{\partial t^2}u_{ii}\,; \quad i,j=\{1,2,3\}\,; \quad i\neq j \tag{2.31}$$

One group of equations (2.30) for the diagonal in the matrix, corresponding to motions in the longitudinal direction along the three different axes. And the second group of equations (2.31) for the remaining terms of the matrix, which corresponds to the transverse wave motions.

Equations (2.30) and (2.31) shows the presence of two different waves, longitudinal and transverse waves as discussed before. Each wave propagating at a different speed. The longitudinal waves (Also called P-waves) travel at a V_p speed. And the transversal or shear waves (S-waves) at V_s. These two types of wave propagation will be discussed in the next section of this chapter.

$$V_p=\sqrt{\frac{\lambda_p+2G}{\rho}} \tag{2.32}$$

$$V_r=\sqrt{\frac{G}{\rho}} \tag{2.33}$$

Replacing the Lamé parameters for Young's modulus and Poisson's ratio, using the relationships given in (2.6) and (2.7). The wave velocities become:

$$V_p=\sqrt{\frac{E\left(1-\nu\right)}{\rho\left(1+\nu\right)\left(1-2\nu\right)}} \tag{2.34}$$

$$V_S=\sqrt{\frac{E}{2\rho\left(1+\nu\right)}} \tag{2.35}$$

If Poisson's ratio is equal to zero, the longitudinal wave velocity (2.34) has the same value as the one found in (2.26). The longitudinal wave velocity is always significantly higher than the transverse wave velocity. The ratio of transverse to longitudinal wave velocity is shown in (2.36). The ratio

between the two velocities is plotted in Figure 2.6. The transverse wave velocity is always less than 0.71 of the longitudinal velocity. The ratio reaches 0.5 with a Poisson's ratio of 1/3 ($0.\overline{3}$), and it tends to become zero as the Poisson's ratio gets to its limit value of 0.5.

$$\alpha_k = \frac{V_S}{V_p} = \sqrt{\frac{(1-2v)}{2(1-v)}} \tag{2.36}$$

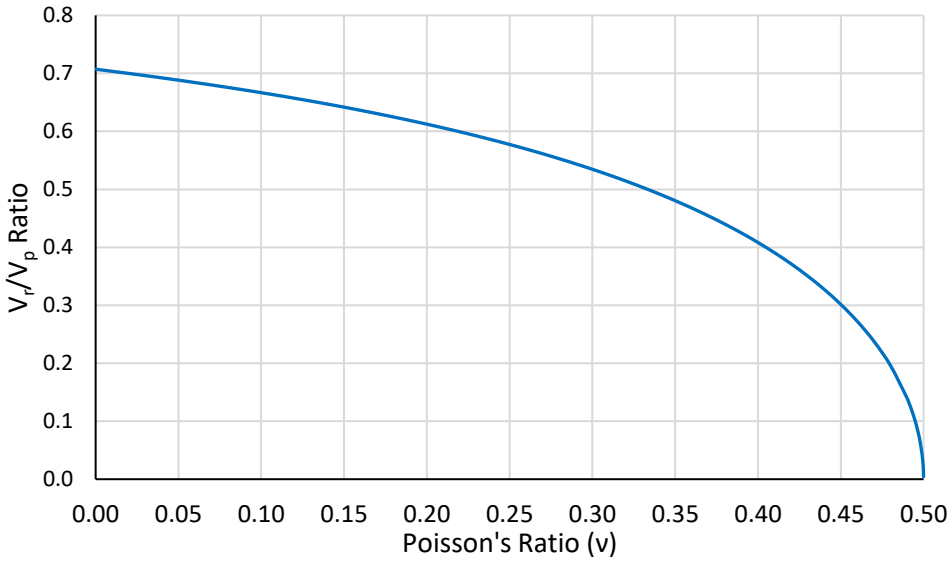

Figure 2.6 V_r/V_p ratio variation as a function of Poisson's ratio

2.6.3 Free Vibrations

The vibrational behaviour of a solid object can be obtained using the wave equation for each particular case. The frequencies that satisfy these differential equations are called natural frequencies and they are also referred to resonant frequencies for the objects. If the solid is excited by a force, its response will be higher around these frequencies.

2.6.3.1 Axial vibration in a Rod

For a thin rod for which equation was derived in 2.6.2.1 obtaining (2.23). By assuming the vibration response of the cylinder is in the form of (2.37).

$$u(x,t) = U(x)\cos(\omega t - \varphi) \tag{2.37}$$

By substituting (2.37) into (2.23) and reducing terms:

$$\frac{\partial^2 U}{\partial x} + \omega^2 \frac{\rho}{E} \frac{\partial^2 U}{\partial t^2} = 0 \tag{2.38}$$

Therefore, the eigenvalue for the differential equation (2.38) is:

$$\lambda_e = \omega \sqrt{\frac{\rho}{E}} \tag{2.39}$$

Solving the general solution shown in (2.40) considering the rod of length *'L'* with for the boundary conditions of force-free at both ends defined by equations (2.41) and (2.42).

$$U(x) = A_1 \cos(\lambda_e x) + A_2 \sin(\lambda_e x) \tag{2.40}$$

$$\frac{\partial U(0)}{\partial x} = 0 \tag{2.41}$$

$$\frac{\partial U(L)}{\partial x} = 0 \tag{2.42}$$

The boundary condition equations become:

$$-A_1 \lambda_e \sin(0) + A_2 \lambda_e \cos(0) = 0 \therefore A_2 = 0 \tag{2.43}$$

$$-A_1 \lambda_e \sin(\lambda_e L) + A_2 \lambda_e \cos(\lambda_e L) = 0 \tag{2.44}$$

Obtaining:

$$A_1 \lambda_e \sin(\lambda_e L) = 0 \tag{2.45}$$

For non-trivial solutions ($\lambda_e \neq 0$), the frequency equation to solve is:

$$\sin(\lambda_e L) = 0 \tag{2.46}$$

For which solutions are:

$$\lambda_e L = n \cdot \pi \tag{2.47}$$

Re-writing equation (2.47), substituting the eigenvalue (2.39) into it and solving for the circular frequency the equation (2.48) is obtained, where *'n'* is the mode number.

$$\omega_n = \frac{n \cdot \pi}{L} \sqrt{\frac{E}{\rho}} \tag{2.48}$$

Changing the circular frequency for cycles per second, considering only the frequency for the first mode of vibration, and, replacing the density for its value for a cylinder as described in where D is the cylinder diameter.

$$\rho = \frac{m}{V} = \frac{m}{AL} = \frac{4m}{\pi D^2 L} \tag{2.49}$$

Then the frequency of the first longitudinal mode becomes:

$$f_l = \sqrt{\frac{\pi}{16}\frac{E \cdot D^2}{m \cdot L}} \approx \sqrt{\frac{E \cdot D^2}{5.093 \cdot m \cdot L}} \tag{2.50}$$

The equation (2.50) defines the natural longitudinal or axial frequency as a function of the cylinder properties, it's elastic modulus, the diameter, its length and its mass. The frequency equation (2.50) is obtained under the same assumptions made to derive the differential equation (2.23). These assumptions are for a thin rod, (i.e. a rod with a diameter extremely small compared with their length), where the Poisson's effect is not as relevant.

2.6.3.2 Flexural vibration in a Rod

To derive the differential equation of motion for a beam element, the same approach as with the axial case is going to be followed. Recurring to Newton's second law ($F=ma$) and applying it to the free body diagram shown in Figure 2.7, where *'S'* represents the shear forces, *'M'* the bending moment, and *'q'* is the external forces applied to the beam element with density 'ρ' and area *'A'*.

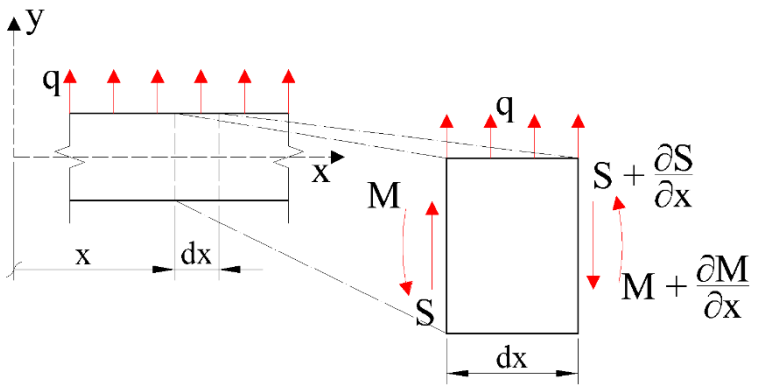

Figure 2.7 Free body diagram of a beam with internal and external forces

Then Newton's second equation would look like (2.51), assuming it's a prismatic beam of constant area and density, and without considering external forces.

$$-\frac{\partial S}{\partial x} = \rho \cdot A \frac{\partial u_y}{\partial t^2} \tag{2.51}$$

For a Euler-Bernoulli beam where plane sections remain plane, the extensional strain can be related to the curvature of the beam. For small deformations, the moment-curvature of the beam can be approximated by (2.52), where *'E'* is the Young's modulus and *'I'* is the moment of inertia in the bending axis of the beam (Kang & Zhong-Ci, 1996).

$$M = EI \frac{\partial^2 u_y}{\partial x^2} \tag{2.52}$$

The internal shear forces and the bending moment are related to each other with the equation:

$$S = \frac{\partial M}{\partial x} \tag{2.53}$$

Substituting equations (2.52) and (2.53) into the differential equation (2.51), the latter becomes:

$$-\frac{\partial^2}{\partial x^2}\left(EI \frac{\partial^2 u_y}{\partial x^2} \right) = \rho \cdot A \frac{\partial^2 u_y}{\partial t^2} \tag{2.54}$$

Re-arranging equation (2.54), and assuming the beam material is isotropic and homogeneous, and therefore independent of *'x'*. The equation of motion for Euler-Bernoulli beams results in:

$$EI \frac{\partial^4 u_y}{\partial x^4} + \rho \cdot A \cdot dx \frac{\partial^2 u_y}{\partial t^2} = 0 \tag{2.55}$$

Assuming as in the axial vibration case, a solution of the type:

$$u_y = U(x)\cos(\omega t - \varphi) \tag{2.56}$$

Substituting equation (2.56) into the differential equation for transverse motion (2.55).

$$EI \cos(\omega t - \varphi) \frac{\partial^4 U}{\partial x^4} - \rho \cdot A \cdot U \cdot \omega^2 \cos(\omega t - \varphi) = 0 \tag{2.57}$$

Reducing the above equation and re-arranging it:

$$\frac{\partial^4 U}{\partial x^4} - \frac{\rho A \cdot \omega^2}{EI} U = 0 \tag{2.58}$$

The eigenvalue for this differential equation then is:

$$\lambda_e{}^4 = \frac{\rho A \cdot \omega^2}{EI} \tag{2.59}$$

With the general solution of the equation (2.58) being in the form of:

$$U(x) = A\sin(\lambda x) + B\cos(\lambda x) + C\sinh(\lambda x) + D\cosh(\lambda x) \tag{2.60}$$

The boundaries conditions for a beam of length *'L'* with both ends free (or in other words with no shear forces nor bending moments at both ends) are:(Graff, 1975):

$$\frac{\partial^2 U(0)}{\partial x^2} = 0\,; \quad \frac{\partial^2 U(L)}{\partial x^2} = 0 \tag{2.61}$$

$$\frac{\partial^3 U(0)}{\partial x^3} = 0\,; \quad \frac{\partial^3 U(L)}{\partial x^3} = 0 \tag{2.62}$$

The boundary conditions ((2.61) and (2.62)) result in the following linear equations:

$$\begin{bmatrix} 0 & -\lambda^2 & 0 & \lambda^2 \\ -\lambda^3 & 0 & \lambda^3 & 0 \\ -\lambda^2\sin(\lambda L) & -\lambda^2\cos(\lambda L) & \lambda^2\sinh(\lambda L) & \lambda^2\cosh(\lambda L) \\ -\lambda^3\cos(\lambda L) & \lambda^3\sin(\lambda L) & \lambda^3\cosh(\lambda L) & \lambda^3\sinh(\lambda L) \end{bmatrix} \begin{bmatrix} A \\ B \\ C \\ D \end{bmatrix} = \begin{bmatrix} 0 \\ 0 \\ 0 \\ 0 \end{bmatrix} \tag{2.63}$$

To solve the system of equations, the determinant of the coefficient matrix must be zero. Solving the determinant leads into the following equation:

$$\cosh(\lambda L)\cos(\lambda L) = 1 \tag{2.64}$$

Solving numerically the above equation for λL, result in the following roots:

$$\begin{aligned} \lambda_{e1} L &\approx 4.730040745 \\ \lambda_{e2} L &\approx 7.853204624 \\ \lambda_{e3} L &\approx 10.99560784 \\ \lambda_{e4} L &\approx 14.13716549 \end{aligned} \tag{2.65}$$

Recalling the eigenvalue (2.59) and fusing it with the roots found in (2.65), the fundamental flexural/transverse frequency equation for the beam is obtained:

$$(\lambda_{en} L)^4 = \frac{\rho A \cdot \omega^2}{EI} L^4 \;\therefore \omega = 2\pi f_t = \frac{(\lambda_{en} L)^2}{L^2}\sqrt{\frac{EI}{\rho A}} \tag{2.66}$$

If a cylindrical beam is considered, the area *'A'* and the inertia *'I'* can be substituted with the formulas for a circle of diameter *'D'*. Leaving the frequency equation (2.66) in terms of the mass, diameter and length of the cylinder:

$$f_t = \sqrt{\frac{\left(\lambda_{en} L\right)^4 E \cdot D^4}{2^8 \pi \cdot mL^3}} \tag{2.67}$$

Reducing and computing numerical values, the flexural frequency for a cylinder becomes:

$$f_t = \sqrt{\frac{E \cdot D^4}{1.6067 \cdot mL^3}} \tag{2.68}$$

The equation (2.68) defines the natural frequency for the first flexural mode of a Euler-Bernoulli, under the assumptions made, during this section, which ignores shear deformation, rotational inertia, and Poisson effect. Therefore, this equation would be valid for rods with a small diameter compared with its length. When the ratio between length and diameter (L/D) is above 20. the equation (2.68) starts to approximate the beam behaviour adequately.

2.6.4 Propagation Modes

Along this section of Wave Propagation Theory, the wave equation and the intrinsic velocity of a wave through a medium has been discussed. In the above subsection (Wave velocity equations), it was already inferred there were two different types of waves moving at different velocities through a homogeneous and isotropic medium. In this subsection, the main types of wave propagation will be briefly discussed.

2.6.4.1 Body Waves

The waves that propagate along the interior of any solid body are called body waves. They were discovered by Poisson in 1829 (Pujol, 2003). There are two types of body waves, longitudinal and transversal waves, or also called P and S waves respectively. The mathematical existence of these two waves was demonstrated in subsection 2.6.2.3.1.

2.6.4.1.1 Compression waves

The first type of wave to be discussed are the waves that involve movements of compression and dilation only. These waves are commonly called P-waves, where P stands for primary or push-pull. They are considered primary waves because they possess the highest wave speed and therefore they

arrive first to any measuring point (Fowler, 2005). Figure 2.8 shows the P-wave propagation within a solid body. The material expands and contracts as the wave travels through the medium.

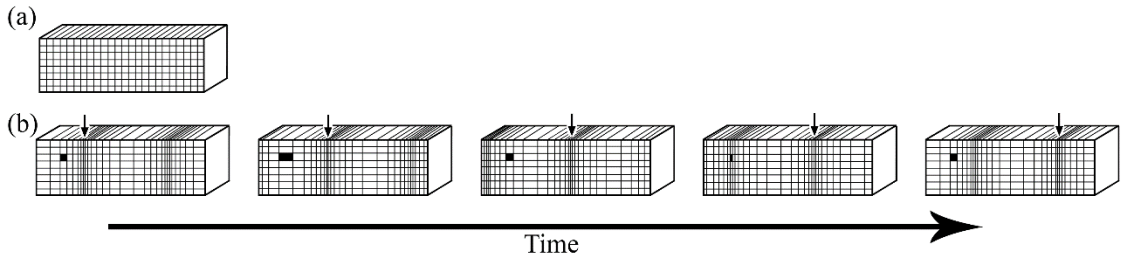

Figure 2.8 Deformation of a solid body (a) due to the P-waves (b). The stages show the wave travelling through the solid body. The arrows mark the crest of the wave at each stage. (Fowler, 2005) p. 101.

The P-wave propagates in a sphere shape from the source point in all directions. In Figure 2.8 the deformation is simplified into 1 dimension. Figure 2.13 shows a transverse section of a half-space where the radial expansion of the P-wave is represented. The surface area of the P-wave as it travels keeps increasing and in the same way, it's energy per unit area decreases. Along the surface of a halfspace, the amplitude of the P-wave decreases in proportion to the ratio $1/r^2$, while within the body it decreases as 1/r (Richart et al., 1970).

2.6.4.1.2 Shear waves

Shear or transverse waves are also called S-waved, where S stands for secondary, shear or shake. They are called secondary waves since they are second to arrive at any point within the solid body. The S-waves do not change the volume of the material, it involves a rotational movement of the material as the waves pass through it. These waves can have horizontal or vertical polarization. Figure 2.9 shows the S-waves with vertical polarization through a solid, the horizontal polarization would be exactly the same as in Figure 2.9, but in the horizontal direction (or with a rotation of 90°. Shear waves occur only in solid bodies, they cannot form in fluids. Fluids are not capable of sustain shear. On fluids like water and air, only P-waves are present (Fowler, 2005).

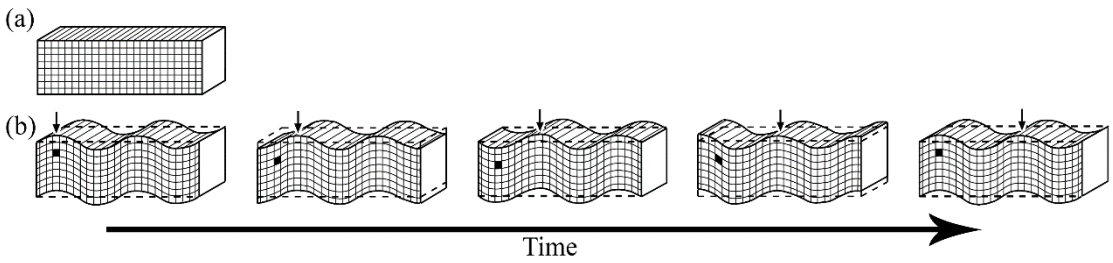

Figure 2.9 Deformation of a solid body (a) due to shear waves (b). The stages show the shear wave progression while travelling through the solid. The vertical component of the shear waves is shown only in the figure. (Fowler, 2005) p. 101.

In the same way, as with the P-waves, S-waves also propagates in all direction within a solid body. Figure 2.9 shows only the waves in a 1 directional space, although they propagate in a sphere shape as shown in Figure 2.13. S-waves also attenuate their amplitudes as a function of the distance to the source in the same ways as P-waves. The reduction in the surface of a half-space happened at a ratio of $1/r^2$, while within the body, the reduction is as 1/r (Richart et al., 1970).

2.6.4.2 Surface Waves

The previous section discussed the waves within an infinite media with no boundaries. This section will discuss the waves propagated along the surface of a half-space. These waves are derived from the same equations shown before (2.29), but imposing appropriate boundary conditions due to the free surface of a half-space. The derivation of the surface wave equations will not be derived in this document, although the reader can look for the mathematical derivations of the equations presented below into Chapter 6 of (Graff, 1975).

Surface waves do not penetrate deep into the medium but have larger amplitudes compared with body waves. Due to the shallow nature of these waves, they spread in a cylindrical waveform as shown in Figure 2.13, and because of this, the amplitude of the surface wave reduces in proportion to $1/\sqrt{r}$. They also have lower wave velocities than the body waves, and therefore they arrive at any given point after the P and the S waves (Fowler, 2005).

There are two main types of surface waves: Rayleigh waves, named after Lord Rayleigh, who predicted them in 1887; and Love waves, named after A. E. H. Love who predicted them in 1911 (Fowler, 2005).

2.6.4.2.1 Raleigh waves

Rayleigh waves occur near the surface of a medium with boundaries. The wave propagation of the Rayleigh wave in an infinite half-space is done in a retrograde motion, which means it will generate elliptical rotation near the surface with the surface rotating backwards with respect to the wave propagation direction, as it is shown in Figure 2.10.

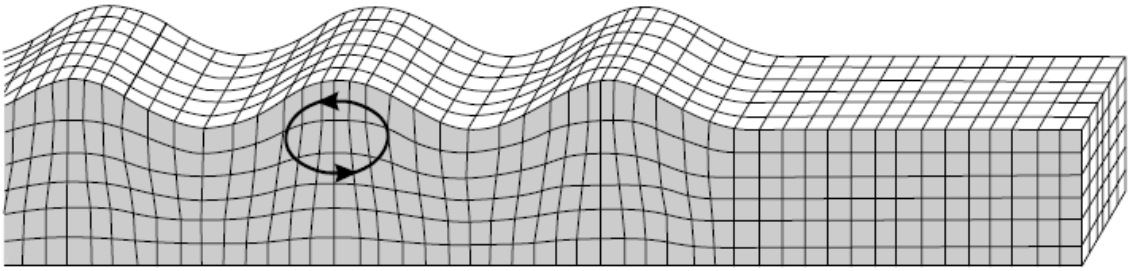

Figure 2.10 Rayleigh wave motion within a body surface. Arrows show the rotation direction of the wave when the wave propagates to the right. (Fowler, 2005) p. 105.

Rayleigh wave on a homogeneous, isotropic infinite half-space medium is not dispersive, which means that its velocity does not depend on the frequency. On the other hand, when the medium is not an infinite half-space, having a relatively close bottom boundary, or when the medium is made of layers with different densities and stiffness, the Rayleigh wave will be dispersive. When a wave is dispersive means that it will travel with two different speeds, called: phase velocity and group velocity. These two velocities were previously defined in section 2.6.2.3.

The horizontal and vertical displacements for the Rayleigh wave are given by (Graff, 1975):

$$u_x = Ai\left(k \cdot e^{-\bar{\alpha}z} - \frac{\bar{\beta}^2 + k^2}{2k} \cdot e^{-\bar{\beta}z} \right) e^{i\cdot(kx-\omega t)} \tag{2.69}$$

$$u_z = A\left(-\bar{\alpha} e^{-\bar{\alpha}z} + \frac{\bar{\beta}^2 + k^2}{2\bar{\beta}} e^{-\bar{\beta}z} \right) e^{i(kx-\omega t)} \tag{2.70}$$

Where 'A' is an amplitude constant, *i* is the imaginary number, k is the wavenumber and α and β are defined by equations (2.71).

$$\bar{\alpha}^2 = -\alpha^2 = k^2 - \frac{\omega^2}{V_P{}^2}; \quad \bar{\beta}^2 = -\beta^2 = k^2 - \frac{\omega^2}{V_S{}^2} \tag{2.71}$$

The frequency equation for Rayleigh surface wave in a homogeneous, isotropic half-space medium is:

$$\left(\overline{\beta}^2 + k^2\right)^2 - 4\bar{\alpha}\bar{\beta}k^2 = 0 \tag{2.72}$$

Defining the following variables

$$K_{RS} = \frac{V_R}{V_S} = \frac{\omega}{V_S k} \tag{2.73}$$

$$\alpha_k K_{RS} = \frac{V_R}{V_P} = K_{RP} = \frac{\omega}{V_P k} \tag{2.74}$$

$$\alpha_k = \frac{V_S}{V_p} = \sqrt{\frac{(1-2\nu)}{2(1-\nu)}} \tag{2.75}$$

And using the following relationships:

$$\frac{\bar{\alpha}^2}{k^2} = 1 - {\alpha_k}^2 K_{RS}\,; \quad \frac{\bar{\beta}^2}{k^2} = 1 - K_{RS} \tag{2.76}$$

Substituting (2.71) with (2.76) relationships into (2.72), expanding and rearing, (2.72) becomes:

$${K_{RS}}^6 - 8{K_{RS}}^4 + \left(24 - 16{\alpha_k}^2\right){K_{RS}}^2 + 16\left({\alpha_k}^2 - 1\right) = 0 \tag{2.77}$$

The equation (2.77) can be considered as a cubic equation by solving for K_{RS}^2. The equation (2.77) does not depend on frequency, and it can be solved for any given Poisson's ratio. The results of solving for different values of Poisson's ratio between 0 an 0.5 are plotted in Figure 2.11. The left axis shows the ratios V_R/V_P and V_S/V_P. The right axis shows the ratio of V_R/V_S (Richart et al., 1970). An equation to approximate the ratio between the R-wave and the S-wave velocities as a function of the Poisson's ratio is shown below (2.78) (Graff, 1975). As can it can be seen in Figure 2.11, the approximate equation gives practically the same ratios for intermediate values of the Poisson's ratio.

$$K_{RS} \approx \frac{0.87 + 1.12\nu}{1 + \nu} \tag{2.78}$$

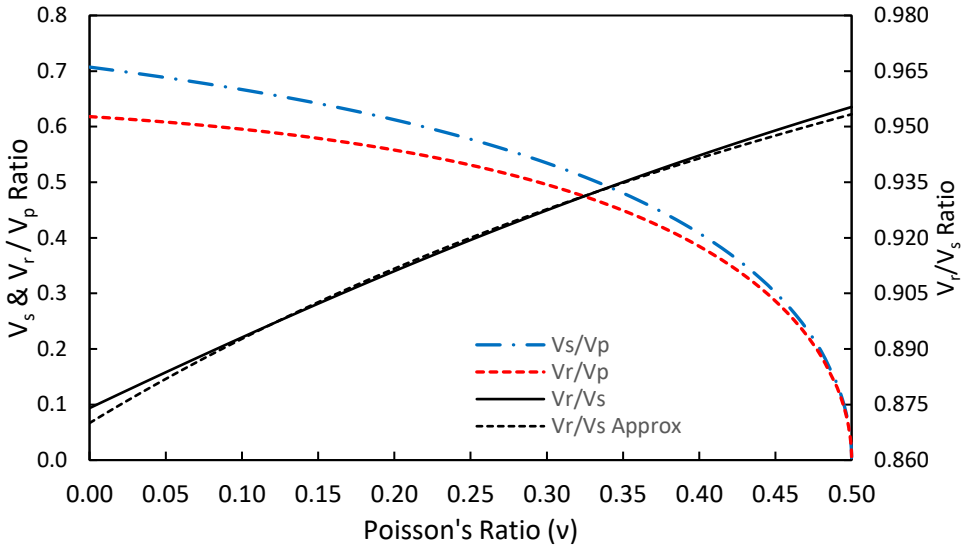

Figure 2.11 Different wave velocity ratios comparison as a function of Poisson's ratio. (Vs/Vp and Vr/Vp ratio axis on the left. Vr/Vs ratio on the right).

As mention before, Rayleigh waves do not penetrate deep into the solid, their larger amplitudes are on the surface and decay exponentially with depth. The depth of penetration depends on the wavelength. The longer the wavelength, (and therefore the lower the frequency) the deeper it gets. This relationship is shown in Figure 2.12. The amplitudes at any given depth can be found using the amplitude factor of equations (2.69) and (2.70) as a function of depth.

$$U_x(z) = k \cdot e^{-\bar{\alpha} z} - \frac{\bar{\beta}^2 + k^2}{2k} \cdot e^{-\bar{\beta} z} \tag{2.79}$$

$$U_z(z) = -\bar{\alpha} e^{-\bar{\alpha} z} + \frac{\bar{\beta}^2 + k^2}{2\bar{\beta}} e^{-\bar{\beta} z} \tag{2.80}$$

Normalizing the depth with the wavelength in equations (2.79) and (2.80), the substitution of the equation (2.81) and the relationships (2.76) is required. Leaving the displacement magnitudes as functions of the Poisson's ratio and normalized depth only.

$$\bar{z} = \frac{z}{\lambda} = \frac{z \cdot k}{2\pi} \therefore z = \frac{2\pi}{k} \bar{z} \tag{2.81}$$

Equations (2.79) and (2.80) become

$$U_x(\bar{z}) = e^{-2\pi\sqrt{1-\alpha_k K_{RS}}\bar{z}} - \frac{2 - K_{RS}}{2} \cdot e^{-2\pi\sqrt{1-K_{RS}}\bar{z}} \tag{2.82}$$

$$U_z(\bar{z}) = -\sqrt{1-\alpha_k K_{RS}}\, e^{-2\pi\sqrt{1-\alpha_k K_{RS}}\,\bar{z}} + \frac{2-K_{RS}}{2\sqrt{1-K_{RS}}}\, e^{-2\pi\sqrt{1-K_{RS}}\,\bar{z}} \tag{2.83}$$

Using $\hat{a} = \sqrt{1-\alpha_k K_{RS}}$ and $\hat{b} = \sqrt{1-K_{RS}}$ substitutions, both equations can be simplified as:

$$U_x(\bar{z}) = e^{-2\pi\hat{a}\cdot\bar{z}} - \frac{\hat{b}^2+1}{2}\cdot e^{-2\pi\hat{b}\cdot\bar{z}} \tag{2.84}$$

$$U_z(\bar{z}) = -\hat{a}\cdot e^{-2\pi\hat{a}\cdot\bar{z}} + \frac{\hat{b}^2+1}{2\hat{}} \quad {}^{-2\pi\hat{b}\cdot\bar{z}} \tag{2.85}$$

The amplitudes resulted from (2.84) and (2.85) are plotted in Figure 2.11. The ratios between the R-wave and the S-wave velocities were found by solving the equation (2.77) for different Poisson's ratios. The magnitudes for both equations were normalized with respect to the surface magnitude of the vertical displacement.

The Rayleigh wave vertical component is greater than the horizontal component. For low values of Poisson's ratio, the vertical displacement is 1.2 times the horizontal at the surface. As the Poisson's ratio reaches its maximum value of 0.5, the vertical/horizontal component ratio increase to 1.8.

The horizontal component changes its direction, and therefore the direction of the particle rotation inverse at a depth between 0.15 and 0.25 wavelengths depending on the Poisson's ratio. The amplitudes of both components decrease exponentially with depth, but as it can be seen in Figure 2.12, the horizontal component approaches zero faster than the vertical component. A higher value of the Poisson's ratio increases considerably the vertical component amplitudes and they also slow down the decay of amplitudes with depth. Although for a Poisson's ratio of 0.25, both components of Rayleigh waves reach almost zero at 1.5 wavelength depth.

Figure 2.13 shows an infinite half-space representing the wave propagation modes discussed until now (P-wave, S-wave, and R-wave). The positions of the waves are relative to their wave velocities for a medium with a Poisson's ratio of 0.25, It shows P-wave velocity is significantly higher than the others, while the Rayleigh wave is the slowest but close to the S-wave velocity.

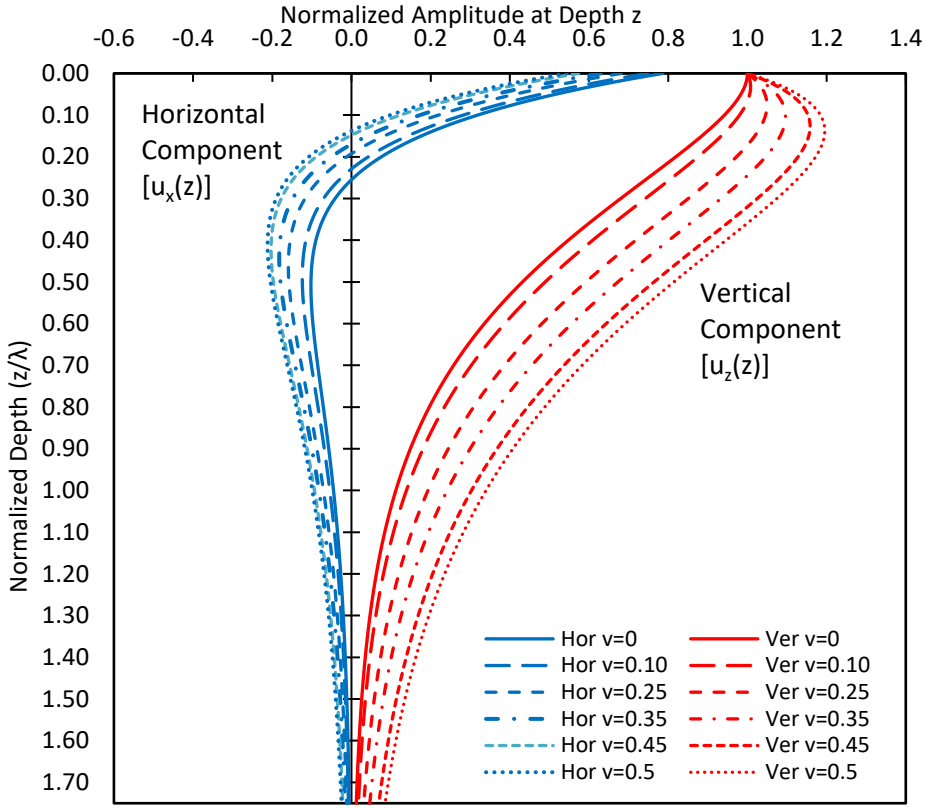

Figure 2.12 Normalized amplitudes for the horizontal and vertical components of the Rayleigh wave at different depths (normalized with wavelengths). Plots for different Poisson's ratio values,

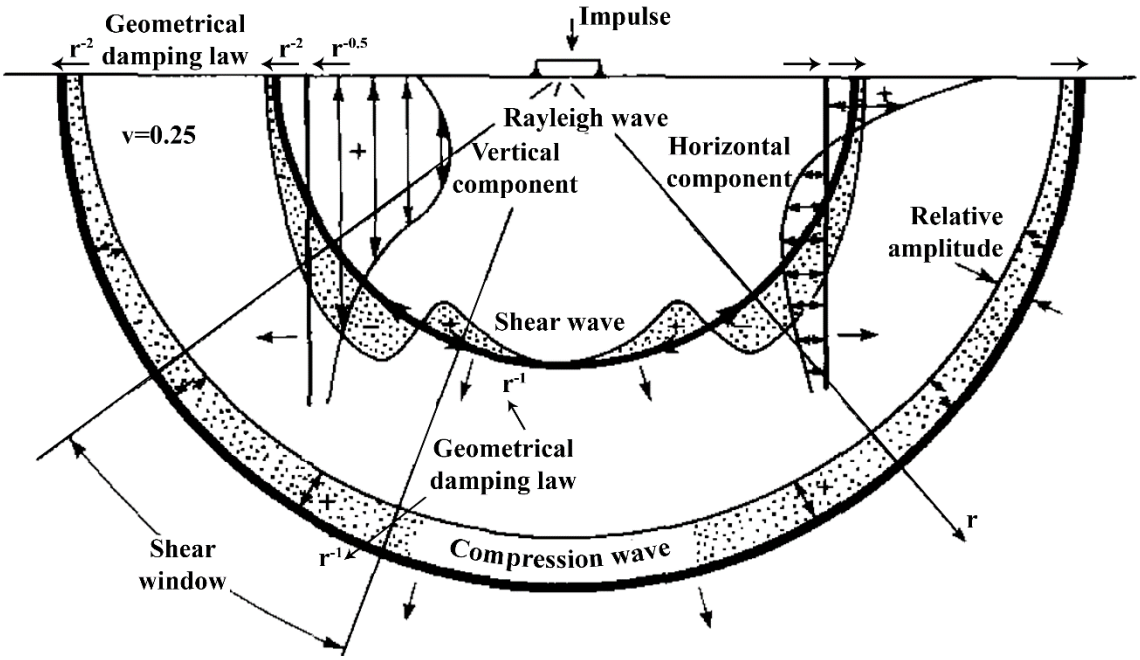

Figure 2.13 Wave propagation within a homogeneous, isotropic elastic half-space, for P, S and R waves. (Richart et al., 1970) p. 91.

The intrinsic spherical propagation of the P and S waves and the cylindrical propagation of the Rayleigh wave is also shown in Figure 2.13. Because of their spherical propagation, both body waves (P-waves and S-waves), experience geometrical damping with their amplitude decreasing in proportion to $1/r^2$ at the surface and 1/r within the body directly under the wave source. On the other hand, the Rayleigh wave amplitudes decrease at a rate of $1/\sqrt{r}$ (Richart et al., 1970).

In 1955, Miller and Pursey determined the energy distribution for a vertically oscillating energy source on the surface of a homogeneous, isotropic elastic half-space along among the three types of waves discussed until now. They found more than half of the energy propagates as Rayleigh waves. The percentual distribution of energy among the three waves can be found in Table 2.2 (Graff, 1975).

Table 2.2 Energy distribution among P, S and R wave for a homogeneous, isotropic, elastic half-space

Wave Type	Energy %
P-wave	7
S-wave	26
R-wave	67
	100

2.6.4.2.2 Love waves

A.H.E. Love was the first to predict the existence of the Love waves also called L-waves. Love waves occur when the S-wave velocity increase with depth. They got generated as a result of reflections of the S-wave horizontal component near the surface. The wave propagation is transverse and horizontal without significant vertical component. The particle motion is shown in Figure 2.14.

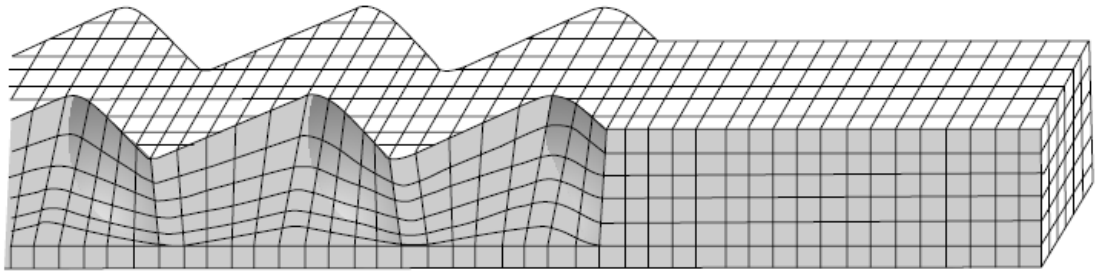

Figure 2.14 Love wave particle motion through a medium. (Fowler, 2005) p. 105.

Love waves will not be of interest to this study given that any of the tests done on the study will generate this kind of wave. As mention before L-waves are produced when S-wave velocity increase with depth, which means the material is layered, increasing in density or stiffness with depth.

2.6.4.2.3 Lamb waves

Lamb waves are a special case of Rayleigh waves that manifest within a plate, instead of an infinite half-space. On a plate with a relatively small thickness, the Rayleigh wave penetrates along the whole depth of the medium. Therefore, the Rayleigh wave will interact with the bottom boundary. This interaction generates a series of reflections from several angles that will interact with each other in a constructive and destructive way. Figure 2.15 shows a cross-section of a plate with thickness t_p, which is the geometry of interest in this section.

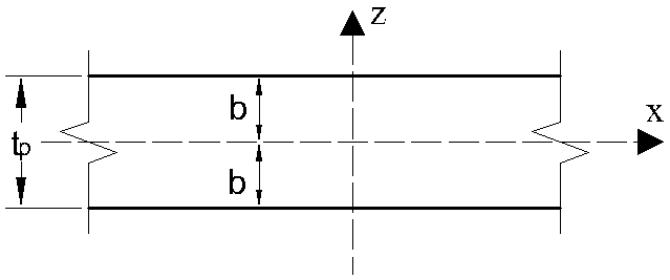

Figure 2.15 Plate diagram with the reference axis

The solution of the wave equation results in two types of displacements along the plate surfaces: Symmetric and antisymmetric. The equations that described the symmetric displacement on the horizontal ($u_x^{<s>}$) and vertical component ($u_z^{<s>}$) on the Rayleigh-Lamb theory are shown below.

$$u_x^{<s>} = Ai\left(\frac{\left(k^2-\beta^2\right)\sin\left(\beta b\right)}{2\alpha\sin\left(\alpha b\right)}\cos\left(\alpha z\right)+\beta\cos\left(\beta z\right)\right)e^{i(kx-\omega t)} \tag{2.86}$$

$$u_z^{<s>} = A\left(-\frac{\left(k^2-\beta^2\right)\sin\left(\beta b\right)}{2k\sin\left(\alpha b\right)}\sin\left(\alpha z\right)+k\sin\left(\beta z\right)\right)e^{i(kx-\omega t)} \tag{2.87}$$

Where b is half the thickness plate and z is the depth coordinate within the plate as described in Figure 2.15. 'k' is the wavenumber and 'ω' is the circular frequency. The variables α and β are the same as defined before in (2.71), and recalled below:

$$\alpha^2 = \frac{\omega^2}{V_P^{\,2}} - k^2; \quad \beta^2 = \frac{\omega^2}{V_S^{\,2}} - k^2 \tag{2.88}$$

On the other hand, the antisymmetric displacements for both, horizontal and vertical components ($u_x^{<a>}$, $u_z^{<a>}$) are presented below:

$$u_x^{<a>} = -Ai\left(\frac{\left(k^2-\beta^2\right)\cos\left(\beta b\right)}{2\alpha\cos\left(\alpha b\right)}\sin\left(\alpha z\right)+\beta\sin\left(\beta z\right)\right)e^{i(kx-\omega t)} \tag{2.89}$$

$$u_z^{<a>} = -A\left(\frac{\left(k^2-\beta^2\right)\cos\left(\beta b\right)}{2k\cos\left(\alpha b\right)}\cos\left(\alpha z\right)+k\cos\left(\beta z\right)\right)e^{i(kx-\omega t)} \tag{2.90}$$

The symmetric and antisymmetric equations for displacements on a plate depending on the depth coordinate 'z', but also in the frequency and its phase velocity, which are correlated to the wavelength or wavenumber. The frequency equations that need to be satisfied for a certain wave number and phase velocity are given below. The equation (2.91) for the symmetric waves and (2.92) for the antisymmetric waves.

$$\frac{\tan\left(\beta b\right)}{\tan\left(\alpha b\right)} = -\frac{4\alpha\beta k^2}{\left(k^2-\beta^2\right)^2} \tag{2.91}$$

$$\frac{\tan\left(\beta b\right)}{\tan\left(\alpha b\right)} = -\frac{\left(k^2-\beta^2\right)^2}{4\alpha\beta k^2} \tag{2.92}$$

Both previous equations can be reduced into a single equation as:

$$\frac{\tan\left(\beta b\right)}{\tan\left(\alpha b\right)}+\left(\frac{4\alpha\beta k^2}{\left(k^2-\beta^2\right)^2}\right)^{\pm 1} = 0\,, \quad \begin{cases} +1=\text{Symmetric} \\ -1=\text{Antisymmetric} \end{cases} \tag{2.93}$$

There can be more than one solution for each particular frequency or wavenumber. Each one of these solutions is called commonly as wave modes. The amplitudes within the depth of the plate for both, horizontal and vertical components for the first symmetrical mode are shown in Figure 2.16. while the first antisymmetric modes are in Figure 2.17. It can be noticed between the symmetric and antisymmetric modes that the amplitudes of the horizontal and vertical components are interchanged.

To better understand the different behaviour of the wave propagation in the different modes, it is useful to analyze the vertical displacement of the plate surface in each wave mode. For this, equations (2.87) and (2.90) will be used taking $\pm b$ as z. The resulting equations for top and bottom surface displacements in the symmetric mode are (2.94) and (2.95) respectively. The equivalent equations for

the antisymmetric modes are (2.96) and (2.97). In all these equations a time zero can be considered and therefore leaving as only variable the wavenumber.

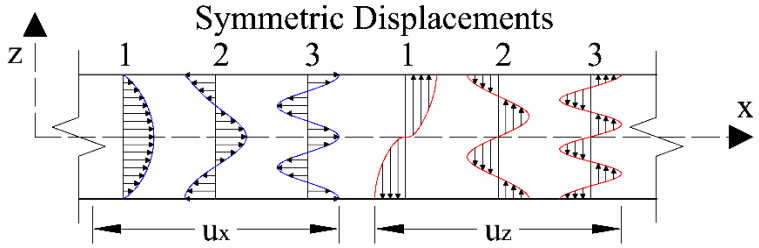

Figure 2.16 Horizontal (blue lines on the left), and vertical (red lines on the right) displacements for the first three Symmetric modes for the lamb waves within a plate

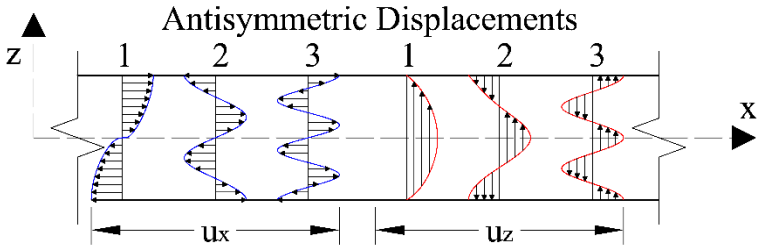

Figure 2.17 Horizontal (blue lines on the left) and vertical (red lines on the right) displacements for the first three Antisymmetric modes for the lamb waves within a plate

$$u_{z-top}^{<s>} = \left(-\frac{\left(k^2 - \beta^2\right)}{2k} + k \right) \sin\left(\beta b\right) e^{i(kx-\omega t)} \tag{2.94}$$

$$u_{z-bot}^{<s>} = \left(\frac{\left(k^2 - \beta^2\right)}{2k} - k \right) \sin\left(\beta b\right) e^{i(kx-\omega t)} \tag{2.95}$$

$$u_{z-top}^{<a>} = -\left(\frac{\left(k^2 - \beta^2\right)}{2k} + k \right) \cos\left(\beta b\right) e^{i(kx-\omega t)} \tag{2.96}$$

$$u_{z-bot}^{<a>} = -\left(\frac{\left(k^2 - \beta^2\right)}{2k} + k \right) \cos\left(\beta b\right) e^{i(kx-\omega t)} \tag{2.97}$$

The top and bottom surfaces of a plate in the symmetric mode (equations (2.94) and (2.95)) for a wavenumber of half the thickness of the plate, or a wavelength of twice the thickness of the plate are plotted in Figure 2.18-Left. The antisymmetric vertical displacements for the same

wavenumber/wavelength are plotted in Figure 2.18-Right. Looking at Figure 2.18 is easy to identify the symmetric wave mode propagate by expanding and contacting the vertical fibres on the plate, while the antisymmetric mode propagates by shearing the vertical fibres in the plate producing the same shape in both plate surfaces.

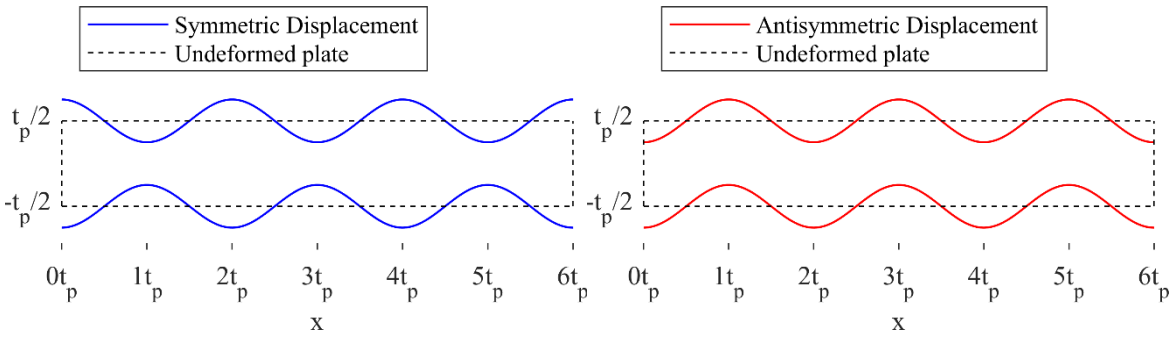

Figure 2.18 Graphic representation of vertical displacements for the lamb waves in the symmetric (left) and antisymmetric mode(right)

The solution to the equation (2.93) leads into the pairs of wavenumber and frequencies that can be translated into wave velocities by the relationship (2.18). The results for the equation (2.93) are plotted in Figure 2.19 considering a Poisson's ratio of 0.25 and normalizing both the phase velocity and wavenumber. The phase velocity was normalized with the Shear wave velocity. And the wavenumber normalized with the plate thickness.

The phase velocity dependant on either the frequency or the wavenumber is called dispersion. Therefore, the lines plotted shown in Figure 2.19 are called dispersion curves. One thing to notice in this figure is that with low wavenumber (or large wavelength) relative to the plate, the symmetric waves propagate faster, while the antisymmetric waves propagate slower. This behaviour is expected knowing how the propagations occur in each mode (Figure 2.18). As the wavenumber or frequency increases, the phase velocity in both propagation modes converges to each other to the same phase velocity. The phase velocity at which they converge is the Rayleigh wave velocity in an infinite half-space. In other words, when the wavelengths are small enough compared to the plate thickness, the surface waves behave as in an infinite media. This happened at wavelengths of half the thickness of the plate and shorter.

In Figure 2.19 there are some dispersion curves in which the phase velocity tends to infinity. These lines correspond to higher vibrations mode, and they start manifesting at the resonant frequencies of

the plate. Depending on the type of resonance frequency they are linked to, is that these lines will converge to the R-wave velocity ($V_R/V_S = 1$) or to the P-wave velocity ($V_R/V_S \approx 1.88$ for Poisson's ratio of 0.25).

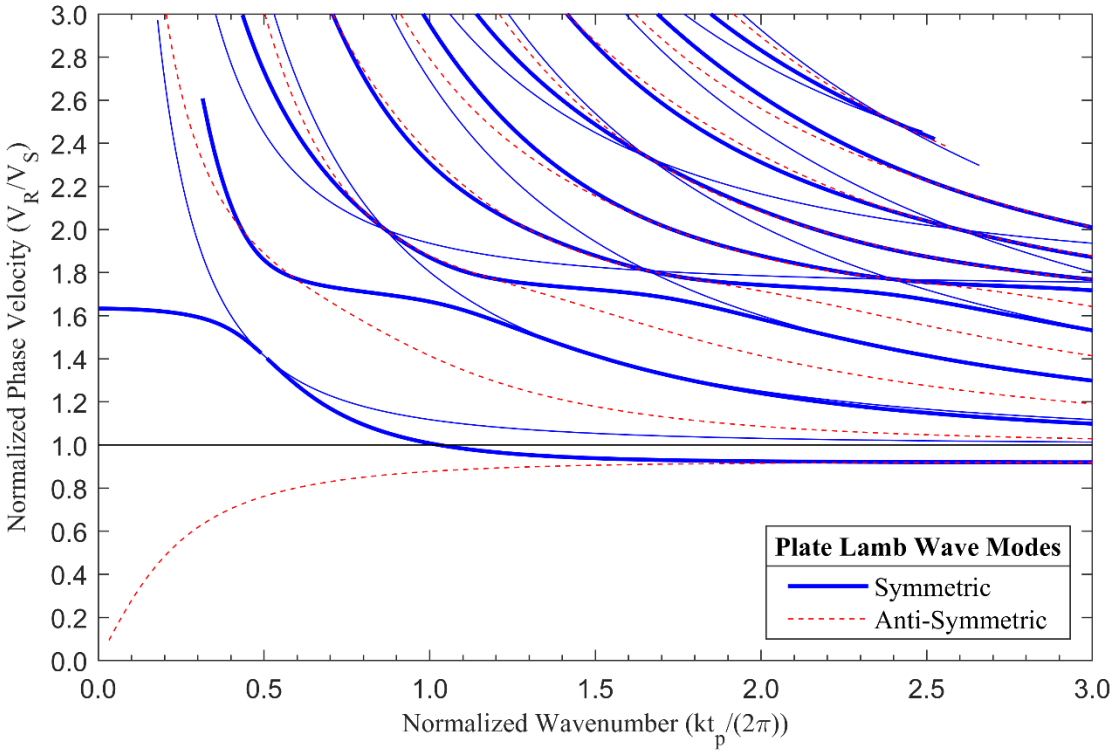

Figure 2.19 Dispersion curve for a plate for a Poisson's ratio of 0.25. Symmetric modes are shown in a blue continuous line and antisymmetric mode in red dashed lines.

2.6.4.2.4 Frequency-equations - Dispersive waves

As previously mentioned, the theory presented above corresponds to a plate. Similar frequency equations for cylindric rods and shells have been derived, for some special cases and their complexity increases. The derivation and theory for these cases will not be studied to detailed here, but the reader can go to (Graff, 1975) chapter 8 for a more comprehensive study on this field.

The frequency equation for the longitudinal modes in a rod is given by:

$$\frac{2\alpha}{r}\left(\beta^2+k^2\right)J_1(\alpha r)J_1(\beta r)-\left(\beta^2-k^2\right)^2 J_0(\alpha r)J_1(\beta r)-4k^2\beta r J_1(\alpha r)J_0(\beta r)=0 \quad (2.98)$$

Where J_n is the Bessel function of the first kind which can be defined by the following series expansion with n being a positive integer:

$$J_n(x) = \sum_{m=0}^{\infty} \frac{(-1)^m}{m!(m+n)!}\left(\frac{x}{2}\right)^{2m+n} \tag{2.99}$$

The dispersion curve for the first three longitudinal modes of a cylinder resulted from (2.98) are plotted in Figure 2.20. The phase velocity and wavenumber in the plot have been normalized with the thin rod velocity (V_{Pr} shown in equation (2.26)) and with the cylinder radius *'r'*. A correction factor to account for the lateral inertia or Poisson effect on the cylinder, first introduced in (Rayleigh & Strutt, 1877), is also plotted in Figure 2.20. This correction reduced the wave velocity with the ratio of (2.100), where *n* is the longitudinal mode number.

$$1 - \frac{n^2 \nu^2 \pi^2 r^2}{2L^2} \tag{2.100}$$

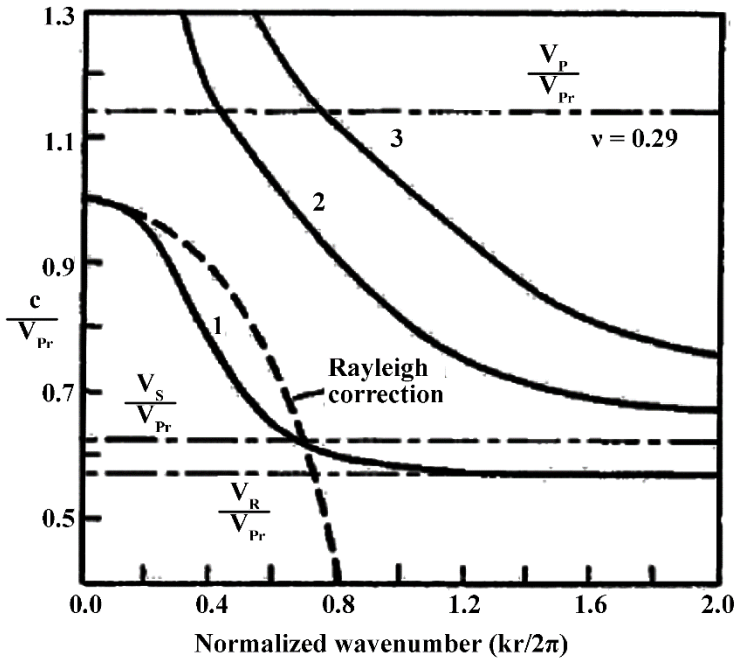

Figure 2.20 Dispersion curves for the first three longitudinal modes in a rod. (Graff, 1975) p. 471.

2.7 Concrete

Concrete is a stone-like material made of mixing fine and coarse aggregates like sand and gravel bound together using cement and water. The main advantage of concrete is that when is fresh it does not hold any shape until it hardens due to the chemical reaction of cement and water. This property allows casting concrete in diverse forms for construction. Due to the availability of concrete main ingredients (sand, aggregates, pozzolanic materials, and water) all around the world, concrete is considered a universal material (Brzev & Pao, 2009; Nilson et al., 2004; Wight & MacGregor, 2012).

The main advantages of concrete against other construction materials are: High compressive strength; Fire resistance; Long service life with low maintenance cost; It can take any shape required. Although, concrete also has the following disadvantages: Low to null tensile strength; Requires mixing, casting and curing, all of these affecting the concrete strength; The labour cost is high compared to steel; Low compressive strength compared to steel leads to larger sections; Cracks are produced due to shrinkage and loads (Hassoun & Al-Manaseer, 2008).

Besides its disadvantages, concrete has spread rapidly as a construction material worldwide, due to it's versatile, especially for massive structures as dams, piers, and footings where it is the most economical material (Hassoun & Al-Manaseer, 2008).

2.7.1 Historical Overview

Concrete like material has been used for thousands of years, with the first lime mortars dating from 12,000 to 6,000 BCE in Crete, Cyprus, Greece, and the Middle East (Nilson et al., 2004). The word "*concrete"* derives from a Latin verb "*concrescere*" which means: "to grow together" or "to harden". Romans used volcanic sand called pozzolana as cement since it reacts with lime and water to harden into a rock-like mass. Many Roman structures were built using this early form of concrete, including some renowned monuments as the Colosseum and the Pantheon in Rome. However, the used of concrete in constructions fell in disuse due to a shortage of cementitious materials in other parts of the world (Brzev & Pao, 2009).

It was until early 1760, in Britain, when John Smeaton used concrete in the first lock on the river Calder. Being this the first modern record of concrete. Later on, in 1796 J. Parker discovered Roman natural cement. In 1811 Vicat produced cement by burning a mixture of clay and lime. Until in 1824, 13 years later, Joseph Aspdin manufactured Portland cement in Wakefield Britain. The cement was

called “Portland” because it resembled stones from the quarries of the Isle of Portland when hardened (Hassoun & Al-Manaseer, 2008).

Reinforced concrete, which is concrete containing steel rebars to compensate for the lack of tensile strength, first appeared in 1855 in France, but mainly for artistic and pottery manufacturing. It was until 1884 when reinforced concrete was used for practical applications in Germany (Brzev & Pao, 2009).

Modern concrete technology began in the second half of the 19th century, introducing the use of twisted square steel rods. The first concrete high-rise building was built in Cincinnati in 1902. And in 1906, the first bridge made of reinforced concrete was built in Massey, Ontario, Canada. Since then, concrete popularity as a construction material has grown largely. In 1976, Toronto’s CN Tower was built using concrete which at the time was the world’s tallest free-standing structure (Brzev & Pao, 2009).

2.7.2 Compressive Strength

As mention before, concrete is capable of withstanding large compression forces but fails rapidly under tension loads. The appearance of cracks usually defined failure for most materials, however, is natural for reinforced concrete used in construction to show cracks even before being loaded. Therefore, for concrete, strength is defined as the maximum stress it can withstand (Mehta & Monteiro, 2005).

A material strength relates to its porosity with the relationship shown in the equation (2.101), where ‘S_0’ is the material strength at zero porosity, ‘k’ is a constant, and ‘p’ is the porosity percentage. Therefore, concrete strength depends not only on the strength of its components (admixtures, cement paste) but also on the porosity of the concrete sample. The cement strength and the bonding between it and the fine and coarse aggregates depend heavily on the cement content of the mix, the curing conditions after casting, and of course on the properties of the coarse aggregate. The porosity also depends on the water-cement ratio and the curing process, but also in the curing and placing method during casting (Mehta & Monteiro, 2005).

$$S = S_0 e^{-kp} \tag{2.101}$$

Although the direct determination of concrete porosity and its individual aggregates properties is impractical, and therefore the development of a precise strength model is not possible. Because of

this, several empirical relationships using different concrete properties has been found. Despite the difficulty of developing a model to predict concrete strength, testing the strength of a concrete sample is relatively easy compared with other of its properties. Because of this reason, the concrete strength is the property generally specified by designers. Other concrete properties such as elastic modulus, impermeability, tensile strength, durability, are harder to test, therefore engineers had tried to relate these properties with the compressive strength (Mehta & Monteiro, 2005).

The compressive strength is determined by testing in compression either cylinders or cubic samples. In North-America, cylinder samples are more common in the practice. Besides the factors affecting the concrete strength mentioned, the shape, dimensions, and concrete age (Figure 2.21) also, affect the ultimate compressive strength. For this reason, these tests have been standardized to a defined load rate, length to diameter ratio (for cylinders), and to the age of 28 days (Hassoun & Al-Manaseer, 2008). In Canada, cylinders of 100 mm diameter and 200 mm in length, are most commonly used (Brzev & Pao, 2009).

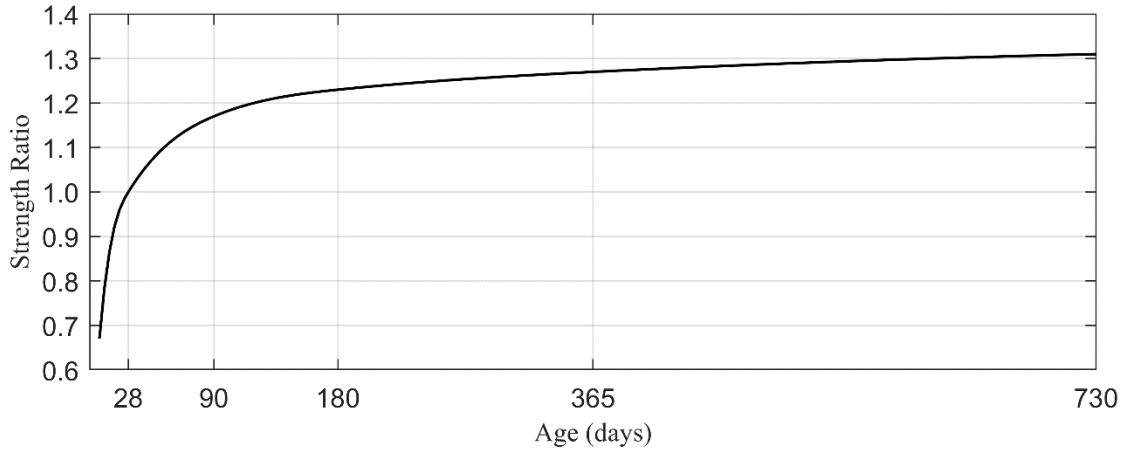

Figure 2.21 Typical strength ratio of concrete for different ages normalized with the age of 28 days. (Hassoun & Al-Manaseer, 2008) p. 16.

In structural design, the prescribed compressive strength is called f'_c. Concrete strength can vary greatly from 20 MPa and 40 MPa, for normal strength concrete, and for high strength concrete, the f'_c can reach values over 70 MPa (Brzev & Pao, 2009). Concrete failure normally happens at a strain range of 0.002 and 0.003, but lightweight concrete typically reaches larger strains at failure around 0.0035 (Nilson et al., 2004).

2.7.3 Elastic Moduli

As discussed before in section 2.2, any stress is associated with a strain, the relationship between them is called elastic modulus. Concrete elasticity is as important as its compressive strength because it allows structural designers to compute deformations and study buildings' behaviour under certain loads. Within a certain stress range, concrete is elastic, which means that once the load es retired, the strain caused by that load would disappear returning the object to its original dimensions (Neville, 1996).

The full stress-strain relationship can be obtained during a compression test by measuring the deformations due to the load. In contrast with other materials like steel, the curve does not follow a perfectly straight line from stress zero until its failure, but instead, it follows a parabolic-like shape. Concrete does not have a plastic range, as steel neither, once the maximum stress capacity is reached, concrete will fail. When the failure load is reached, concrete will start to crack and crumble internally losing load capacity, quickly leading to a total collapse of the sample. High-strength concretes tend to be more brittle and fail quicker after reaching its maximum strength (Nilson et al., 2004). Typical stress-strain curves are shown in Figure 2.22.

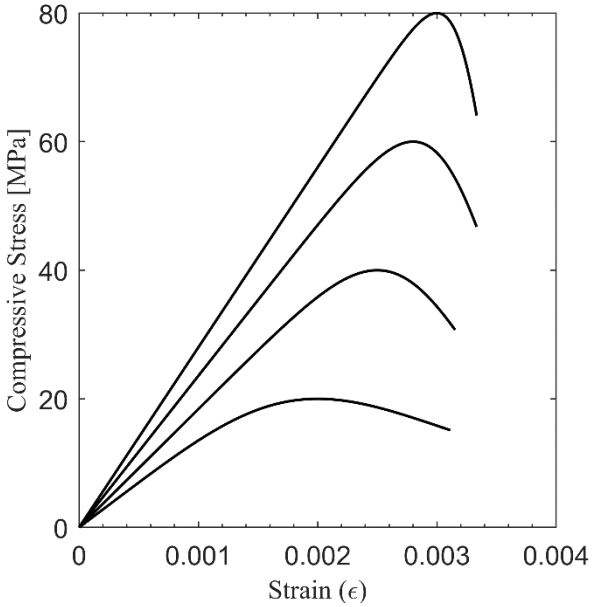

Figure 2.22 Different stress-strain curves for concrete using the equation (2.104) with different parameters.

The exact shape of the stress-strain curve is not an inherent property of concrete, it depends on several factors, including the test setup. It’s not of vital importance to formulate an equation for the

stress-strain, nevertheless, some attempts have been done to develop an equation for it. Desayi and Krishnan proposed one of the most successful equations (2.102), where *'ε_c'* is the strain at maximum stress and *'E_{it}'* stands for the initial tangent slope of the curve, which Desayi and Krishnan proposed to be equal to (2.103), twice the slope of a straight line to the point in the curve of maximum stress (f'_c) (Neville, 1996).

$$\sigma(\varepsilon) = \frac{E_{it}\varepsilon}{1+\left(\frac{\varepsilon}{\varepsilon_c}\right)} \tag{2.102}$$

$$E_{it} = 2\frac{f'_c}{\varepsilon_c} \tag{2.103}$$

Although, Carreira and Chu proposed a more general structure of the previous equation (2.102), that allows an arbitrary selection of the initial tangent slope. Carreira and Chu equation form is shown in (2.104), the parameter β is defined by the equation (2.105). β needs to be equal to one or greater. Carreira and Chu equation can describe two types of materials: When $E_{it} \approx f'_c/\varepsilon_c$ (or when $\beta \to \infty$), the equation (2.104) describes a perfectly elastic material; and when β=1.0 it describes a perfectly plastic material. Therefore, Carreira and Chu's equation describes the stress-strain curve for a mid-case between these two extreme material behaviours (Carreira & Chu, 1985).

$$\sigma = \frac{\beta f'_c\left(\varepsilon/\varepsilon_c\right)}{\beta - 1 + \left(\varepsilon/\varepsilon_c\right)^2} \tag{2.104}$$

$$\beta = \frac{1}{1-\frac{f'_c}{\varepsilon_c E_{it}}} \tag{2.105}$$

As mentioned before, the stress-strain curve is not linear, which means that the Young's modulus will depend on the strain and not being a constant as in Hooke's law (2.1). This complicates things, given that in previous sections a constant assumption was that the material was perfectly linear elastic, and it would complicate things the structural design in the daily practice. Therefore some definitions for the Young's modulus of concrete has been developed, to assign a single value to it.

The three more popular definitions are: The initial tangent slope of the stress-strain curve, the slope of a secant line between two points in the stress-strain curve, the slope of a tangent line at a given stress or strain. These definitions are graphically defined in Figure 2.23 with a blue, red and green line respectively. The secant modulus is the most common definition and the one used by the Canadian Standard Association (CSA_A23.3, 2014), using the slope between the 50E-6 strain and 40% of the f'_c stress, as shown in the secant slope of Figure 2.23.

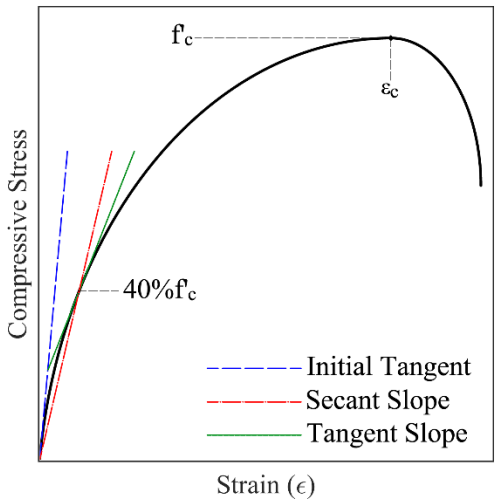

Figure 2.23 Graphic representation for the different definitions of Young's modulus for concrete based on the curve slope

These elasticity moduli definitions depend on testing the concrete samples, therefore the elasticity modulus can be known until testing the sample after 28 days after casting. It's not possible to give a default value for Young's modulus of concrete because concrete properties depend on many factors, as discussed in this section. Therefore, there still the need for a definition of Young's modulus for concrete that can be known before casting the concrete. This is particularly true for structural design.

Structural designers cannot arbitrarily prescribe a concrete with certain f'_c and certain Young's modulus, both values need to be in agreement with each other and they have some correlation. It can be inferred from Figure 2.22 that as f'_c increase, the slope (i.e. Elasticity modulus) also increases. Therefore, some empirical equations have been developed by different structural building codes in different regions. Some of them are shown in Table 2.3, where f'_c, refers to the compressive strength for concrete tested on a cubic sample instead of a cylinder. The equations shown in Table 2.3 were plotted in Figure 2.24, using 2200 and 1500 as the concrete density for normal and lightweight concrete.

Table 2.3 Empirical equations to estimate Young's modulus of concrete according to several standards and building codes around the world.

Standard/Code	Equation [MPa]	
1) (CSA_A23.3, 2014) for concrete with ρ_c between 1500 and 2500 kg/m^3.	$E = \left(3300\sqrt{f_c'} + 6900\right)\left(\rho_c / 2300\right)^{1.5}$	(2.106)
2) (CSA_A23.3, 2014) for normal weight concrete between 20 and 40 MPa	$E = 4500\sqrt{f_c'}$	(2.107)
3) (ACI_318, 2014) for concrete with ρ_c between 1450 and 2550 kg/m^3.	$E = 0.043\left(\rho_c\right)^{1.5}\sqrt{f_c'}$	(2.108)
4) (ACI_318, 2014) for normal-weight concrete	$E = 4700\sqrt{f_c'}$	(2.109)
5) (ACI_363R, 1992) for high strength concrete between 21 and 83 MPa	$E = 3320\sqrt{f_c'} + 6900$	(2.110)
6) (EN, 1992) European code for concrete with basalt aggregate.	$E = 26400\left(f_c' / 10\right)^{0.3}$	(2.111)
7) (EN, 1992) European code for concrete with quartzite aggregate.	$E = 22000\left(f_c' / 10\right)^{0.3}$	(2.112)
8) (EN, 1992) European code for concrete with limestone aggregate.	$E = 19800\left(f_c' / 10\right)^{0.3}$	(2.113)
9) (EN, 1992) European code for concrete with sandstone aggregate.	$E = 15400\left(f_c' / 10\right)^{0.3}$	(2.114)
10) (TSE, 2000) Turkish building code for normal concrete weight	$E = 3250\sqrt{f_c'} + 14000$	(2.115)
11) (AIJ, 1985) Japanese structural concrete code for normal concrete	$E = 21000\left(\rho_c / 2300\right)^{1.5}\sqrt{f_c' / 20}$	(2.116)
12) (BS_8110_2, 1985) British standard for concrete	$E = \left(\rho_c / 2400\right)^2\left(20000 + 200 f_{cu}'\right)$	(2.117)
13) Mexico City building code for high strength concrete ($f'_c \geq 40$ MPa) with limestone aggregate	$E = 2660\sqrt{f_c'} + 8300$	(2.118)
14) Mexico City building code for high strength concrete ($f'_c \geq 40$ MPa) with basalt aggregate	$E = 2660\sqrt{f_c'} + 3300$	(2.119)
15) Mexico City building code for concrete with limestone aggregate	$E = 4000\sqrt{f_c'}$	(2.120)
16) Mexico City building code for concrete with basalt aggregate	$E = 3000\sqrt{f_c'}$	(2.121)
17) Guadalajara building code for normal weight concrete	$E = 3100\sqrt{f_c'}$	(2.122)
18) (IS., 2000)Indian standard for normal weight concrete	$E = 5100\sqrt{f_c'}$	(2.123)

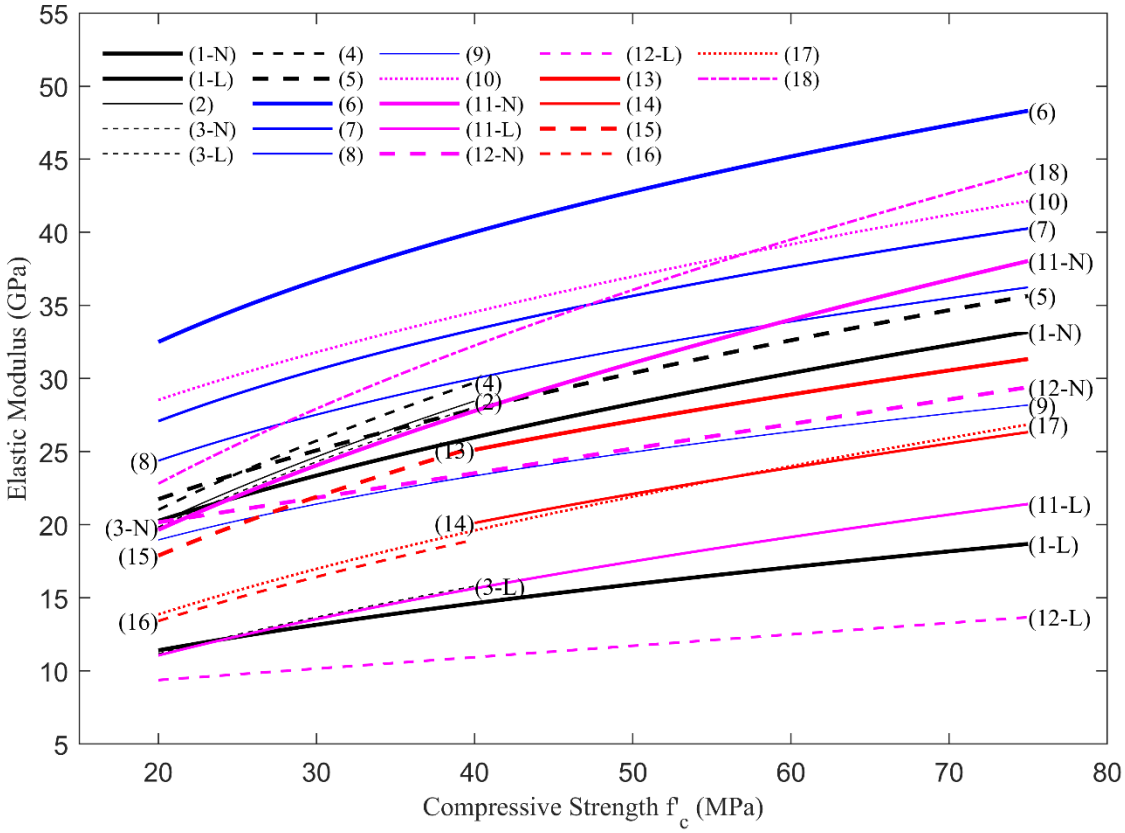

Figure 2.24 Empirical Equation from Table 2.3, plotted. For equations involving concrete density, there are two lines plotted labelled as 'N' and 'L' for normal and lightweight concrete. Densities of 2200 and 1500 kg/cm^3 were used.

The empirical equations from Table 2.3 spread out covering a large range of elastic modulus. At low compressive strength, the range goes from 10 to almost 35 GPa, while at high-strengths it goes from 15 GPa up to50 GPa. The lowest values correspond to lightweight concrete, which usually contains lots of air/porosity. The equation that estimates the lowest elastic moduli for normal weight concrete is the equation (2.121), which corresponds to Mexico City's building code for concretes with basalt aggregates. While on the other hand, the highest elastic moduli are obtained using equation (2.111), which corresponds to the Eurocode estimation for basalt aggregate. The Canadian standard (1-N) (2.106) is in the midrange among the empirical equations presented.

2.7.4 Poisson's Ratio

Another property intimately related to solid deformation is the Poisson's ratio as it was discussed in previous sections. In concrete, the Poisson's ratio is typically between 0.15 and 0.2, and the general consensus is its value does not depend on the concrete strength, age, or moisture content (Neville,

1996). Even on high-strength concretes the Poisson's ratio still fall within this range (ACI_363R, 1992).

The Poisson's ratio in concrete is determined at the same time as the elastic modulus is being tested, by measuring both longitudinal and lateral deformations. The procedure of measurement will be described later in Chapter 4.

2.8 Static and Dynamic Differences

Generally, for most of the real-life applications, the materials are subjected to relatively large deformations or strains. This is especially true for structural designs, where the structural elements, such as beams or columns can reach deformations of several centimetres. The definitions given previously for the elastic modulus and Poisson's ratio in concrete, are in accordance with the structural design requirements since they demand tests at stresses near the maximum capacity. These mechanical properties are called 'static' because their tests are done by slowly increasing the load, at rates around 0.25 MPa/s (ASTM_C469, 2014).

On the other hand, these mechanical properties can be also obtained using the wave propagation theory described earlier in this section. These tests use vibrations, which are induced by rapidly loading and unloading the sample at rates above 5000 Hz. Therefore, these tests are considered as dynamic tests, hence the properties obtained using these methods are also called 'dynamic'.

Due to the high frequency used in the dynamic tests, the load amplitudes are very low. The higher the frequency, the lower the amplitude. For this reason, these tests generate very low strains (Carette & Staquet, 2016).

For dynamic measurements using impact resonance test (described in later Resonant Method section and the one used for this research), Bay and Stokoe found the strains were about $6x10^{-6}$ (Bay & Stokoe, 1992). While for the static test the strain level is around $1x10^{-3}$ as can be seen in Figure 2.22. Therefore, the strains in a dynamic test can be over 100 times smaller than the static tests.

Given the non-linear relationship for stress-strain in concrete, the dynamic modulus tends to be higher than the static modulus. As can be seen in Figure 2.23, the slope (and therefore the stiffness) is higher at low strains. The dynamic elastic modulus is generally considered to be equal to the initial tangent modulus from static tests (Kolias & Williams, 1980). This has been confirmed in (Bay & Stokoe, 1992), where they compared the Young's modulus of static and dynamic tests using the same strain levels.

As stated in 1962 by Jones (Maholtra, 1974), It's not possible to define a general relationship between static and dynamic elastic moduli, due to concrete nature which depend on many factors, specially for the stress-strain relationship which not only depend on the concrete admixtures, aggregates, age, curing conditions, cement-water ratio, but also depends on the testing setup.

Nevertheless, there has been extensive research in this area since then, trying to relate these two moduli for particular cases or mixes. Starting with (Powers, 1938) who tested square beams, and compare the elastic modulus obtained by static and sonic methods. In 1975 Popovics proposed a general equation as a function of the dynamic modulus and density to be adjusted to specific cases/mixes (S. Popovics, 1975). In most recent years, Shkolknik proposed a relationship between the two moduli based on thermo-fluctuation theory, developing an equation as a function of the stress ratio, stress rate and temperature (Shkolnik, 2005).

And nowadays, the British code (BS_8110_2, 1985) allows estimating the static elastic modulus using the dynamic modulus with the equation (2.126), whenever is more convenient to do so. The British code claim, it can estimate the static modulus with an accuracy of ± 4 GPa.

Table 2.4 Empirical equations relating static and dynamic elastic moduli.

Standard/Code	Equation [GPa]	
1) (S. Popovics, 1975)[2]	$E_S = 427.505\left(E_D^{\,1.4} / \rho_c\right)$	(2.124)
2) (Lydon & Balendran, 1986)	$E_S = 0.83E_D$	(2.125)
3) (BS_8110_2, 1985)	$E_S = 1.25E_D - 19$	(2.126)
4) (Nilsen & Aitcin, 1992)	$E_S = \frac{(1-\nu)}{1.7(1+\nu)(1-2\nu)}E_D + 3.94$	(2.127)
5) (Han & Kim, 2004)	$E_S = E_D\left(1 - 0.708e^{-0.0268E_D}\right)$	(2.128)
6) (Shkolnik, 2005)[3]	$E_S = E_D - 808\frac{\sigma}{f_c'}(\ln \dot{\epsilon}$ [MPa]	(2.129)

A summary of the most important equations that have been proposed, relating static and dynamic moduli are presented in Table 2.4. Despite some of these relationships are functions of more

[2] It was proposed originally as a general form. The values shown in the tables are for the specific concrete samples they tested during their research.

[3] This equation is expressed in MPa. σ is the stress at which the static elastic modulus is being measured as the tangent slope of the stress-strain curve. And $\dot{\epsilon}$ is the stress rate in MPa/s. The equation assumes the tests are done at 20° C.

variables/parameters besides the dynamic modulus of elasticity, these equations have three different structures:

$$E_S = c_1 E_D + c_2 \tag{2.130}$$

$$E_S = c_1 E_D^{\,c_2} \tag{2.131}$$

$$E_S = E_D \left(1 - c_1 e^{-c_2 \cdot E_D}\right) \tag{2.132}$$

Similarly, the dynamic Poisson's ratio has larger values than the static one, varying between 0.2 and 0.3 (Neville, 1996). However, it is also independent of the compressive strength, humidity or age (ACI_363R, 1992). Although, young concrete (less than 2 days), can reach Poisson's ratios over 0.4, decreasing rapidly with time (Jones, 1949; Simmons, 1955).

Chapter 3
Signal Processing

3.1 Introduction

This chapter will present the framework for the signal processing used for the development of this work. It will start by defining what is a signal and how these signals are represented digitally. Next, it will introduce the main signal processing tools used during the extent of this work. These tools will be divided into three subsections based on the domain they analyze. (Time or frequency domain or both).

3.1.1 Signals

A signal is anything that can be measured and represented as a function of one or more variables. The following are some examples of signals: The sound pressure or sound within a room during a period of time, the light impulses transmitted through fibre optic cables, the number of items sold daily by a store, etc. If it can be recorded, it's a signal (Karu, 2001).

Signals can be divided into two categories: Continuous and discrete signals. Most of the signals in the real world are continuous, which means that they hold values at every single instance. For example, a car moving from point *'A'* to point *'B'* in a time *'t'*, will have an infinite number of coordinates positions between these two points. The car does not skip any coordinate. Although a GPS tracking the car movement, will not register infinite coordinate values, but rather a finite number distributed during the period of time. The signal obtained by the GPS would be a discrete signal. The figure below shows a continuous signal (Figure 3.1 a) and a discrete representation of it (Figure 3.1 b). The continuous signal is given as a function '*y*' of time, while the discrete signal is a function of the sample number, each sample represents a given point in time (Karu, 2001).

Despite this, it is possible to record some signals continuously (a vinyl record is an example of this), it's not a practical approach. Nowadays the use of digital systems demands the data to be digital as well, which means the data needs to be comprised of bits (0's and 1's).

This work will then focus on the processing of discrete signals, given that all the signals to be processed are being recorded digitally.

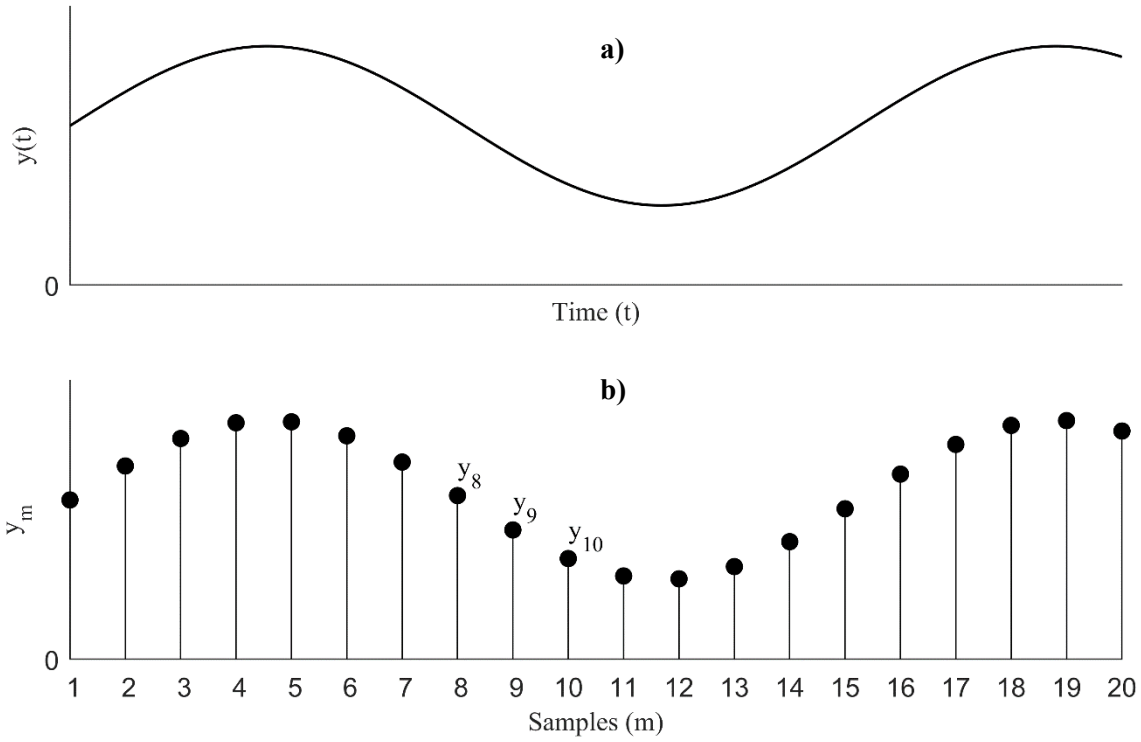

Figure 3.1 Graphic representation of continuous (a) and discrete signal (b).

Sampling is the action of taking samples from a continuous signal. Intuitively, a higher sampling rate is better. But it's not practical to choose the highest sampling rate possible every time. For example, 1 GHz sampling would mean to store one billion data points for each second recorded. If each data point requires 1 bit, it translates into a 125Mbytes of data. Hence the importance of choosing the minimum sampling rate that accurately represents a given signal to reconstruct it properly.

Undersampling a signal can cause information loss that causes the reconstructed signal to have a lower frequency. Figure 3.2 shows a signal (red-dashed line) sampled at the black dots, if those points were used to try to reconstruct the sampled signal, the result would be a sinusoidal wave with $1/8^{th}$ of the original frequency (blue-continuous line).

To avoid the distortion on the reconstructed signal the sampling frequency needs to be greater than twice the maximum frequency desired to represent. This is known as the sampling theorem (3.1).

$$f_s > 2f_{\max} \tag{3.1}$$

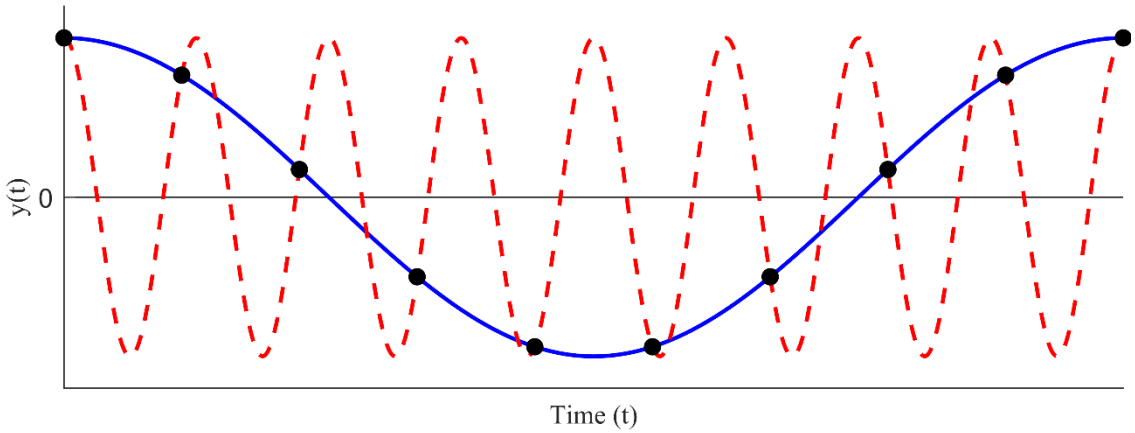

Figure 3.2 Undersampling for the sinusoidal wave with a high frequency (dashed red line) results in being reconstructed into a lower frequency signal (continuous blue line).

It is possible to sample signals with respect to another variable beside time. For example, in a compression test, the signal can be sampled with a certain strain rate. Those will not be discussed in this chapter.

3.2 Time Domain

When the signals are expressed as a function in time, it said they are in the time domain. This would be the case for most of the signals in its raw form. This section will introduce tools that are useful to process the signal in its time domain.

3.2.1 Cross-Correlation

Cross-correlation is a signal processing tool to measure the similarity between two signals. It can be used in several ways, such as: To compare signals in a quantitative way, to filter a set of signals based on their similarity to a reference signal, or to align signals in time. Cross-correlation is mathematically very similar to convolution. When both signals 'f_a' and 'f_b' are continuous and real the cross-correlation value between the two signals is defined by (3.2) (Papoulis, 1962).

$$R_{ab} = \int_{-\infty}^{\infty} f_a(\tau) f_b(t+\tau)\, d\tau \tag{3.2}$$

From (3.2) can be seen the correlation is the area below the curve of the product of function 'f_a' by the displaced function 'f_b'. The translation of the continuous definition to a discrete version of the

functions is shown in the equation (3.3) where: 'x_a' and 'x_b' are two discrete signal vector with *'N'* samples. Equation (3.3) computes the correlation for the signal *'a'* with signal *'b'* lagged 'k' samples. The same operation needs to be done for as large as the require lag of the function *'b'*. Resulting in a cross-correlation vector. The maximum lag possible for moving the function *'b'* is equal to *2N+1*.

$$R_{ab}(k) = \begin{cases} \sum_{n=1}^{N-k} x_a(n)\, x_b(n+k) & m \geq 0 \\ R_{ba}(-k) & m < 0 \end{cases} \tag{3.3}$$

If a total or unique correlation value for both signals is desired (like the one resulting from (3.2)), it can be obtained by summing all elements of vector R_{ab}. When the cross-correlation is done on the same signal (R_{aa}), the operation is called auto-correlation.

Nevertheless, the values resulting from these operations are somehow hard to evaluate by themselves. It is useful to normalize the cross-correlation values to convert them into cross-correlation coefficients. The normalization is done using autocorrelation values at zero lag for both signals as shown in (3.4) (Mathworks, 2019).

$$\bar{R}_{ab}(k) = \frac{R_{ab}(k)}{\sqrt{R_{aa}(0)\, R_{bb}(0)}} \tag{3.4}$$

An example of the cross-correlation used to align two sinusoidal signals displaced with respect to each other 250 samples is shown in Figure 3.3. Signal *'a'* is represented by the blue continuous line, while signal *'b'* is represented by the red dashed line in Figure 3.3-a, while Figure 3.3-b shows the cross-correlation coefficients (normalized values), between these two signals at each lag. The maximum cross-correlation coefficient happens at a lag of -250 samples. This would indicate we need to move signal *'b'* 250 samples earlier (to the left), to align both signals.

The above example is basic but it allows to illustrate clearly how the cross-correlation works and how it can be used.

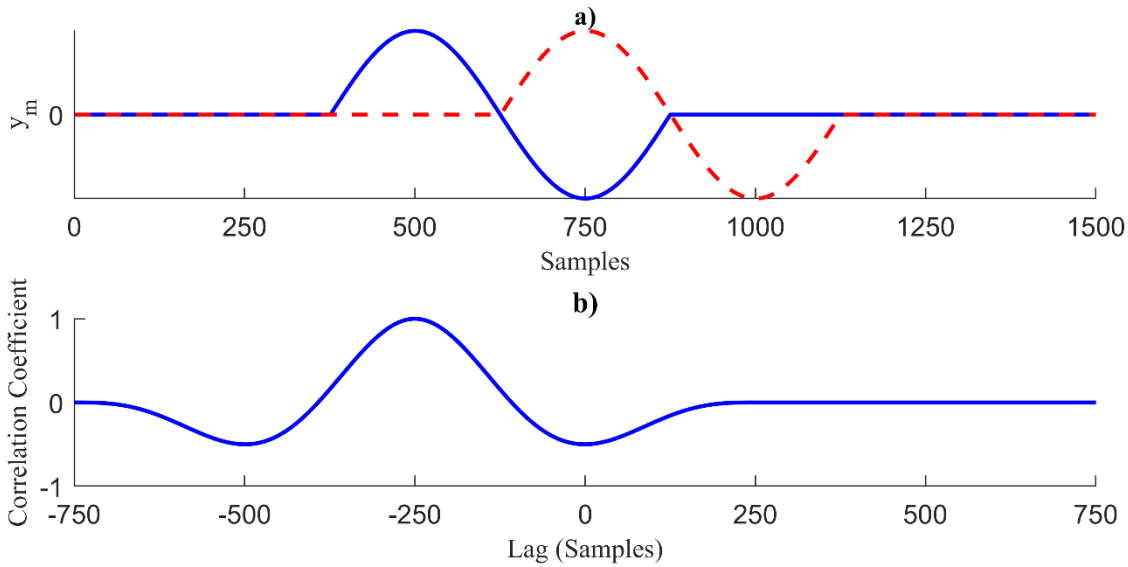

Figure 3.3 Example of a cross-correlation application to align two signals. The same sinusoidal signal is shifted by 250 samples (a). The normalized correlation coefficients for the signals (b).

3.3 Frequency Domain

A signal can be as simple as the ones shown in Figure 3.1 to Figure 3.3, where they are composed of a single sinusoidal wave with a constant frequency. Or it can be as complicated as one can imagine, containing several frequencies at the same time or with their frequency content changing with time.

This chapter will introduce the concept of signal decomposition into simpler sinusoidal waves and the tools to transform the signals from a function of time to a function of frequency. When a signal is expressed as a function of frequency, it is said is in its frequency domain.

3.3.1 Fourier Series

Any periodic signal can be approximated by a sum of sinusoidal waves (3.5), this set of sums are called Fourier series. This same summation can be represented in different ways using trigonometric and the Euler identities, transforming the equation (3.5) into its magnitude phase form (3.6) and its exponential form (3.7) respectively (Karu, 2001).

$$f(t) = A_0 + \sum_{n=1}^{\infty} A_n \cos(n\omega t) + \sum_{n=1}^{\infty} B_n \sin(n\omega t) \tag{3.5}$$

$$f(t) = A_0 + \sum_{n=1}^{\infty} C_n \cos(n\omega t + \theta_n) \tag{3.6}$$

$$f(t) = \sum_{n=-\infty}^{\infty} D_n e^{in\omega t} \tag{3.7}$$

On the above equations, the coefficients represent the magnitudes or the participation factor for each frequency ($n\omega$). The coefficient A_0 is equal to the average of the signal also called the DC component of the signal. A_n and C_n are real numbers while B_n is an imaginary number. D_n is a complex number. All of these coefficients are related to each other with the following identities (Karu, 2001).

$$A_0 = D_0 \tag{3.8}$$

$$A_n = 2\,\mathrm{Re}\{D_n\} \tag{3.9}$$

$$B_n = -2\,\mathrm{Im}\{D_n\} \tag{3.10}$$

$$C_n = \sqrt{A_n^{\,2} + B_n^{\,2}} \tag{3.11}$$

$$\theta_n = -\arctan\left(B_n \big/ A_n\right) \tag{3.12}$$

The coefficients of the Fourier series of a periodic and continuous signal *f(t)* can be computed using the following formula (Oppenheim, Willsky et al., 1996).

$$D_n = \frac{1}{T}\int_0^T f(t) e^{-jn\omega t} dt \tag{3.13}$$

3.3.2 Fourier Transform

The Fourier Transform is the operation that can be applied to a signal (i.e. function) to represent it as a function of their frequencies content. Therefore, it shifts the function from the time domain to its frequency domain. The Fourier Transform is defined by the integral (Papoulis, 1962)

$$F(\omega) = \int_{-\infty}^{\infty} f(t) e^{-i\omega t} dt \tag{3.14}$$

The Fourier Integral is similar to the expression (3.13) which computed the coefficients for the Fourier series of the signal *f(t)*, with the difference of the integration limits. Therefore, it can be

concluded that the Fourier Transform computes the participation coefficient for a particular frequency *'ω'*. The Fourier Integral is also similar to the Convolution/Cross-Correlation integral (3.2) with 'f_b' as an exponential function with a certain frequency. So, the Fourier Transform could also be understood as a measure of similarity between the signal *f(t)* and a sinusoidal wave with frequency *'ω'*.

The study presented in this thesis will analyze only discrete signals. Therefore, it's more useful to represent the Fourier Integral in its discrete form defined by the equation (3.15) (Oppenheim et al., 1996), where *'x'* is a vector in the time domain with *'N'* samples, and *'X'* is the vector transformation into its frequency domain. One value of *'X'* for each frequency *'ω'* (3.16).

$$X_m = \sum_{n=1}^{N} x_n e^{-in\omega_m \Delta t} \tag{3.15}$$

$$\omega_m = \frac{2\pi m}{N\Delta t} \tag{3.16}$$

From equation (3.16) can be seen, the Fourier Transform frequency solution for a discrete signal depends on two factors: The number of samples on the signal vector, and the difference in time between samples (Δt). The inverse of Δt represents the sampling frequency of the signal. Therefore, the equation (3.16) becomes:

$$\omega_m = \frac{2\pi f_s m}{N} \tag{3.17}$$

Then the frequency resolution is inversely proportional to the sampling frequency (f_s) and directly proportional to the length of the vector or number of samples on the signal (N).

Consider the signal defined by the equation (3.18). This signal contains four frequencies (1, 4, 10 and 20 Hz). Sampling the signal (3.18) at 1 kHz, the time-domain representation along with its frequency is shown in Figure 3.4-a and Figure 3.4-b respectively.

$$f(t) = 0.4\sin(1 \cdot 2\pi t) + \sin(4 \cdot 2\pi t) + 0.6\sin(10 \cdot 2\pi t) + 0.2\sin(20 \cdot 2\pi t) \tag{3.18}$$

Notice the coefficients for each sinusoidal frequency in the equation (3.18) are normalized to their maximum coefficient. Similarly, the frequency spectrum (Figure 3.4-b) has been also normalized. The magnitude in the frequency domain at each of the frequency components of (3.18) have the same value as their coefficients in (3.18).

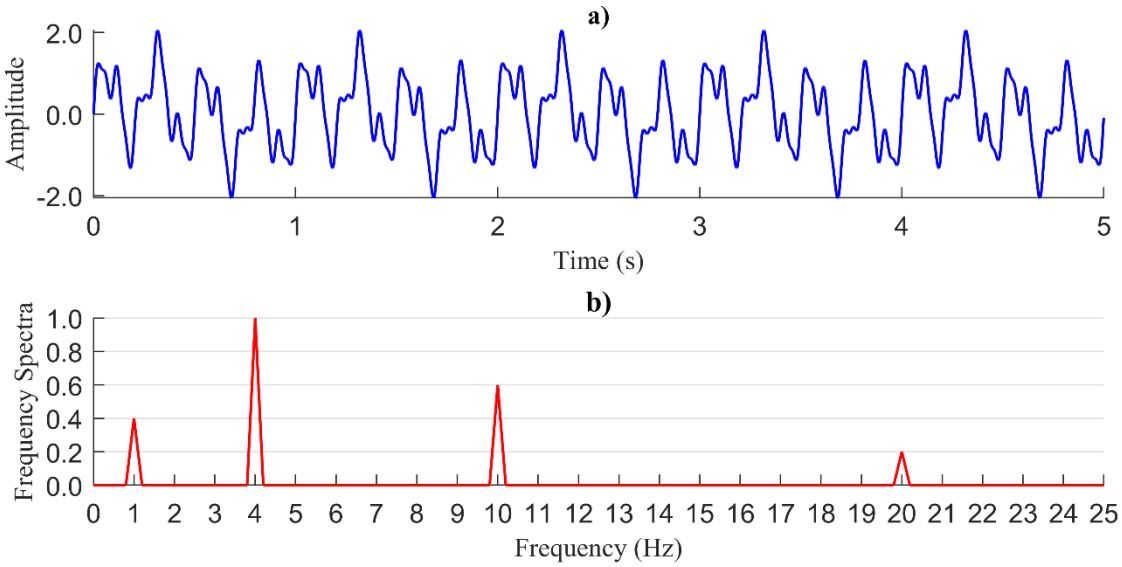

Figure 3.4 Normalized FFT (b) of the periodic signal shown in the equation (3.18) (a)

3.3.2.1 Fast Fourier Transform (FFT)

The Fourier Transform is a very powerful tool, which is used extensively in different fields. Although it's computationally expensive. It requires to solve a large number of operation and it grows exponentially as the size of the vector increase. The computational time required would make the use of the tool impractical for large-signal vectors. Therefore some algorithms have been implemented to improve drastically the computational speed. The Fourier Transform computed using these algorithms receive the name of Fast Fourier Transform (FFT) (Zonst, 2005).

The review and explanation for these algorithms are out of the scope of this work but they can be found in any book specialized in algorithms for signal processing.

3.3.2.2 Filters

A filter can remove certain frequency content from a signal. Filters can be divided into four types depending on the frequency range they preserve: Lowpass, Highpass, Bandpass and Notch. The idealized frequency content of these four filter types is shown in Figure 3.5. The idealized filters multiply the frequency range to be removed by zero by leaving the frequencies of interest intact.

The names of the types of filters are very intuitive: Lowpass filters leave frequencies below the cutoff frequency (f_{cf}) intact; Highpass filters, on the other hand, leave frequencies higher than the cutoff frequency A bandpass filter let the frequencies within the range of the cutoff frequencies f_l and

f_2 the same as in the original signal. Conversely, notch filters remove frequencies between the cut-off frequencies f_1 and f_2 (Karu, 2001).

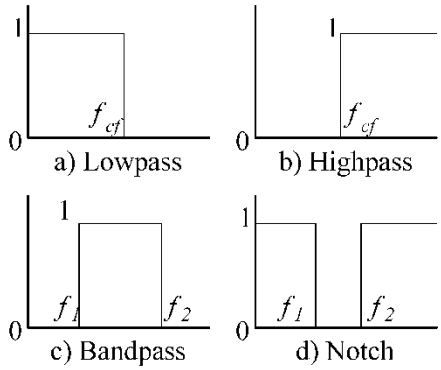

Figure 3.5 Types of filters shown with their ideal shapes: Lowpass (a), High-pass (b), Bandpass (c), and Notch (d). (Karu, 2001) p. 78.

Nevertheless, ideal filters are not possible to design in real life because for a signal with a frequency response in the shape of a rectangle, like the ones shown in Figure 3.5, it would be required an infinite long discrete vector. Still, non-idealized filters can be designed. The shape of these filters will not be flat and the transition between bands would not be perfectly sharp. Figure 3.6 shows an example of a non-idealized lowpass filter (Karu, 2001).

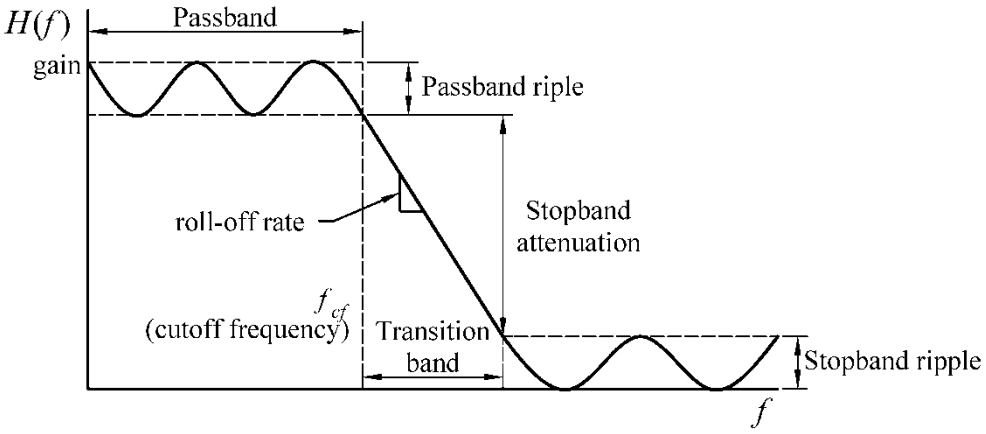

Figure 3.6 Filter diagram with its terminology for a non-idealized lowpass filter. (Karu, 2001) p.79

The terminology showed in Figure 3.6 is summarized in the following list (Karu, 2001):

- **Passband**: Frequency range of to preserve.
- **Stopband**: Frequency range to eliminate.

- **Transition band**: Transition frequency range to go from the passband to the stopband.
- **Gain**: Amplification on the passband.
- **Stopband attenuation**: Difference in dB between the passband and the stopband gain.
- **Passband/Stopband ripple**: Fluctuation peak to peak in the frequency response in the passband/stopband respectively.
- **Roll-off rate:** Steepness of the slop on the transition zone.
- **Order**: Number of points taken in the system function. A short transition band requires a higher order.
- **Cut-off frequency**: Start or end frequency of the passband zone.

There are several polynomials functions that can be used as filters, among the most common are: Butterworth, Chebyshev and Elliptical. The digital filters used for this study will be Butterworth. Butterworth filters are relatively flat (with no ripples) compared with other types.

Filters not only affect the frequency content of a signal, but some of them will produce a shift in phase on the signal. If the phase shift is a linear function of the signal, means that the whole signal will have a time delay difference from the input signal. This can be solved easily by shifting back the signal accordingly to the time delay of the filter. Furthermore, if a filter has a phase shift non-linear, it means that each frequency will be delayed differently.

On all the filters used in this study, the phase shift was linear, and therefore the time delay was constant for the whole signal.

3.3.3 Phase Velocity Dispersion

As it was discussed in the section Wave Propagation Theory. Some wave types are dispersive, which means that each frequency propagates at a different velocity. To obtain the phase velocity dispersion of the wave, at least two measurement points along the direction of propagation of the wave are needed. Having more measurement points can help improve the resolution of the dispersion.

In this section, a mathematical method to decompose a signal into its phase velocity content is briefly explained. The method presented in this section is based on (Ryden, Park Choon et al., 2004).

The frequency content (3.19) of the wave propagation displacement at the measurement point *'m'*, obtained using the Fast Fourier Transform (FFT) can be described by the multiplication of the amplitude *'A_m'* and its phase *'P_m'* (3.20). Similarly, the phase function expressed as its exponential form $e^{-i\omega t}$ is defined now as the equation (3.21), by changing the time variable as the relationship between the travel distance *'x_m'* and the phase velocity *'c'*.

$$F_m(\omega) = FFT(u_m(t)) \tag{3.19}$$

$$F_m(\omega) = A_m(\omega) P_m(\omega) \tag{3.20}$$

$$P_m(\omega) = e^{-i\omega x_m / c} \tag{3.21}$$

In this way, the equation (3.21) allows computing the participation coefficient for the phase velocity *'c'* at the frequency ω at point *'m'*. Equation (3.21) results in a matrix with a size equal as the length of frequency vector from the FFT and the arbitrary phase velocity vector used.

More detail on the testing procedure using this phase-velocity decomposition will be given in the section Multichannel Analysis of Surface Waves (MASW).

3.4 Time & Frequency

3.4.1 Short Fast Fourier Transform (SFFT)

Until now, the current chapter has introduced tools to analyze signals in the time and the frequency domain. This section will introduce a new approach to one of the FFT introduced before, to overcome its shortcomings. Although the FFT is a very powerful tool, its main drawback is that it only characterizes the frequency content and their participation as a whole, but it does not return any information about the location of these frequencies in time.

For example, a signal defined by (3.22) which has two different frequencies happening at a different point in time. This signal has a frequency of 1 Hz from zero to 4 seconds, and then its frequency increase to 4 Hz from 4 to 6 seconds. The time signal has been plotted in Figure 3.7-a

$$f(t) = \begin{cases} 0.4\sin(1 \cdot 2\pi t) & 0 < t \le 4 \\ \sin(4 \cdot 2\pi t) & 4 < t \le 6 \end{cases} \tag{3.22}$$

The normalized frequency domain of the signal (3.22) has been plotted in Figure 3.7-b. The ripples in the frequency spectra are caused due to the sudden change in frequency in the time domain. Nevertheless, the main frequencies components are identified correctly by the FFT, including the participation coefficient. The magnitude of the frequency spectra at 1 Hz is twice the coefficient of (3.22) because the 1Hz frequency prevails on time twice the time of the 4 Hz frequency. But as it was mentioned before, the frequency spectra do not give any information besides the participation coefficient of each frequency on the signal.

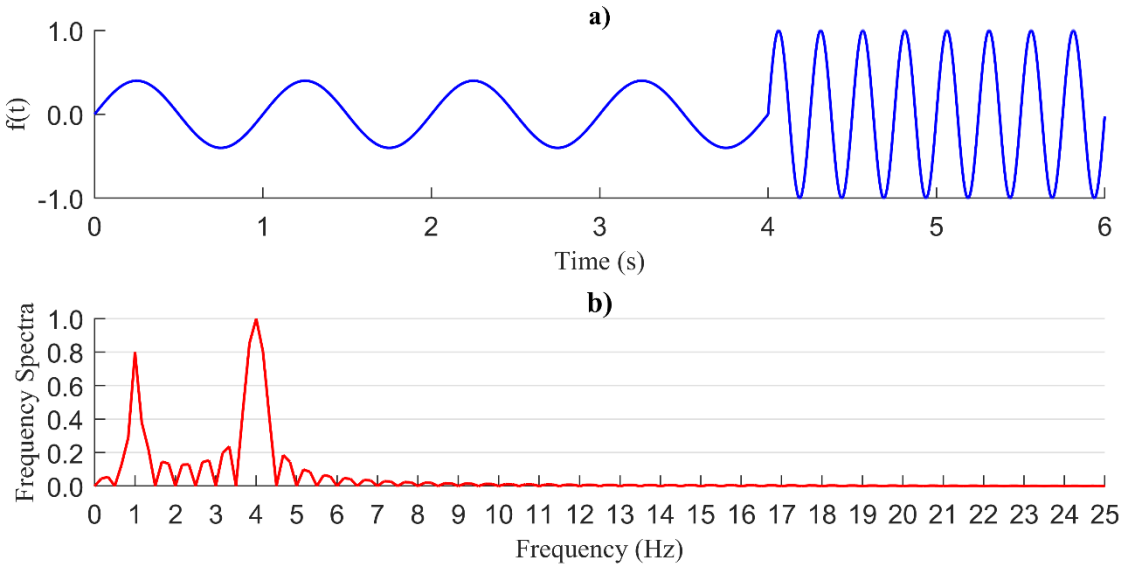

Figure 3.7 Time signal (a) from the equation (3.22) with two different frequencies along with the time interval. Its frequency domain obtained using FFT (b), showing the two main frequency components.

The location in time of frequencies is useful because it helps isolate the portions of the signals that are relevant. Selecting a time window of the signal is another way to filter a signal, without losing or altering any information.

The Short Fast Fourier Transform (SFFT) follows the same mathematical principle and algorithm of the traditional FFT, but instead of taking the whole-time signal, it divides the signal into small portions and analyzes these fragments in the traditional way. By doing this, the result is a frequency content at different points in time of the signal.

For a continuous signal, the SFFT is defined by (3.23), which is the same formulation as the FFT but the signal is modified by being multiplicated by a window function centred around the time *'t_c'*.

The window function discards any information on the signal outside the window. This way the FFT function becomes a function of two variables, frequency and time (Allen, 1977).

$$F\left(\omega,t_c\right)=\int_{-\infty}^{\infty} f\left(t\right)w\left(t-t_c\right)e^{-i\omega t}dt \tag{3.23}$$

Similarly to previous equations, the SFFT has a discrete representation (3.24) which is the one to be used on the signals analyzed during the present work. The equation (3.24) result is a matrix, which can be plotted as a surface or a colormap plot. The dimension *'k'* is as long as the resolution of the frequency vector, which is determined by the length of the window function. The second dimension *'l'* is the time shift of the window.

$$X_{kl}=\sum_{n=1}^{N} x_n w_{n-l} e^{-in\omega_k \Delta t} \tag{3.24}$$

Nevertheless, the SFFT has also some drawbacks. Due to the reduced time window, the frequency resolution decreases. It becomes a trade-off between frequency or time resolution. Choosing a time window large enough will improve the frequency resolution but decrease the time resolution. Likewise, if the time window is very small, the time resolution will improve, but the frequency resolution will be reduced.

The formulation for a swept sine will be introduced as an aid to illustrate the advantages and drawbacks of the SFFT. A swept sine is a sinusoidal signal that changes its frequency as a function of time. It is defined by the equation (3.25) (Lalanne, 2014), where *'Φ'* is the frequency function. When *'Φ'* is a constant, the swept sine reduces to the sinusoidal wave (2.10).

$$f\left(t\right)=\sin\left(2\pi\int\Phi\left(t\right)dt\right) \tag{3.25}$$

For the example presented below, the frequency function will be defined as the equation (3.26). The frequency will increase starting from zero and reaching its peak of 5Hz at 5 seconds and then reducing its frequency again to zero by time. The time signal of the swept sine with a frequency function equal to (3.26) has been plotted Figure 3.8-a. The instant frequency at each time (i.e. equation (3.26)) is plotted in Figure 3.8-b.

$$\Phi=5-\frac{\left(t-5\right)^2}{5} \tag{3.26}$$

The normalized FFT of the swept sine is shown in Figure 3.8-c. It shows the swept sine is formed by frequencies below 5 Hz, with most of the signal focused on the higher frequencies. Nevertheless, when a SFFT is performed in the same signal, the image from Figure 3.8-d is obtained. The darker the colour, the more energy the frequency posses at the given time. It's found the shape resembles the instant frequency used to build the swept sine (Figure 3.8-b). But the image is not very sharp due to the low frequency/time resolution of the SSFT.

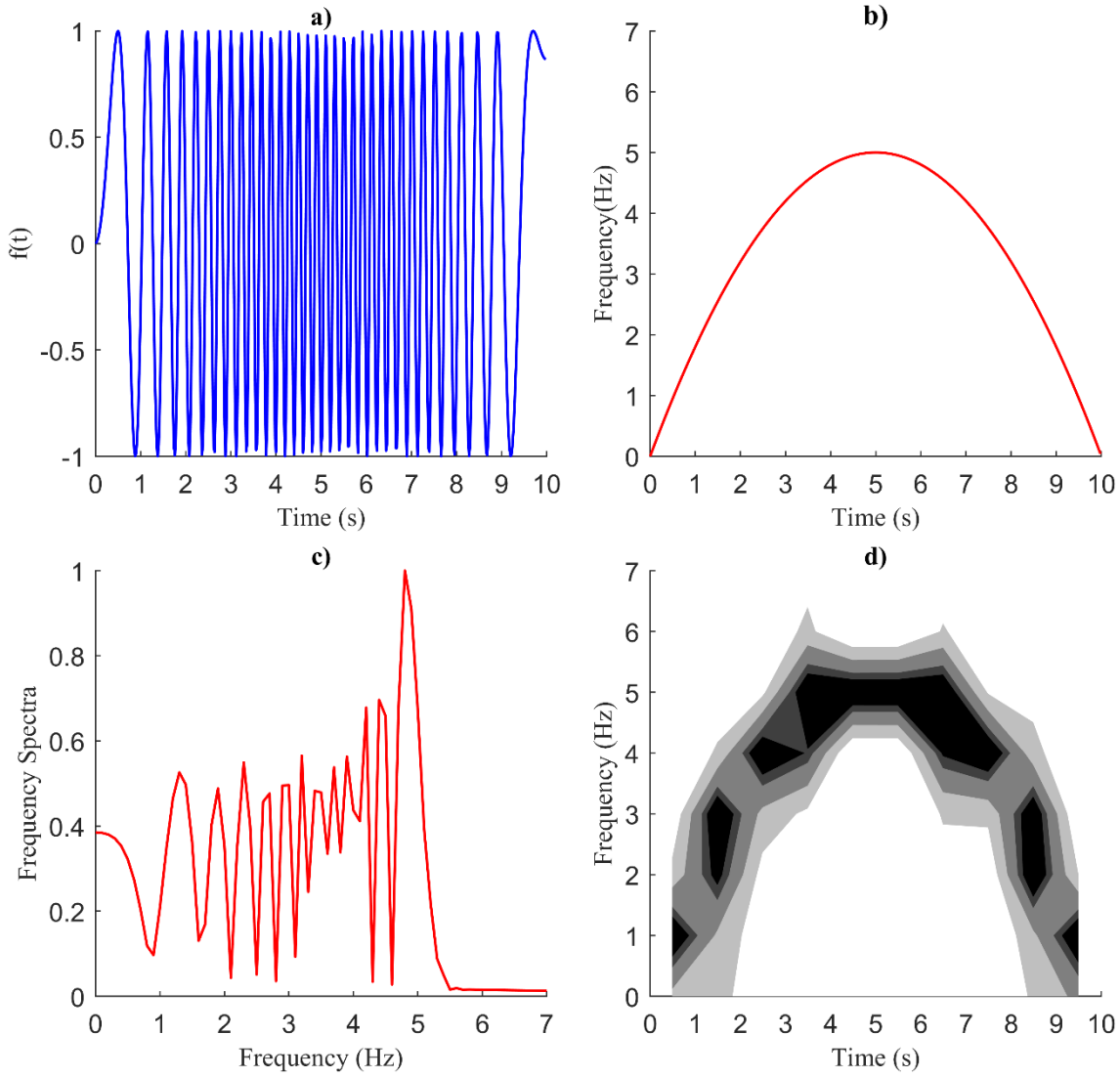

Figure 3.8 Plots showing the advantages and disadvantages of using Short FFT (d) to analyze a signal. Time signal (a) from the equation (3.25). The frequency function (3.26) used to generate the swept sine is plotted in (b). The normal FFT of the signal is plotted in (c).

But, despite the lack of definition, the SFFT shows the same information as the FFT that the frequency content was below 5 Hz, and also show where in time these frequencies are located.

3.5 Chapter Summary

During this chapter, the concept of signals was introduced, categorizing them into two types: continuous and discrete. The signals of interest for this study are discrete so all the formulations for the different tools were also presented in their discrete form.

The cross-correlation is used for measuring the similarities between two signals and it allows aligning signals that are shifted in phase. This is useful to obtain the average of different readings of the same signal phenomenon recorded at different times.

Afterwards, the Fourier Transform was introduced, allowing to change a signal from their time domain to their frequency domain. The limitations of the Fourier Transform were discussed, pointing out it doesn't give any information about the location in time of the frequencies, and the frequency resolution depends on the sampling frequency and length of the signal recorded. The large computational tax of the Fourier Transform force to use an algorithm to improve computational efficiency (speed) and those set of algorithms are called Fast Fourier Transform (FFT).

The Short Fourier Transform (SFFT) was then introduced as a modification of the FFT that tries to overcome its limitation for locating the frequency content in time. Nevertheless, the SFFT requires a trade-off between frequency and time resolution. This trade-off is represented by an example.

The brief mathematical background to decompose a series of signals in their phase velocity as a function of the frequency was presented. With this laying out the path to analyze waves that are dispersive such as surface waves.

Chapter 4
Testing Methods

4.1 Introduction

In this chapter, different testing methods for concrete are going to be introduced. These tests will be divided into two categories: static and dynamic tests. Each one of these tests obtains different values for the same mechanical properties on certain material. The reason for this was previously explained in section Static and Dynamic Differences.

In section 2.7 *"Concrete",* it was discussed the properties of concrete depend on many factors such as aggregate types, proportions on the fine and coarse aggregate, age of concrete, size, humidity, air content, etc. It's extremely hard to estimate reliably the concrete strength, or elastic modulus just based on the concrete mix. Therefore, its common practice to verify the properties of the concrete used for any construction, which is done by testing the hardened concrete.

There are several test methods depending on the country or region within a country. Nevertheless, the different test methods can be divided into two types based on the test specimen tested: cubes or cylinders. Cubes are used mostly in European countries. While cylinders are common practice for all of North America, Australia and New Zeland (Neville, 1996).

The tests presented in this chapter are tests that have been standardized and are going to be used as a reference during the development of this work. This chapter will focus on the test methods prepared and backed up by the American Society for Testing Materials International (ASTM International).

There are two common sizes for cylinders to be used for compression tests: 150 mm in diameter and 300 mm in length; And 100mm diameter and 200 mm length. The latter has become more popular because it requires less force to reach their maximum stress (f'c), due to their smaller area, especially for high-strength concrete. The reduced force required by 100 by 200 mm cylinders allows using less expensive compression machines to do the static tests.

All concrete samples tested for this research were done in cylinders of 100 mm diameter and 200 mm diameter, therefore the discussion on this chapter is center on the requirements for this cylinder size.

4.1.1 Casting and Curing of Test Specimens

For casting cylinders of 100 by 200 mm (diameter by length), the concrete needs to be poured into moulds in two layers. Each layer needs to be rodded 25 times with a rounded end rod of 10 mm diameter evenly distributed along the cross-section. After each layer is rodded, the mould needs to be lightly tapped on the sides 10 to 15 times to allow large air bubbles to escape. The tapping can be done using an open hand or a mallet (ASTM_C192, 2018).

Once the concrete has been poured in cylinder moulds and the top surface has been finished to a flat surface. The cylinder moulds shouldn't be moved until the removal of the moulds. There are three different practices for the removal of the mould and curing of the cylinders depending on the purposes and casting conditions for those cylinders. These practices are summarized in Table 4.1.

Table 4.1 ASTM practices for mould removal and curing for concrete specimens based on their purpose

Curing Condition	Purposes	Mould Removal & Curing	Standard
Laboratory	• Mixture proportion for project concrete • Evaluation of concrete mix • Correlation with non-destructive tests • Specimens for research purposes	The moulds should be cover to avoid the evaporation of water on unhardened concrete. The specimen should be removed from their moulds 24±8 hrs after casting Curing the specimens placing them in either water storage tanks or a moist room	**(ASTM_C192, 2018)**
Standard Field Curing	• Acceptance testing for concrete strength • Quality control	Initial Curing: Store the cylinders with their moulds for 48 hrs after casting at a temperature between 16-27 °C. Protect the specimens from direct sunlight, and place them in any of the following environments to reduce moisture loss: (1) immerse them with plastic lids in water, (2) place them inside a container, (3) place them inside a damp sandpit, (4) cover specimens with lids, (5) place them inside plastic bags, or (6) cover them with wet fabric. Final Curing: Within 30 minutes of removing the moulds keep the surfaces of the specimens in contact with water at all times at a temperature of 23 ± 2 °C. This can be done with wáter storage tanks or moist rooms.	**(ASTM_C39, 2018)**

Field Curing	• Determine if the structure is capable • Comparison with standard cured specimens • Adequacy of curing of concrete in the structure • Form or shoring removal time requirements	Keep the cylinders as near as the where the concrete was deposited. Replicate any protection made for the formwork of the cast elements on the surfaces of the cylinders. Cure the cylinder the same way as the concrete structure. Remove moulds at the same time as the formwork removal.	**(ASTM_C39, 2018)**

If the cylinders are held in the field or they need to be transported to the laboratory for testing, they should not be moved until 8 hrs after the final settings have passed. During transportation, appropriate measures to protect the specimens of cold weather or moisture loss should be taken, besides cushion material needs to provided to avoid damage from impacts. Transportation time should be less than 4 hrs.

4.1.2 Precision for Test Methods

The precision required by the ASTM standards is defined based on the coefficient of variation of the samples prepared from the same concrete batch and tested at the same age, at the same laboratory by a single operator (ASTM_C670, 2015).

The acceptable range between the highest and lowest values obtained by the tests is defined in terms of the coefficient of variation (COV) and the number of test results. To obtain the maximum acceptable range the COV needs to be multiplied by factor shown in Table 4.2 (ASTM_C670, 2015).

Table 4.2 Multipliers for the coefficient of variation to compute maximum acceptable range depending on the number of samples/tests. (Harter, 1970) pp. 372-374.

# Tests	Multiplier of COV	# Tests	Multiplier of COV
2	2.77	18	4.93
3	3.31	22	5.08
4	3.63	26	5.20
5	3.86	30	5.30
10	4.47	36	5.43
12	4.62	40	5.50
15	4.80	50	5.64

4.2 Static Methods

Static tests use load rate relatively low and therefore are considered they are static tests. Another characteristic of these types of tests is that the strain range is quite large above $1x10^{-3}$ up to the failure of concrete (~$3.5x10^{-3}$).

The values obtained with these tests are the ones used for the structural design of concrete buildings because during its lifetime they are exposed to large loads that will deform the structure near its limits. Therefore, these tests are more representative of concrete behaviour in a real-life scenario.

4.2.1 Compressive Strength Test

4.2.1.1 Specimen requirements

The standards do not specify a certain diameter or length for the cylinders to be tested, but rather a ratio L/D between 1 and 2 (ASTM_C39, 2018).

Before the compression tests, both ends of the cylinders need to be perpendicular to the axis with a maximum deviation of 0.5° (1mm in 100 mm cylinder). Both ends also need to be plane with an error margin of 0.05 mm. Otherwise, the specimens need to be sawed, ground or capped to meet these requirements (ASTM_C39, 2018).

4.2.1.2 Test setup

The concrete cylinders should be tested as soon as possible after removing them from their moist storage, the tolerances depend on the age of the specimens and they are given in Table 4.3. The machine used to test the cylinders should be capable of applying sufficient load into the cylinder to reach its maximum strength and record the maximum load with an accuracy of ±1% (ASTM_C39, 2018).

The load needs to be applied at a rate of 0.25 ± 0.05 MPa/s. For machines that are displacement controlled, the displacement of the bearing plates needs to be adjusted to achieve the proper loading rate which will depend on the size of the specimen, elastic modulus of the specimen and the stiffness of the machine (ASTM_C39, 2018).

Table 4.3 Tolerance for compression testing of concrete specimens after being removed from the moisture storage. (ASTM_C39, 2018) p. 5.

Test Age	Tolerance
24 h	0.5 h
3 days	2 h
7 days	6 h
28 days	20 h
90 days	2 days

4.2.1.3 Calculation

The compressive strength *'fc'* will be computed as the maximum load divided by the area of the cylinder. In case the ratio length-diameter (L/D) is less than 1.75, the compressive strength needs to be corrected by multiplying with the factors shown in Table 4.4. For other L/D ratios, the respective correction factors can be computed by interpolation (ASTM_C39, 2018).

Table 4.4 Correction factors for compressive strength of specimens with L/D ratio different than 2. (ASTM_C39, 2018) p. 6.

L/D:	1.75	1.5	1.25	1
Correction Factor:	0.98	0.96	0.93	0.87

In case the density of the concrete is required, it can be estimated by either using specimen dimensions or submerged weighing (ASTM_C39, 2018).

4.2.1.3.1 Required precision

For the compressive strength of cylinders of 100 mm diameter by 200 mm length, the maximum coefficient of variation permitted is 3.2% (ASTM_C39, 2018).

4.2.2 Elastic Modulus & Poisson's ratio Test

4.2.2.1 Specimen requirements

The specimen requirements for elastic modulus and Poisson's ratio tests are the same as with the compressive strength test: cylinders with L/D ratio between 1 and 2, both ends should be within ± 0.5° from the transverse axis, and both ends surfaces need to be plane with a tolerance of 0.05 mm. Otherwise, specimens need to be capped, sawed or ground (ASTM_C469, 2014).

4.2.2.2 Test setup

It is allowed to obtain the elastic modulus and compressive strength of a concrete cylinder during the same loading. Therefore, the same test setup described for the Compressive Strength Test is also applicable for the elastic modulus test. (Accuracy of recordings ±1%, and with a load rate of 0.25 ±0.05 MPa/s). Although the elastic modulus standard gives another loading rate of 1 mm/min, which is based on the displacement of the loading plates (ASTM_C469, 2014).

Nevertheless, additional precautions are needed to test cylinders for their elastic modulus. The cylinder needs to be loaded at least three times from zero to 40% of the estimated ultimate load. Once the final load is reached, the specimen needs to be unloaded at the same rate at which it was loaded. During the last loading, the loading can continue to reach failure and obtained the compressive strength of the specimen. (Unloading is not needed for the final loading) (ASTM_C469, 2014).

During the loading, the following parameters need to be recorded: load, longitudinal, and transverse deformation. These recordings need to be at least at the following two points: 1) the 50 microstrains in the longitudinal direction, and 2) the 40% of the ultimate compressive strength. Although a continuous recording of the three parameters is ideal to determine the stress-strain curve (ASTM_C469, 2014).

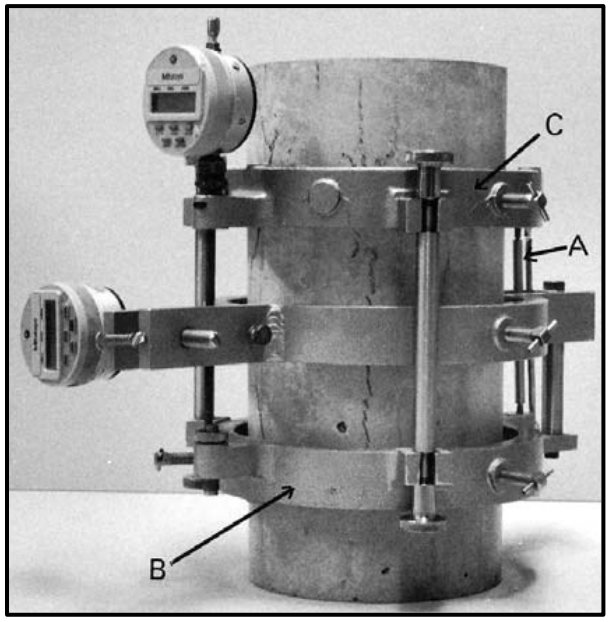

Figure 4.1 Example of rings system to attach unbounded gauges to a concrete cylinder to measure longitudinal and transversal deformation. (ASTM_C469, 2014) p. 2.

To measure the longitudinal and transverse deformations the use of a compressometer and an extensometer is required. These can be of two kinds, bounded or unbounded. Bound gauges can be difficult to attach to continually moist cured specimens. Unbounded gauges are attached to the cylinder with a ring system as shown in Figure 4.1 (ASTM_C469, 2014).

4.2.2.3 Calculation

The static modulus of elasticity is defined by the secant tangent between the 50 millionths longitudinal strain ('ε_1') and at 40% the maximum compressive strength ('σ_2'). This can be better expressed in the equation (4.1) (ASTM_C469, 2014).

$$E_s = \frac{\sigma_2 - \sigma_1}{\varepsilon_2 - \varepsilon_1} \tag{4.1}$$

Where:

E_s = Static modulus of elasticity to the nearest 200 MPa.

σ_1 = stress at 50 millionths strain ('ε_1').

σ_2 = 40% the maximum compressive strength (f'_c).

$\varepsilon_1 = 50 \times 10^{-6}$.

ε_2 = strain at 40% the maximum compressive strength (f'_c).

The static Poisson's ratio is defined by equation (4.2) (ASTM_C469, 2014).

$$\nu_s = \frac{\varepsilon_{t2} - \varepsilon_{t1}}{\varepsilon_2 - \varepsilon_1} \tag{4.2}$$

Where:

ν_s = Static Poisson's ratio to the nearest 0.01.

ε_{t1} = transverse strain produced at the mid of the cylinder at the 50 millionths longitudinal strain.

ε_{t2} = transverse strain produced at the mid of the cylinder at 40% the maximum compressive strength (f'_c)

4.2.2.3.1 Required precision

The coefficient of variation required for the elastic modulus and Poisson's ratio is ± 4.25% (ASTM_C469, 2014).

4.3 Dynamic Methods

In contrast to static tests, dynamic tests use fast loading and unloading with very low amplitudes producing very low strains, around $1x10^{-6}$ (Bay & Stokoe, 1992). Because of the small strains produced into the specimens, dynamic tests are also referred to as non-destructive tests. Due to these small strains, the values obtained from dynamic tests are not demonstrative of real structural applications as the static tests do.

Nevertheless, non-destructive methods have many advantages, the most notorious of them is that the equipment needed is relatively inexpensive compared with the destructive methods that require large machines capable of apply large loads (Up to 600 kN), especially for high-strength concrete (Nilsen & Aitcin, 1992). Also, these types of tests can also be repeated in the same specimen given its non-destructive nature, which allows not only better control over the tests, but also to monitor the specimen's mechanical properties over time (Lemmens, 1990).

4.3.1 Ultrasonic Testing

The objective of measure the wave velocity of concrete take advantage of the wave propagation theory, previously discussed in section 2.6, on which wave velocity is related to the mechanical properties of the material such as Young's modulus, Shear modulus, and Poisson's ratio with equations (2.34) and (2.35).

Although there are several methods to estimate the wave velocity of concrete, only the approach of directly measuring the wave velocity is discussed in this section. (By direct measurement of the time taken for a pulse to travel through the material).

4.3.1.1 Specimens requirements

The ASTM standard to measure wave velocity in concrete (ASTM_C597, 2016) states that the wave velocity is independent of the dimensions of the specimen. The only requirement it sets for the specimen is that its least dimensions need to be larger than the wavelength of the pulse used during the tests.

Although in the standard for determining elastic constants by means of UPV in rocks (ASTM_D2845, 2008), it is recommended that the wavelength of the dominant frequency of the pulse to be less than one-fifth of the diameter of the sample.

$$\lambda \leq \frac{D}{5}$$

More recently, Wiciak tested different pulse frequencies in different ratios L/D of concrete cylinders, finding the P-wave velocity could have an error in the estimation of around 20% when using impulse frequencies with a wavelength equal to the diameter. To avoid a wrong estimation of the P-wave velocity, Wiciak recommends the following ratio for concrete cylinders (Wiciak et al., 2019):

$$\lambda \leq \frac{D}{3}$$

4.3.1.2 Test setup

The main concept of Ultrasonic Pulse Velocity (UPV) tests is sending a pulse through the concrete cylinder and measure the time it takes for the pulse to travel. The frequency of the pulse used is recommended to be between 20 and 100 kHz, to minimize attenuation signals. Although using higher frequencies is not prohibited (ASTM_C597, 2016). A schematic figure of the test setup required is shown in Figure 4.2.

The transducer used at both ends should have similar characteristics, with a flat response in the range of one half and three times their resonant frequency. If needed the receiver voltage can be amplified (ASTM_C597, 2016).

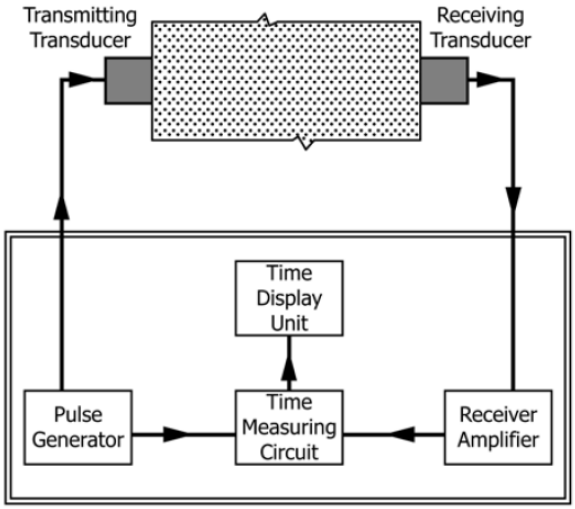

Figure 4.2 Diagram of the test setup required for UPV tests. (ASTM_C597, 2016) p. 2.

The pulse should be able to be repeated at least 3 times per second, but allowing enough time between pulses for the previous pulse has completely decayed and cannot be detected anymore by the receiver transducer (ASTM_C597, 2016). There are no requirements for the type of pulse to be used.

The time measuring device should be capable of taking time measurements or sampling the signal at least each microsecond. In other words, the minimum sampling frequency for the signals should be 1 Mhz (ASTM_C597, 2016).

4.3.1.3 Calculation

To compute the wave velocity the formula below is used:

$$c = L/t$$

Where:

c = Wave velocity (V_p or P-wave velocity if P-wave transducers were used; V_S or S-wave velocity if S-wave transducer were used. It needs to be reported to the nearest 10 m/s.
L = length of the concrete cylinder (With 0.5% precision).
t = time taken for the pulse to travel through the cylinder (With 0.1 μs precision).

Knowing the P and S wave velocity in concrete, it is possible to estimate the dynamic modulus of elasticity and the Poisson's ratio using equations (2.34) and (2.35). If only one of the wave velocities is known, assuming a Poisson's ratio would be needed.

4.3.2 Resonant Method

This method uses the relationship between the resonant frequencies of a solid body with its mechanical properties. The theory behind it was discussed in the section Free Vibrations. This method was first introduced by (Powers, 1938) trying to match the musical tone produced by concrete beams using calibrated bells (Mehta & Monteiro, 2005). Since then several studies and approaches have been proposed to measure the resonance frequency, using different instruments such as accelerometers, transducers, hydrophones, microphones etc.

The most important advantage of this method is the simplicity of the measurement with high accuracy and its applicable even for very porous materials. Although its main limitation is its simplicity is only valid for certain specimen shapes and sizes. For example, for certain specimens, the

resonance frequencies could be either too low or too high and therefore needing more accurate equipment. Or on the other hand, if it's a complicated shape it can be hard to find the equations for the resonance frequencies. Or it can be hard to identify the right frequencies from the different vibrations modes possible.

When using the resonant method, it is crucial to consider the proper equations that include rotational inertia and Poisson effects. As it was discussed in sections 2.6.3 and 2.6.4.2.4. Failing to account for these effects result in bad estimations, as for example, the mismatching Poisson's ratio found for Simmons by mixing P-wave velocity equations (2.34), longitudinal resonant frequency equation (2.48) and the torsional resonant frequency equations (Simmons, 1955).

4.3.2.1 Specimens requirements

The standard for evaluating the dynamic modulus and Poisson's ratio using resonance frequencies in concrete (ASTM_C215, 2014) considers both cylinders and rectangular prisms. But as mentioned, the current work is focused on cylinders. The standard ASTM C215 sets as specimen requirement a ratio L/D not lower than 2. The dimensions of the specimens need to be measured with tolerance within ±0.5%.

4.3.2.2 Test setup

ASTM C215 describes two different approaches to measure the resonance frequency: *Forced resonance method*, and the *impact resonance method*. This research is focused on the *impact resonance method*, therefore only this methodology is going to be introduced in this section.

The impactor shall be able to excite the highest resonant frequency expected from the cylinders. The standard advice a 19 mm solid steel ball mounted on a thin rod is capable of exciting resonant frequencies up to 10 kHz (ASTM_C215, 2014). This will be further discussed in section Hammer and support selection.

The sensor specified by the standard is an accelerometer with mass not larger than 30 g with a flat response on the range of 0.1 to 15 kHz. The resonant frequency of the accelerometer should be at least twice the maximum expected resonant frequency (ASTM_C215, 2014).

To measure the cylinder response, the signal needs to be sampled at least 2.5 times the maximum expected frequency with a minimum of 2048 samples. The signal recording should be set for the frequency measurement can be computed with an accuracy of ±1% (ASTM_C215, 2014).

The specimen needs to be supported in a certain way depending on the resonant frequency desired to measure (longitudinal, transversal, or torsional). In a similar way, the accelerometer position and the point of impact will depend on the resonant frequency measured. The different setups specified by the standard are shown in Figure 4.3. The accelerometer can be attached to the cylinder using glue or grease. In case that the cylinder is wet, the point of contact where the cylinder is going to be located can be dried using air jet.

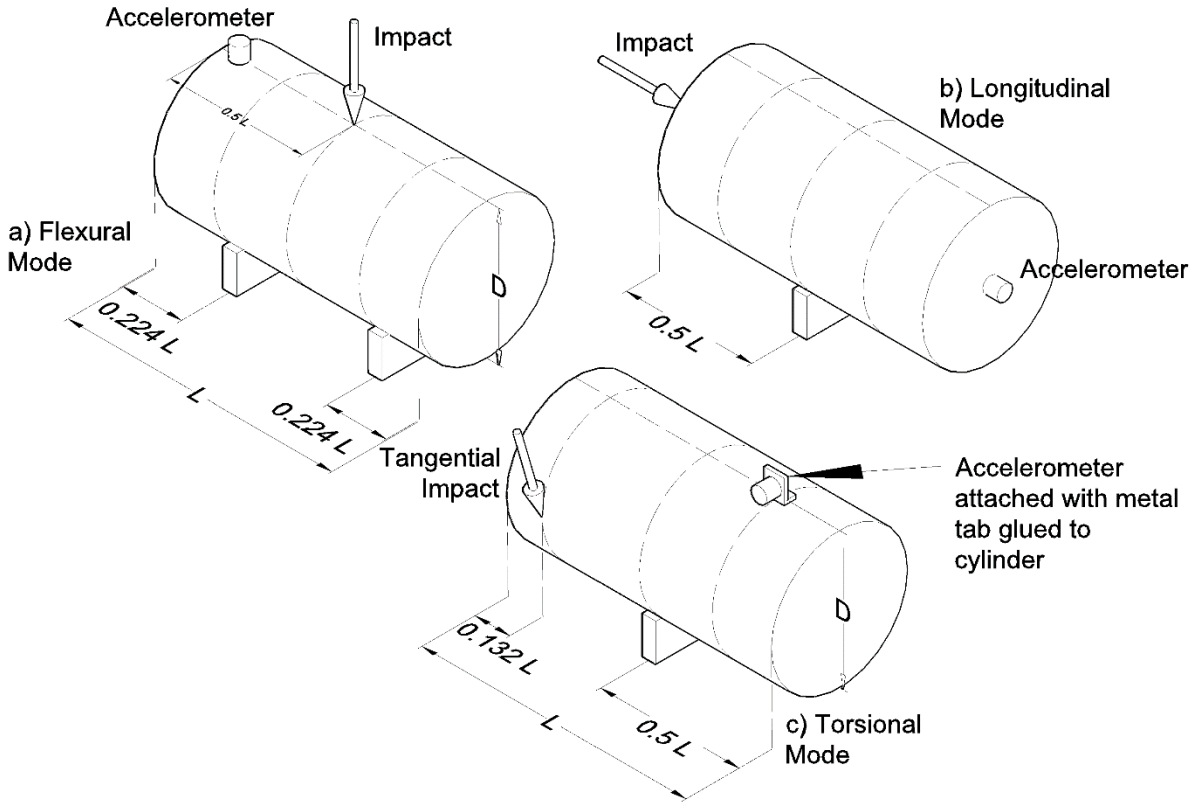

Figure 4.3 Location for the supports, accelerometer and point of impact to test for the (a) flexural, (b) longitudinal, and (c) torsional resonant frequencies in concrete cylinders. (ASTM_C215, 2014).

4.3.2.3 Calculation

The standard (ASTM_C215, 2014) gives two equations (4.3) and (4.4) to compute the dynamic modulus of elasticity. The dynamic modulus using the longitudinal resonant frequency is represented by 'E_{dl}', while 'E_{df}' represents the dynamic modulus computed using the flexural resonant frequency.

$$E_{dl} = 5.093 \cdot \frac{L \cdot m}{K_L \cdot D^2} f_l^2 \tag{4.3}$$

$$E_{df} = 1.6067 \frac{L^3 \cdot T_m \cdot m}{D^4} f_f{}^2 \tag{4.4}$$

On the equations above, *'m'* is the mass, *'L'* is the cylinder length, *'D'* is the cylinder diameter, and the longitudinal and flexural frequencies are represented by *'f_l'* and *'f_t'*. The variable T_m is a correction factor that accounts for the finite diameter and the Poisson's ratio.

Both equations involve corrections factor, *'K_L'* and *'T_m'* respectively. Disregarding these correction factors these past tow equations were derived previously (equations (2.50) and (2.68)).

The factor for the longitudinal dynamic modulus (*'K_L'*) is omitted in the standard for concrete (ASTM_C215, 2014), although it is included in the standard for miscellaneous materials (ASTM_E1876, 2015).

The longitudinal correction factor was initially proposed by Love (Love, 1944), and it is usually referred to as Love's correction factor (J. S. Popovics et al., 2008). The factor tries to compensate for ignoring the rotational and the lateral inertia on the differential equation of free axial vibration in a rod (2.38). Love's correction factor is defined by the expression (4.5). It is a function of the Poisson's ratio *'ν_d'*, and the slender ratio *L/D*.

$$K_L = 1 - \frac{\pi^2 \nu_d{}^2 D^2}{8L^2} \tag{4.5}$$

Love's correction factor (4.5) has been plotted in Figure 4.4 for different slender ratios *L/D* and Poisson's ratios. The left side of the figure (Figure 4.4-a) shows a wide range of L/D and shows that for ratios above 20 the correction factor is approximate 1 regardless of the Poisson's ratio. The lower the Poisson's ratio, the correction factor is closer to 1. Figure 4.4-b shows a close up to the slender ratio of interest for this study (*L/D* around 2). The variation due to the Poisson's ratio for slender ratio equal to 2, is around 8%.

Likewise, the factor *'T_m'* is an approximation of the solution for the differential equation of a Shear beam, also called Timoshenko's beam (Pickett, 1945). The assumptions made to derive the flexural frequency equation for a beam in the section '*Free Vibrations'* are no longer valid for short beams. The factor *'T_m'* tries to include the lateral, torsional and shear effects for Timoshenko's beam.

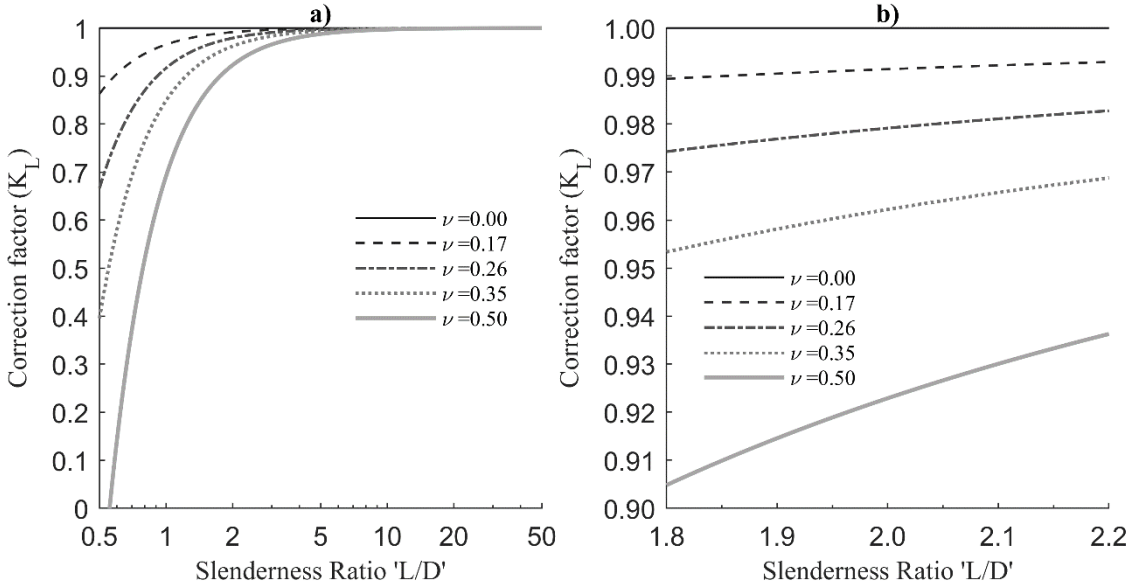

Figure 4.4 Love's correction factor (4.5) for different Slender ratios L/D. (a) L/D ratio ranges between 0.5 and 50, and (b) close up to Slender ratios of interest (around 2).

The correction factor *'T_m'* can be computed using a combination of a table, interpolation and a small equation given in standard (ASTM_C215, 2014). Nevertheless, in the analogous standard for miscellaneous materials (ASTM_E1875, 2013), the equation (4.6) is given, which allows computing directly from the dynamic Poisson ratio *'ν_d'* and the slenderness ratio (*L/D*) the correction factor. This expression returns the same values as the ASTM C215 and is more convenient for coding algorithms.

$$T_m = 1 + 4.939\left(1 + 0.0752\cdot\nu_d + 0.8109\cdot{\nu_d}^2\right)\left(\frac{D}{L}\right)^2 - 0.4883\left(\frac{D}{L}\right)^4 - \frac{4.691\left(1 + 0.2023\cdot\nu_d + 2.173\cdot{\nu_d}^2\right)\left(\frac{D}{L}\right)^4}{1 + 4.754\left(1 + 0.1408\cdot\nu_d + 1.536\cdot{\nu_d}^2\right)\left(\frac{D}{L}\right)^2} \quad (4.6)$$

The equation (4.6) has been plotted in Figure 4.5 for different slender ratios *'L/D'* from 0.5 to 50 (Figure 4.5-a) and a close up into the slender ratio range of interest for this study (1.8 to 2.2) (Figure 4.5-b). Figure 4.5-a makes evident the correction factor approach to 1 for L/D ratios above 20. On the other hand, Figure 4.5-b highlights the relevance of the Poisson's ratio, for an L/D ratio the correction factor *'T_m'* varies from 2.07 to 2.32 for Poisson's ratio of 0 and 0.5 respectively, which means a variation of 12% between both extremes.

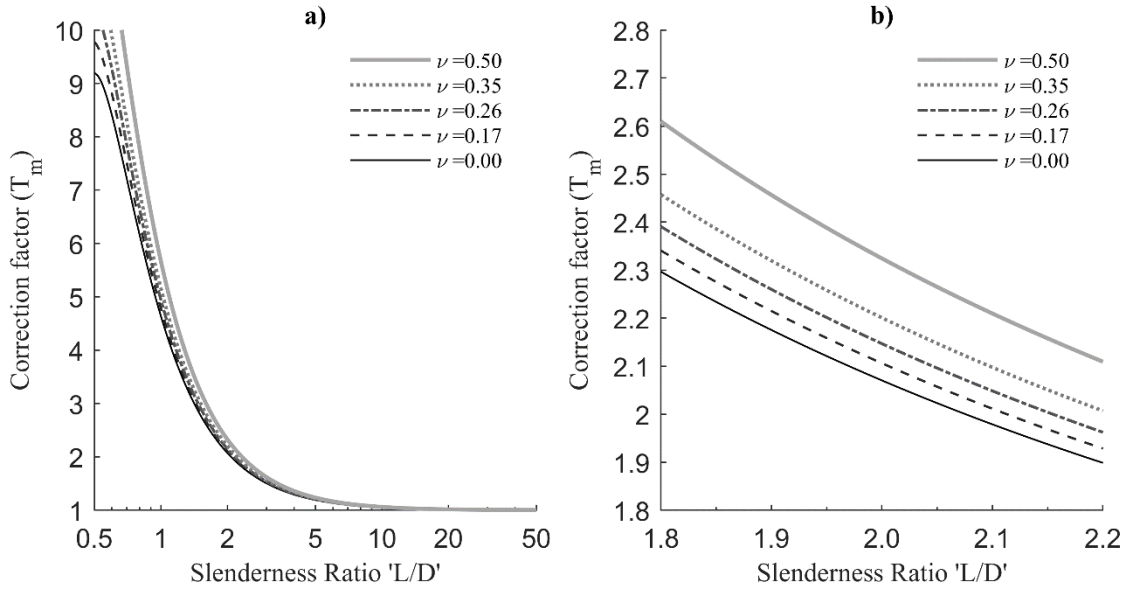

Figure 4.5 Correction factor *'T_m'* obtained with the equation (4.6) for different slender ratios and Poisson's ratios. (a) L/D ratios from 0.5 to 50. And (b) close up to L/D ratios from 1.8 to 2.2.

Although in theory, both dynamic moduli estimated using longitudinal and flexural frequencies should be equal, the dynamic modulus estimated using the transverse resonant frequency results in higher values than using the longitudinal resonant frequency for ASTM C215 (J. S. Popovics et al., 2008). This might be due to a combination of two factors, the lack of correction factor in the longitudinal dynamic modulus, and different strain levels experienced in each vibration mode. Recalling the section *'Elastic Moduli'* the instantaneous elastic modulus depends on the strain.

For computing the Shear modulus (*'G_d'*) the ASTM C215 standard gives the equation (4.7). Which is almost identical to the longitudinal dynamic modulus, but using the torsional resonant frequency *'f_t'*.

$$G_{dt} = 5.093 \frac{L \cdot m}{D^2} f_t^2 \tag{4.7}$$

The dynamic Poisson ratio can be estimated by knowing both the dynamic modulus of elasticity and the dynamic shear modulus with the equation (4.8). Since the flexural dynamic modulus requires the dynamic Poisson's ratio, typically the longitudinal dynamic modulus equation (4.6) is used in combination with the torsional resonant frequency (4.7) to compute the Poisson's ratio.

$$\nu_d = \frac{E_d}{2G_d} - 1 \tag{4.8}$$

The standard ASTM E1876, propose a methodology to estimate the dynamic modulus and the Poisson's ratio using an iterative process using the longitudinal dynamic modulus equation (4.3) and the dynamic shear modulus (4.4), by proposing and arbitrary initial Poisson's ratio and iterate until a difference tolerance between the new Poisson's ratio and the previous one is less than 0.02 (ASTM_E1876, 2015).

According to the ASTM C215, the dynamic Poisson's ratio can vary between 0.1 and 0.25. With lower values for dry specimens, and higher values for saturated specimens. Nevertheless, even higher values can be expected for concrete samples at an early age.

4.3.2.4 Precision

The precision required for a single operator testing for the flexural resonant frequency is 1.0% in the range of 1.4 to 3.3 kHz. Although for longitudinal and torsional resonant frequencies the standard (ASTM_C215, 2014) does not provide any information or guideline.

4.3.2.5 Related research

Due to the relevance the resonant method has in this work, additional information will be provided in this section. Therefore, this chapter will briefly discuss other testing methodologies used by other researchers regarding the resonant method.

Some researchers have already tried using the resonant methods using other types of sensors besides accelerometers. From coils surrounding the concrete shaft to measure the longitudinal frequency and a phonogram stylus for the torsional frequencies (Davis & Opat, 1983), also using phonogram stylus for both vibration modes (Gaidis & Rosenberg, 1986) , to the use of microphones on detecting the the resonance frequencies of the concrete cylinders (Boileau et al., 1981; Ito & Uomoto, 1997). With all these types of sensors being capable of detecting the resonant frequencies satisfactorily.

Most of the research in this area follows the setup proposed by the ASTM standard, but some of them have tried other support positions, and with different sensor and impact locations than in ASTM C215. For example:

- (Boileau et al., 1981) used a microphone with wide broadband from 5Hz to 160kHz instead of using an accelerometer, being capable of detecting flexural and longitudinal resonant frequencies.
- (Davis & Opat, 1983) test the rod by clamping it vertically to a stand with the coil sensor in the middle of the length of the rod, and the stylus on the top. This allows them to on a single test measure both torsional and longitudinal resonant frequencies.
- (Ito & Uomoto, 1997) support the concrete beam at the recommended position of the ASTM C215 (nodes of free vibration for flexural mode) using wires and a microphone. But they varied the location of the microphone along the bottom surface of the beam. Finding the best locations to obtain the maximum amplitudes of the resonant frequencies using the microphones.
- (Han & Kim, 2004) placed the cylinder vertically, and on the top surface, they attached the accelerometer almost at the center of the circular face. The impact was done on the same top surface almost at the center. The longitudinal resonant frequency was found which was used to compute the dynamic elastic modulus.

There is also extensive research regarding the calculation approach for the dynamic modulus, based on the resonant frequencies in concrete. These other works discuss the validity of the equations from ASTM C215 for the longitudinal resonant frequency and proposing different methodologies to compute the dynamic elastic modulus and Poisson's ratio. These works are briefly reported below:

- (Tefft & Spinner, 1962) they tried to get an empirical correction factor for the longitudinal resonance frequency by testing several cylinders with different *L/D* ratios.
- (Kolluru, Popovics et al., 2000) used the ratio between the first two longitudinal resonant frequencies obtained by a single resonant test, to compute both the dynamic Poisson's ratio and the elastic modulus. They obtained the equations relating the Poisson's ratio with the frequency ratio using the Rayleigh-Ritz method. They compared the results they obtained with the ones obtained using ASTM C215, and the P-wave velocity for reference materials. Finding their approach had around 10% less error in estimating both material properties (E_d and ν_d) compared with the standard ASTM C215.

- (J. S. Popovics et al., 2008) Thet state that the longitudinal dynamic modulus is less accurate than using the flexural resonant frequency. But they found out the accuracy is improved by including the Love's correction factor. They claimed that by including Love's correction, both dynamic moduli agree with each other. In general, they found the flexural resonant frequency estimates higher values for E_d.
- (Wang, Chang et al., 2012) correction factor for longitudinal frequency and uses iteration to found poison's ratio.

4.3.3 Multichannel Analysis of Surface Waves (MASW)

Contrary to the previous tests, the Multichannel Analysis of Surface Waves (MASW) has not been standardized, either for concrete or any other material. MASW tests are mostly used in geotechnical engineering for the elastic properties of soils near the surface (Dikmen, Arısoy et al., 2010). There are some standards with methods that use a similar setup to the MASW using seismic refraction and reflection such as (ASTM_D5777, 2018) and (ASTM_D7128, 2018).

This test aims to measure the wave propagation along a line. Due to the dispersive nature of the surface waves in a layered or a finite medium, each frequency will travel at a different speed. By recording the wave at different distances, it is possible to measure the velocity scattering at each frequency.

4.3.3.1 Test setup

MASW uses a linear array of sensors to detect the wave propagation of the impulse source at the beginning of the array. Figure 4.6 shows a typical setup for MASW tests, *'T_r'* represents the transmitter of an impulse signal, and the *'R_i'* represents the receiver sensors located at a distance x_i from the source ('T_r'). The first distance x_1 is usually called *Initial Offset*, and de distance between two consecutive receivers (x_i and x_{i+1}) is called *Interval Offset*. The total length of the receiver array, i.e. the distance between the first and the last receiver ($x_N - x_1$) is called the *Spread Length* (X_L).

Despite the popularity growth of the method in geotechnical engineering, there is no consensus on the rules for the MASW field setup regarding the initial and interval offsets or the spread length. Although, some recommendations have been made. For example (S. X. Zhang, Chan et al., 2004) reported that Heisey recommended an interval offset between 0.67 and 2 times the maximum wavelength of the Rayleigh wave; Sanchez-Salinero said that the usable wavelength is less than 1.5

times the interval offset and that the initial offset should be the same as the interval offset; And Roesset suggested a ratio between the initial and the interval offset between 1 and 2, and a ratio between the initial offset and the wavelength should be between 0.5 and 2. These recommendations are mostly based on empirical data.

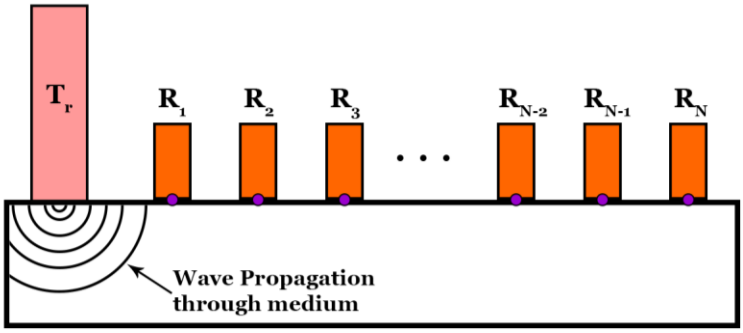

Figure 4.6 Typical setup for the MASW test. Transmitter 'T_r' sending a pulse into a medium with a linear array of receivers 'R_i' at a distance 'x_i' from the impulse source.

However, (S. X. Zhang et al., 2004) found analytically and corroborated with experimental results that a spread length equal to (4.9) with an initial offset equal to (4.10) yield in a phase velocity dispersion curve with the best resolution. On the equation below, 'λ_{max}' is the maximum usable wavelength, 'V_{Rmin}' is the minimum expected Rayleigh wave velocity, and 'ΔV_R' is the Rayleigh wave velocity range expected.

$$X_L = \frac{\lambda_{\max} V_{R_{\min}}}{2 \cdot \Delta V_R} \tag{4.9}$$

$$x_1 = X_L / 2 \tag{4.10}$$

Using surface waves to asses the mechanical properties of rods have also been researched(Jones, 1962). An example of a set of times signals using MASW in a concrete cylinder from this work is shown in Figure 4.7 to better illustrate the test procedure. The full description of the setup used to get these signals will be further discussed in the chapter Experimental Program – Methodology.

In Figure 4.7, the time signals have been plotted vertically (i.e. the vertical axis corresponds to the time and is inverted), All the signals have been normalized to themselves for plotting purposes. The impulse signal used to start the vibration in the cylinder is plotted at the origin (i.e. position at zero distance). Each signal has been plotted in the horizontal axis at the respective distance x_i where the receiver R_i was located during the measurement.

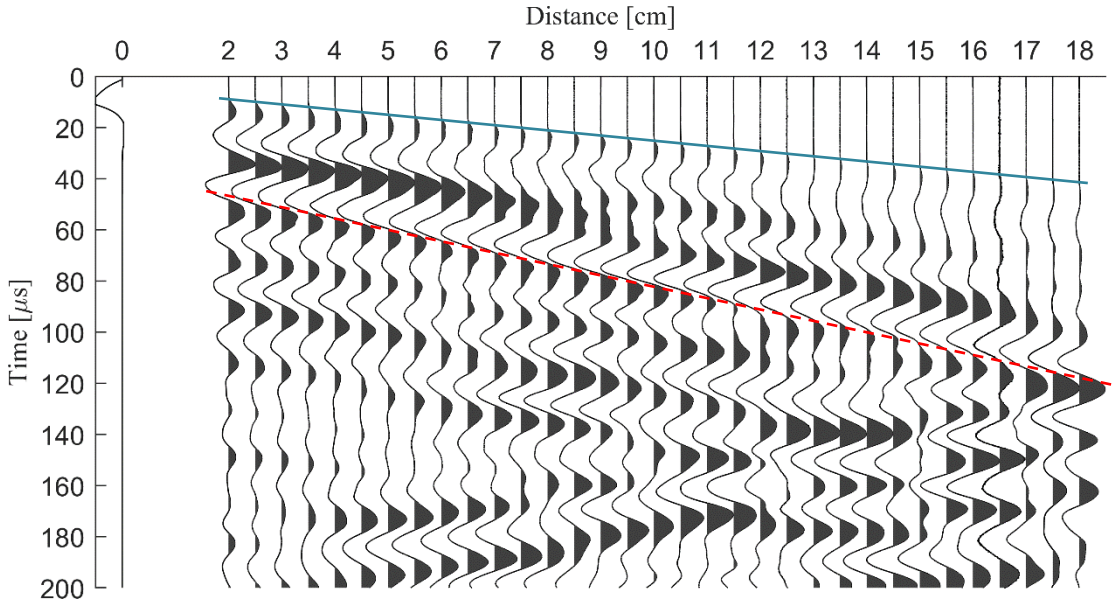

Figure 4.7 Typical time signal array for an MASW test. Each time signal ('R_i') is plotted on the horizontal axis at the distance ('x_i') at which it was taken with respect to the impulse source ('T_r'). The time signals are plotted vertically.

By looking into Figure 4.7 it becomes evident that the first signal at a distance of 2 cm, is more compacted in time than the last signal measured at a distance of 18 cm. This is the result of the phase velocity dispersion. In the same figure, two lines have been drawn to highlight the presence of at least to different waves travelling at different speeds (slopes). A continuous blue line shows the P-wave velocity and the red dashed line what could be the Rayleigh wave velocity. Between these two lines, other intermediate slopes can be found.

4.3.3.2 Calculation

To process a data set like the one shown in Figure 4.7, the formulas (3.19) - (3.21) should be used. The process is pretty straightforward. The first thing is to compute the FFT for all receiver signals and normalize the frequency spectrum with respect to themselves. These vectors represent the amplitude in the equation (3.20) and since it does not contain information on the phase velocity it can be normalized without losing any information (Ryden et al., 2004). The normalized frequency spectrum matrix will be named as $\hat{F}_{lm}$ with as many rows as the frequency resolution of the FFT, and as many columns as a number of signals.

To compute the phase velocity dispersion *'Ph'*, the equation (4.11) shall be used. The formula is expressed in Einstein notation where:

x_m: is the distance from the source to the receiver *'m'*.

c_k: is an arbitrary velocity vector with the range of interest and with a certain phase velocity resolution.

ω_l: is the frequency vector from the FFT analysis.

'i': is the imaginary number equal to √-1.

$$Ph_{kl} = \left| \hat{F}_{lm} e^{i\omega_l \frac{x_m}{c_k}} \right| \tag{4.11}$$

The result of the equation (4.11) is a matrix that creates a dispersion image of phase velocity in the vertical axis and frequency in the horizontal axis. The resulting matrix has as many rows as the velocity vector ('c ') length and with as many columns as the frequency vector ('ω') length.

4.4 Chapter Summary

In this chapter, the most relevant testing methods for the current work were discussed. Those tests were divided as static and dynamic tests, depending on the strain levels used to asses the mechanical properties.

The chapter starts by introducing how the concrete cylinder should be prepared since the moment they are cast into the moulds until the moment they are going to be tested, including different curing procedures to follow depending on the purpose for those cylinders (e.g. for research purposes, quality control or strength assessment of structural elements).

The static tests, the UPV and resonant tests of concrete cylinders were introduced along with their respective ASTM standards. For each one of them, their test setup, calculation procedure and the precision required were summarized.

Special emphasis was set on the resonant method test given its relevance for the current work. In this section, other research findings were commented, highlighting that the UPV tests usually produce higher dynamic elastic modulus values than the resonant tests for concrete cylinders with an *L/D* ratio around 2. And it may exist a difference between the longitudinal and flexural dynamic modulus in the resonant tests, being the former one least accurate when disregarding the correction factor (J. S. Popovics et al., 2008).

Finally, the MASW technique is introduced. Although it's not a standardized test, the typical test setup was described and some guidelines given for researchers for choosing the optimal test setup were listed. An example of the data set obtained from an MASW test was shown along with a description of the calculation of the phase velocity dispersion image for a data set.

Chapter 5
Experimental Program – Methodology

This chapter will describe the methodology and test setup used for the tests involved in the current work. Starting with an overall picture of the tests and a description of the test specimens used for this work.

The methodology for the tests will be divided into two sections, similar to the previous chapter '*Testing Methods'*, but starting with the dynamic tests and later on the static tests. To follow the chronological order in which the tests were conducted in the specimens.

5.1 Methodology Overview

As it was discussed in the first chapter '*Introduction',* the current research has three main objectives: 1) Validate the usage of non-professional microphones like the ones included in regular modern devices nowadays, such as cellphones, for its usage in the resonant testing method of concrete cylinders; 2) Correlate dynamic and static elastic moduli of concrete; 3) Propose a methodology to estimate the static elastic modulus of concrete using early age dynamic measurements.

To achieve this goal one static and three dynamic methods were used. The dynamic tests performed were: The resonant test, the MASW test, and the ultrasonic pulse velocity test. For the static test, only the compression test was performed on the cylinders to evaluate their static elastic modulus.

The resonant test method is discussed further and is divided into subsections due to the special interest of this test for this research. It's divided into five sections:

1) Microphone selection: Methodology to validate the capabilities of different microphones and determine the best location to place them for the resonant test.

2) Hammer selection: Methodology and test setup to choose the best impulse device for exciting the resonant frequencies of the concrete cylinders tested.

3) Frequency Selection Algorithm. The algorithm to detect the right frequency peaks from the frequency spectrum recorded from the microphone is described and explained in this section.

4) Accelerometer test. Final setup for the resonant test using an accelerometer and the hammer selected as a result of the hammer selection tests.

5) Microphone test: Final setup for the resonant test using the microphone, its position and the hammer selected on their respective selection section.

5.1.1 Concrete Mix Batches

This section will introduce the different concrete mix used during the development of the current work. A batch of concrete is defined by an amount of concrete mixed at a certain time with specific mix proportions The main role that each batch had for the development of this work is also discussed. When available, the mix design specifications are provided for each batch.

This work used five different batches of concrete. The batches were named in sets of one hundred from zero to four. The reason for naming the batches this way was to allow naming the cylinders with a number related to their batch number.

Batches 000 and 200 were cast for Fartosy research and kindly lend some cylinder samples for this research. Similarly, the batches 100 and 300 were cast for (Wiciak et al., 2019)and Sleiman research respectively, providing some of the cylinders for this work. Batch 400 was elaborated specifically for this research. The exact date of casting for batches 000 and 300 are unknown. Nevertheless, the concrete can be considered to be over one year old at the time of every test. This information is summarized in Table 5.1 along with the size of the cylinder lot from each batch used for this research.

Table 5.1 Concrete batch names with their respective origin, casting date and the number of cylinders used during this work

Batch Name	Origin	Casting Date	# Cylinders
000	(Fartosy, 2018)	Unknown	17
100	(Wiciak et al., 2019)	2018-01-31	5
200	(Fartosy, 2018)	2018-04-23	21
300	(Sleiman, 2017)	Unknown	13
400	Own Elaboration	2018-10-17	48
			104

The mix design proportion of the concrete batches are shown in Table 5.2. Unfortunately, there was no information available for the batches 100 and 300, belonging to the Rania and (Sleiman, 2017) research.

Each one of these batches served a specific role in this research. These will be described in the following list:

- *Batch 000*: Define the final setup for testing all cylinders. On this batch different microphone and accelerometer positions, supporting methods and hammers were tested to select the best setup.

- *Batch 100*: Compare the static testing difference. The cylinders of this batch were loaded with a high load rate and two methods of measuring the longitudinal displacement during loading were used: The press internal displacement gauge and a compressometer attached to the cylinders using the ring system shown in Figure 4.1
- *Batch 200*: Monitor the dynamic and static modulus of elasticity evolution with time. The specimens of this batch were kept in a moisture room until the day of the compressive test.
- *Batch 300*: Add samples of mature concrete for the E_d-E_s relationship. To validate the relationships proposed.
- *Batch 400*: Monitored the development of both elastic moduli with time. Validate observations made from Batch 200. This batch had better control, with the highest frequency sampling in time during the first 28 days after casting. The batch cylinder remained in the moist room until day 28. Used to formulate forecasting elastic moduli based on early dynamic measurements.

Table 5.2 Mix Design proportion for concrete batches

Constituent		WeightProportion				
		Batch				
		000	100	200	300	400
Gravel	19 mm		UNKNOWN		UNKNOWN	30.5%
	12.5 mm	37.8%		38%		
Sand		31.0%		31%		20.6%
GU Cement		21.5%		22%		9.3%
Slag or Flyash						1.7%
Euclid Air Extra						6.9%
Superplasticizer						26.3%
Water		9.7%		10%		4.7%
w/c %		45%	-	45%	-	42%
Air Content %		6.5%		6.5%		7.4%

5.1.2 Specimens

The specimens used during the development of this research are in its entirety concrete cylinders with a diameter and length of around 10.2 cm and 20.0 cm respectively. The cylinders were weighted and their diameter and length measured at different ages. The diameter was measured at both ends in two perpendicular directions, the average of the four diameters measured was the diameter taken for the

calculations. In a similar way, the length of the cylinders was measured in two different points along the circumference of the cylinder, the average of the two measurements was set as the length to be used. The diameter and length obtained this way are referred to in the following tables as '*Average Dimensions*'.

This section will show the respective diameter, length and weight for all the cylinder tested. The information is shown in Tables Table 5.3 - Table 5.9. In the following paragraph each one of them will be introduced:

Table 5.3 Dimensions, weight and respective densities for cylinders of batch 000

Specimen Number [SN]	Weight (grs)	Average Dimensions (cm)		Area (cm^2)	Density (kg/m^3)
		Diameter	Length		
001	3,810.4	10.24	20.20	82.4	2289.8
002	3,583.3	10.05	19.70	79.4	2291.0
003	3,834.4	10.22	19.70	82.1	2372.0
004	3,774.7	10.23	20.00	82.2	2296.2
005	3,733.8	10.18	20.00	81.4	2294.6
006	3,816.9	10.22	20.40	82.0	2282.5
007	3,654.7	10.23	19.40	82.2	2291.2
008	3,757.1	10.26	20.00	82.7	2270.8
009	3,664.4	10.21	19.70	81.8	2273.3
010	3,667.9	10.14	19.60	80.8	2316.1
011	3,767.3	10.25	20.10	82.5	2271.9
012	3,781.3	10.30	20.30	83.3	2236.4
013	3,895.3	10.26	20.20	82.6	2334.1
014	3,863.1	10.23	20.30	82.2	2313.8
015	3,691.1	10.22	19.80	82.1	2271.8
016	3,650.8	10.21	19.60	81.9	2275.4
017	3,830.0	10.25	20.20	82.5	2298.7
Average:	3,751.6	10.22	19.95	82.0	2,292.9
Std dev:	84.70	0.05	0.29	0.84	29.06
COV:	2.3%	0.5%	1.4%	1.0%	1.3%

Specimens in batch 000 were donated for this research from (Fartosy, 2018), the cylinders were obtained already cast and with over one year old. Since the moment they were acquired until its compressive test they were kept at room temperature and without any type of moist control. There was a total of 17 cylinders from this batch named from 001 to 017. These cylinders were weighed and measured at only one time. The specimens' dimension, weight and the computed area and density using the measurements are shown in Table 5.3.

Specimens from batch 100 were part of (Wiciak et al., 2019) research, but cast by Rania. A total amount of 5 cylinders were lent for this research to perform the resonant method test on them. They were kept in a moisture room from day 1 until day 51, just taking them out on the 28th day for the resonant method test. These cylinders were only measured at the age of 28 days old and weighed at 28 and 51 days old. The specimens' dimensions, respective area and the weight and respective density for both dates measured are shown in Table 5.4.

Table 5.4 Dimensions, weight and densities for cylinders of batch 100

Specimen Number [SN]	Weight (grs) at Age:		Average Dimensions (cm)		Area (cm^2)	Density (kg/m^3) at Age:	
	28 d	51 d	Diameter	Length		28 d	51 d
101	3,801.3	3,730.3	10.23	20.25	82.1	2,286.1	2,243.4
102	3,809.7	3,760.3	10.13	20.15	80.5	2,348.2	2,317.8
103	3,784.4	3,734.9	10.23	20.35	82.1	2,264.7	2,235.1
104	3,793.7	3,745.1	10.20	20.35	81.7	2,281.4	2,252.2
105	3,772.3	3,736.2	10.20	20.30	81.7	2,274.2	2,252.4
Average:	3,792.3	3,741.4	10.20	20.28	81.6	2,290.9	2,260.2
Std dev:	13.02	10.62	0.04	0.07	0.59	29.54	29.50
COV:	0.3%	0.3%	0.4%	0.4%	0.7%	1.3%	1.3%

Cylinders from batch 200 were cast from concrete meant for (Fartosy, 2018) research. Contrary to the cylinders from batches 000,100 and 300, where the cylinders were handed out or lend it out for this work. The author directly prepared the specimens from the fresh concrete according to (ASTM_C192, 2018). 21 cylinders were cast and remain inside the moist room until they were tested for its compressive strength and static elastic moduli, only taking them out briefly testing them accordingly to section 4.1.1.

The specimens from batch 200, were named with a number from 201 to 221. Their diameter and length were measured at day 1 after casting only, assuming the shape dimension would not vary significantly along its curing time. The average dimension and the respective area for each cylinder can be found in Table 5.5. Nevertheless, they were weighted every time any non-destructive test was about to be performed on them. The average density for all the cylinders in batch 200, at all the different ages on which the weight was measured, are shown in Table 5.6.

Table 5.5 Dimensions for cylinders of batch 200 at the age of 1 day.

Specimen Number [SN]	Average Dimensions at day 1		
	Diameter (cm)	Length (cm)	Area (cm^2)
201	10.20	19.83	81.7
202	10.26	19.98	82.7
203	10.24	20.15	82.3
204	10.19	20.25	81.5
205	10.20	20.30	81.7
206	10.18	20.20	81.3
207	10.20	20.30	81.7
208	10.19	20.15	81.5
209	10.16	20.10	81.1
210	10.21	20.10	81.9
211	10.21	20.25	81.9
212	10.20	20.20	81.7
213	10.18	20.20	81.3

Specimen Number	Average Dimensions at day 1		
	Diameter (cm)	Length (cm)	Area (cm^2)
214	10.19	20.20	81.5
215	10.21	20.30	81.9
216	10.20	20.15	81.7
217	10.19	20.25	81.5
218	10.21	20.25	81.9
219	10.18	20.30	81.3
220	10.24	20.40	82.3
221	10.25	20.20	82.5
Average:	10.20	20.19	81.77
Std dev:	0.03	0.12	0.41
COV:	0.2%	0.6%	0.5%

Table 5.6 Average densities for cylinders of batch 200 at all ages on which the measurements were taken

		Age (days)					
		1	2	3	4	7	10
Specimen Numbers		[201-221]	[201-221]	[202-221]	[204-221]	[206-221]	[208-221]
# Specimens		21	21	20	18	16	14
Density (kg/cm3):	Avg	2,242.5	2,250.4	2,246.0	2,252.8	2,259.7	2,261.4
	Std	18.8	21.3	31.4	25.3	19.4	21.4
	COV	0.8%	0.9%	1.4%	1.1%	0.9%	0.9%

The densities computed with the respective weight at each age for cylinders in batch 200 are plotted in Figure 5.1 as blue dots. The average density for all cylinders at each given date is also plotted in Figure 5.1 as a continuous black line, along with a ± 1 standard deviation as a dashed black line. The full weight measurements for batch 200 can be found in Appendix A in Table A1.1 and Table A1.2

Now, moving into specimens from batch 300. As mentioned before, they were donated from (Sleiman, 2017) research. A total of 13 cylinders belong to this batch. They were already cast and over a year old when they were received for this work. Their dimensions and weight were only measured one time which are shown in Table 5.7 with the respective area and density per cylinder.

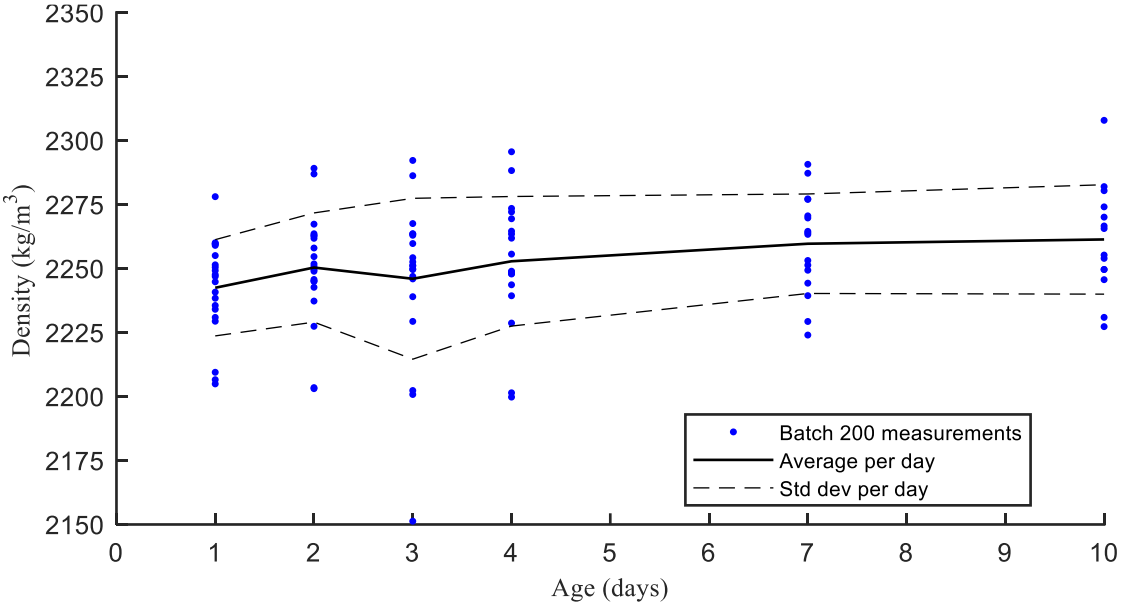

Figure 5.1 Individual densities and respective average and standard deviation per day for all cylinder measurements taken for batch 200.

Table 5.7 Dimensions, weight and respective densities for cylinders of batch 300

Specimen Number [SN]	Weight (grs)	Average Dimensions (cm) Diameter	Length	Area (cm^2)	Density (kg/m^3)
301	3,715.4	10.18	19.40	81.4	2,352.9
302	3,817.9	10.23	19.70	82.2	2,358.4
303	3,829.3	10.22	19.80	82.0	2,359.4
304	3,771.3	10.18	19.80	81.3	2,342.3
305	3,853.4	10.25	20.00	82.6	2,333.4
306	3,726.7	10.17	19.50	81.3	2,352.0
307	3,810.5	10.21	19.80	81.9	2,350.0
308	3,780.3	10.25	19.60	82.5	2,338.8
309	3,762.5	10.22	19.40	82.0	2,365.2
310	3,768.1	10.20	19.70	81.8	2,338.7
311	3,822.9	10.23	19.80	82.1	2,351.1
312	3,855.4	10.20	19.80	81.7	2,382.6
313	3,825.7	10.21	19.70	81.8	2,372.9
Average:	3,795.3	10.2	19.69	81.89	2,353.7
Std dev:	43.21	0.02	0.17	0.39	13.60
COV:	1.1%	0.2%	0.9%	0.5%	0.6%

Finally, for batch 400, the concrete mix was personally made for the author for this research. A total of 48 cylinders were cast following the guidelines of (ASTM_C192, 2018) and kept stored in a moist room until the 28th day after casting when all the specimens were removed from any moisture control for good. During that time, the specimens were taken out from the moist room briefly to

performed test on them and right afterward they were returned to the moist room. Dimensions for all the cylinders in batch 400 were measured on day 1 (Table 5.8). Additional dimension measurements for the remaining cylinders (443-448) were also recorded at the age of 128 and 156 days (Table A1.3).

Table 5.8 Dimensions for cylinders of batch 400 at an age of 1 day

Specimen Number [SN]	Average Dimensions at day 1			Specimen Number	Average Dimensions at day 1		
	Diameter (cm)	Length (cm)	Area (cm^2)		Diameter (cm)	Length (cm)	Area (cm^2)
401	10.18	19.88	81.3	427	10.23	20.14	82.2
402	10.18	19.85	81.4	428	10.21	20.21	81.9
403	10.19	19.85	81.6	429	10.16	20.23	81.1
404	10.20	19.76	81.7	430	10.20	20.41	81.7
405	10.18	20.04	81.3	431	10.20	20.13	81.7
406	10.17	19.89	81.2	432	10.21	20.33	81.8
407	10.18	19.84	81.4	433	10.17	19.90	81.3
408	10.28	20.39	83.1	434	10.21	19.98	81.9
409	10.17	19.92	81.2	435	10.16	20.17	81.1
410	10.17	20.07	81.2	436	10.20	20.46	81.8
411	10.20	20.08	81.8	437	10.21	19.95	81.8
412	10.19	20.13	81.5	438	10.22	20.15	82.1
413	10.21	20.06	81.9	439	10.21	20.23	81.8
414	10.15	19.91	80.9	440	10.22	19.99	82.1
415	10.17	19.86	81.2	441	10.20	20.46	81.7
416	10.20	19.88	81.8	442	10.16	20.17	81.0
417	10.19	19.86	81.6	443	10.19	19.93	81.5
418	10.20	19.91	81.7	444	10.16	20.13	81.1
419	10.19	19.95	81.6	445	10.24	20.15	82.3
420	10.24	20.03	82.3	446	10.15	19.99	81.0
421	10.20	20.18	81.7	447	10.22	19.86	82.1
422	10.21	20.09	81.9	448	10.20	20.13	81.8
423	10.24	20.10	82.3		**Diameter**	**Length**	**Area**
424	10.23	20.00	82.2	**Average:**	10.20	20.05	81.67
425	10.23	20.23	82.2	**Std dev:**	0.03	0.18	0.43
426	10.22	19.63	82.0	**COV:**	0.3%	0.9%	0.5%

Every time the cylinders were going to be tested by a non-destructive method the cylinders were also weighted. The full information about the weight and density at different measurement ages for cylinders in batch 400 can be found in Appendix A in Tables Table A1.4 to Table A1.13. Although the average, standard deviation and coefficient of variation for the intact cylinders in batch 400 at every measured age are also shown in Table 5.9.

Table 5.9 Average densities for cylinders of batch 400 at all ages on which measurements were taken

Age (days)	Specimen Numbers	# Cyl	Density (kg/cm^3) Avg	Std	COV	Age (days)	Specimen Numbers	# Cyl	Density (kg/cm^3) Avg	Std	COV
1	[401-448]	48	2,268.0	24.1	1.1%	17	[431-448]	18	2,272.2	27.3	1.2%
2	[405-448]	44	2,271.0	24.5	1.1%	18	[431-448]	18	2,272.2	26.9	1.2%
3	[409-448]	40	2,274.1	25.4	1.1%	19	[431-448]	18	2,270.7	27.7	1.2%
4	[409-448]	40	2,274.9	25.6	1.1%	20	[434-448]	15	2,268.0	25.5	1.1%
5	[409-448]	40	2,275.0	25.1	1.1%	21	[434-448]	15	2,267.6	25.6	1.1%
6	[413-448]	36	2,274.7	25.4	1.1%	22	[437-448]	12	2,265.4	27.7	1.2%
7	[416-448]	33	2,273.8	25.7	1.1%	23	[437-448]	12	2,265.0	28.1	1.2%
8	[419-448]	30	2,274.7	26.0	1.1%	24	[440-448]	9	2,268.7	31.3	1.4%
9	[419-448]	30	2,274.6	25.9	1.1%	26	[440-448]	9	2,268.6	31.2	1.4%
10	[422-448]	27	2,274.5	26.8	1.2%	28	[440-448]	9	2,265.8	31.4	1.4%
11	[422-448]	27	2,276.0	26.8	1.2%	43	[443-448]	6	2,239.3	31.2	1.4%
12	[422-448]	27	2,274.1	26.9	1.2%	47	[443-448]	6	2,237.0	31.3	1.4%
13	[425-448]	24	2,278.2	27.1	1.2%	57	[443-448]	6	2,231.6	31.3	1.4%
14	[425-448]	24	2,276.3	27.6	1.2%	65	[443-448]	6	2,228.8	31.0	1.4%
15	[428-448]	21	2,277.1	28.7	1.3%	128	[443-448]	6	2,239.5	23.5	1.0%
16	[428-448]	21	2,276.0	28.9	1.3%	156	[443-448]	6	2,240.6	27.4	1.2%

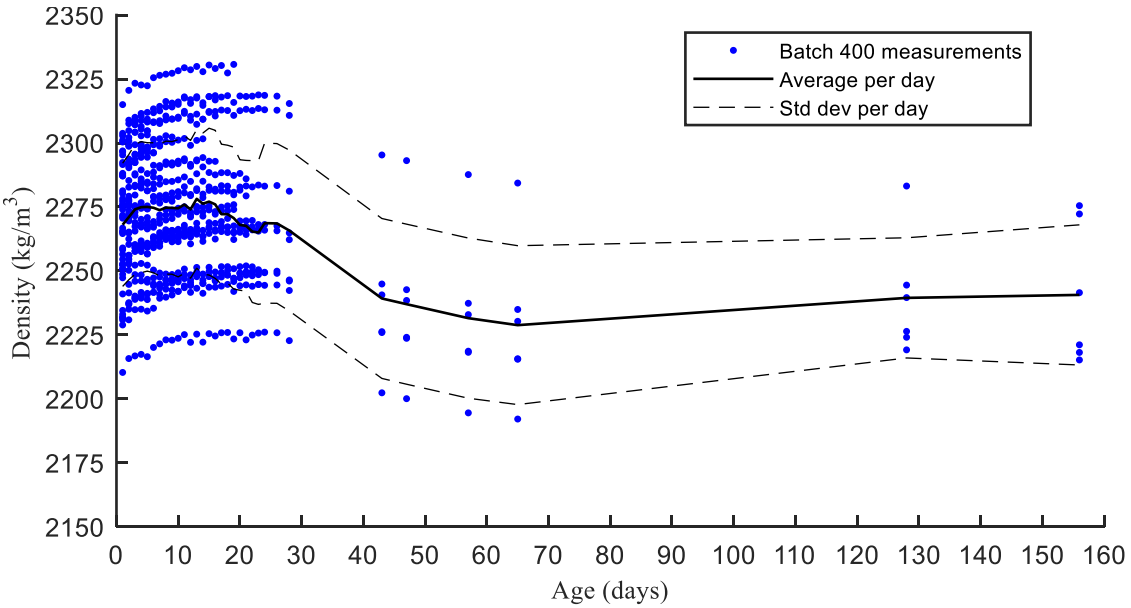

Figure 5.2 Individual densities and respective average and standard deviation per day for all cylinder measurements taken for batch 400.

All density records for specimens in batch 400 are shown in blue dots in Figure 5.2. In the same figure, the average densities and one ± standard deviation (from Table 5.9) are also plotted as a continuous and dashed black line respectively. Decay in the density can be observed beyond the 28th

days after casting, which is the age at which the cylinders were taken out from the moist room for good.

5.1.3 Testing Planning

This section will describe the order in which the tests were carried out and the ages at which each set of cylinders were tested. The latter can be inferred from the previous section but it will be explained explicitly on this one.

The stages of testing were as follows in chronological order:

a) Microphone testing to investigate their capabilities.

b) Position of the microphone relative to the cylinder for the best detection of resonant frequencies.

c) Hammer testing to determine the one that excites best the resonant frequencies of cylinders.

d) Testing of all cylinders fully matured (batches 000,100, 300) using the best setup found based on the previous test stages.

e) Testing with the final test setup the cylinders in batch 200 at early ages (≤ 10 days) and again once fully matured (at the age of 140 days). In Table 5.10 the schedule for different tests used on this batch of cylinders is shown: Resonant test recording the response using accelerometers and microphones, and the compressive test that ultimately destroys the cylinders.

Table 5.10 Schedule of testing cylinders of batch 200. Number of cylinders tested at each age using three tests: Resonant test using accelerometers and microphones, and the compressive test

Age (days)	Num of Cyl Tested		
	Resonant Test		Comp. Test
	Acc	Mic	
1	21	21	
2	21	21	1
3	20	20	2
4	18	18	2
7	16	16	2
10	14	14	2
140	12	12	12

f) Testing the cylinders of batch 400. For these cylinders the frequency of testing was higher, testing almost every day for the first 28 days after casting. And also performing more additional tests

than in batch 200: Ultrasonic Pulse Velocity (UPV) and also a multichannel analysis of surface waves (MASW). The schedule of testing with the number of cylinders tested on the different testing methodologies at different ages is shown in Table 5.11.

Table 5.11 Schedule of testing cylinders of batch 400. Number of cylinders tested at each age using five tests: Resonant test using accelerometers and microphones, UPV, MASW and the compressive test

Age (days)	Num of Cyl Tested					Age (days)	Num of Cyl Tested				
	Resonant Test		Other NDT		Comp. Test		Resonant Test		Other NDT		Comp. Test
	Acc	Mic	UPV	MASW			Acc	Mic	UPV	MASW	
1	48	48			4	**17**	18	18			
2	44	44			4	**18**	18	18			
3	40	40				**19**	18	18			3
4	40	40				**20**	15	15			
5	40	40			4	**21**	15	15	1		3
6	35	36			3	**22**	12	12			
7	33	33			3	**23**	12	12	3	3	3
8	30	30				**24**	9	9			
9	30	30			3	**26**	9	9			
10	27	27				**28**	9	9	3	3	3
11	27	27				**43**	6	6			
12	27	27			3	**47**	6	6			
13	24	24				**57**	6	6			
14	24	24			3	**65**	6	6			
15	21	21				**128**	6	6	6		
16	21	21			3	**156**	6	6	6	6	6

5.2 Dynamic Tests

This section will describe the different methodologies for the three main testing methods used for this work: 1) Resonant method; 2) MASW; and 3) UPV. Each one of those will be divided into two main subcategories: the testing setup and the analysis methodology followed. However, the resonant method will be further divided to describe the methodologies used for the microphone and hammer selection and the algorithm for the resonant frequency detection.

5.2.1 Resonant Method

The resonant method to obtain the dynamic elastic modulus in the standard version was already described in Chapter 4, section 4.3.2. Nevertheless, the methodology used for this research will not be exactly as the standard. Therefore, the methodology followed will be fully described.

The reasoning for not following the (ASTM_C215, 2014) test setup and methodology is to find other test setups that overcome its disadvantages and find an easier to use with less expensive equipment to perform the resonant test in concrete cylinders. The main disadvantages of the ASTM C215 test setup (Figure 4.3) are:

- Supporting the cylinder is not as easy as just placing it vertically. Either the flexural or longitudinal support setup is a bit inconvenient. For the flexural frequency, marking the cylinder at the nodal vibration points is needed. And for the longitudinal frequency, balancing the specimen at the center is required. The supports need to be very thin and shaped with the cylinder diameter, a typical workaround this is to hang the cylinder with wires (Boone, 2005).
- The location for placing the accelerometer requires glueing it to the cylinder. This is particularly true for the longitudinal frequency setup, where the accelerometer is placed on one side of the cylinder. Glueing the accelerometer to the cylinder requires extra preparation for attaching it and detaching it.
- Specialized, expensive, and not very portable equipment used. The equipment needed for the test (accelerometer, preamplifier, oscilloscope) although cheaper and easy to move compared with the static test, it still is relatively expensive and not as portable as a mobile phone. The equipment required would need to be transported in a car and have access to a power source (Boone, 2005).

However, the methodology to be used for this research and described in detail in section 5.2.1.4 overcome these practical disadvantages by using a mobile phone microphone and placing the cylinder vertically on a foam block.

To validate the methodology to be proposed in 5.2.1.4, different tests were performed: First, to validate the frequency range capabilities for different microphone options (5.2.1.1.1). Second to determine the best location for the microphone around the cylinder. Third to choose the hammer that better excites the cylinder in the frequency range of interest (5.2.1.2). Later on the algorithm for the right frequency detection from the frequency spectrum will be described (5.2.1.3). And finally, the final setup proposed using both sensors accelerometer and the mobile phone microphone (5.2.1.4).

5.2.1.1 Microphone selection

Methodology for the different tests used to select both the best audio recording device and the position at which they would need to be placed for better results.

5.2.1.1.1 Device

This section will describe the methodology followed for selecting the best audio recording device (microphone) to detect frequencies in the range of interest (4-11 kHz for the concrete cylinders to be tested in this study).

The test setup used to test the recording devices used laptop speakers to produce a tone of a certain frequency and placing the microphone device at 30 cm from the speaker. To generate the tone an online tone generator tool was used (Szynalski, 2018). The previously described setup is represented in Figure 5.3. 20 Pitches were produced at different frequencies starting from 1 kHz and every 1 kHz up to 20 kHz, and each pitch was recorded with the microphone device. A recording without any pitch only recording the ambient noise was also registered to have a baseline.

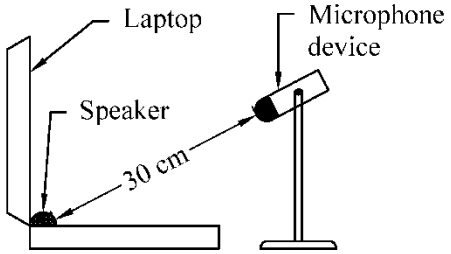

Figure 5.3 Schematic diagram for test setup for testing the frequency response of different microphone devices.

All recordings were made using the same sampling frequency (48 kHz) and the time used for the analysis was constant to compare between them. The signals were processed with the FFT and verifying the signal contained the frequency matching the pitch tone.

Two different laptop speakers were used for the tests, to compare between sources and in case of a microphone not detecting a particular frequency, investigate if it is due to the microphone or due to the speaker.

Three different recording devices were used, a smartphone and two laptops. But among these devices also different microphones were used. Sometimes the microphone built-in into the device was used and others the microphone from a headphone set was used instead. In the case of the

smartphone, it has 2 built-in microphones, one in the back and one in the front. The rear built-in microphone was always used.

Similarly, in each recording device, different recording software was used to compare and make sure they were not pre-processing the signal to optimize it for conversations that are usually held within 500 Hz to 4 kHz and they might apply a bandpass filter to the recorded signal.

The different combinations in the test setup for laptop speakers, recording devices, the microphones and recording apps used to test the microphone capabilities are listed in Table 2.1. Likewise, the details for the laptops, the smartphone, microphones and apps used are listed in Table 5.13.

Table 5.12 Different test setup combinations for pitch source, recording device, microphones and recording apps used to determine the best option to use for the resonant testing

#	Laptop Pitch Source	Recording Device	Microphone Used	Recording App
1	Laptop 1	Smartphone	Built-in Mic	RecForge II
2	Laptop 1	Smartphone	Headphones Mic	RecForge II
3	Laptop 1	Laptop 2	Built-in mic	Matlab
4	Laptop 1	Laptop 2	Headphones Mic	Matlab
5	Laptop 1	Laptop 2	Built-in Mic	Audacity
6	Laptop 1	Laptop 2	Headphones Mic	Audacity
7	Laptop 1	Laptop 2	Headphones Mic	Adobe Audition
8	Laptop 2	Smartphone	Built-in Mic	RecForge II
9	Laptop 2	Smartphone	Headphones Mic	RecForge II
10	Laptop 2	Laptop 1	Headphones Mic	Matlab

Table 5.13 Details for devices and software listed in Table 5.12

Device/Software	Details
Laptop 1	Lenovo® Thinkpad X1 Carbon (1st Gen)
Laptop 2	Dell Inspiron® 15-5577
Smartphone	Moto G4 Plus® (Model XT1641)
Headphones 1	Sony® MDR-EX110AP In-ear Headphones
RecForge II	Android® RecForge® II Version 1.2.7.5g
Matlab	Matlab® R2018b (9.5.0.944444) 64-bit
Audacity	Audacity 2.2.1
Adobe Audition	Adobe® Audition® CS6 Version 5 Compilation 708

5.2.1.1.2 Position

Having validated the microphone capabilities for detecting frequencies of interest the next thing to decide is where the microphone needs to be placed around the concrete cylinder to better capture the resonant frequencies. (Ito & Uomoto, 1997) already proved microphones were capable of picking up the resonant frequencies of square concrete beams and they found the location of the microphone around the beam is important to better capture their flexural frequencies. The best results for their study were obtained when placing the microphone near the specimen (around 1 cm) and at a location where the maximum displacements due to the flexural mode were expected.

This chapter will describe the test methodology to find one single location for the microphone and impact point on the cylinder, for which both, longitudinal and flexural, resonant frequencies are best detected.

Figure 5.4-Left shows the different impact locations used to excite the cylinder, and in Figure 5.4-Right the different microphone positions are shown. The combinations for impact locations and microphone positions used for testing are listed in Table 5.14 with a total number of 10 different combinations. Each impact location and microphone positions are also briefly described on this table. As it is shown in Figure 5.4 the cylinder was held vertically, placed over a foam block of 19x29 cm and 8.5 cm depth, to isolate the cylinder from other vibration sources and reduced the wave transmission into the support base.

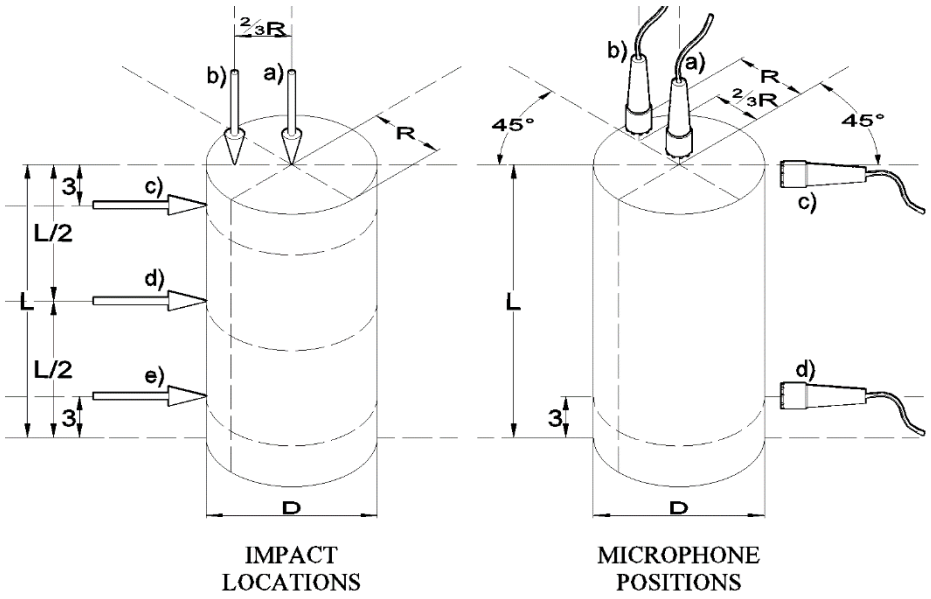

Figure 5.4 Diagram for different impact locations (Left), and different microphone positions (Right)

Table 5.14 Different test setup combinations for impact and microphone locations based on the reference letter from Figure 5.3

#	Impact Location		Microphone Location	
Comb	Ref	Description	Ref	Description
1	a)	Top surface - At center	b)	Top surface - Near the edge
2	b)	Top surface - Near edge	a)	Top surface - At the center
3	b)	Top surface - Near edge	c)	Side near the top at the opposite side of the impact
4	b)	Top surface - Near edge	d)	Side near the bottom at the opposite side of the impact
5	c)	Side near the top surface	a)	Top surface - At the center
6	c)	Side near the top surface	c)	Side near the top at the opposite side of the impact
7	d)	Side at mid-length	a)	Top surface - At the center
8	d)	Side at mid-length	c)	Side near the top at the opposite side of the impact
9	e)	Side near the bottom surface	a)	Top surface - At the center
10	e)	Side near the bottom surface	c)	Side near the top at the opposite side of the impact

An accelerometer was also used to measure the cylinder response and compare the frequency content from the microphone to the one obtained from the accelerometer. The setup for the accelerometer match the combination # 3 from Table 5.14, on which the impact was done at the top surface near the edge (Figure 5.4-Left b)) and the accelerometer was placed on the same top surface near the edge but at the opposite side of the impact location (Figure 5.4-Right b)).

The accelerometer used was a Dytran accelerometer model 3055B3 as shown in Figure 5.5. Its resonant frequency (>35 kHz) is way above the frequency range to be measured and it has a linear response on the frequency range of 1 to 10,000 Hz. The accelerometer sensitivity is 500 mV/g (Dytran, 2004). The accelerometer was coupled to the concrete surface using Dow Corning® High Vacuum Grease.

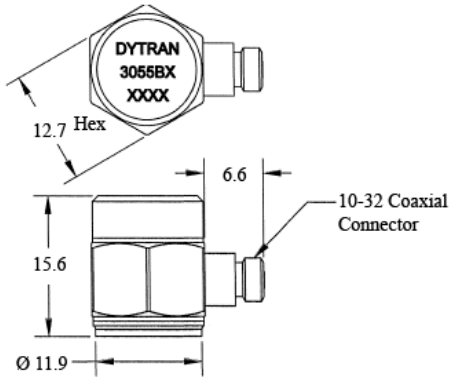

Figure 5.5 Drawings for accelerometer used for concrete cylinder resonant testing. [mm] (Dytran, 2004).

To excite the cylinder an impulse hammer from Dytran Instruments as shown in Figure 5.6 was used every time. The impulse hammer has a force sensor that allows recording the impulse force applied to the cylinder at the moment of impact with three different sensitivity ranges. For these tests, the sensitivity switch was set at 10 mV/LbF. For this test, one of the supplied impact tips was partially drilled and a steel bearing of ¼" diameter was glued to the created cavity.

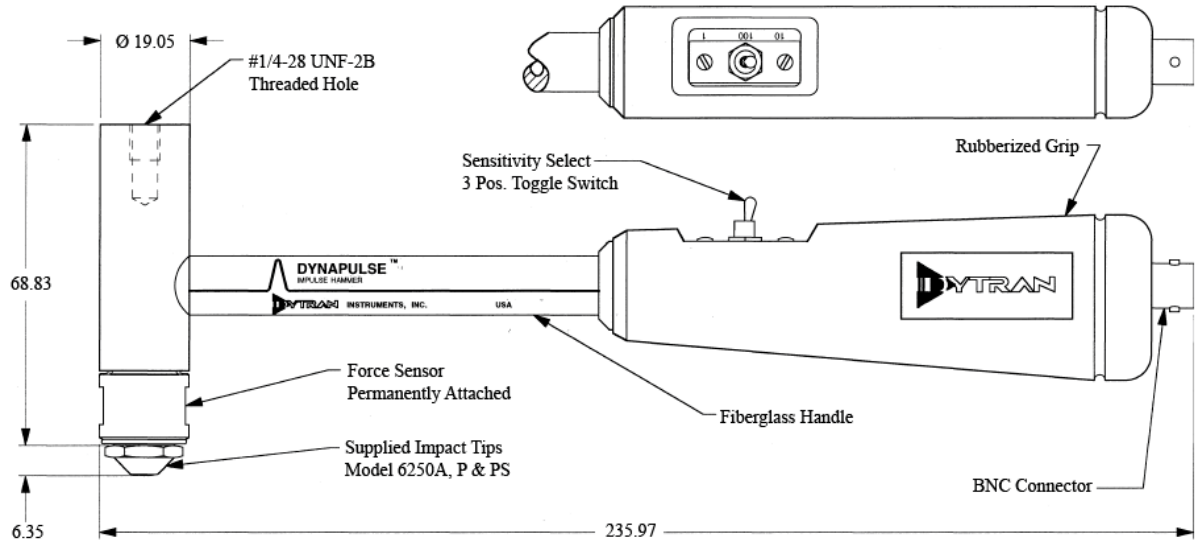

Figure 5.6 Drawing for the Dytran Impulse Hammer 5850B used to excite cylinder during tests to locate the best position for the microphone. [mm] (Dytran, 1995).

The microphone used was a professional microphone borrowed from Professor John Vanderkoy. The microphone had a BNC connector which allows recording the sound pressure directly by an oscilloscope. All three measuring devices, impulse hammer, accelerometer and microphone required to be powered by an ICP® power supply model 483A. The microphone was placed as close as possible (~1 cm) to the cylinder surface and held by a metallic stand to keep the distance constant during the tests.

The test setup for the equipment is described with a block diagram in Figure 5.7. The impulse hammer, accelerometer and microphone are connected to the ICP® Power Supply which not only supplies power to the devices but also receives and retransmits the signal readings from each one of them to an Oscilloscope. The oscilloscope then uses the hammer signal as a trigger to start recording the signals from the sensors. The data recorded then is collected and processed to obtain their frequency transform and observe the resonant frequencies of the cylinders.

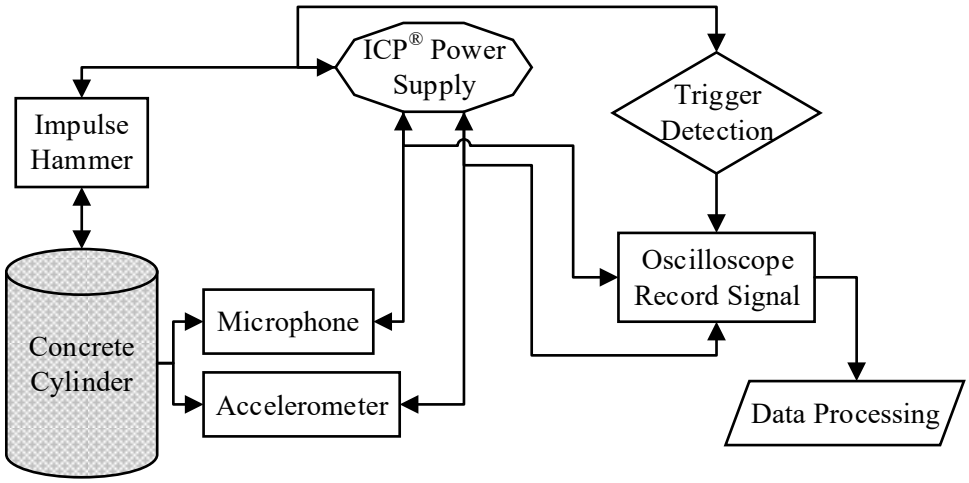

Figure 5.7 Block diagram of the test setup used to determine the best microphone location for resonant testing of concrete cylinders

5.2.1.2 Hammer and support selection

This section will introduce the methodology to determine the best combination for the support and impulse hammer for exciting the resonant frequencies of concrete cylinders for this research (around 20 cm length by 10 cm diameter). Some basic theoretical principles that haven't been introduced before will also be presented.

In the previous section, an instrumented impulse hammer from Dytran was used for the testing aimed to determined the best location for the microphone. Nevertheless, this option might not be the best way to excite the cylinder for the frequency range of interest. The test methodology described in this section will asses the frequency response on the cylinder due to different impulse hammers.

Besides, the Dytran instrumented impulse hammer still is a lab piece of equipment, that requires more equipment to work (ICP® Power Supply and an Oscilloscope), which is outside of the main goal of the research of finding something affordable and portable to allow the elastic modulus estimation easily performed on-site.

5.2.1.2.1 Introduction

The easiest way to excite the cylinder on the frequency range of their resonant frequencies is by using an impact impulse. The force-time function of an impact depends on the time of contact (*'t_c'*) of the impact and can be approximated by a half-sine cycle from the equation (5.1) (Carino & Sansalone, 1986). The duration of the impact *'t_c'* determines the frequency content of the impact. In

Figure 5.8-a the force-time function is plotted along with their normalized frequency response in Figure 5.8-b. As can be seen in Figure 5.8-b most of the impact energy (around 98%) is contained below a frequency equal to 1.5 times the inverse of the time of contact (*'t_c'*) (Y. Lin, Sansalone et al., 1991). For this reason, the maximum frequency that can be excited with an impact of a duration of *'t_c'* will be considered to be equal to (5.2) and will be named as f_{max}.

$$F(t) = A\sin\left(\frac{\pi}{t_c}t\right) \quad \text{for: } 0 \le t \le t_c \tag{5.1}$$

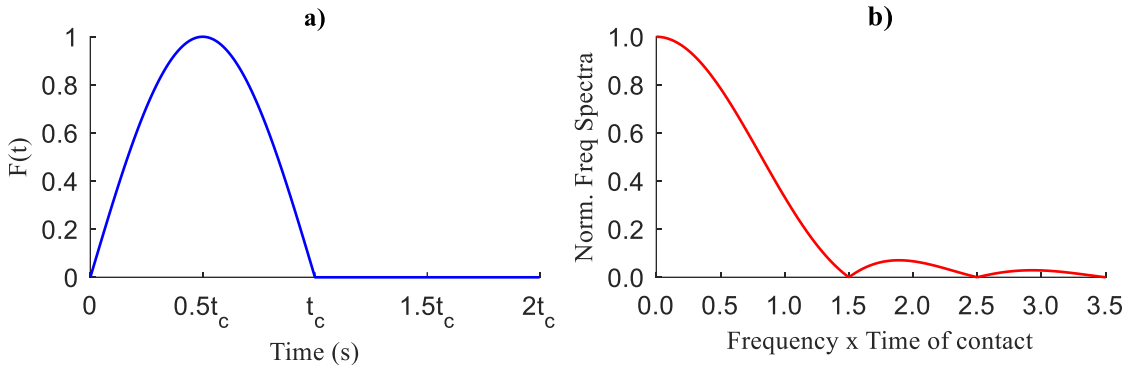

Figure 5.8 a) Approximation of force-impact function as a half sine. b) Normalized frequency content for the force impact function approximation of a half sine.

$$f_{\max} = \frac{1.5}{t_c} \tag{5.2}$$

According to the Hertz Theory, the time of contact of an elastic impact of a steel sphere of diameter d_s can be estimated by the expression (5.3) where d_s is in meters and t_c in seconds (Ohtsu, 2016).

$$t_c = 0.0043 \cdot d_s \tag{5.3}$$

The usage of steel sphere impacts as an impulse method for resonant tests is not new and has been implemented before for other researches, e.g. both, (Ohtsu, 2016). and (Ito & Uomoto, 1997) used a 20 mm diameter steel sphere dropped from 10 cm and 5 cm height respectively.

A list of the times of contact and the respective maximum usable excitation frequency for different steel sphere diameters is given in Table 5.15 for quick reference. In Table 5.15 some steel sphere diameters are highlighted in gray, which correspond to the diameters used for the testing methodology presented later in this section.

Table 5.15 Maximum frequency content for steel sphere impacts of different diameters (d_s)

Sphere Diameter (d_s)		Time of contact [µs]	Max Frequency f_{max} [kHz]
[in]	[mm]		
1/8	3.2	13.7	109.9
1/4	6.4	27.3	54.9
1/3	7.9	34.1	43.9
3/8	9.5	41.0	36.6
4/9	11.1	47.8	31.4
1/2	12.7	54.6	27.5
3/4	19.1	81.9	18.3
1	25.4	109.2	13.7
1 1/4	31.8	136.5	11.0
1 3/8	34.9	150.2	10.0
1 1/2	38.1	163.8	9.2

5.2.1.2.2 Test methodology

The methodology followed to determine the best support and impulse hammer used different combinations between two supports and thirteen impulse hammers.

The two supports used were as follows: 1) A foam block with 19x29 cm and 8.5 cm depth dimensions just as in the methodology presented in the previous section. The concrete cylinder was placed at the center of the foam block as shown in Figure 5.9-a. 2) The second type of support was just placing the cylinder vertically over a table (Figure 5.9-b).

In the future, when referring to the support system used will be abbreviated by SP followed by a number, SP01 for the foam support and SP02 for the cylinder supported in a wood table.

The test setup for all the tests related to defining the best support and impulse hammer combination was as shown in Figure 5.9. The impact point on the cylinder by the impulse hammer was located at the top surface near the border, at approximately 1/3 of the cylinder radius (~1.5 cm) from the edge, It is equivalent to the microphone position *"b"* from Figure 5.4. The impact point is marked as a red arrow and a dot in Figure 5.9.

The frequency vibration was measured with the same accelerometer from the previous section (Figure 5.5) and with the definitive microphone selected from the previous methodology, which is the smartphone built-in mic. The position on which both sensors were located at the moment of the test was on the top surface at the opposite border from the impact point, at an approximate distance from

the border of 1/3 of the cylinder radius (~1.5 cm). The accelerometer was coupled to the concrete cylinder using Dow Corning® High Vacuum Grease (Figure 5.9-a).

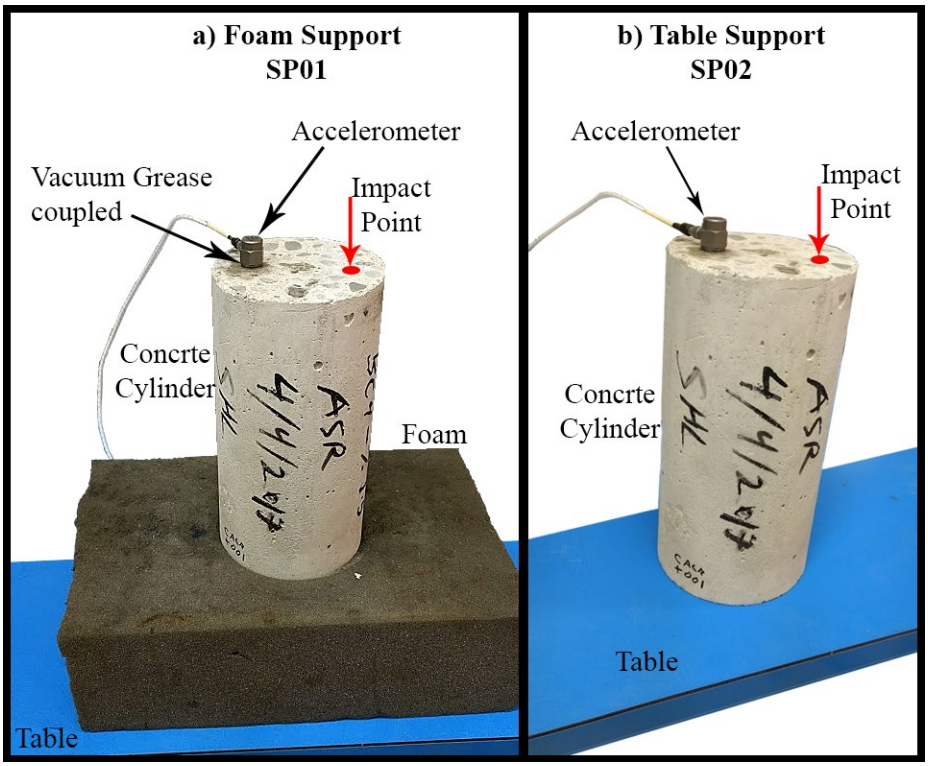

Figure 5.9 Different support types tested to determine the best alternative for resonant testing method

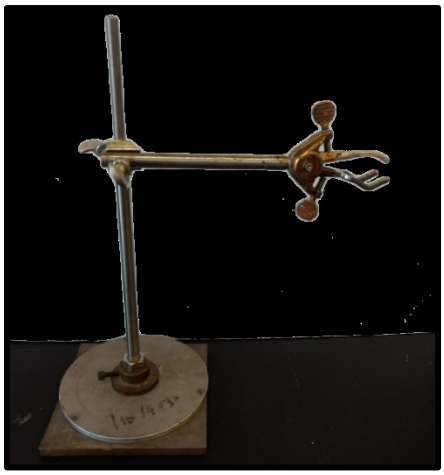

Figure 5.10 Retort stand used to hold the smartphone at a constant close distance from the specimen during the resonant tests

The smartphone was held by retort stand with a clamp (Figure 5.10). The smartphone as placed on a way for which the rear built-in microphone was less than 3 cm away from the same position described for the accelerometer. The reason for using the retort stand was to keep the tests as constant as possible from each other.

The different impulse hammers used are listed in Table 5.16 with a total number of 13 different hammer setups. A picture for each of these hammers is shown in Figure 5.11. The hammers are numbered from H01 to H13 and they are going to be referred this way for the rest of the current work.

Table 5.16 Different hammer types tested for the resonant method test with their respective reference number

Hammer Reference Numbers	
[H]	**Description**
1	Dytran Hammer with supplied impact tip
2	Dytran Hammer with flat-tip screwdriver magnetically attached
3	Dytran Hammer with flat-tip screwdriver glued
4	Dytran Hammer with steel bearing (Ø 1/4") glued to supplied impact tip
5	Dytran Hammer with steel bearing (Ø 1/2") glued to supplied impact tip
6	Dytran Hammer with supplied impact tip drilled and steel bearing (Ø 1/4") glued to it
7	Dytran Hammer with supplied impact tip drilled and steel bearing (Ø 7/16") glued to it
8	Dytran Hammer with supplied impact tip drilled and steel bearing (Ø 1/2") glued to it
9	Dytran Hammer with supplied impact tip drilled and steel bearing (Ø 3/4") glued to it
10	Steel bearing (Ø 7/16") attached to a set of neodymium magnets
11	Steel bearing (Ø 3/4") attached to a set of neodymium magnets
12	Dropping a steel bearing (Ø 7/16") from a ~5cm height
13	Dropping a steel bearing (Ø 3/4") from a ~5cm height

All hammer setups from H01 to H09 are the same Dytran Impulse Hammer from Figure 5.6 but with different tips. H01 uses one of the supplied aluminum tips from Dytran. Setups H02 and H03 used a flat-tip screwdriver as the hammer tip, the first is attached magnetically to magnet screwed into the hammer, while the second one (H03) is glued to one of the supplied tips. Hammers H04 and H05 use steel bearings of ¼” and ½” diameter respectively glued to one of the supplied tips. To increase the glued surface and improved the contact between steel bearing and the supplied hammer tips, the tips were drilled slightly at the tip to create a convex surface and then glue to it different steel bearing diameters. Hammer setups from H06 to H09 use tips with the drilling and glue approach with steel bearing diameters of ¼”, 7/16”, ½” and ¾” respectively.

For hammers H10 and H11, a series of 6 round neodymium magnets with a diameter of ½” (12.7 mm) and ¼” (6.35 mm) depth were piled together to form a handle of 38.1 mm long. At the top of the

handle, an SAE hex nut #10 was glued to it. The hole in the hex nut allows placing a steel bearing on it and keep it immobile at one spot while still being magnetically attached to the handle. H10 uses a 7/16” diameter steel bearing, while H11 uses ¾” diameter.

Finally, for hammer H12 and H13, the magnetic handle was disregard and the cylinder excitation was done by dropping the steel bearings with 7/16” and ¾” diameter from around 5 cm height into the top cylinder surface. The impact point was aimed to be the same point as the one impacted with the other types of hammers, nevertheless only the first impact was hitting near the same spot, after the first bouncing, any slight inclination in the cylinder made the bearing bouncing quite inconsistent. Although H12 and H13 are not technically hammers, to keep the nomenclature consistent they were still named as hammers.

Figure 5.11 Pictures of the different types of hammers with their respective reference number according to Table 5.16

The different tests combining the two supports and the hammers were breakdown into 3 stages which are listed in Table 5.17-Table 5.19. The first stage was done with the hammer setups H01 to H05 and using only the accelerometer to record the cylinder vibrational response.

Table 5.17 Support and hammer test combination for the 1st Stage of testing. The readings were done with the accelerometer only.

# Comb	Support		Hammer	
	Ref	Desc.	Ref	Brief description
1-1	1	Foam	1	Dytran Hammer
1-2	1	Foam	2	Hammer - flat-tip screwdriver magnetic
1-3	1	Foam	3	Hammer - flat-tip screwdriver glued
1-4	1	Foam	4	Hammer glued - Ø 1/4" bearing
1-5	1	Foam	5	Hammer glued - Ø 1/2" bearing
1-6	2	Table	1	Dytran Hammer
1-7	2	Table	2	Hammer - flat-tip screwdriver magnetic

The second stage start involving the microphone and due to the results observed from the first stage new hammer setups were implemented. It is in this stage where hammers H06 to H11 were tested in combination with the two different supports. The list of combinations tested is in Table 5.18.

Table 5.18 Support and hammer test combination for the 2nd Stage of testing. The readings were done with both accelerometer and microphone.

# Comb	Support		Hammer	
	Ref	Desc.	Ref	Brief description
2-1	1	Foam	6	Hammer drilled + glued - Ø 1/4" bearing
2-2	1	Foam	7	Hammer drilled + glued - Ø 7/16" bearing
2-3	1	Foam	8	Hammer drilled + glued - Ø 1/2" bearing
2-4	1	Foam	9	Hammer drilled + glued - Ø 3/4" bearing
2-5	1	Foam	10	Magnet handle - Ø 7/16" bearing
2-6	1	Foam	11	Magnet handle - Ø 3/4" bearing
2-7	2	Table	7	Hammer drilled + glued - Ø 7/16" bearing
2-8	2	Table	8	Hammer drilled + glued - Ø 1/2" bearing
2-9	2	Table	9	Hammer drilled + glued - Ø 3/4" bearing
2-10	2	Table	10	Magnet handle - Ø 7/16" bearing
2-11	2	Table	11	Magnet handle - Ø 3/4" bearing

Finally, the third and last stage used hammers H12 and H13, for which the steel bearing was drop over the cylinder top surface. Due to the difficulty of avoiding the steel bearing to hit the accelerometer and that the oscilloscope trigger was activated several times for each of the impacts bearing impacts at each bounce, only the smartphone microphone was used for this stage of testing. The combinations of support and hammer for stage three are listed in Table 5.19.

Table 5.19 Support and hammer test combination for the 3rd Stage of testing. The readings were done with the microphone only.

# Comb	Support		Hammer	
	Ref	Desc.	Ref	Brief description
3-1	1	Foam	12	Dropping Ø 7/16" bearing
3-2	1	Foam	13	Dropping Ø 3/4" bearing
3-3	2	Table	12	Dropping Ø 7/16" bearing
3-4	2	Table	13	Dropping Ø 3/4" bearing

The connection setup for the equipment used is described with a connection diagram in Figure 5.12. When the accelerometer was used, it was connected to the ICP Power Supply, which provides power to the accelerometer and receives the response and transmits it to the oscilloscope. The oscilloscope will start recording the signal using the increase in the accelerometer signal as the trigger.

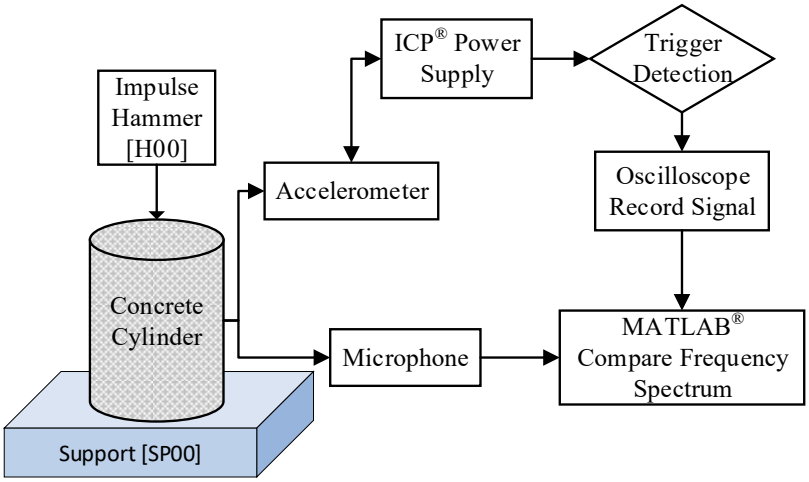

Figure 5.12 Test setup diagram for testing different support and impulse hammer combinations

For the microphone readings, a sound recording was done using the same software as in the previous section (SourceForge II). The audio recording had a sampling rate of 48 kHz. The recording was started a few seconds before the first impact with the hammer and continue recording for a variable length of time from 10 seconds to up 120 seconds, during this time, several impacts with the hammer were made, and therefore each of the cylinders acoustic response were recorded into one single audio file. Later on, both the acceleration data and the audio file were processed using MATLAB® using the algorithms presented in 5.2.1.5.

5.2.1.3 Frequency selection algorithm

Selecting the right peak frequencies of a frequency spectrum it's not trivial. A signal hardly is composed of only one frequency, it is usually composed of several of them. In a resonant frequency test, these extra frequencies could come from different sources, such as ambient vibrations, hammer vibration, other vibrations modes including higher modes.

For this reason, the resonant test standards (ASTM_C215, 2014; ASTM_E1875, 2013; ASTM_E1876, 2015) specify to locate the sensor and impact location at maximum displacement nodes for a certain vibration mode while being a minimum displacement node for other modes. This way the peak with maximum amplitude is typically the resonant frequency looked for. Although still other vibrations modes can still be detected.

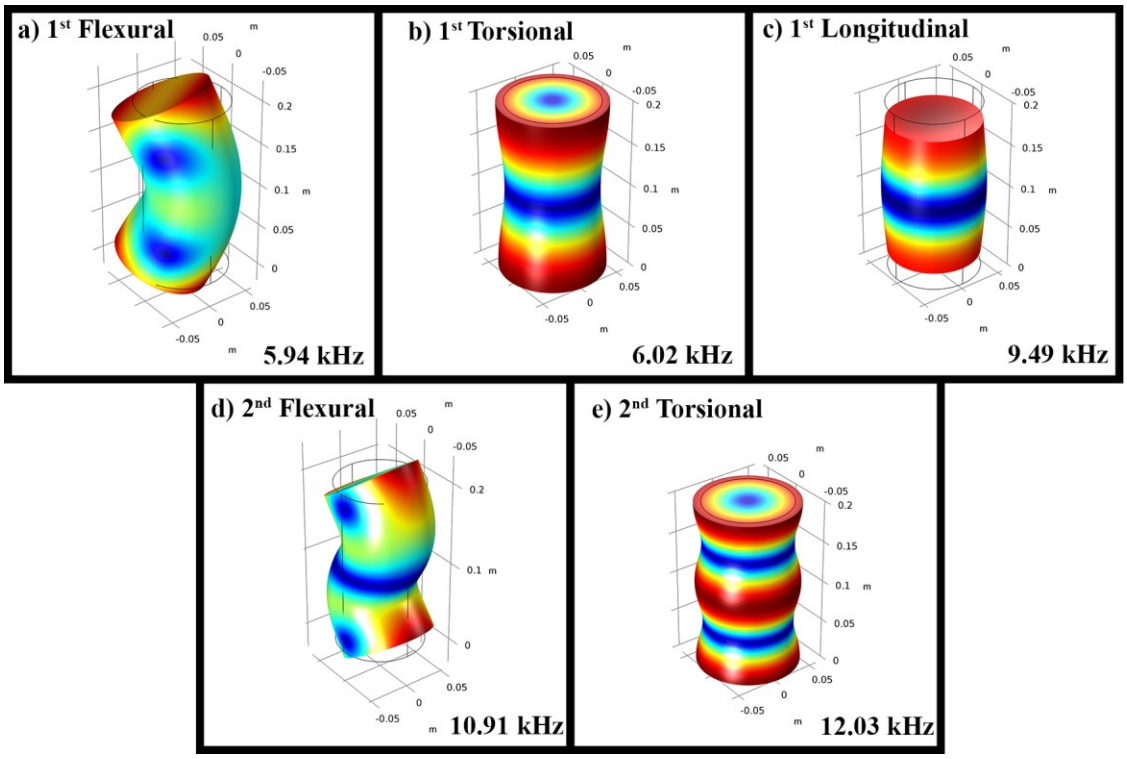

Figure 5.13 Fundamental modal shapes within the frequency range of interest [4-12 kHz] for a concrete cylinder with D=10.20 cm, L=20.05 cm, ρ_c=2350 kg/cm^3, E_d=35 GPa and ν_d=0.28. Obtained by FEM.

Figure 5.13 shows the different fundamental vibration modes for a typical concrete cylinder using the mean values expected for the specimens used in this research for diameter, length, density, dynamic Young's modulus and Poisson's ratio. There are at least 5 theoretical vibrations modes in the expected frequency range and some of the resonant frequencies are very close to each other, for

example, the 1st flexural and 1st torsional modes (Figure 5.13-a&b), and the 1st longitudinal and 2nd flexural modes frequencies as well (Figure 5.13-c&d). This could cause confusion when trying to select the proper frequency peak from the spectrum.

When the accelerometer and the impact locations are not in the nodal zones of maximum displacements, like the tests done in the current research, selecting the relevant resonant frequency from the spectrum could become challenging, especially when trying to automatized the peak selection. Figure 5.14 shows an example of a frequency spectra from an accelerometer that has three major peaks and two small ones that could cause confusion for selecting the longitudinal frequency.

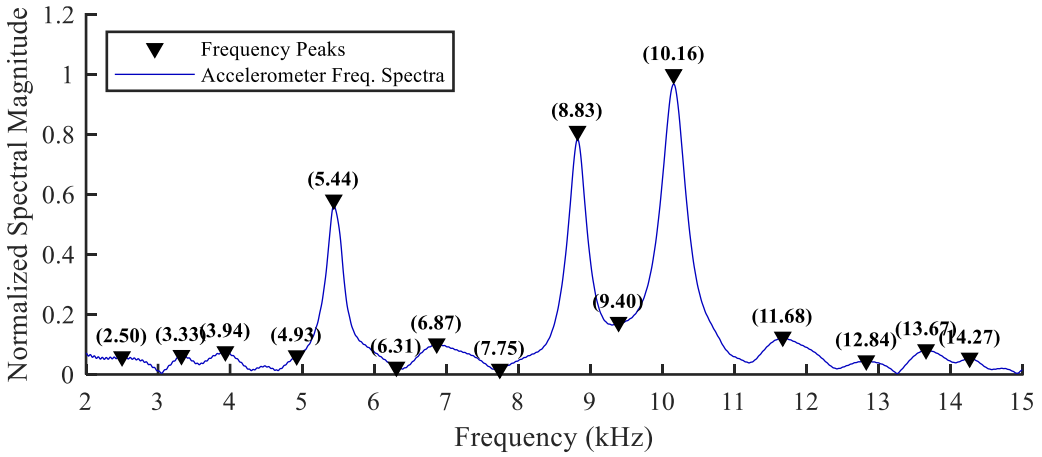

Figure 5.14 Example of a normalized frequency spectra for one of the cylinders tested[4] for which selecting the longitudinal resonant frequency could be confusing.

The challenge of selecting the right frequencies increase when using microphones to record the acoustic response from the cylinder. Due to the indirect measurement of the vibration through a non-contact sensor, detecting the sound pressure variation around the cylinder, several other frequencies non-related with the cylinder will be picked up by the microphone. The audio recording will contain any other ambient noise present at the moment of the tests, the vibration of the impulse hammer.

Therefore, is crucial to develop a reliable algorithm to select the right frequencies from a microphone frequency spectrum. Figure 5.15 shows an example of the frequency spectra obtained from a microphone measurement during one of the resonant tests performed on the current research. The frequency spectrum is noisier than the ones obtained from accelerometer readings (Figure 5.14).

[4] Frequency spectra corresponding to the cylinder SN422 tested at 3 days old, with SP01, H11 and accelerometer and impact location being at positions b from Figure 2.1

It contains at least 5 frequencies that could be easily confused due to its magnitude and the frequency range they are located. The frequencies that correspond to the flexural and longitudinal resonant frequencies for this particular cylinder and test are 5.71 and 9.16 kHz.

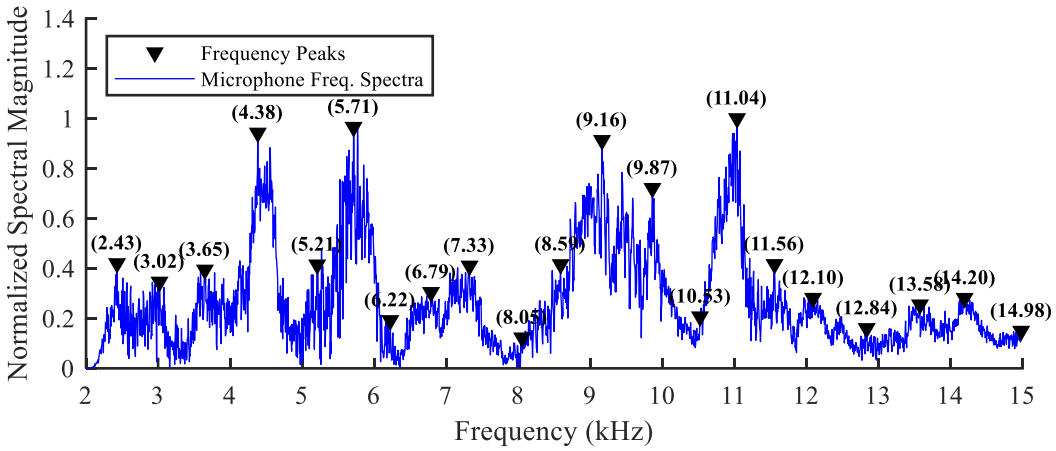

Figure 5.15 Example of a normalized frequency spectrum from an audio recording of one of the impact-resonant tests performed in one of the concrete cylinders[5] of this research.

(Ito & Uomoto, 1997) research also used microphones, although they were specialized microphones capable of connecting to an oscilloscope, which probably made them obtained clean signals. They were able to identify the right peaks by mapping the frequency response along a surface observing the increase in magnitude for the resonant frequencies in their maximum displacement nodes.

5.2.1.3.1 Ratio

The main characteristic to choose the right longitudinal resonant frequency is based on the intrinsic ratio that exists between the flexural and the longitudinal frequency. The ratio between these two frequencies 'R_f' is defined by the expression (5.4) which results from assuming the dynamic modulus obtained from the longitudinal and flexural resonant frequencies are equal. For this, equations (4.3) and (4.4) are solved for the resonant frequency *'f_l'* and *'f_f;* and then divided by each other.

$$R_f = \frac{f_f}{f_l} = \frac{D}{L}\sqrt{\frac{5.0930}{1.6067 \cdot K_L T_m}} \tag{5.4}$$

[5] Frequency spectra corresponding to the cylinder SN216 tested at 10 days old, with SP01, H09 recorded with microphone built-in of smartphone. The microphone and impact loation being at positions *'b'* from Figure 2.1

Recalling from section 4.3 the corrections factors K_L and T_m (Equations (4.5) and (4.6)) only depend on the slender ratio 'D/L' and the Poisson's ratio.

In section 5.1.2 the average diameter and length for the specimens tested in this work were found to be 10.2 and 20.05 cm. And from what was discussed previously in section 2.7.4, the dynamic Poisson's ratio tends to be higher than the static values especially for early ages concretes. Assuming a v_d of 0.28 the frequency ratio 'R_f' expected is 0.6269.

A frequency ratio 'R_f' of 0.6259 is found when using the 1st flexural and longitudinal resonant frequencies that yield from a Finite Element Analysis (FEA) made in COMSOL®, using the same concrete cylinder properties (Figure 5.13). The difference between these two theoretical ratios is neglectable being less than 0.16%.

5.2.1.3.2 Ratio range

Despite the almost null difference between the ratios *'R_f'* found between the finite element model and the equations, the reality will be different from this. For practical reason, it is easier to define a ratio range on which all the cylinders tested will fall into rather than computing a specific ratio for every specific cylinder. Even trying to set a ratio for every single cylinder based on their dimensions there would still be some variability expected due to the unknown Poisson's ratio, and that the cylinder shape is not a perfect cylinder.

To define the ratio range a Monte Carlo Simulation will be performed on the equation (5.4), for which the random variables are *'D'*, *'L'* and *'v_d'*, The diameter and length will be modelled as normally distributed variables and the Poisson's ratio with a Beta distribution. The distribution parameters were taken equal to the mean and twice the standard deviation of all the measurements (Table 5.20) taken of the research specimens. The reason for taking double the standard deviation is to account for extra variability due to shrinkage or expansion due to the curing conditions and other imperfections in the cylinders such as an elliptic geometry in the cylinder surfaces due to defective moulds.

Table 5.20 Mean and standard deviation for diameter and length for all measurements taken to the concrete cylinders used for this research

	Diameter *D* [cm]	**Length *L* [cm]**
μ	10.201	20.017
σ_{sd}	0.038	0.223
COV	0.004	0.011

The mean for the dynamic Poisson's ratio will be assumed to be 0.28 due to it is reported by (Neville, 1996) to be between 0.2 and 0.3 but it has been found it can reach ratios over 0.4 for early age concrete (Simmons, 1955). The standard deviation for the v_d will be assumed to be 0.1.

The normal distribution of a random variable 'x' is defined by (5.5). The normal distribution, distribute evenly to both directions the values becoming rarer as they become apart from the mean. It has theoretically an infinite range at both boundaries range.

$$PDF_{Norm}\left(x \mid \mu, \sigma_{sd}\right) = \frac{1}{\sqrt{2\pi\sigma_{sd}^2}} e^{-\frac{(x-\mu)^2}{2\cdot\sigma_{sd}^2}} \tag{5.5}$$

Nevertheless, the Poisson's ratio has well-defined boundaries between 0 and 0.5. A normal distribution would estimate values beyond these boundaries. A Log-Normal distribution would only avoid negative values but would still accommodate values beyond the 0.5 ratios. Therefore to model the Poisson's ratio a Beta distribution defined by the expression (5.6). The Beta distribution is limited for values between 0 and 1, which can be overcome by a simple variable substitution. Another advantage of the Beta distribution for the Poisson's ratio is that it is skewed towards one of the sides based on the mean value, which is true for v_d which is likely to have higher values than lower values.

$$PDF_{Beta}\left(x \mid \alpha, \beta\right) = \frac{1}{B\left(\alpha, \beta\right)} x^{\alpha-1}\left(1-x\right)^{\beta-1} \tag{5.6}$$

The Beta distribution (5.6) uses the Beta function defined by (5.7) to normalize the distribution to 1, and it is a function of two parameters, α and β. These two parameters can be related to the mean and standard deviation by equations (5.8) and (5.9) (Johnson, Kotz et al., 1995).

$$B\left(\alpha, \beta\right) = \int_0^1 t^{\alpha-1}\left(1-t\right)^{\beta-1} dt \tag{5.7}$$

Solving the system of equations (5.8) and (5.9) for the mean 0.28 and standard deviation of 0.1 yields the values of 2.89 and 2.27 for α and β respectively.

$$\mu = \frac{\alpha - 1}{\alpha + \beta - 2} \tag{5.8}$$

$$\sigma_{sd}{}^2 = \frac{\alpha \cdot \beta}{\left(\alpha + \beta\right)^2\left(\alpha + \beta + 1\right)} \tag{5.9}$$

The probability distributions obtained by simulating the three random variables along with their 2.5 and 97.5 percentile values are shown in Figure 5.16. The figure also shows the maximum value for each random variable. As it was expected for the Poisson's ratio distribution (Figure 5.16-c) is skewed to higher ratios and limited within the real range of 0 and 0.5. These distributions were obtained by running 30 million simulations using MATLAB®.

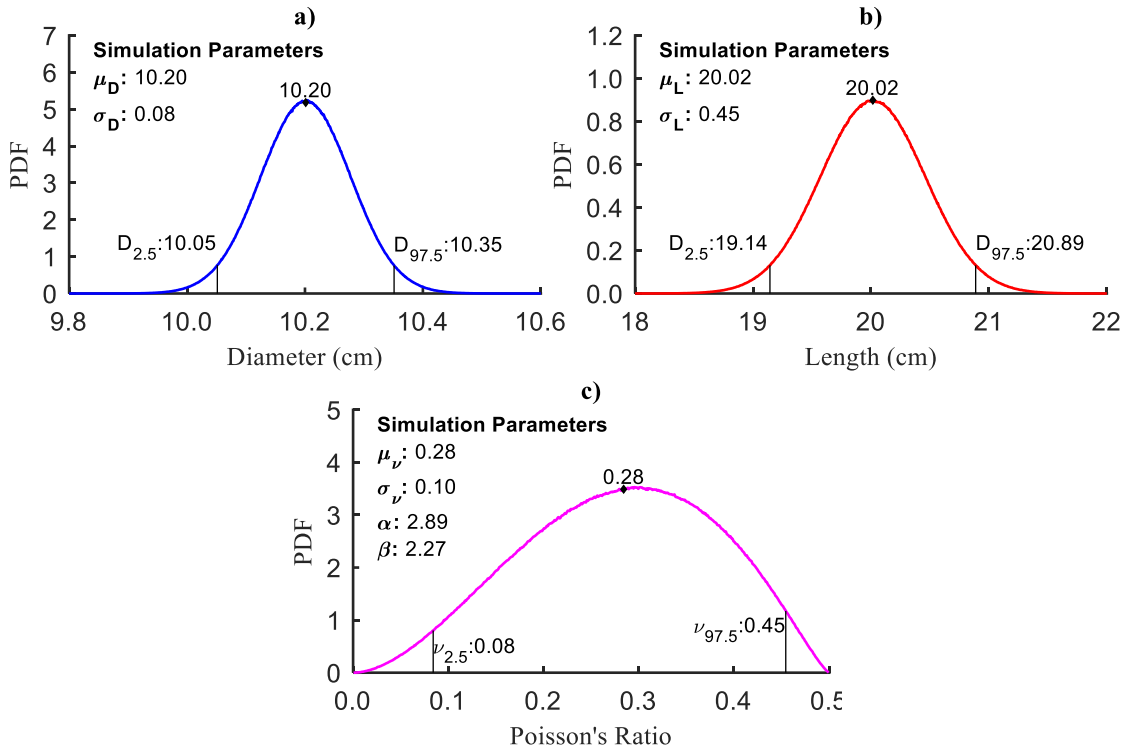

Figure 5.16 Probability Density Functions [PDF's] for the three random variables computed for the Monte Carlo Simulation of the frequency ratio (R_f)

Every value set for each variable was used to compute a frequency ratio *'R_f'* and the resulting probability distribution for the frequency ratio is shown in Figure 5.17. The mean value for the resulting distribution is equal to 0.62, while the minimum and maximum frequency ratios were 0.57 and 0.66. These results are also listed in Table 5.21

Table 5.21 Minimum, maximum and mean values for the frequency ratio, 'R_f', yielded by the Monte Carlo Simulation

	R_f
R_{fmin}	0.5722
μ	0.6190
R_{fmax}	0.6646

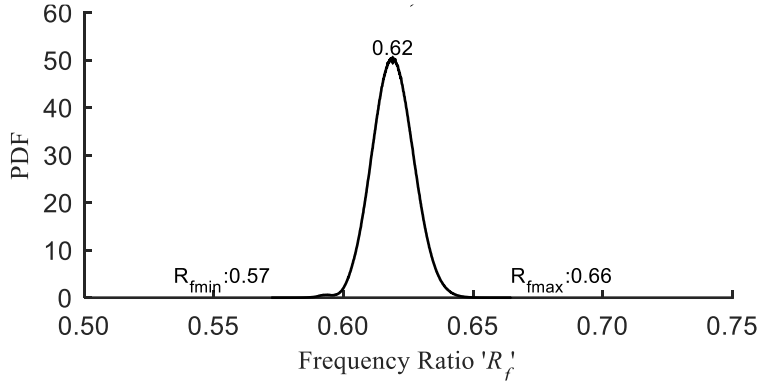

Figure 5.17 Probability Density Function [PDF] for the frequency ratio (R_f) obtained by Montecarlo Simulation

5.2.1.3.3 Quality index

It is now safe to assume that the ratio between the flexural and the longitudinal resonant frequency (*'R_f'*) will always fall between 0.57 and 0.66 with a center value of 0.62. Nevertheless, only this is insufficient to find the right peaks on a frequency spectrum, its only the first step. The frequency spectrum might be quite noisy having lots of other frequency peaks unrelated with the cylinder vibrations, especially for the microphone readings. These other frequencies could coincidentally match the expected ratio range.

Because of this reason, a 'Quality Index' (*'Q'*) for the peaks selected is proposed. The term quality intends to evaluate in terms of good or bad a particular subject. The Quality Index intends to grade from 0 to 1 the frequency peak selection for a particular signal, 0 being the worst and 1 being the best possible scenario possible for the particular signal.

The Quality Index will serve as well as an additional tool to evaluate how good a particular test is for evaluating both flexural and longitudinal frequencies. Serving as an objective tool to compare test setups. It will be used constantly along with the present work for diverse applications.

The index evaluates three characteristics of the peak selection/frequency spectrum: 1) Frequency peak ratio *'R_f'*. 2) The relative magnitude within the frequency spectrum of the two peaks, and 3) The prominence of the peaks selected. The Quality Index *'Q'* is defined by the expression (5.10), which is the product of three independent indexes, one for each one of the characteristics evaluated.

$$Q = Q_R \cdot Q_M \cdot Q_P \tag{5.10}$$

The three minor quality indexes will be named as follow: *'Q_R'* Ratio Quality Index, *'Q_M'* Magnitude Quality Index, and *'Q_P'* Prominence Quality Index. All of these indexes also are graded between 0 and 1. Due to *'Q'* is the result of the product of all three minor indexes, if one of them is equal to zero, the overall quality index *'Q'*, will also be zero.

- **Ratio Quality Index (Q_R):** It grades the peak selection by their frequency ratio *'R_f'*, dividing the lower frequency by the higher frequency. If the ratio falls beyond the expected ratio boundaries found by the Monte Carlo Simulation (Table 5.21), *'R_{fmin}'* and *'R_{fmax}'*, the *'Q_R'* will be equal to zero. If by the other hand, the ratio falls within this range, then a value from 0 to 1 will be assigned to *'Q_R'* by linear interpolation of the frequency ratio *'R_r'* as it is shown in Figure 5.18.

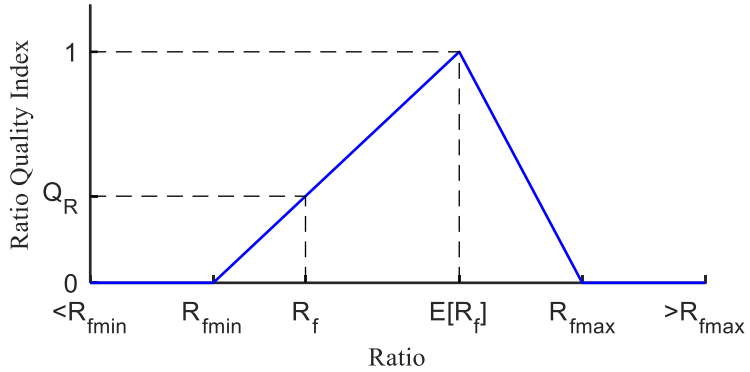

Figure 5.18 Graphic representation for the definition of Ratio Quality (Q_R) Index

- **Magnitude Quality Index (Q_M):** It grades the peaks selected based on their magnitudes. It is defined by the expression (5.11), It normalizes the product of the selected peak magnitudes (P_{km_1} and P_{km_2}) by the product of the magnitude of the two highest frequency peaks ($P_{km_{\max 1}}$ and $P_{km_{\max 2}}$). Q_M es equal to 1 when the selected peaks are the two highest peaks. This is the only minor quality index that cannot have a value of zero. Because for a peak to be a peak it needs to rise and therefore having a magnitude larger than zero.

$$Q_M = \frac{P_{km_1} . P_{km_2}}{P_{km_{\max 1}} \cdot P_{km_{\max 2}}} \tag{5.11}$$

- **Prominence Quality Index (Q_P):** This index grades the peaks based on the prominence of the selected peaks compared with the nearer peaks. It's a way of measuring how much the

peaks stand out in the frequency spectrum and penalized/discard those peaks that have several peaks around it with similar amplitudes. Figure 5.19 illustrates how *'Q_P'* is defined. The frequency difference between the two selected peaks (Δf_n) will be used to define a *"prominence region"* centred around each of the selected peaks. The average (μ) and standard deviation (σ_{sd}) of the magnitudes of the peaks within the region but excluding the peak selected will be used as parameters for defining the thresholds for *'Q_P'* for each particular peak. The lower and upper threshold lines will be defined by average *'μ'* and by the average *'μ'* plus 3 times the standard deviation *'σ_{sd}'*, respectively. If the selected peak is below the lower threshold, the respective *'Q_P'* will be equal to zero. On the other hand, if the peak is above the upper threshold then the respective *'Q_P'* will be set to one. If the selected peak is between the two thresholds *'Q_P'* will be computed by linear interpolation. Finally, the *'Q_P'* to be taken for the peak selection will be the lesser of the two *'Q_P'* from both selected peaks.

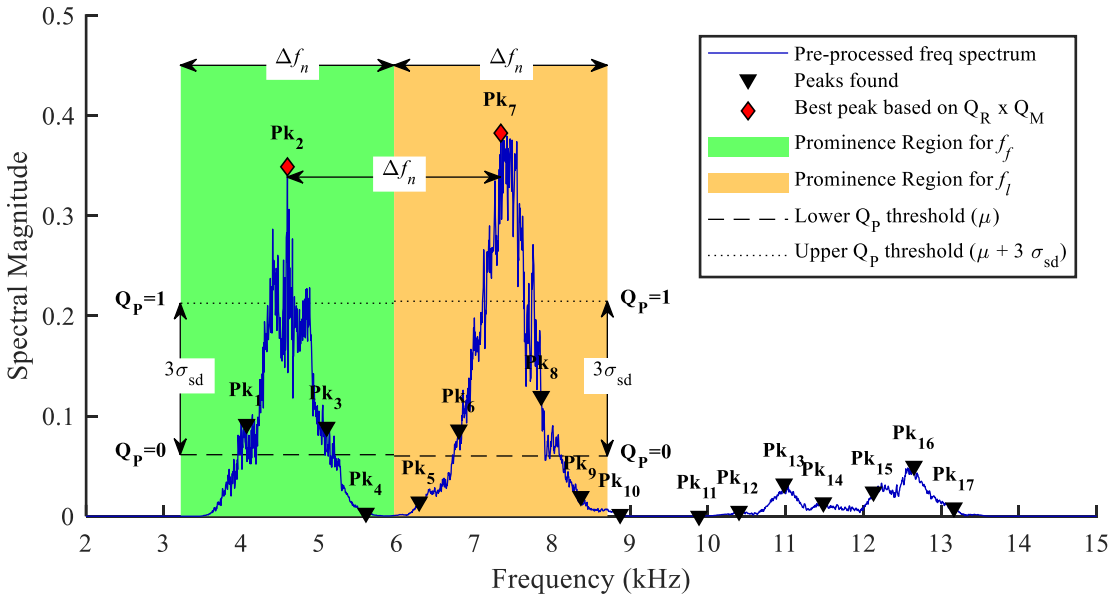

Figure 5.19 Prominence quality index diagram explanation for a frequency spectrum[6] example.

[6] The frequency spectrum shown in Figure 5.19 correspond to the test done in cylinder SN 205 with Age of 1 day old, recorded with the smartphone microphone at position (b), impacted with hammer H11 at location (b). The frequency spectrum shown has been preprocessed accordingly with the methodology explained in section 5.2.1.5.1

For example, for the frequency spectrum shown in Figure 5.19, the two selected peaks are Pk_2 and Pk_7. The region for each peak is highlighted by a green and pink shade. The lower and upper thresholds for Pk_2 defining $Q_P = 0$ and $Q_P = 1$, are defined by the mean and standard deviation of the magnitude of the peaks within the green shaded region but excluding the selected peak (Pk_2), i.e. Pk_1, Pk_3 and Pk_4. Due to the selected peak is above the upper threshold, $Q_P = 1$, then the Q_P for Pk_2 is equal to 1. The same procedure is repeated for the second peak selected Pk_7 and the minimum value of the computed Q_P will be the value taken as definitive for the peak selection.

5.2.1.3.4 Algorithm Overview

The procedure to select the peaks given a number of peaks (Pk_i) with their respective frequencies (f_i) and magnitudes (M_i) will be briefly described. The criteria for locating the peaks in a frequency spectrum are explained in the previous section.

A Partial Quality Index (Q^*) will be introduced and defined as the product of *'Q_R'* and *'Q_M'* (Equation (5.12)). The Q^* index will be computed for all possible sets of two frequencies from the peak vector (Pk_i).

$$Q^* = Q_R \cdot Q_M \tag{5.12}$$

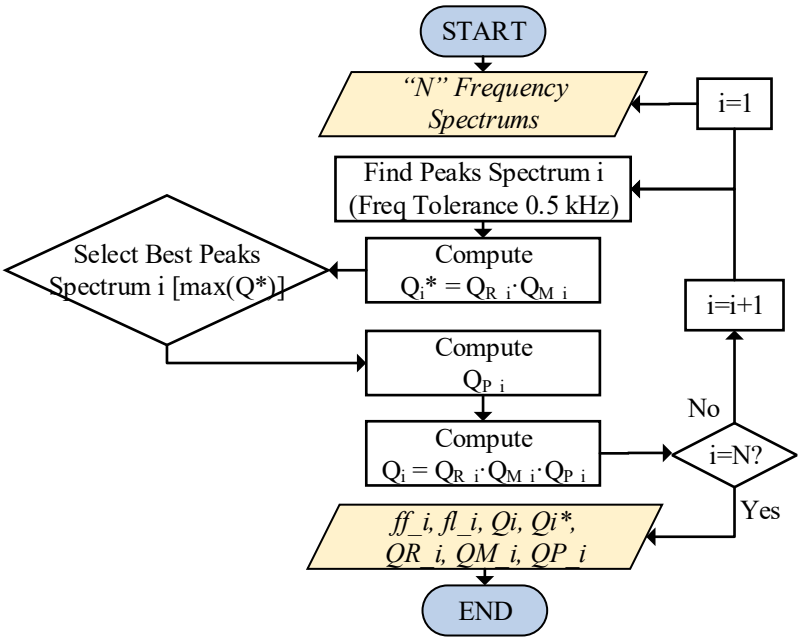

Figure 5.20 Frequency selection algorithm flowchart

The set of 2 frequencies with the highest value of Q^* will be selected. Notices how it is virtually impossible to have two sets of two frequencies with the same Q^* due to the Q_M index. Then the Prominence Quality Index (Q_P) will be computed for the set of peaks selected. The algorithm flowchart is shown in Figure 5.20.

5.2.1.4 Final resonant test setup

Now the final test setup resulted from testing different microphone devices, hammers, support systems, impact locations as well as different positions to place both accelerometers and microphones. The methodology followed to tests these different combinations was previously discussed in the current section. The details of the results of those methodologies will not be given here, but rather in the Results & Analysis chapter. This methodology was used to test all specimens in batch 200, 300 and 400, the ages for testing each one of them was already discussed in section 5.1.3.

The cylinder is to be placed vertically over a foam block of 29x19 cm and 8.5 cm depth as in Figure 5.21-a. This support method corresponds to the support SP01 presented in section 5.2.1.2. The audio recording device selected for this final setup was the rear built-in microphone from a smartphone device (Figure 5.21-b). The hammer named *"H11"* in section 5.2.1.2 was selected. The hammer *"H11"* consists of a ¾" diameter steel bearing attached magnetically to a handle made of a set of 6 neodymium magnets piled together (Figure 5.21-c). The handle had a length of 38.1 mm and between the steel bearing and the magnet, an SAE hex nut #10 was glued to it, to give more stability to the steel bearing.

Every single cylinder was tested twice in the same way but using different sensors, one test recorded with the accelerometer, and the other one recorded with the microphone. The tests with both sensors were performed right after each other. The purpose of having both accelerations data and acoustic data was to compare the results obtained to each other.

For the microphone test, the smartphone was placed horizontally above the top surface of the cylinder as shown in Figure 5.21-a. The smartphone was held by a retort stand like the one shown in Figure 5.10 at approximately 2.5 cm above the cylinder surface, trying to place the rear built-in microphone (Figure 5.21-b) at a distance of one-third of the cylinder radius from the edge. Once the smartphone was properly placed, a continuous audio recording with 48kHz sampling frequency was started, during which several impacts with hammer H11 were done. The impacts were made at the opposite side of the location of the microphone at one-third of the cylinder radius from the edge as

shown in (Figure 5.21-a). The interval between impacts, the number of impacts and the duration of the recording varied between tests. The output file was on a waveform audio file format (WAV).

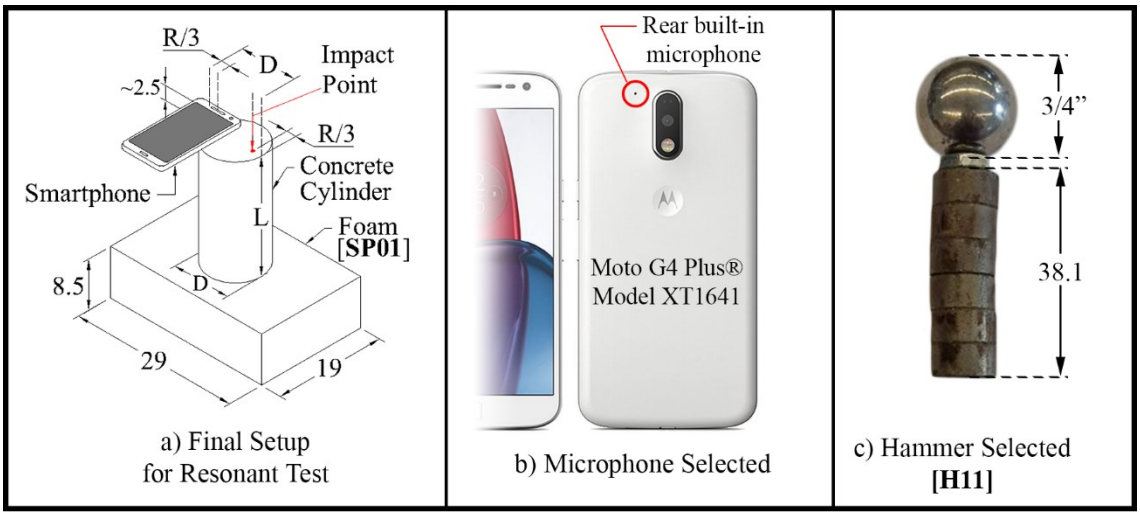

Figure 5.21 a) Final selection for the test setup to performed the resonant test in concrete cylinders, along with the b) acoustic recording devices and c) hammer selected to performed the test

The tests recorded with the accelerometer followed mostly the same setup described above, but replacing the microphone by the accelerometer, at the same position around one-third the cylinder radius from the edge. The accelerometer was coupled to the concrete cylinder using Dow Corning® High Vacuum Grease as in Figure 5.9-a. The cable setup for the equipment was the same as the one shown in Figure 5.12. Similarly, as with the microphone test, several impacts were made to the cylinder with the hammer H11, although the oscilloscope performed a time signal average of 16 of those impacts, resulting in a single set of data in a comma-separated file (CSV).

5.2.1.5 Signal processing algorithm

This section will present the algorithm followed for processing the vibration signals from the cylinder, measured with both the microphone and the accelerometer.

5.2.1.5.1 Microphone signal processing algorithm

First, the microphone processing will be detailed. As mentioned during the test description, the audio recording done with the smartphone would last above 10 seconds and in this time interval, several impacts will be made into the concrete cylinder. Therefore, a single audio file will contain several resonant impact test so the time signal would look like in Figure 5.22.

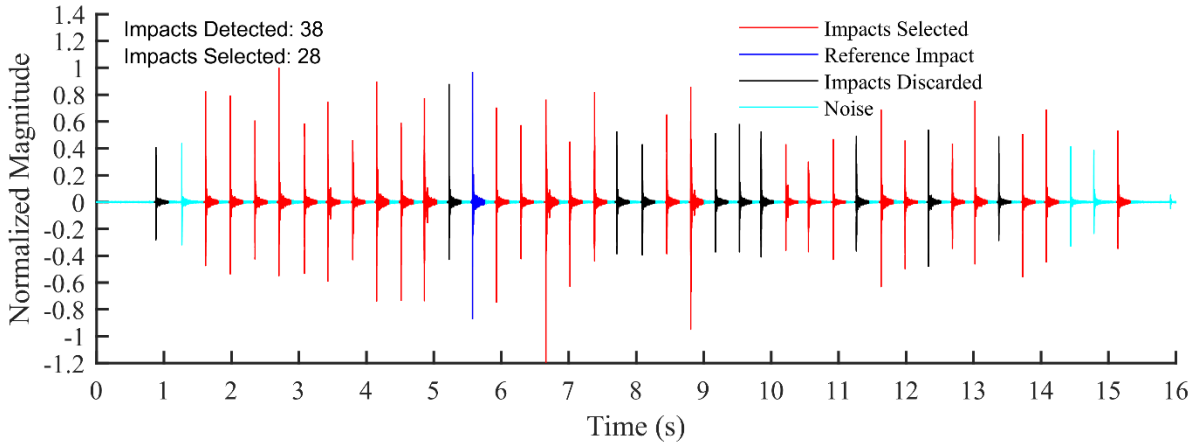

Figure 5.22 Example for complete audio recording[7] in time domain using the smartphone back microphone. Portions of the signal corresponding to noise, impacts discarded, useful impacts and reference impact are plotted in different colours.

The whole recording would be the input of the algorithm detailed in Figure 5.23. The first step of the algorithm is to detect the individual impacts from the whole recording, so all the noise can be disregard. The subprocess algorithm for detecting individual impacts is shown in Figure 5.24. This subprocess will now be described in the following paragraph.

First, a high pass filter with a cut-off frequency of 2.5 kHz is applied to the whole microphone recording signal. This will filter most of the environmental noises and voices on the recording. After the signal has been filtered the potential impacts are to be detected based on their frequency content. For this, the signal is divided into segments of 100 ms, each segment is normalized with themself and their frequency energy in the range of 5 to 13 kHz is computed (This is the expected range for the resonant frequencies). All segments holding more than the average energy in the frequency interval for all segments are selected as potential impacts. From these segments, the maximum amplitude in the time domain is found. If the time between maximum amplitudes between segments is less than 200 ms, then the maximum of the two is taken as reference and a window of 200 ms is set around it, with an initial delay before the maximum value of 20 ms (10% of the total time interval).

[7] Recording shown correspond to the cylinder tested at the age of 10 days old, using the final setup for the resonant test (Cylinder places on a foam support, impacted with hammer H11 at location (b) and the response recorded with the smartphone microphone ar position (b). The signal shown has already been filtered with a High-Pass filter of 2.5 kHz

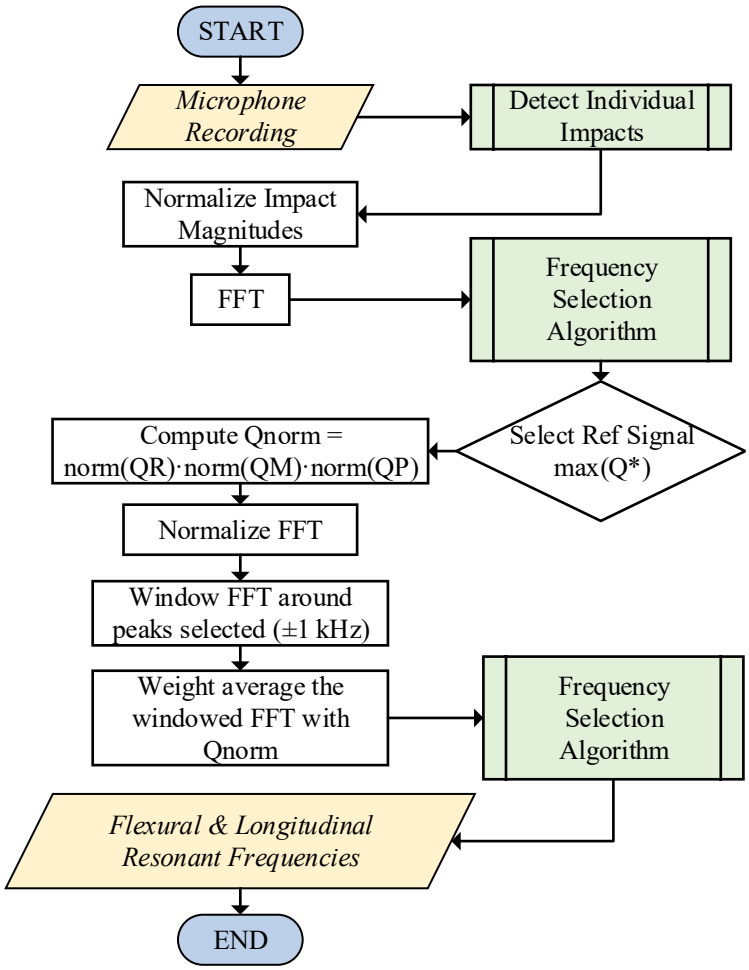

Figure 5.23 Microphone signal processing algorithm flowchart. It's used to identify the flexural and longitudinal resonant frequencies along with the quality index for the signal.

Once the potential impacts segments have been detected, they are normalized with themselves and their frequency spectrum is computed. A subprocess for finding the resonant frequencies and quality indexes for each frequency spectrum is then applied. This subprocess was previously introduced in Figure 5.20 and will be summarized in the following paragraph.

The highest peaks with a minimum distance between each other of 500 Hz are found within the frequency spectrum in the range of 4 to 20 kHz. Then the product of the Q_R by Q_M for all possible combinations of two selected peaks is computed. This product is named Partial Quality Index "Q*".

Based on the peaks with maximum Q* the possible resonant frequencies for that spectrum are selected. Then, the Q_P for those peaks is computed along with the Overall Quality Index "Q". The

subprocess then returns the possible resonant frequencies, f_f and f_i along with the respective quality index for all frequency spectrums.

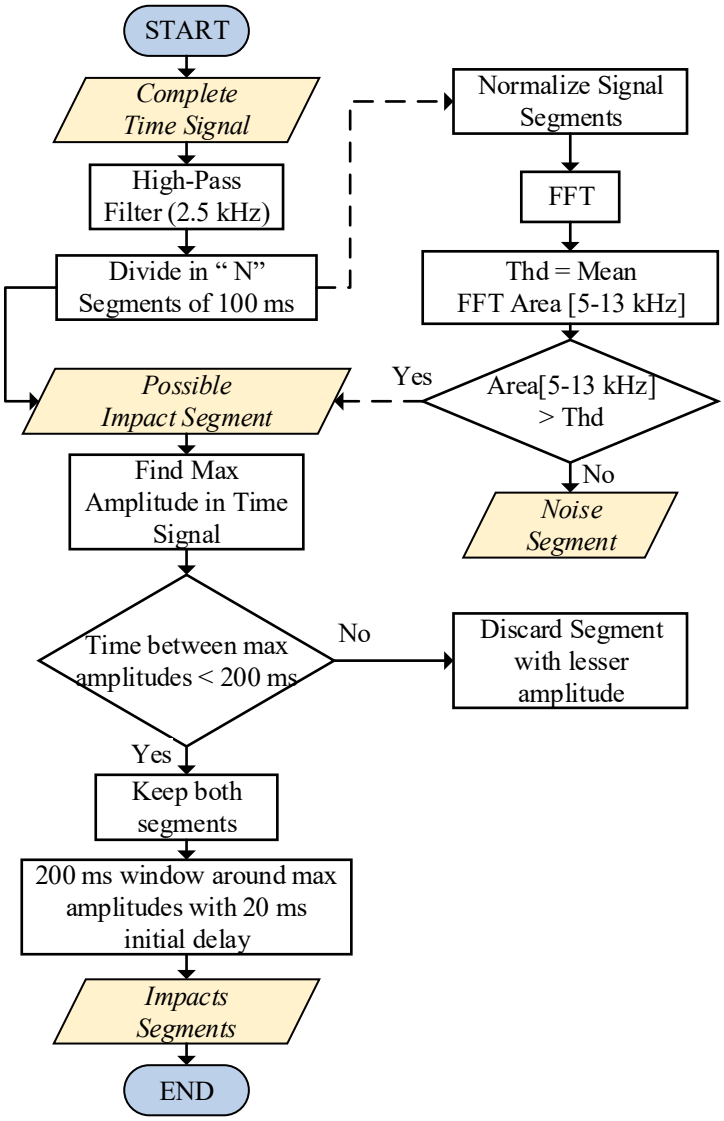

Figure 5.24 Impact detection algorithm flowchart. It's used to detect resonant test impacts from a full microphone recording.

The impact segment with the maximum Q^* will be considered as the reference impact segment. Each of the quality indexes (Q_R, Q_M and Q_P) are normalized with themselves and compute a normalized Quality Index Q_{norm} as the product of them. The frequency spectrums for all the impact segments are also normalized with themselves and windowed with a cosine tapered window with a

total width of 2 kHz and a mid flat portion of 500 Hz around each of the potential resonant frequencies found in each of the frequency spectrums.

Once the frequencies spectrums have been windowed, the weighted average of all of them using the normalized Quality Index "Q_{norm}" for each of them as a weight factor. In this process, all of the impact segments for which the Quality Index is zero will be discarded from the resulting frequency spectrum. Finally, the same procedure for finding peaks and Quality indexes is repeated in the weighted average frequency spectrum and the resulting frequency peaks will be the flexural and longitudinal resonant frequencies obtained from the microphone test for the cylinder.

5.2.1.5.2 Accelerometer processing algorithm

The process for detecting the resonant frequencies of the accelerometer signals is more straightforward. Due to the absence of low frequencies content and mostly only vibrations coming from the cylinder due to the coupling between the sensor and the specimen. The averaging of the impacts made in the cylinder is automatically done by the oscilloscope. So the analysis can be directly performed to the resulting time signal.

The frequency spectrum of the time signal is computed and then introduced as input for the algorithm detailed in Figure 5.20. This algorithm was also described previously in the respective section.

5.2.2 MASW

As was discussed previously in section 2.6.4.2, most of the wave energy from a vibration source is transmitted through surface waves. The Rayleigh waves are dispersive when they travel in a non-homogeneous half-space infinite medium, therefore it is expected that the surface waves in a cylinder will show some dispersion due to the interactions with the cylinder surfaces due to wave reflections. In this section, the methodology and test setup for measuring the Rayleigh wave velocity in the concrete cylinder will be described.

5.2.2.1 Test Description

For an MASW test, several vibrations measurements at different points within the line of wave propagation need to be done. This allows observing the phase velocity scattering at a different distance from the impulse source. Nevertheless, the main challenge of doing the MASW in a quality

control concrete cylinder is their reduced length (~20 cm). As discussed in section 4.3.3, the length of the measuring array affects the maximum wavelength (i.e. the minimum wavenumber to be detected).

Table 5.22 List of cylinders SN tested by MASW test and the age at which they were tested

Specimen Number [SN]	Age (days)	Specimen Number [SN]	Age (days)
437	23	443	156
438	23	444	156
439	23	445	156
440	28	446	156
441	28	447	156
442	28	448	156

The concrete cylinders tested by MASW with the respective age at which they were tested are listed in Table 5.22. It can be noticed that the tests were performed at the same age at which the cylinders were tested in the compression (destructive test). The MASW tests were performed just before testing them in compression, this way the Rayleigh wave velocity results could be related to their static properties.

A single step pulse of 54 kHz was sent through one of the sides of the cylinder using a transducer with a matching resonant frequency. The transducer was located near the surface edge, close to the side on which wave propagations were planned to be measured. To keep the pressure constant between the transducer and the cylinder, the transducer was held tight using 3D printed holders (Figure 5.25-c).

The wave propagation was measured at 33 different points along the same line, starting at 20 mm from the source and then measuring each measuring point spaced every 5 mm. The total length of the measuring point array was 160 mm, therefore the distance between the pulse source and the last measuring point R_{33} was 180 mm (Figure 5.25-b).

The wave propagation was measured at these points using a CLV-2534 Compact Laser Vibrometer from Polytec® (Polytec, 2014), which allows doing precise non-contact vibrational measurement using the Doppler effect up to half nanometer displacements. Due to the high sensitivity of the laser, both, laser and cylinder were placed over an isolation table to reduce the vibrational noise from ambient sources (Figure 5.25-c).

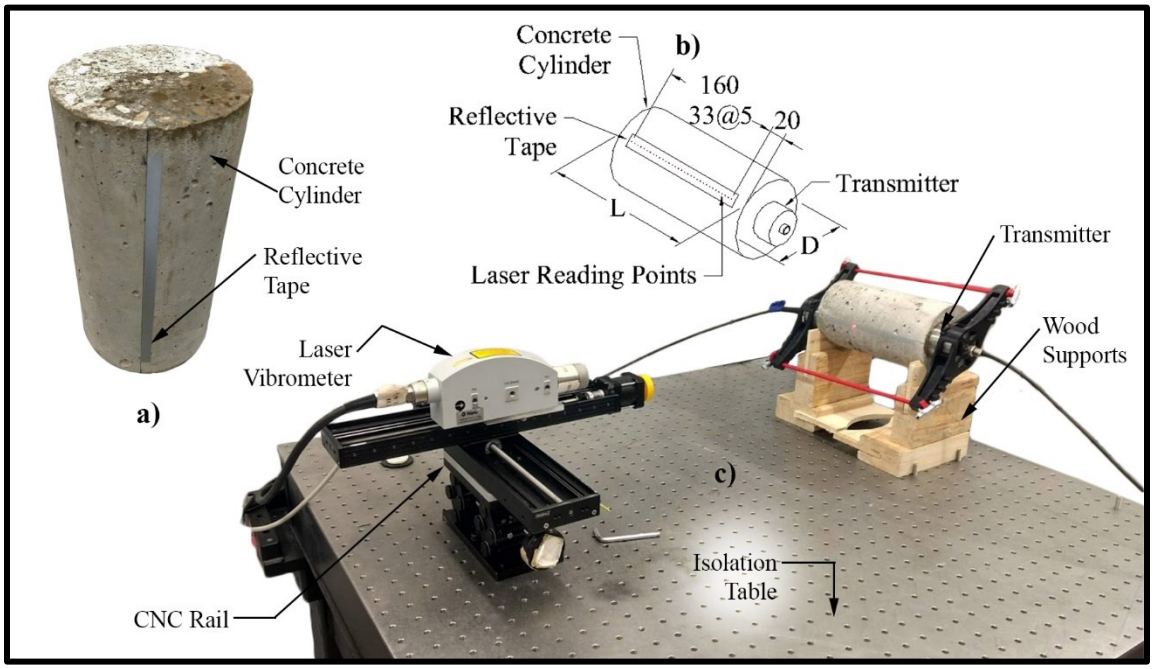

Figure 5.25 MASW test setup showing the a) a concrete cylinder with the reflective tape attached to it, b) a diagram of the measuring points, and c) an actual picture while the test was being done.

The laser vibrometer technology depends on the reflectiveness off the surface to measure, given the low reflectivity of the concrete, to increase the strength of the laser signal, a thin reflective tape was attached to the cylinder, covering the length where the vibrations were going to be measured. The reflective tape used is shown in Figure 5.25-a & b.

The laser sensor head was attached to a Computer Numerical Control (CNC) rail, which allows automating the laser head relocation to the next measuring point, once a vibration reading at the current point has been finalized. By doing this, increasing the distance between points accuracy.

The full cable connection for the MASW test setup is explained further in Figure 5.26. A function generator produces a burst of step signal of 1 cycle with 54 kHz frequency with an amplitude of 8 Volts peak-to-peak every 50 ms. The step signal is sent to a piezo driver that amplifies the signal by a factor of 20, i.e. increasing the signal to over 160 V. The signal from the piezo driver is copied in two, one amplified and another one reduced by a factor of 10 (i.e. ~16 V). The amplified is sent to the transducer which will transform the electrical energy to a mechanical pulse into the cylinder. The reduced signal from the piezo driver is connected to the Data Acquisition System (DAQ), which will use this signal as a trigger to start the recording of both the impulse signal and the vibrational response obtained from the laser vibrometer.

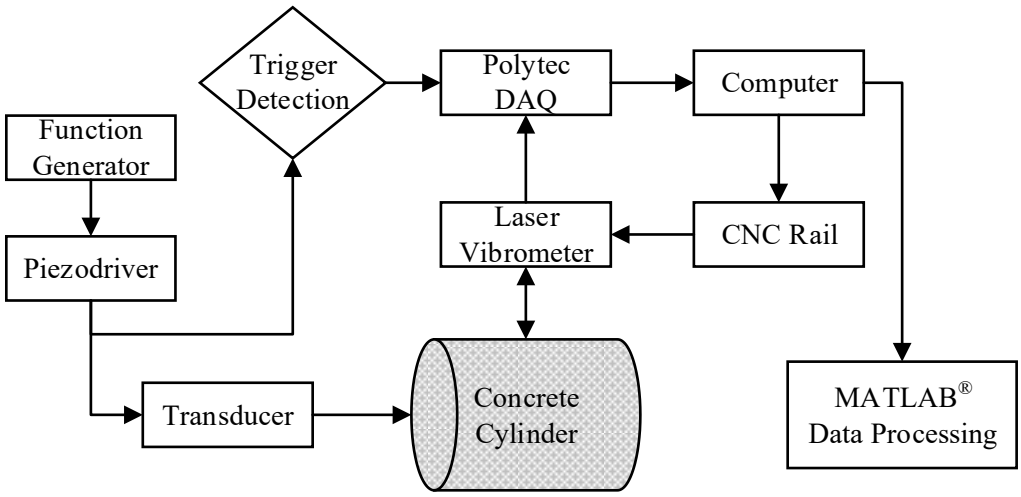

Figure 5.26 Cable connection diagram for the equipment used for the MASW test

The laser DAQ will repeat the measurement 512 times and performed an average of the signals recorded at the same point. The averaging helps to reduce the noise in the signal. Once the averaging of the signal is completed, the DAQ saves the data into a computer, which will also send a command to the CNC Rail to move (and therefore the laser vibrometer) by 5 mm, to the next measuring point. This process is repeated until the 33rd measuring point is reached.

The data obtained from these tests can be divided into 3 different variables: Time, Trigger impulse, and the vibrational response. One set for each measuring point. Although the time and trigger impulse are the same for every point, so they can be considered as only one set of data.

5.2.2.2 Signal Processing Methodology

The readings obtained from the laser vibrometer in the 33 measuring points along the surface of the need to be processed. The signals for one of the tests is shown in Figure 5.27. It shows how a typical time signal look. The left side of Figure 5.27Figure 2.7 shows the time signals for the 33 channels, each one of them normalized with respect to themselves. The signal shown in the bottom is the pulse sent and starting from the bottom to the top, the surface readings on the cylinder are presented in order of closeness to the transmitter location. The horizontal axis represents the time.

In Figure 5.27, two wave transmission slopes can be found. One along the red crosses marked and another one following the first wave package. The former should match the P-wave velocity on the cylinder material. While the latter correspond to the Rayleigh wave velocity.

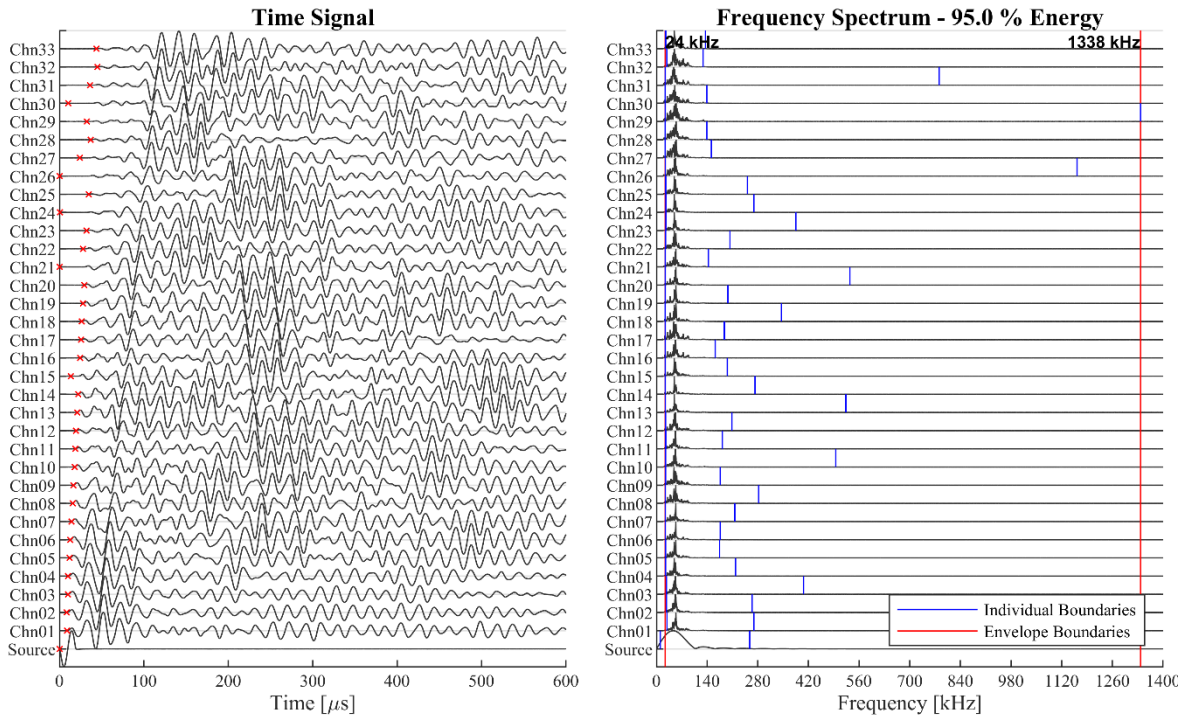

Figure 5.27 Time signal (left) and their respective frequency spectrum (right) for the laser vibrometer reading on the surface of a concrete cylinder[8].

The red crosses shown in Figure 5.27 intend to indicate the first wave arrival at each point. For this, the first wave arrival detection algorithm described in (Sokolowski, Obuchowski et al., 2016) was followed. This algorithm uses a curve-fitting into the second moment characteristics of the signal. These red crosses help to identify where to start windowing the signal.

Figure 5.27-Right shows the frequency spectra for each one of the signals from the left. It also shows a blue vertical line in each frequency spectrum pointing out the 2.5 and 97.5 percentiles of the area below the frequency spectra curve. The frequency bandwidth between these two values contains 95% f the energy. This information is useful to determine the frequencies that were excited due to the pulse.

From the raw signals (Figure 5.27-Left) only a portion of the signals will be taken into consideration for computing the frequency-wavenumber and the phase velocity dispersion images. The purpose of windowing a portion of the signal is to only include the first wave package, that

[8] Data from test in cylinder 446 in the 156th day old after casting. Using a step pulse of 54 kHz.

containing only the pulse sent with its respective spatial frequency dispersion. Trying to discard any wave resulted from any internal reflection in the cylinder.

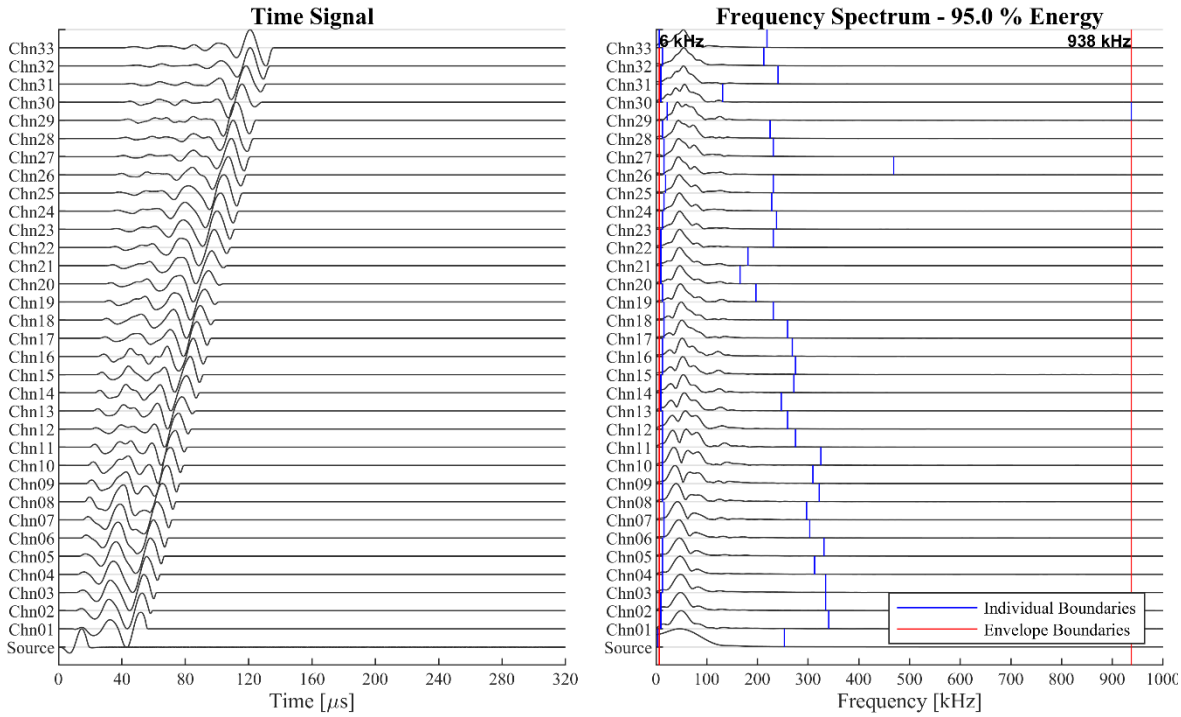

Figure 5.28 Windowed Time Signals (Left) for processing and computing the frequency-wavenumber and its respective phase dispersion curve. The right plot shows the frequency spectra for each signal.

The window is done by drawing two straight lines over the signals in Figure 5.27-Left. The first line is drawn trying to follow the P-wave arrival pattern along all the channels. The second line that would define the end of the window, is drawn in such a way that it follows a specific wave package and simultaneously does not include any wave reflections. The wave reflections can be identified by different wave package slopes.

The window used is a tukey or cosine tapered window. The end result of windowing the signal and padding with zeros look like in Figure 5.28-Left. The right plot in Figure 5.28 shows the frequency spectra for the windowed signals from the left.

The windowed signals are stored in a matrix where each row represents a moment in time, and each column represents a point in space. A 2D FFT is meant to be applied to this matrix. However, before doing so, two additional paddings will be performed to increase both the wavenumber resolution and the maximum wavenumber. The first padding is an upsampling process that adds a certain number of

columns of zeros between each of the original columns in the matrix. Each one of these newly added columns will have a spatial coordinate between the spatial coordinates of the original columns next to them. The second padding, adds columns of zeros at the end of the matrix corresponding to points beyond the last measuring point.

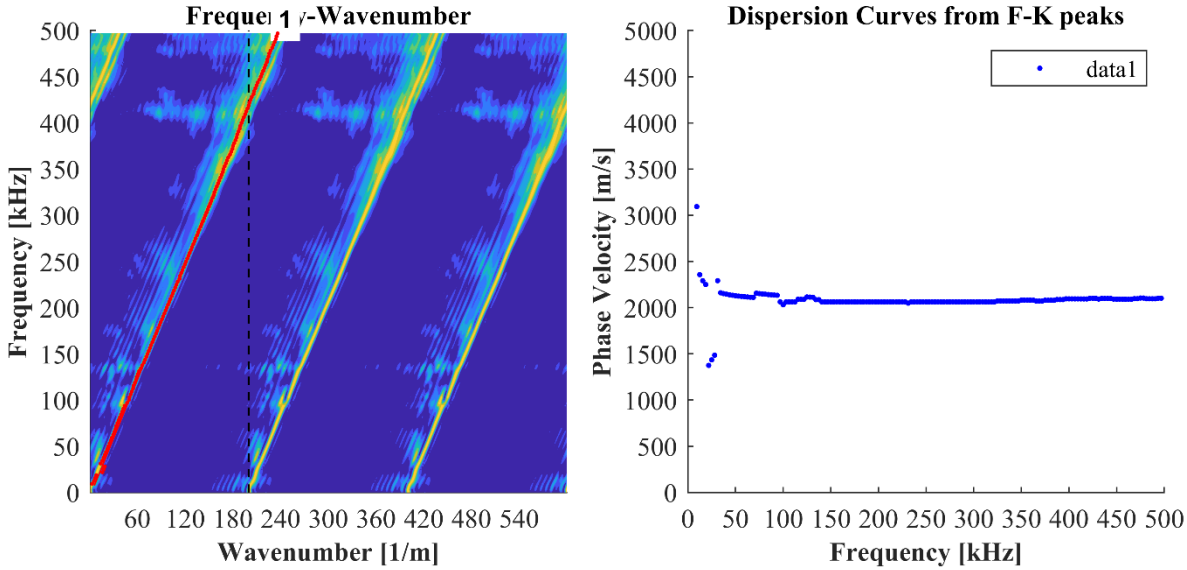

Figure 5.29 (Left) Frequency-wavenumber contour plot obtained from processing the data from Figure 5.28. The right plot shows the phase velocity-frequency translation from the maximum energy points selected with red dots in the left figure.

The 2D FFT is done in opposite directions of the matrix. One FFT for each column and then to the resulting matrix another FFT is performed on it, but now one per each row. This results in a matrix where the columns represent a spatial frequency or wavenumber, and the rows the traditional time-frequency. The resulting matrix plotted as contour plot looks like Figure 5.29-Left. From this figure, a line is drawn following the high energy points. The closest peaks to the line in the 2D plot re then selected and translated into a Phase Wave Velocity – Frequency plot (Figure 5.29-Right).

However, most of the dispersion in the concrete cylinder happens in the low frequencies (below 50 kHz) So to properly being able to appreciate the dispersion a longer sensor array is needed. Nevertheless, the cylinder only has 20 cm length so it's not possible to properly observe the dispersion in the lower frequencies.

Although the information obtained from Figure 5.29-Right is still usable because an almost straight and horizontal line can be clearly detected. This line represents the Rayleigh wave velocity. These

velocities will be then compared with the theoretical Rayleigh wave velocities from the resonant frequencies and the assumed Poisson's ratio.

5.2.3 Ultrasonic Pulse Velocity

The wave propagation velocity within a material is related to their mechanical properties, in a homogeneous an infinite media, it depends only on their stiffness, density and Poisson's ratio. Nevertheless, when the medium has boundary conditions there might exist also shape and frequency factors that affect the wave propagation in a material. This was discussed further in section 4.3.1. In this section, the methodology followed to test the concrete cylinders to evaluate the P-wave propagation in them as a way of finding their modulus of elasticity and compare it with the one obtained from the Resonant Test Method.

5.2.3.1 Test Description

The UPV test is relatively simple, two transducers with the same resonant frequency are to be placed on opposite surfaces of the cylinder as shown in Figure 5.30. The transducers are coupled to the concrete cylinder using Magnaflux® Ultragel® II High-Performance Ultrasonic Couplant, which fills any voids between the transducer and the concrete surface allowing a better wave transmission between them.

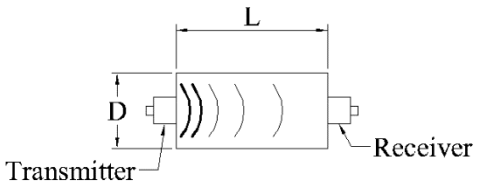

Figure 5.30 UPV test setup diagram.

The device setup for the UPV test is as follows: A function generator will send a pulse with a certain shape and frequency and an amplitude of 8 Volts Peak-to-Peak. The pulse is sent equally to an oscilloscope and to a piezo driver that amplifies the signal by a factor of 20, i.e. increasing the signal to over 160 V. The signal from the piezo driver is copied in two, one amplified and another one reduced by a factor of 10 (i.e. ~16 V). The amplified signal is sent to the transducer which will transform the electrical energy to a mechanical pulse into the cylinder. The reduced signal from the piezo driver is connected to the oscilloscope, which will use this signal as a trigger to start the recording of the three inputs connected to it: The signal as it was sent from the function generator, the

output reduced signal from the piezo driver, and the signal from the receiver transducer. A diagram from the connection setup can be seen in Figure 5.31.

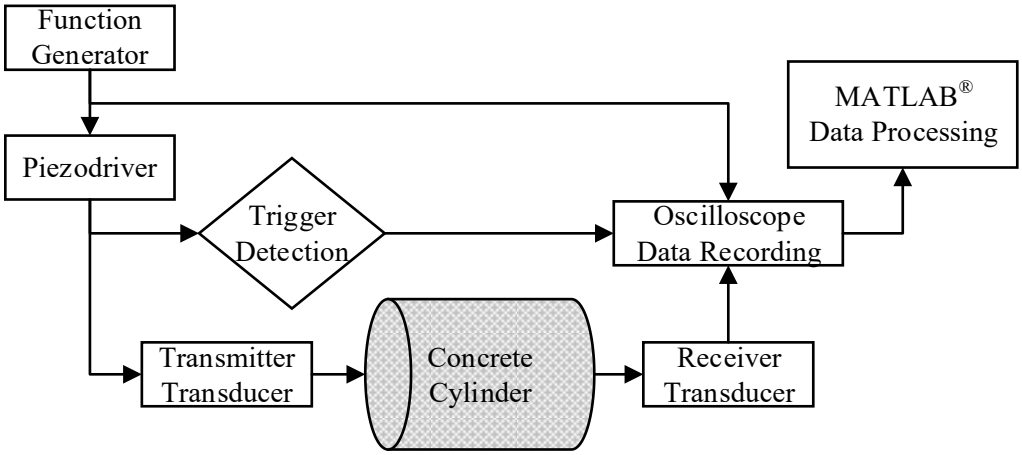

Figure 5.31 Connection setup diagram for the UPV test.

Not all the cylinders were tested with the UPV technique, only selected cylinders from batch 400 were used. The list of cylinders tested with the respective ages at which the test was done is listed in Table 5.23. The table also indicates the type of pulse and the frequency used to perform the UPV test. The latter is indicated by a number that correlates with Table 5.24. The pulses sent are either (1 & 3) sinusoidal or (2) rectangular, with a frequency of (1 & 2) 54 kHz or (3) 150 kHz.

Table 5.23 List of cylinder tested by UPV test with the ages at which they were tested and the impulse frequency used based on the frequencies given in

SN	Ages (days)		Impulse Frequency [IF]	
435	21		2	
437	23		1	2
438	23		2	
439	23		2	
440	28		2	
441	28		2	
442	28		2	
443	128	156	1	3
444	128	156	1	3
445	128	156	1	3
446	128	156	1	3
447	128	156	1	3
448	128	156	1	3

Table 5.24 Different signal impulses used for the UPV test

Impulse Frequency [IF]	Description
1	1 Sinusoidal Cycle of 54kHz
2	1 Rectangular Cycle of 54 kHz
3	1 Sinusoidal Cycle of 150kHz

The results will be compared with the dynamic modulus obtained with the longitudinal resonant frequency, using the equation (5.13). This equation is derived from solving for E_D in the equation (2.34). Two approaches will be taken for comparison. First, the comparison will be made assuming the same assumed Poisson's value for all the dynamic modulus calculations from the resonant frequencies (i.e. 0.25).

$$E_D = V_P^{\,2} \frac{\rho(1+\nu)(1-2\nu)}{1-\nu} \tag{5.13}$$

And a second approach will be using the longitudinal resonant frequency and the P-wave velocity found. An optimization process will be taken, to found the Poisson's value that forces the dynamic modulus computed using both the resonant frequency and the wave velocity to converge.

5.2.3.2 Signal Processing Methodology

The methodology for processing the signals obtained from the tests described above will be presented in this section. The first thing to take into account is that for each test setup used, an additional test with the same setup as described previously is done, with the difference that the transducers are placed directly against each other. This additional test will yield in the electronic delay the test setup has. This is the time it takes from the moment the pulse is sent, to travel through the circuit, and be detected in the oscilloscope.

The signals from the electronic delay test look like Figure 5.32-Left. The same algorithm (Sokolowski et al., 2016) to detect the first wave arrival used for the MASW test is also used here to automatized the first wave arrival detection from the UPV tests.

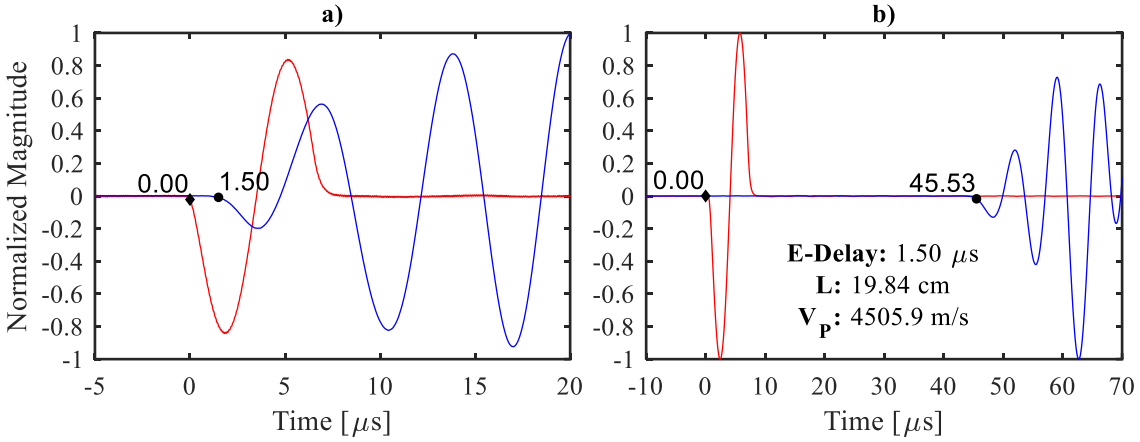

Figure 5.32 Wave velocity computation process. a) Electronic time signal delay obtained by placing a transducer of 150kHz against each other. b) Flying time for the pulse to travel through the cylinder[9]

The first step for computing the wave velocity is to compute the "Time of Flight" of the wave. For this, the first wave arrival is found for both, the pulse sent, and the receiver signal. The difference between these two times minus the electronic delay is the time of flight. The wave velocity is then computed by dividing the travelled distance, (i.e. the cylinder length) by the time of flight.

5.3 Static Tests

5.3.1 Test Description

The static test was mostly done as the standards (ASTM_C469, 2014) and (ASTM_C39, 2018) describe, and they have previously summarized in section 4.2. In this section, only the differences performed with respect to the standards will be addressed. Additionally, the exact equipment used for the test will also be mentioned.

The static tests were performed using a load-frame with a maximum load capacity of 600 kN (MTS 64.605) shown in Figure 5.33. Before testing, the cylinders were properly ground at the age of 1 day old, leaving two smooth and parallel surfaces. The cylinders were placed directly into the machine, without any additional capping or instrumentation, as it is shown in Figure 5.33-Right. One key difference between the procedure followed and the one indicated by the standard (ASTM_C469, 2014) was that the strains were not measured directly from the test specimens, as was shown in

[9] Signal shown in Figure 5.32 correspond to the cylinder 443 using a sinusoidal pulse of 150 kHz with transducers with same resonant frequency. The test was done at the age of 128 days of the cylinder.

Figure 4.1. Instead, the strains were measured using the frame load built-in extensometer. These extensometers are capable of measuring displacements with 0.2 µm resolution.

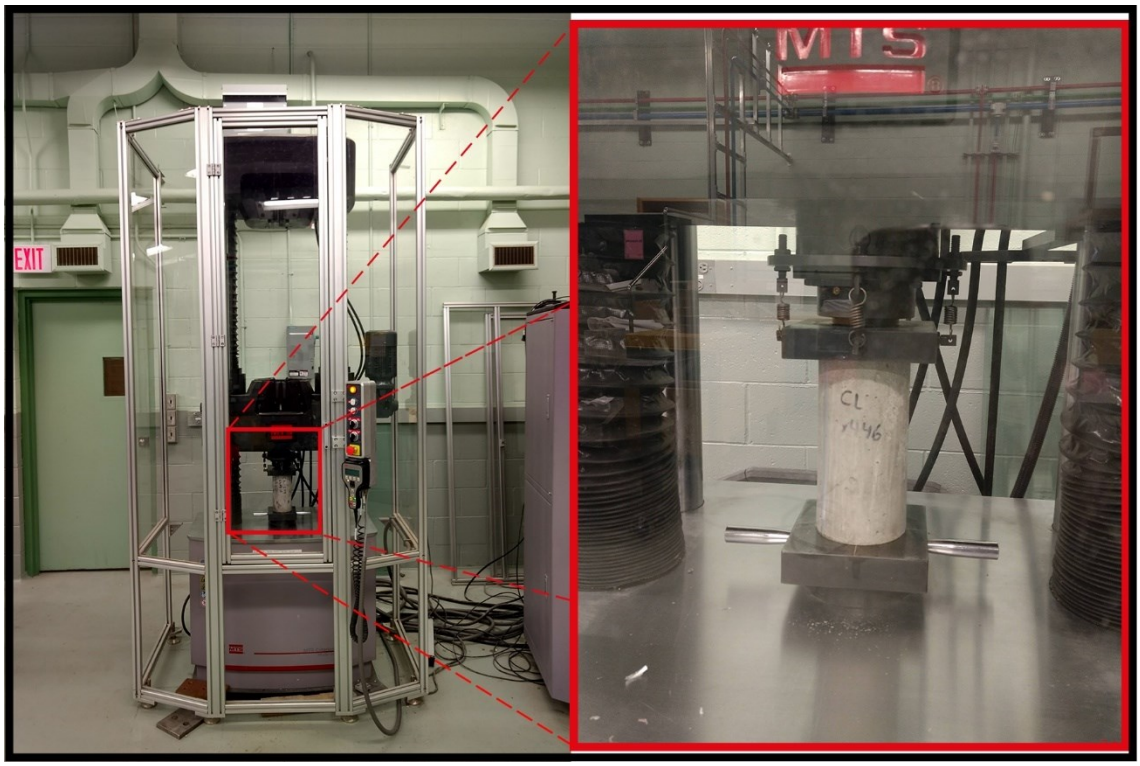

Figure 5.33 Test setup used for the static modulus test and the compressive strength. The left side shows the whole compressive machine used. And the right side shows a close up of the cylinder being tested. The lack of direct strain measurement can be noted in the right figure.

For each set of specimen tests at a certain date, the first tested cylinder was preloaded 3 times to reach approximately 40% of the expected f'c. The loading kept going until the cylinder failure was reach. For the next cylinders from the same concrete to be tested on the same day, the preloading load was set based on the f'c found in the first cylinder.

Among the differences between the practice and the standard was the load rate use to load the specimens. The load rate used vary among the cylinders. A complete list of the load rate used for each cylinder is detailed in Table 5.25. The requirement for the stress rate in the standard is 0.25 ±0.05 MPa. The average and standard deviations shown are the average values for the respective values for each loading in the group of cylinders.

When loading the specimens, the load rate is specified in the load frame as a displacement per time, and not as a stress per time. While in Table 5.25 seems like the load settings were changed almost at

every test, the reality was other. There were only 3 different displacement/time rate used. One for cylinders in batch 100, another for cylinders 201 to 209, and a third one for the remaining cylinders. The slowest displacement rate used for cylinders 201 to 209, while the fastest was at batch 100.

Table 5.25 Load rate used during the elastic modulus and compressive tests for each cylinder.

Cylinder Numbers	Age [days]	Load Rate (MPa/s)		
		μ	σ	COV
[001 - 017]	443	0.40	0.08	21.1%
[101 - 105]	56	1.87	0.11	5.7%
[201 - 209]	1-10	0.05	0.01	15.7%
[210 - 221]	140	0.50	0.01	2.0%
[301 - 313]	483	0.49	0.02	3.2%
[401 - 404]	1	0.28	0.00	1.6%
[405 - 408]	2	0.32	0.00	1.5%
[410 - 412]	5	0.39	0.01	1.7%
[413 - 415]	6	0.38	0.00	1.1%
[416 - 418]	7	0.40	0.01	2.8%
[419 - 439]	9-23	0.43	0.01	3.4%
[440 - 442]	28	0.47	0.01	3.0%
[443 - 448]	156	0.46	0.01	3.0%

Batch 400 although it was loaded at the same displacement rate, it would seem the setting change with the time, but it wasn't changed. The displacement rate at the beginning of the test aimed to get a stress rate in the range required for the standard. However, as the stiffness (i.e. Young's modulus) increased, the stress required to achieve the same displacement also increases, and therefore increasing the stress rate with time.

Batch 00 was loaded with the least uniform load rate. Batch 00 is possibly composed of two concrete mixes, with different stiffness. This will be addressed in the result sections of the static tests.

5.3.2 Data Processing

Processing the load and displacements recorded by the load frame would be typically very straightforward. To transform these values into a stress-strain curve, the load needs to be divided by the cylinder area, and the displacements by the cylinder length. Then to compute the Young's modulus, as previously detailed in section 4.2.2.3, it is required to compute the slope between the point with 50 millionth strain and the point with the 40% of the f'c.

However, the displacements the load frame recorded are shifted due to an initial settlement of the load frame components. An example of the raw stress-strain curves computed based on the raw data from the load frame is shown in Figure 5.34. The figures also show the three pre-loading stages done before the ultimate loading stage.

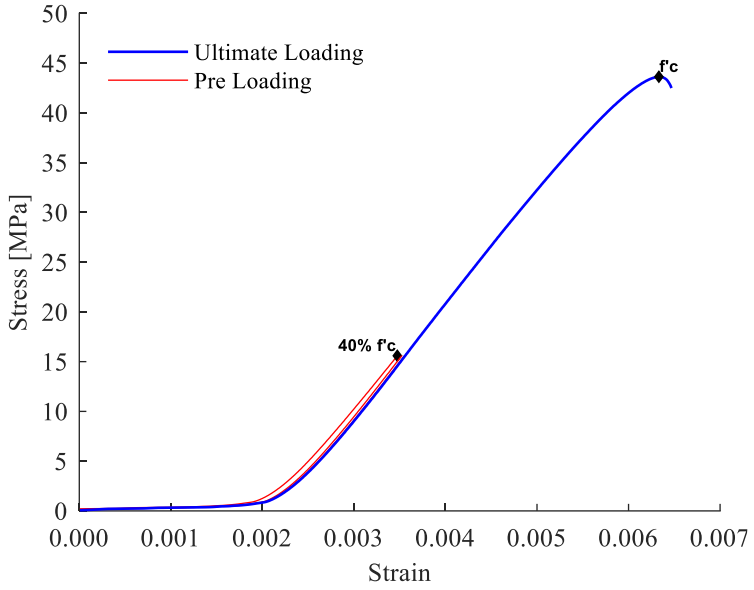

Figure 5.34 Raw stress-strain curve for one of the cylinders tested[10]. It shows the three preloading phases and the ultimate loading when the f'c was reached

If the Young's modulus were to be computed with the curve shown in Figure 5.34, the 50 millionth strain would clearly produce errors in the calculation. So, the initial loading that has a low stiffness needs to be discarded. The point located at 1/5 from the maximum curvature to the inflection point of the stress-strain curve will define the clipping point. The data before this point will be discarded.

Rather than just extending the data from the curve until its intersection with the horizontal axis, using the initial slope of the curve the following procedure was followed: The remaining data will be used to minimize the sum of the squared difference with a theoretical stress-strain curve. The equation considered as theoretical stress-strain was the one proposed by (Carreira & Chu, 1985) and discussed in section 2.7.3.

For the minimization problem, there are two optimization variables: a) the shifting strain of the stress-strain curve; b) the initial tangent slope 'E_{it}'. The last parameter can be defined as a function of

[10] The data belongs to the cylinder 441 tested at the 28th day old.

the critical slope (i.e. the minimum slope possible), which is equal to the ratio between f'c and ε_c. The second parameter is actually a factor with a minimum value of 1 that multiplies to this ratio.

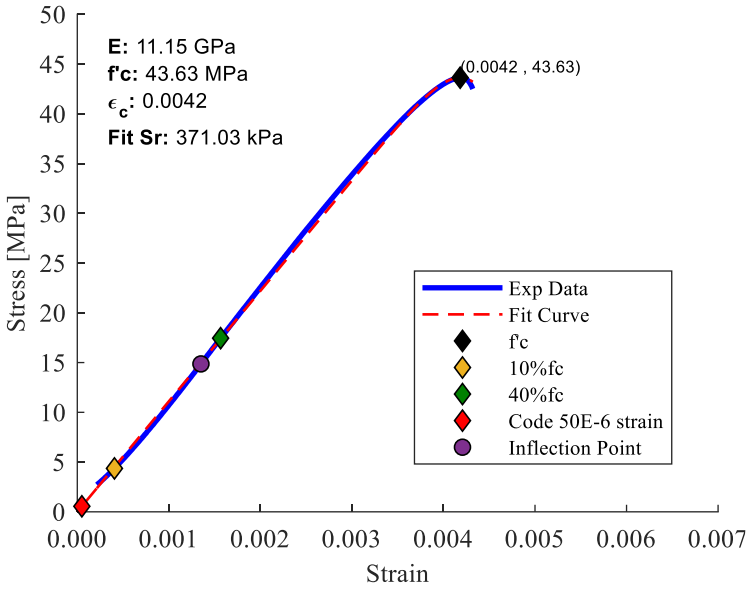

Figure 5.35 Processed stress-strain curve for the same cylinder shown in Figure 5.34. The curve was stripped from the first portion of data and shifted to obtain the best fit of a theoretical stress-strain relationship. Several key points in the stress-strain curve were plotted.

Nevertheless, the theoretical equation used, its still an approximation, and it was found that doing a simple minimization of the squared difference results in curves that didn't follow the initial slope of the stress-strain curve. And it was greatly influenced by how fast the failure happened. To improve the fitting results, the squared errors were weighted based on the portion of the stress-strain curve they were evaluating. The weight system is summarized in Table 5.26. The data points before the 10% the f'c, and the points after the 40% f'c will be considered with a value of 1, while the values in between the 10 and 40% the f'c, will have 3 times larger relevance.

Table 5.26 Weights used for computing the SSE in the stress-strain curve fitting

Weight	Strain-Strain Section
1	[0 - 10] % fc'
3	[10 - 40] % fc'
1	[40 - 100] % fc'

Once the fitting and shifting have been done. The fitted curve will be used to estimate the 50 millionth strain, to compute the Young's modulus.

Chapter 6

Results & Analysis

6.1 Dynamic Tests

6.1.1 Resonant Frequency Method

6.1.1.1 Microphone Selection

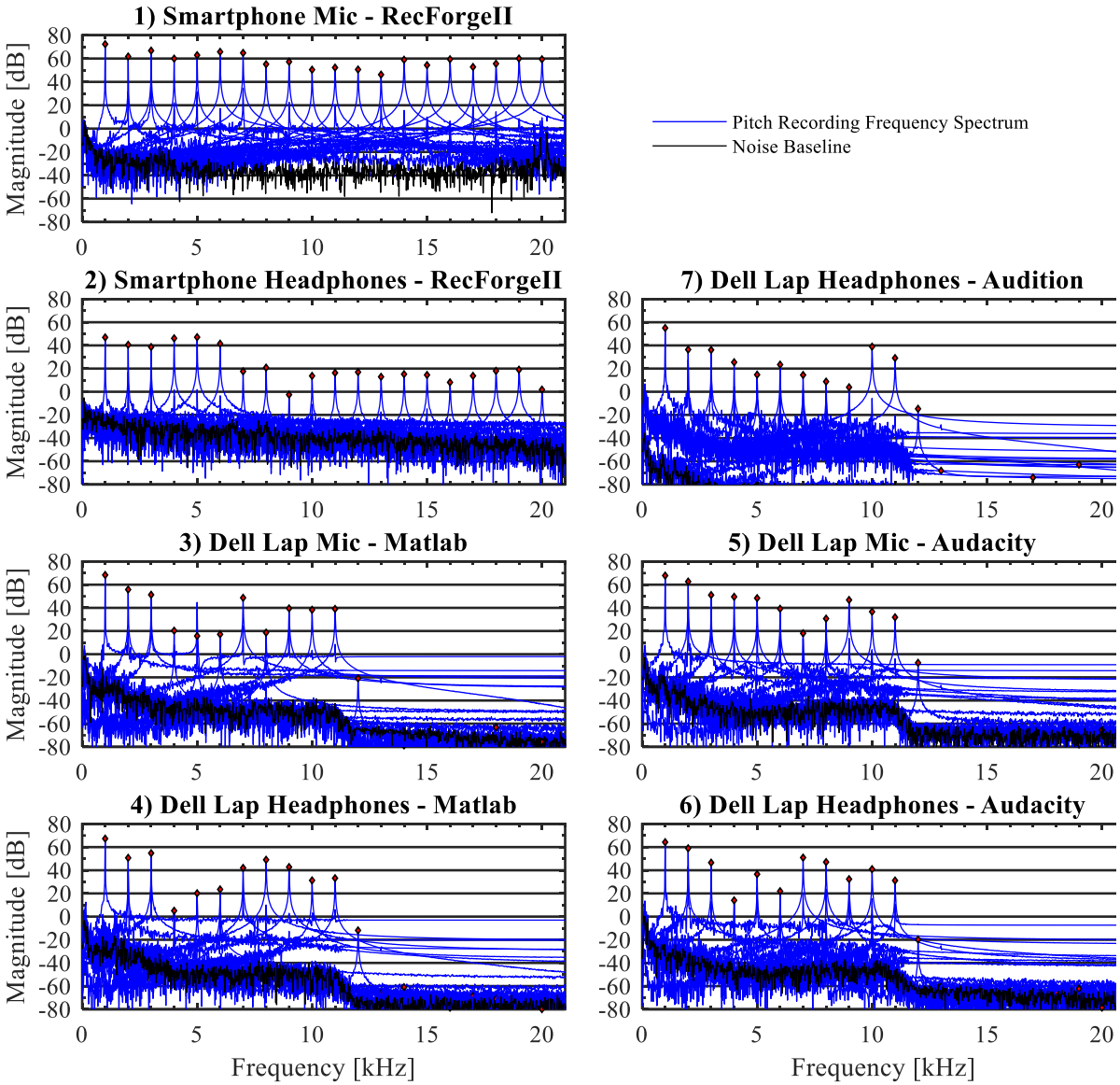

Figure 6.1 Frequency response range for different microphones to pitch sounds from 1 to 20 kHz. Numbers on each plot correlate with the setup combinations from Table 5.12

As was discussed previously in section 5.2.1.1.1, the first step is to validate the microphone capabilities for registering the frequencies in the range of interest (4-11 kHz). Different microphones were tested by recording pitches from 1 to 20 kHz at 1 kHz interval. The test setup was previously explained in 5.2.1.1.1.

Figure 6.1 shows the frequency spectra plotted in decibels for the first 7 test combinations from Table 5.12. All of these tests were recorded using the same speakers to produce the pitches just changing the microphone used for the recording. The microphone used for each of the signals is indicated in the titles of each subplot along with a reference number that matches the ones in Table 5.12.

The pitch recordings are plotted in Figure 6.1 as blue solid lines. Additionally, of recording the different pitches, the environmental noise present at the moment of the test was also recorded and it is plotted as black solid lines. These noise spectrums work as a baseline, to identify how much energy the different pitch frequencies have.

In all cases, the time window used for computing all frequency spectrum was 50 ms. This time was extracted from the mid-portion of a longer recording. The frequency resolution obtained for the frequency spectra is then 20 Hz.

By looking at Figure 6.1 it becomes evident that the best alternative of microphone for using on the tests is the built-in microphone from the smartphone (Figure 6.1-1). The reason for this is that it has a relatively flat response over the whole frequency spectrum with a slight decrease (~10 dB) in magnitude between 10 and 14 kHz. It also has the largest amplitudes overall compared with the rest of the microphones.

Nevertheless, analyzing the rest of the plot the following conclusions are reached:

- The frequency response from the signals recorded with the earbuds shows lower frequency spectral energy than their contra part with the built-in microphones from the devices. They also seem to not have a flat response, in general, the energy registered beyond 6 kHz is less than without using the earbuds. This is concluded by comparing Figure 6.1- *"1"* and *'2"*; Figure 6.1- *"3"* and *'4"*; Figure 6.1- *"5"* and *"6"*.
- The sound card from the Dell Laptop seems to have either an analog or digital low-pass filter built it into it, with a cut-off frequency around 11 kHz. Given the spectral amplitudes even for the noise baseline become almost zero after 11 kHz regardless of the software

used for the recording. Several attempts for deactivating this filter were tried, such as trying with different sound card drivers and deactivating any audio enhancing software pre-installed into the computer. All of these were unsuccessful. This is concluded by looking at Figure 6.1- *"3"* to *"7"*.

- The software used to record the signal on the computer seem to affect the spectral magnitudes. This is probably to the software auto-adjusting the microphone volume according to their own parameters. Nevertheless, regardless of the software used the frequency spectrum is not flat, showing more or less the same shape in all cases even when using the earbuds. Therefore, it is also concluded that the sound card might perform equalization of the microphone signal to enhance it for voice recording.

6.1.1.2 Microphone Position

This section will present the results obtained by placing a professional microphone in different locations around the cylinders, while the cylinder is impacted at different points with the same hammer. The test setup and impact combinations were further explained in section 5.2.1.1.2.

Figure 6.2 shows the normalized frequency spectrums for the microphone at different positions, plotted in a blue solid line. The frequency spectrum from an accelerometer placed near the border on the top surface of the cylinder is also shown in all plots from Figure 6.2 as a red dashed line. The accelerometer response let us visually identify in each plot if the location of the microphones were able to pick up both, flexural and longitudinal resonant frequencies from the cylinder.

The test combination numbers in Figure 6.2 correlates with the test setup combinations from Table 5.14. The results for combinations #1, #2, #5 and #9 are the only ones where both resonant frequencies can be located easily. However, it's only for test setup combinations 1 and 2, where the amplitudes of the peaks are relatively larger compared with the peaks beyond 5 kHz. This means that placing the microphone on the side makes more difficult to record the longitudinal resonant frequency. And better results are obtained when the microphone is located near the top surface and the impact is also done in the top of the cylinder.

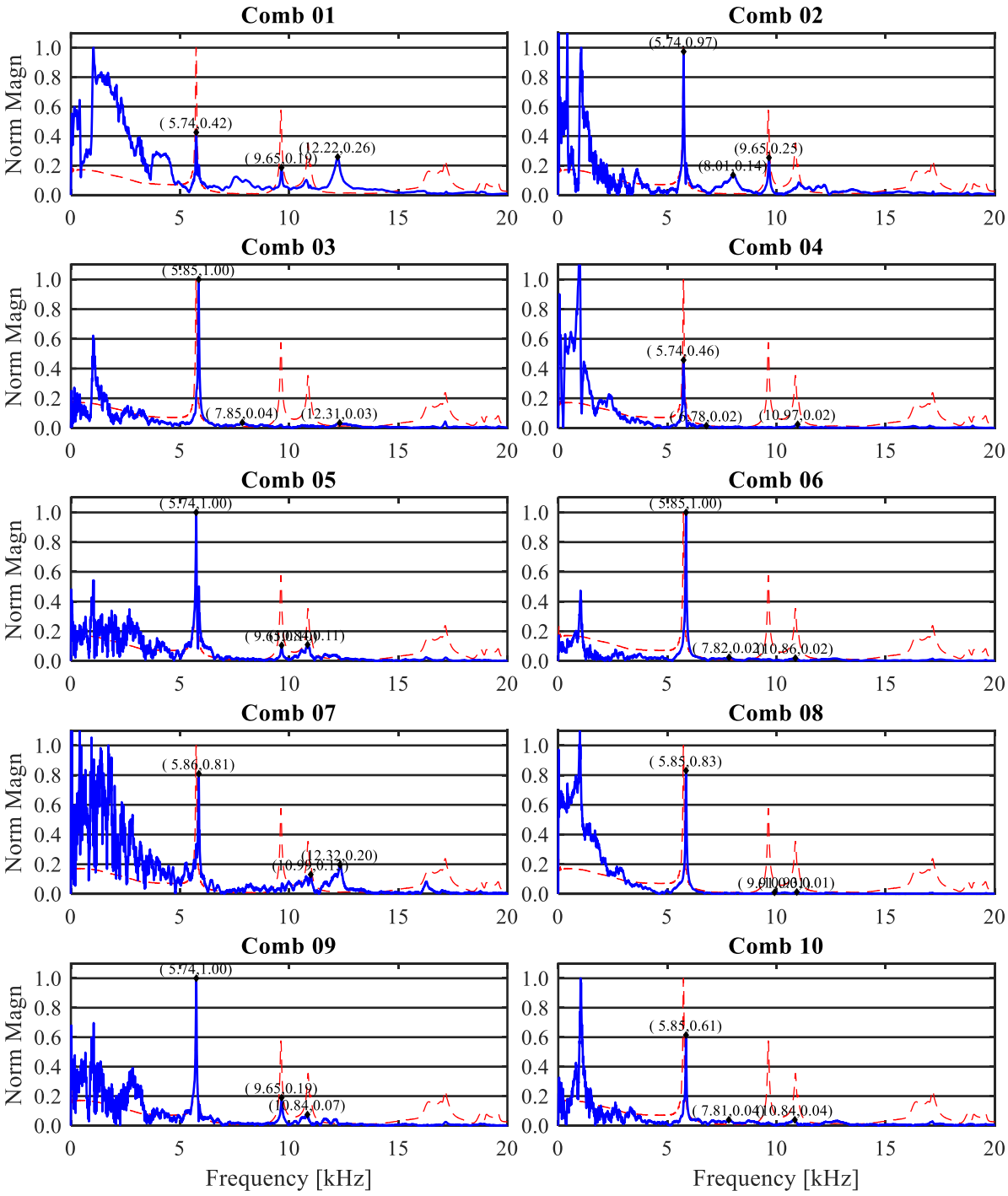

Figure 6.2 Frequency spectrum comparison for different impact and professional microphone locations. The combinations numbers refer to the table Table 5.14

Nevertheless, combination #1 will not be considered as an alternative. Theoretically, if the impulse is done exactly in the center of the cylinder only the longitudinal resonant frequency would be detected. But given it's an experimental test, the impact hardly was done at the center, therefore some of the impact energy manifested as flexural vibration. Still, this combination was the only one for which the flexural resonant frequency wasn't the highest peak.

Similarly, the test setup combination #2 wouldn't have been able to pick up the axial vibration. But due to the same reason of inaccuracy of placing the sensor exactly at the center, plus the microphone being a non-contact sensor and therefore being capable of recording sounds within certain angle direction, the axial resonant frequency was still able to be registered.

In order to prove these two previous statements and verify the best theoretical location for impact and sensor for picking up both resonant frequencies, a finite element analysis was performed. The model considered the same parameter definitions as the ones described in Figure 5.13. In this analysis, the impact was defined to be at 2/3 the radius from the center on the top surface of the cylinder with a duration of the impact of 81.9 μs (Table 5.15) and with a force function computed with the equation (5.1). The accelerations were registered in two different locations from the same top surface, at the center and at 2/3 the radius from the center at the opposite side of the impact location.

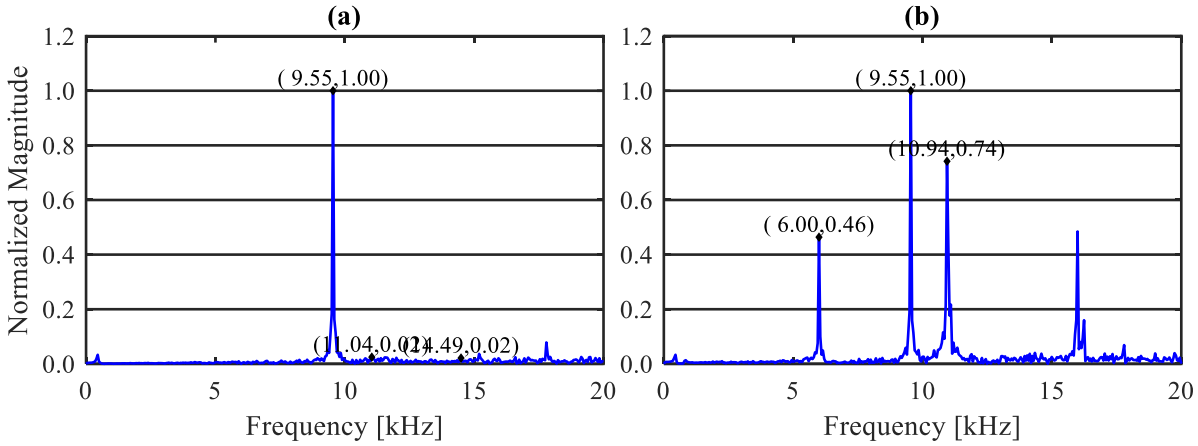

Figure 6.3 Frequency response from an FEA of a concrete cylinder with the same properties as in Figure 5.13. The simulated impact was at 2/3r from the center, and the acceleration was registered at the (a) center, and (b) at 2/3r from the center at the opposite side.

The frequency spectrum for the accelerations registered at the center (a) and at the opposite border (b) are plotted in Figure 6.3. The results were as mentioned before, with the sensor being exactly at the center the only frequency detected was the first longitudinal resonant frequency. On the other

hand, when the sensor is at 1/3 the radius from the border on the opposite side of the impact location, three main resonant frequencies were registered: First flexural (6 kHz), first longitudinal (9.55 kHz) and second flexural (10.94 kHz). The longitudinal mode shows more energy than the other frequency peaks.

In conclusion, the best alternative for performing the test is locating the point of impact and the sensor at 2/3 the radius from the center on the top surface both at opposite directions from each other.

6.1.1.3 Hammer Selection

In this section the results for testing different impulse hammer in combination with different supports (either a foam block or a table), while keeping the same microphone device and location, according to the methodology explained in section 5.2.1.2. The results will be presented with 5 figures, according to Table 6.1.

Table 6.1 Summary of the figures presented in this section (6.1.1.3). The figures referenced in this table show the results for testing with different supports and hammers.

Figure	Support	Sensor	Hammer	Test Combination	
				Table	Comb #
Figure 6.4	SP01 - Foam	Accelerometer	H01-H05	Table 5.17	[1-5]
Figure 6.5	SP02 - Table	Accelerometer	H01-H02	Table 5.17	[6-7]
Figure 6.6	SP01 - Foam	Both	H06-H11	Table 5.18	[1-6]
Figure 6.7	SP02 - Table	Both	H07-H11	Table 5.18	[7-11]
Figure 6.8	Both	Microphone	H12-H13	Table 5.19	[1-4]

Figures Figure 6.4 and Figure 6.5 shows the normalized frequency spectra for the test setups referenced in Table 5.17, for the first 5 and the last 2 test setup respectively. These two figures show only results for the accelerometer and using the Dytran Hammer introduced in earlier sections, using tips just glued to the supplied impact tips. For Figures Figure 6.4 the support used was a foam block, while for Figure 6.5 the cylinder was placed on a table, as shown in Figure 5.9.

Similarly, Figures 6.6 and Figure 6.7 shows the normalized frequency spectra obtained with the test setups from Table 5.18, for the first 6 and last 5 setup combination respectively. The test combinations results shown in these figures use two main types of impulse hammer: The Dytran hammer with the supplied impact tip drilled and glued to different steel bearing (H06-H09); And different steel bearing attached to a handle made of magnets (H10-H11). Figure 6.4 test setups used the foam block as support, while the est setups for Figure 6.5 was a table. Both figures show the

results obtained with both sensors, accelerometer and the built-in microphone from the smartphone. As described in section 5.2.1.2.

Finally, Figure 6.8 shows the normalized frequency spectra for the test setups from Table 5.19, for which the impulse "hammer" was dropping steel bearings of two different diameters directly over the top surface of the cylinder. It includes the results from the tests using the foam block and the table as supports. Only the microphone was used for these tests.

Now that the figures have been introduced, the results shown on each set of figures are going to be discussed to reach conclusions from each one.

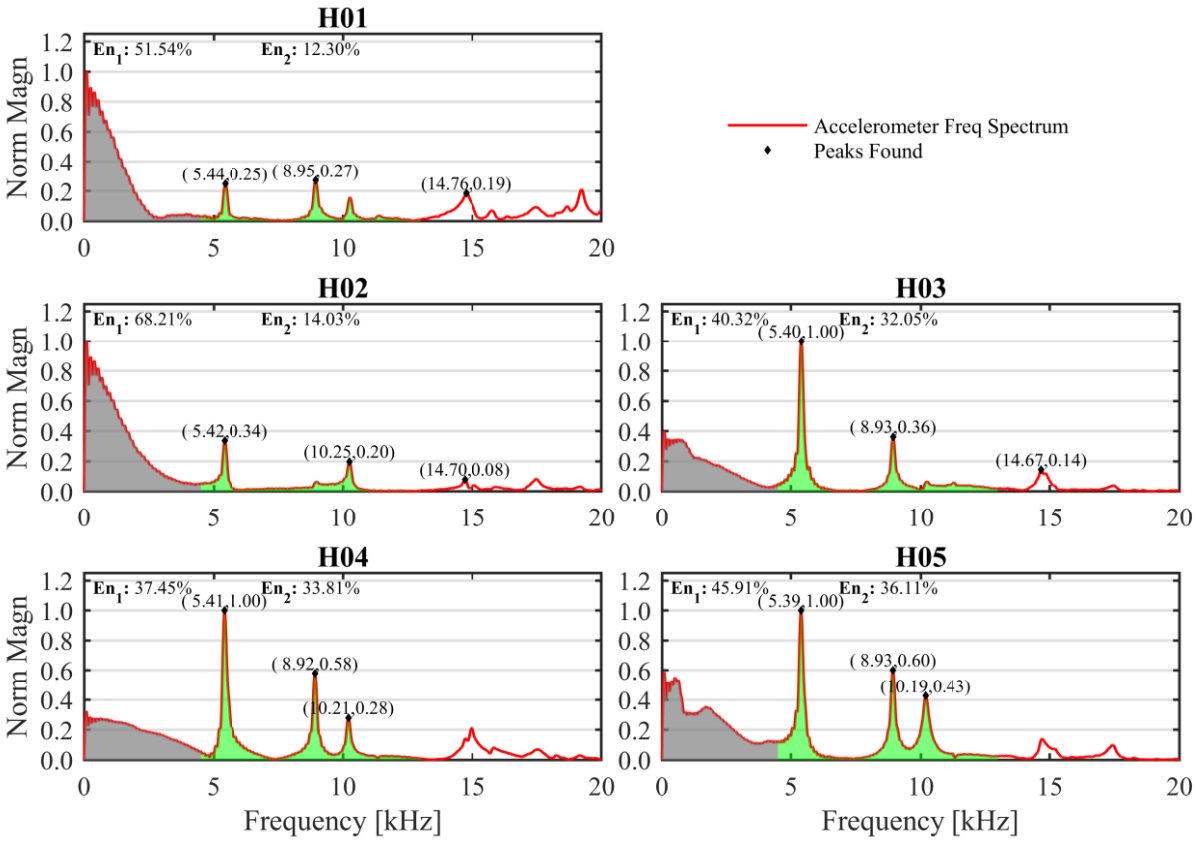

Figure 6.4 Frequency spectrum comparison for the first 5 combinations from Table 5.17. The same support (Foam), impact location, and accelerometer position are constant. The only varying condition is the impulse hammer tip according to each plot titles and the definitions from Table 5.16

The first thing to notice from Figures Figure 6.4 and Figure 6.5 is that regardless of the hammer used in all cases using the accelerometer was possible to detect both resonant frequencies, first flexural and longitudinal, and even the second flexural mode of vibration. However, a considerable

amount of energy (~50%) is focused on the low frequencies. The area below the frequency spectra for frequencies between 0 and 4.5 kHz is plotted in gray colour for both figures. Similarly, for frequencies between 4.5 and 13 kHz is plotted in green colour. The percentual area with respect to the whole area is also indicated in each subplot.

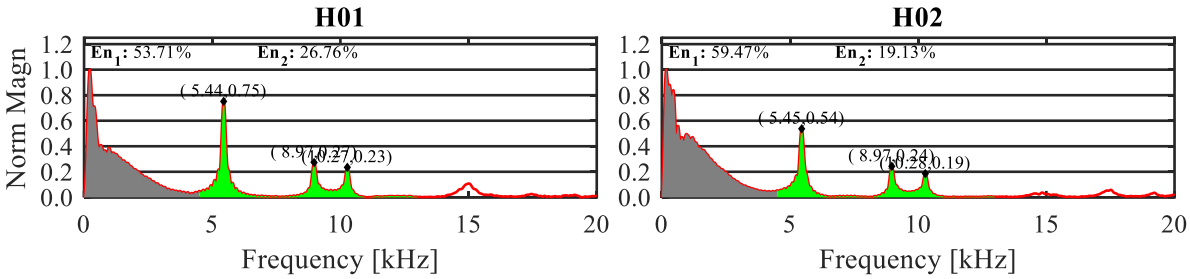

Figure 6.5 Frequency spectrum comparison for the last two combinations from Table 5.17. The same support (Table), impact location, and accelerometer position are constant. The only varying condition is the impulse hammer tip according to the titles in each plot and the definitions from Table 5.16

In Figure 6.4 is noticed how by using only the hammer with the supplied impact tip, more than 50% of the energy is contained in the low frequencies while only 12% is held in the frequency range of interest. By using steel bearings attached to the hammer the low-frequency energy amount is reduced and more is focused on the frequency range of interest, reaching 36% with the largest steel bearing diameter (H05 - Ø1/2").

Now looking at figures 6.6 and 6.7, something similar happens. First, the subplots corresponding to the Dytran Hammer (H05-H09) for the accelerometer signals for both figures will be analyzed. The accelerometer frequency spectra start focusing more energy in the frequency range of interest as the steel diameter increases, reducing the high energies in the low-frequency range. There is also an improvement by drilling the supplied tip and then gluing the steel bearing, rather than just gluing it to the supplied impact tip. This can be noticed by comparing Figure 6.4-H05 and Figure 6.6-H08, for which the same steel bearing diameter is used but attached differently. In the latter figure almost none energy is contained in the low-frequencies.

In contrast, the frequency spectra from the microphone for the tests using the Dytran hammer (Figure 6.4 H06-H09), in all cases showed high low energy in the low-frequencies, although they reduce with the increase in diameter. But the resonant frequencies were not clear enough.

When the impulse hammer made of steel bearing and a magnetic handle was used, both, accelerometer and microphone frequency spectra were reduced drastically. Although they still

showed a sharp high energy peak below 500 Hz. The two steel bearing diameter tests show clearly the flexural and longitudinal frequencies, using both sensors (Figure 6.4 H10-H11). As expected from the Hertz Impact theory introduced in section 5.2.1.2.1, the small steel bearing diameter was capable of exciting higher frequencies (Figure 6.4 H08-H10). Therefore choosing the steel bearing with larger diameter (H11 - Ø3/4") is a better option for the final test setup.

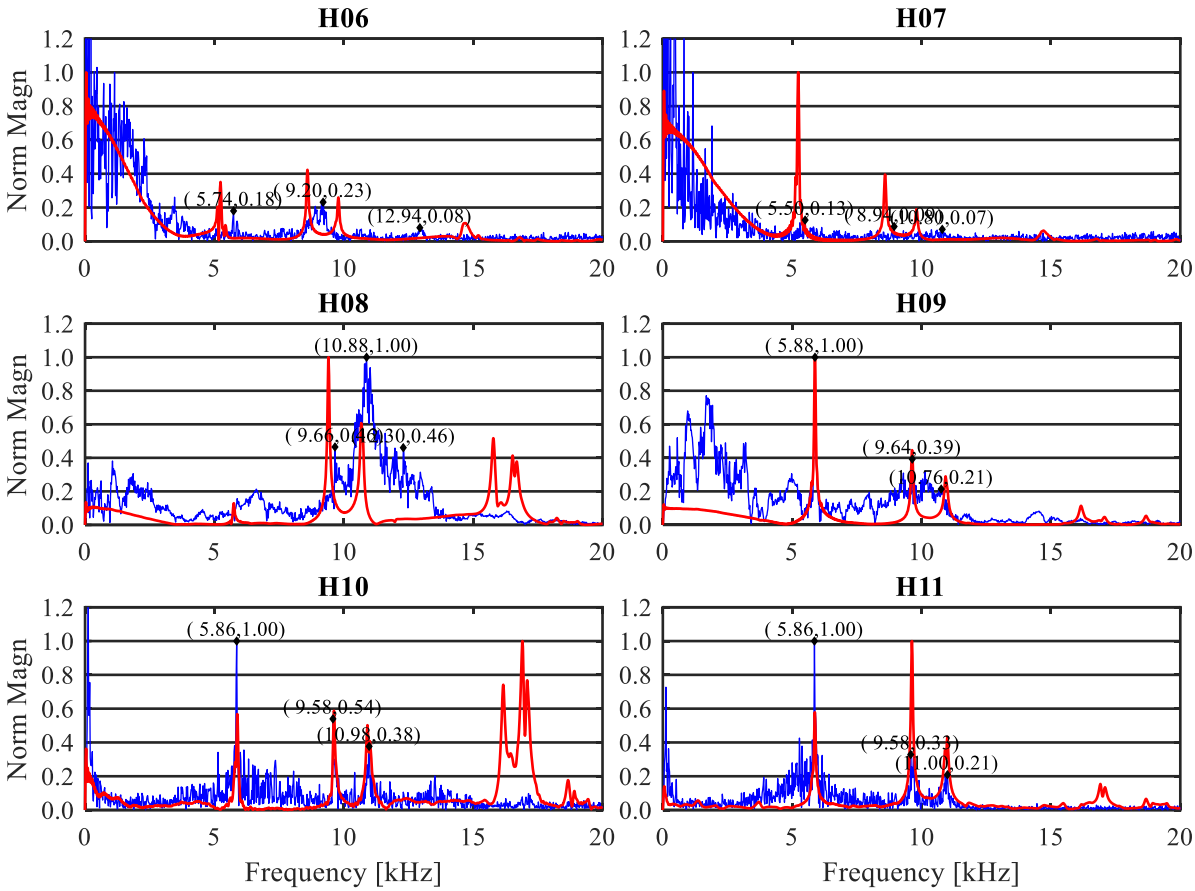

Figure 6.6 Frequency spectrum comparison for the first 6 combinations from Table 5.18. The same support (Foam), impact location, and accelerometer position are constant. The only varying condition is the impulse hammer tip according to each plot titles and the definitions from Table 5.16

For the accelerometer's signals, there is very little difference between using the foam or the table as support methods. However, with the microphone with the table as support, the low-frequency content remained high regardless of the hammer used for the test. This holds true also for impulse hammer H10 and H11 (Figure 6.7) that only involved a steel bearing dropped over the cylinder. Therefore the foam block showed to be the best way to support the cylinder when the test is done using a microphone. The reason for this is due to the table vibrating along the cylinder at lower frequencies.

Nevertheless, the frequencies could still be detected with the microphone by using the right impulse hammer. Filtering the low frequencies could help get rid of these unwanted frequencies.

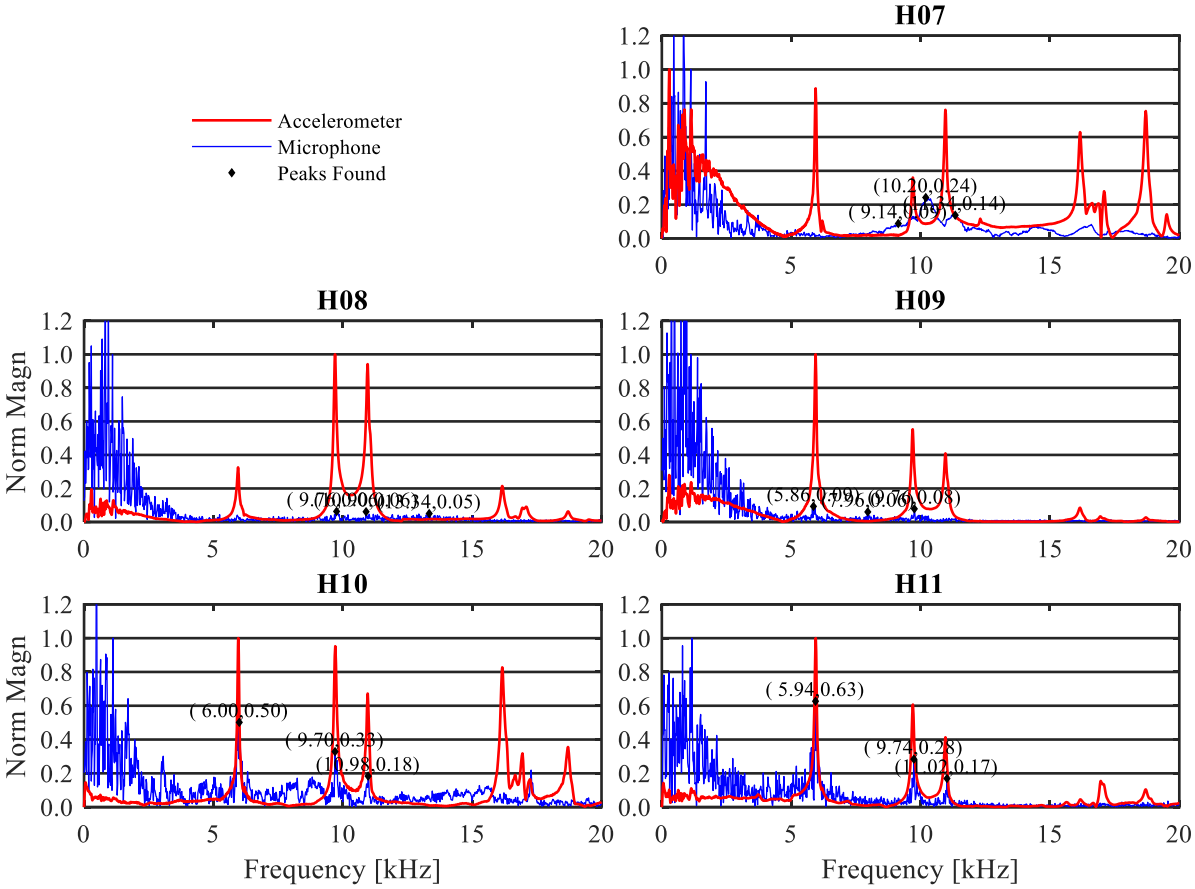

Figure 6.7 Frequency spectrum comparison for the last 5 combinations from Table 5.18. The same support (Table), impact location, and accelerometer position are constant. The only varying condition is the impulse hammer tip according to each plot titles and the definitions from Table 5.16

Finally, Figure 6.8 shows the results of using just the steel bearing dropped over the cylinder top face as the impulse. The same two different diameters from the above figure were used. The frequency spectra are considerably cleaner than using the steel bearings with the magnetic handle. Nevertheless, this testing format is ironically more complicated than using the handle. When dropping the steel bearing, it bounces on the cylinder and it can bounce on other surfaces besides the cylinder. This might produce errors while processing the signals by identifying frequencies unrelated to the concrete cylinder tested.

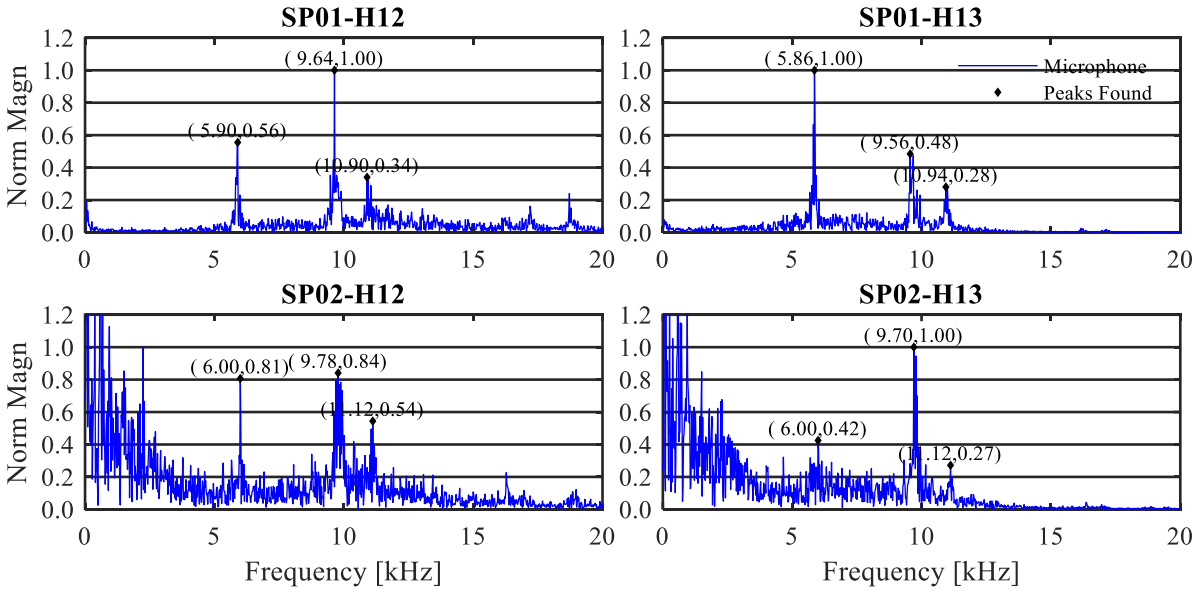

Figure 6.8 Frequency spectrum comparison for test combinations from Table 5.19. The location of the impact and the accelerometer position are constant. Although, the support and impulse "hammer" changes according to each plot titles and the definitions from Table 5.16

In conclusion, among the test setup tested, the best alternative when using the microphone for recording the resonant frequencies of a standard concrete cylinder is using the impulse hammer H11 (steel bearing of ¾" diameter with a magnetic handle). Although, another more rigid handle would be preferable. The magnetic attachment was used for being more practical with no machining involved, especially for the steel bearing being made of hardened steel.

6.1.1.4 Final Setup Test

This section will show the results from using the final test setup described in section 5.2.1.4 in all the cylinders available. The signal processing for the data available that lead to the results described below was done according to section 5.2.1.5. The section compares the differences found between using the accelerometer and the microphone as sensors for the test. It starts by comparing the frequencies differences, then showing the dynamic modulus of elasticity computed for both sensors and showing the dynamic modulus development with time. The sections end with some conclusions for the results introduced along the section.

6.1.1.4.1 Microphone – Accelerometer Frequency Differences

This section focus on the difference in terms of the resonant frequencies found between using the accelerometer or the microphone for the same test.

The percentual difference between the longitudinal resonant frequency found using the microphone and the accelerometer, normalized with respect of the accelerometer frequency are plotted as histograms in Figure 6.9. The figure shows 5 different subplots, separating the differences by batch and also one histogram that includes all the cylinder tested. Figure 6.9 does not show results for batch 100, because there were only 5 cylinders tested in this batch, therefore plotting a histogram is not relevant. Each of the subplots includes the 2.5 and 97.5 percentile values, showing between what difference percentage fall 95% of the tests performed.

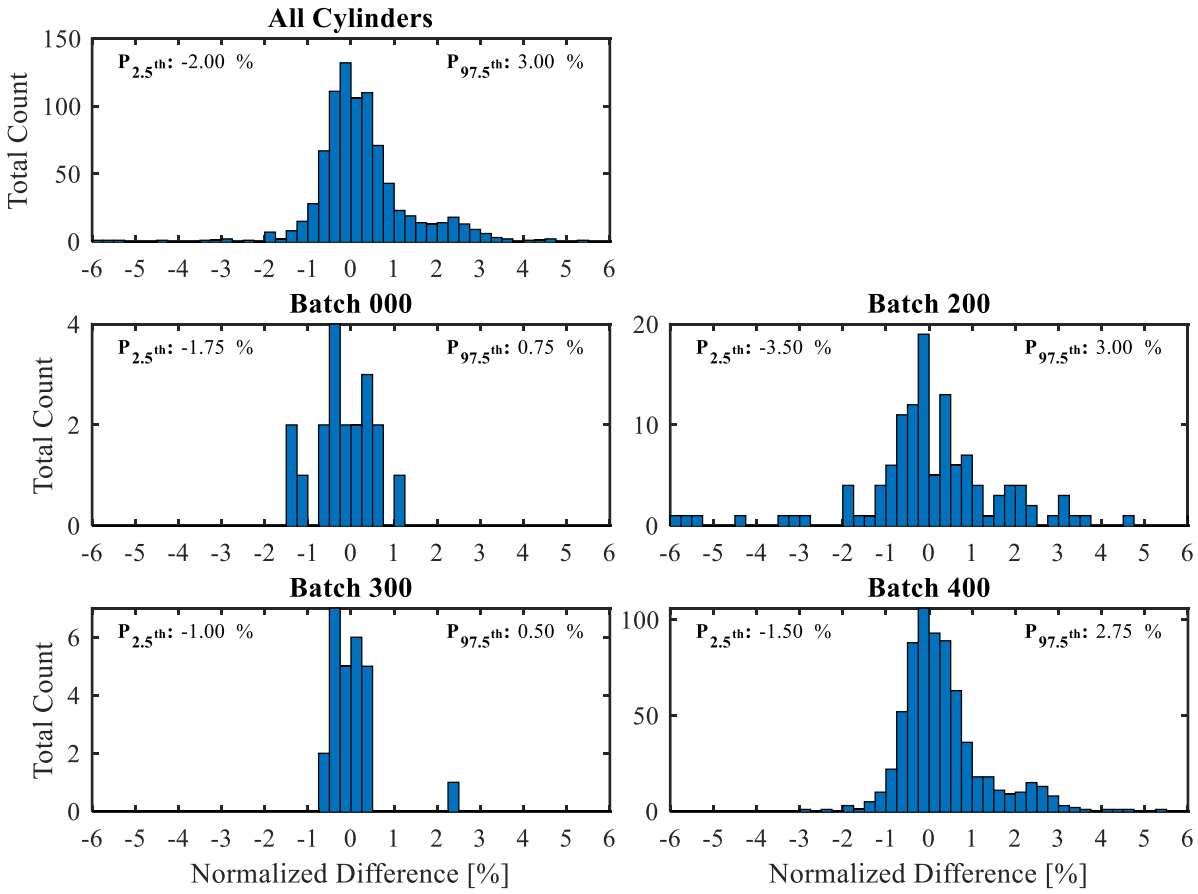

Figure 6.9 Frequency difference between longitudinal resonant frequencies found using the microphone and the accelerometer. The difference is normalized with respect to the accelerometer results and shown in percentage.

The most consisting batches with less difference between the resonant frequencies found with both sensors are batch 000 and batch 300, with errors between -1.75 and 0.75 %. The largest differences were with batch 200 with most of the cases falling between -3.5 and 3%. This is probably due to was the first batch tested with the final setup, and there might be a learning curve on how to perform the test consistently.

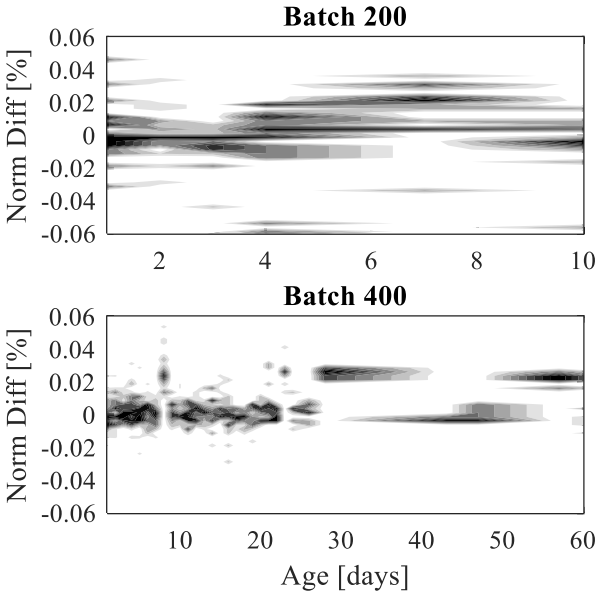

Figure 6.10 Histogram of the percentual frequency difference between microphone and accelerometer results in time for both batches tested at different ages (Batch 200 and 400).

Similarly, Figure 6.10 shows the difference histogram for the cylinder tested by batch at each age. All histograms by day are normalized by themselves. The histograms in time show that either the microphone overestimating the frequencies of the accelerometer picking lower frequencies at certain dates. In batch 200 the difference looks more spread out, but most of the shift is focused between days 6 and 8. While for batch 400, the results seemed more consistent until the 28th day with the exception of two dates. After that, the results seem to disagree more with the results from the accelerometer.

One possible cause is that after the 28th days, the cylinders in batch 400 were taken out from the moisture room, and therefore losing moisture. The moisture content might be caused by the frequency shift in those cases. More about these differences will be discussed later on when looking at the dynamic modulus comparison with time.

6.1.1.4.2 Microphone Dynamic Modulus Results

The modulus of elasticity involves the cylinder weights, therefore by comparing the dynamic modulus obtained with the accelerometer and microphone, the moisture content is considered and it would be possible to see if there is a correlation as it was mentioned in the previous section.

The average dynamic modulus of each batch computed using both longitudinal and flexural frequencies and found with both microphone and accelerometer are shown in Table 6.2. The differences between the average dynamic modulus computed by either resonant frequencies between their sensor contra part are less than 0.5% for batch 00, 200, and 300, However, batch 100 and batch 400 show larger discrepancies between sensors, with up to 6%. The difference between the dynamic modulus computed using the longitudinal and flexural frequencies, with a fix Poisson's ratio equal to 0.25 ranges -5.5 and 2%, being negative for batches 000, 200 and 300, and positive for the batches 100 and 400 (which are the batches with larger discrepancies between dynamic modulus from the microphone and accelerometer).

Table 6.2 Average dynamic moduli for all concrete batches at their maturity, computed using the longitudinal and flexural resonant frequencies measured with the microphone and accelerometer

Batch	Dynamic Modulus [GPa]							
	Longitudinal				Flexural			
	Microphone		Accelerometer		Microphone		Accelerometer	
	μ	σ	μ	σ	μ	σ	μ	σ
000	33.10	2.64	33.05	2.58	31.33	2.64	31.55	2.68
100	27.04	0.77	28.19	1.05	27.48	0.76	28.08	0.62
200*	38.68	0.35	38.80	0.41	37.78	1.19	37.89	1.71
300	36.79	1.37	36.69	1.32	34.82	1.69	34.92	1.48
400*	36.67	1.71	34.97	1.64	37.39	2.22	35.28	1.74

* The averages were computed only the data from 446th day and the 28th day for batches 200 and 400 respectively.

The batches with dynamic modulus more spread out, or in other words with a higher coefficient of variation are the batches 000 and 400 with 8% and 4.7%. The batch less spread out is batch 200 with a coefficient of variation of 0.9%.

The tests performed on the cylinders were done at different points in time. The results for the dynamic modulus using the longitudinal resonant frequency and a fix Poisson's ratio are plotted in Figure 6.11 with respect to time. These plots illustrate how to spread out are the modulus of elasticity obtained in each batch. Figure 6.11 also illustrates how the dynamic stiffness of the concrete cylinders evolve with time for the batches tested from day 1 (batch 200 and 400).

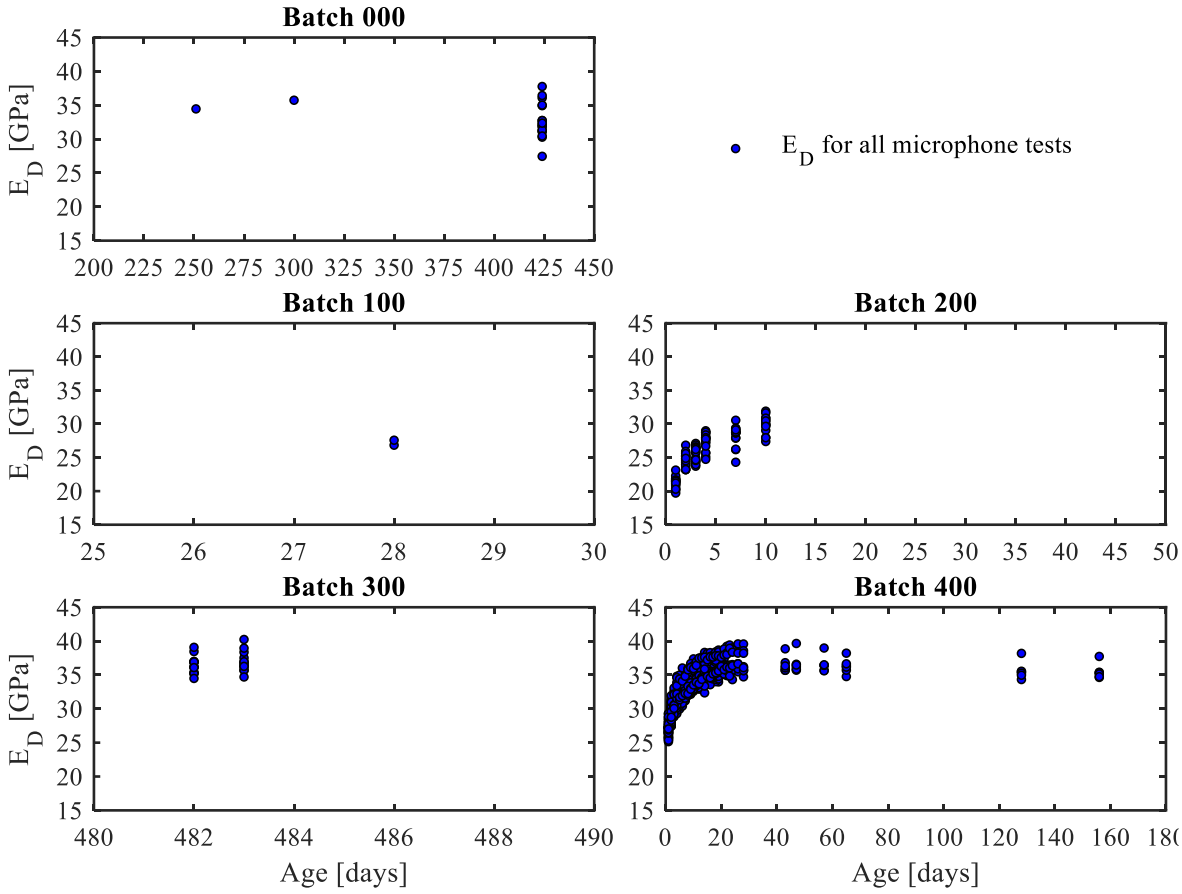

Figure 6.11 Dynamic modulus results for all tests done to all cylinders of each batch. The dynamic modulus shown corresponds to the results from the microphone.

Figure 6.12 shows the average dynamic modulus computed using both the accelerometer and microphone data per day for batch 200 and 400, along with the standard deviation at each day. These plots clarify what was seen in the previous subsection with the histograms from Figure 6.10. The dynamic modulus that shows a sudden shift at certain dates is the one computed from the accelerometer data rather than the microphone. The microphone results are more consistent with each other.

When plotting the dynamic modulus for all cylinders as a function of time with semi-log axes (Figure 6.13) it becomes clear the relationship can be linearized. The subplots in the top row from Figure 6.13 shows the dynamic modulus in time for batch 200 and the bottom row for batch 400. The left column of subplots shows all the data available for each batch, while the right column of subplots only shows the average dynamic modulus per day.

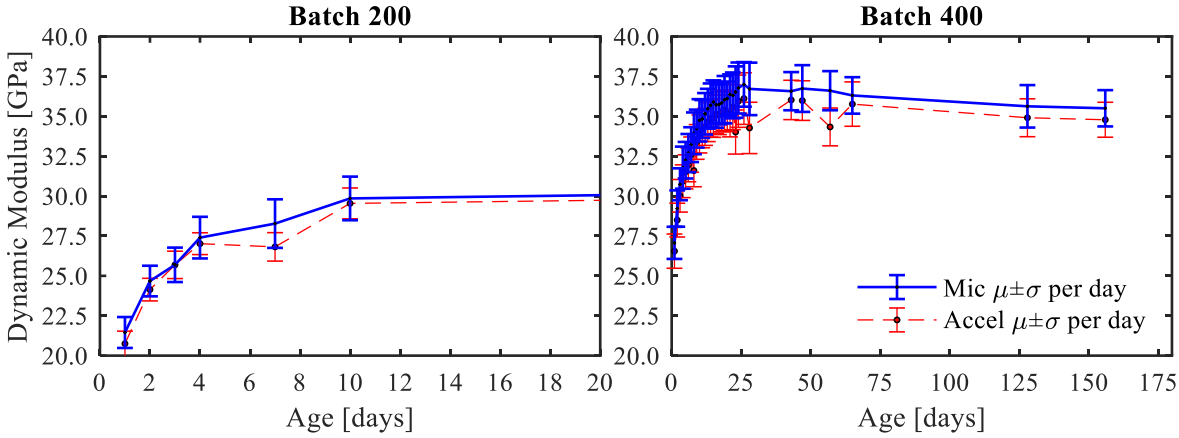

Figure 6.12 Comparison of the average and standard deviation for the dynamic modulus per day for the two batches monitored in time (Batch 200 and 400).

Performing a linear regression to each data set, (shown as black dashed lines), the fitting seems adequate with a relatively low standard error of the estimation with 1.22 and 1.25 GPa all data points from batch 22 and 400 respectively. This error represents around 5% of the estimated dynamic modulus.

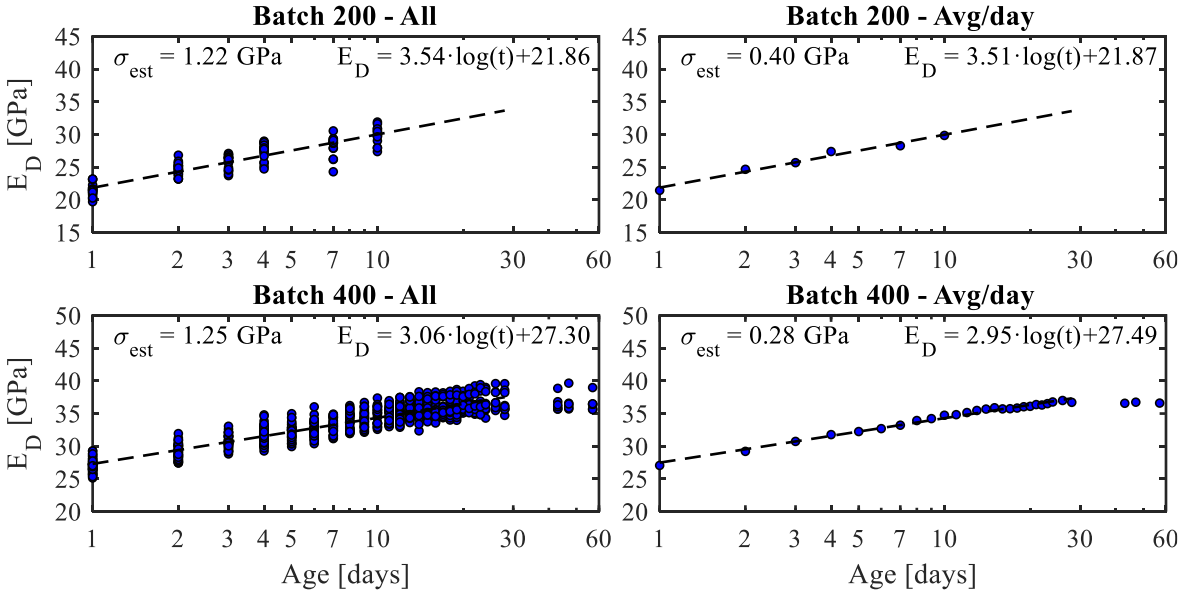

Figure 6.13 Dynamic modulus for batch 200 (top plots) and 400 (bottom plots), for all data (left plots) and average moduli per day (right plots), plotted in a semilogarithmic plot. The linear regressions and their standard errors of the estimation are also shown.

However, the standard error of the estimation 'σ_{est}' for the linear regression considering only the average value per day is significantly reduced to less than a fourth, becoming 0.4 and 0.28 GPa for batch 200 and 400 respectively. Using the average dynamic modulus per day makes more sense given that the objective is to characterize the dynamic modulus for the concrete batch and not a specific concrete cylinder.

All the linear regression equations are shown in their respective subplots in Figure 6.13. For computing the linear regressions shown above, only data from cylinders younger than 28 days old were considered. It is considered that the concrete reaches it's maturity on the 28th day, besides there was a change in curing condition at this point in time. All remaining cylinders from batch 400 were taken out from the moisture room on the 28th day.

6.1.1.5 Concluding Remarks

Once the frequency and dynamic modulus results obtained with the accelerometer and microphone has been compared and processed the following conclusions can be made:

The results between the two sensors do vary between -2 and 3%, but the central value of zero. The results are skewed, with a tendency for the microphone to obtain higher frequencies.

The results obtained from the microphone, are more consistent than the ones obtained with the accelerometer. The results from the accelerometer showed a sudden drop in the stiffness from the cylinders at certain days. This might be due to humidity changes or test inconsistencies due to the physical coupling between the accelerometer and the cylinder.

The dynamic modulus increases steadily with time with very little variation in time. The coefficient of variation for all cylinders tested each day remained constant with time. The dynamic modulus development linearly increases as a function of the logarithm of age.

When computing the linear regression with the average dynamic modulus per day, the error of the estimation is quite low, being less than 1% of the estimated values.

6.1.2 Surface Waves

The surface wave results will be discussed in this section. The ultimate results for the Rayleigh wave velocities found from the MASW tests described in section 5.2.2 for the cylinder tested are listed in Table 6.3. The table compares the results from the MASW test with the resonant test using the microphone.

Using the assumed Poisson's ratio (0.25) and the longitudinal resonant frequency, the dynamic modulus is computed. This dynamic modulus is then used to compute the P, S and R wave velocities. The difference between the velocity measurement and the one estimated with the resonant frequency is shown in m/s and in percentage.

Table 6.3 Rayleigh wave velocity results analysis in comparison with the dynamic modulus of elasticity computed with the longitudinal resonant frequencies

SN	Exp. V_R (m/s)	f_l (Hz)	v	Ed (Gpa)	V_P (m/s)	V_S^* (m/s)	V_R^* (m/s)	Diff (m/s)	Diff (%)
437	2211.7	9945	0.25	36.11	4,391.4	2,535.4	2,332.5	120.88	5.5%
438	2267.1	9795	0.25	35.71	4,367.7	2,521.7	2,320.0	52.89	2.3%
439	2322.6	9855	0.25	36.72	4,411.5	2,547.0	2,343.2	20.60	0.9%
440	2426.6	9895	0.25	35.84	4,378.0	2,527.6	2,325.4	101.18	4.2%
441	2319.8	10090	0.25	39.62	4,566.9	2,636.7	2,425.8	106.00	4.6%
442	2314.0	10035	0.25	38.60	4,478.5	2,585.7	2,378.8	64.84	2.8%
443	2267.7	9790	0.25	34.22	4,305.4	2,485.7	2,286.9	19.20	0.8%
444	2241.3	10065	0.25	37.70	4,461.4	2,575.8	2,369.7	128.36	5.7%
445	2183.0	9795	0.25	35.40	4,321.6	2,495.1	2,295.5	112.49	5.2%
446	2217.8	9950	0.25	35.37	4,373.8	2,525.2	2,323.2	105.37	4.8%
447	2321.9	9950	0.25	35.08	4,352.3	2,512.8	2,311.8	10.13	0.4%
448	2205.7	9785	0.25	34.78	4,316.2	2,492.0	2,292.6	86.94	3.9%

The average percentual difference between the two R-wave velocities is 3.4%, with the maximum difference being 5.7%. These differences are within lab results variability, and therefore they also validate the results obtained using the microphone for the resonant test.

Finding the Poisson's value that force the convergence of both Rayleigh wave velocity was attempted. However only four cases the convergence was found, with Poisson's ratios around 0.3. Most of the cylinders required a Poisson's value of 0.5 to minimize the difference, but still, the difference was not zero.

6.1.3 Ultrasonic Pulse Velocity

This section will present the results from the ultrasonic pulse velocity (UPV) tests according to the test methodology explained in section 5.2.3. Table 6.4 shows the average velocity obtained by averaging the wave velocities for all the cylinders tested on the same day with the same test setup.

The results shown in Table 6.4 were separated by the impulse frequency used, because it is known that the wave velocity in rods depends on the frequency, being higher with higher frequencies

reaching closer to the actual P-wave velocity (Wiciak et al., 2019). Nevertheless, it's not clear to observe this phenomenon in Table 6.4. The same cylinders (#443 to #448) were tested with UPV at 128 and 156 days and the wave velocity from the 128th day tested with a sinusoidal pulse of 150 kHz was 7.5% than the tests from 1 month later using a lower frequency of 54 kHz.

Table 6.4 Average wave velocities computed for the tested cylinders at each date grouped by the pulse frequency used for the test.

Age (days)	SN	Avg Wave Velocity [m/s]		
		1 Sin 54 kHz	1 Rec 54 kHz	1 Sin 150kHz
21	435	-	4,541.4	-
23	[437-439]	4,762.5	4,650.8	-
28	[440-442]	-	4,644.7	-
128	[443-448]	-	-	4,660.3
156	[443-448]	4,334.3	-	-

It is hard to see this as a direct consequence of the pulse frequency because due to the cylinder not being in a moisture room they kept loosing moisture and the cylinder stiffness might actually be reduced. However, in Table 6.5 the column "Avg E_{DL}" shows the average dynamic modulus obtained with the microphone measurements and from the 126th day to the 156th day there was actually an increase in the stiffness. This can also be observed in Figure 6.12-Batch 400 but less clear than in the table below.

Table 6.5 Average dynamic modulus 'E_D" computed using the wave velocity and a fix Poisson's ratio of 0.25. The results are compared with the respective average E_D from the resonant test for the same cylinders and the same testing date.

Age (days)	SN	Avg E_D from V_P [GPa] Fix ν=0.25			Avg E_{DL} [GPa]	Norm Difference [%]		
		1 Sin 54 kHz	1 Rec 54 kHz	1 Sin 150kHz		1 Sin 54 kHz	1 Rec 54 kHz	1 Sin 150kHz
21	435	-	38.75	-	34.70	-	11.7%	-
23	[437-439]	42.61	40.67	-	35.03	21.6%	16.1%	-
28	[440-442]	-	40.54	-	36.25	-	11.8%	-
128	[443-448]	-	-	40.15	34.88	-	-	15.1%
156	[443-448]	34.79	-	-	35.17	-1.1%	-	-

The dynamic moduli shown in Table 6.5 were computed using the equation (5.13) considering a Poisson's ratio equal to 0.25. This is the same Poisson's ratio assumed for computing the dynamic modulus of elasticity with the longitudinal and flexural resonant frequency. Nevertheless, the values

obtained using the assumed Poisson's ratio varies greatly from the resonant method results, with differences over 20%.

If both equations to compute the dynamic modulus, the one using the resonant frequency (4.3) and the UPV (5.13) are equal to each other, the Poisson's ratio can be obtained. Using the cylinder longitudinal resonant frequencies and their P-wave velocities, the Poisson's ratios from Table 6.6 are obtained. The dynamic modulus resulting from solving the equation are also shown in Table 6.6.

Table 6.6 Average Poisson's ratio *"ν"* and dynamic modulus *"E_D"* per pulse and age, computed by solving for the Poisson's ratio that makes both elastic moduli from the UPV and Resonant Test equal.

Age (days)	SN	Avg Dynamic Poisson's Ratio			Avg Dynamic Elastic Modulus [GPa]		
		1 Sin 54 kHz	1 Rec 54 kHz	1 Sin 150kHz	1 Sin 54 kHz	1 Rec 54 kHz	1 Sin 150kHz
21	435	-	0.30	-	-	34.99	-
23	[437-439]	0.32	0.31	-	35.64	35.34	-
28	[440-442]	-	0.30	-	-	36.55	-
128	[443-448]	-	-	0.30	-	-	35.24
156	[443-448]	0.24	-	-	35.13	-	-

Table 6.6 shows that the dynamic modulus is actually higher than the one assumed, being close to 0.3. However, this is true for the ages of up to 128 days. When the concrete has matured long enough the dynamic Poisson's ratio reduced to 0.24, closer to the value assumed. This is in accordance with what was reported by (Jones, 1949; Neville, 1996; Simmons, 1955).

Table 6.7 Coefficient of variation of the Poisson's and Dynamic Elastic Moduli computed from Table 6.6

Age (days)	SN	COV Dynamic Poisson's Ratio			COV Dynamic Elastic Modulus [GPa]		
		1 Sin 54 kHz	1 Rec 54 kHz	1 Sin 150kHz	1 Sin 54 kHz	1 Rec 54 kHz	1 Sin 150kHz
21	435	-	2.4%	-	-	0.1%	-
23	[437-439]	1.4%	5.1%	-	0.1%	0.9%	-
28	[440-442]	-	2.2%	-	-	1.8%	-
128	[443-448]	-	-	3.7%	-	-	2.5%
156	[443-448]	10.7%	-	-	2.8%	-	-

The coefficients of variation for the Poisson's ratio and dynamic modulus are shown in Table 6.7. The first thing to notice is that the variation in the Poisson's ratio is not neglectable with most of the cases being between 2 and 5%, and with a maximum value of 10% for the most matured concrete.

However, the effect of the Poisson's ratio variability has less impact on the dynamic modulus with a variation of less than 2% in most cases and the highest being almost 3%.

6.1.4 Concluding Remarks

After analyzing the results from the resonant test, Rayleigh wave velocity and P-wave velocity in the concrete cylinders, the following conclusion can be made:

The test methodology using a microphone showed good results and good consistency with a deviation from their own linear tendency in a semilogarithmic plot of less than 1%. The consistency is better than using accelerometers, probably due to coupling effects.

Due to the linearity in a semilogarithmic plot, the dynamic modulus could be estimated for future ages by monitoring its development during the first 3 days of tests.

The Poisson's ratio assumed for computing the dynamic modulus with the resonant frequency (ν=0.25) was low. A higher value could have been used. This was found by solving for the Poisson's ratio using the dynamic modulus equations as a function of the longitudinal resonant frequency and the P-wave velocity. The Poisson's ratio found was around 0.3 for ages between 21 and 128 days old.

Monitoring the resonant frequencies along with the P-wave velocity in concrete from day 1 would have been helpful to monitor the Poisson's ratio development with age. However, the UPV test although a simple test, it requires more time than the resonant test using the microphone, demanding to invest significantly more time during the test phase. It wouldn't be practical as a daily day monitoring technique for large batches of concrete cylinders.

Regarding the Rayleigh wave velocity results. They reinforce the validity of the frequencies found with the resonant test with a convergence of ±5%, using the assumed Poisson's ratio (0.25). When it was possible to found the Poisson's value that force the convergence, Poisson's ratios around 0.3 were found.

6.2 Static Tests

The static test results, from the compressive and modulus of elasticity, will be presented in this section. The average values by batch, the development on time of these properties will be shown and discussed.

6.2.1 Compressive Strength

The compressive strength was tested as discussed in the respective section (5.3). This section will only present the results regarding the ultimate compressive strength for each tested cylinder. The average compressive strengths by batch are given in Table 6.8. For batch 200 and 400, the values shown correspond to the last day at which the concrete cylinders were tested.

Table 6.8 Average, standard deviation an coefficient of variation (COV) for the compressive strength for all concrete batches

Batch	*f'c* [MPa]		
	μ	σ	COV
000	32.89	8.67	26%
100	35.67	0.12	0%
200[11]	43.86	1.46	3%
300	43.71	2.85	7%
400[12]	46.25	2.27	5%

The most inconsistent batch was #000 with a coefficient of variation over 25%. The concrete cylinders from batch 000 were not cast by the author of this work, they were donated from another research. Therefore, this might be evidence that actually these batch of concrete cylinder actually contained more than one concrete mix. The other anomaly happened with batch 100. These cylinders were also lent from another research project belonging to Wiciak, Piotr as it was previously mentioned at the beginning of Chapter 5. These cylinders were not crushed, they were only loaded to the 40% of the estimated f'c. So it expected the variability of the f'c is so low given it was fixed during the tests. Besides these two batches, the rest have consistent results with the largest coefficient of variation of 7%.

The concrete cylinders from batches 000, 100 and 300 were tested on the same day for each batch. On the other hand, the concrete cylinders from batch 200 and 400 were tested under compression at different ages, starting from 1 day after casting, and up to the 447th day for batch 200 and on the 156th day for batch 400. The average compressive strength '*f'c*' per day for the concrete cylinders from both batches is plotted in Figure 6.14. The left column of subplots in the figure is plotted with both axes linearly scaled, while the right column of subplots the time axis is in the logarithm scale.

[11] Only matured cylinders from batch 200 were considered (Age 447 days).
[12] Only matured cylinders from batch 400 were considered (Age 156 days).

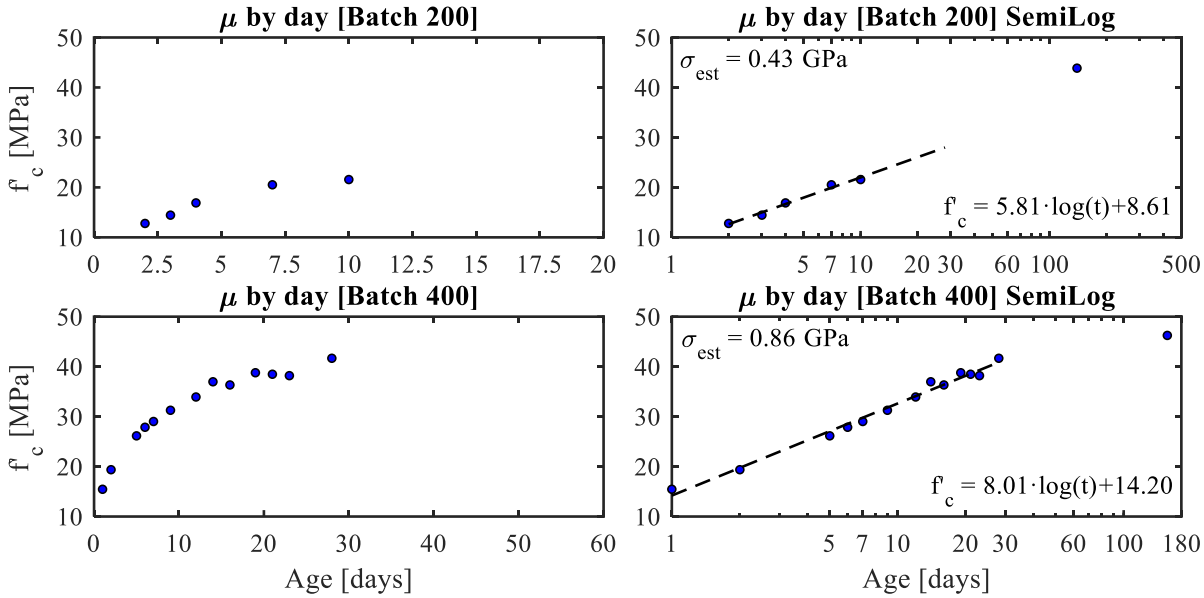

Figure 6.14 Average compressive strength *"f'c"* development with age for batch 200 (top) and batch 400. Left plots have a linearly scaled axis, while the right plots have a semilogarithmic axis. Linear regressions with its standard error of the estimations are also shown.

The compressive strength just as the dynamic modulus follows a linear trend in the semilogarithmic scale. This is already taken into consideration by (ASTM_C918, 2013) to use early age measurements of the compressive strength to estimate the ultimate compressive strength on the 28th day. The method proposed by the ASTM C918 takes into consideration curing conditions like the temperature for the computation. By doing a linear regression to both data with ages younger than 28 days old, the error or deviation from the data linearity can be estimated. The standard errors of the estimations are 0.43 and 0.86 GPa for batch 200 and 400. This error is more than 3 times the estimation error obtained from the linear regression to the dynamic modulus of elasticity. These errors relatively with themselves represent between 1 and 6 % of error.

The increase in the estimation error might be due to the compressive strength being more susceptible to additional factors than the dynamic modulus through the resonance method, plus being more sensitive to those factors. For example, the ultimate compressive strength would be considerably affected by small imperfections in the cylinder surfaces that might induce stress concentrations on the cylinder, instead of evenly spreading the stress along the whole surface. Another factor affecting the *f'c* more than to the E_D are the cavities inside the concrete due to the strain level used in each test.

6.2.2 Young's Modulus

The static modulus of elasticity obtained in accordance with the standard and the description and particularities explained before in section (5.3) will be presented in this section. The average modulus of elasticities by batch with their respective standard deviation and coefficient of variations are presented in Table 6.9. Similarly, as with the compressive strength results, the average of the modulus of elasticity for batch 200 and 400 were computed for the last day tested for each, this is the 447th day and the 156th day old respectively.

Table 6.9 Average, standard deviation an coefficient of variation (COV) for the static elastic modulus for all concrete batches

Batch	*E* [GPa]		
	μ	σ	COV
000	9.25	2.47	27%
100	8.83	0.41	5%
200	11.82	0.26	2%
300	11.17	0.38	3%
400	10.46	0.36	3%

The elasticity moduli obtained from the test specimens (Table 6.9) are considerably lower (between 1/3 and ½) of the typical expected values. As mentioned in 2.7.3 the elastic modulus depends on many factors including the test setup and machinery used for loading the specimen (Neville, 1996). The low values obtained from the tests were due to the lack of direct strain measurement on the test specimens, and using the load frame built-in extensometer instead.

However, this is not relevant for the purpose of this work, because the final conclusions still propose the relationship with the static modulus should always be calibrated with respect to the desired concrete mix and test setup. Besides, the results obtained with the displacement gauges from the MTS machine, they are consistent with themselves, which can be corroborated with Figure 6.15. In this figure, a clear trend between the elastic modulus and the age of the cylinder can be seen.

The coefficient of variation for batch 000 is considerably large (over 25% as well). This reinforces the hypothesis mentioned in the previous subsection (6.2.1), about the concrete cylinders being made from two different concrete batches. Nevertheless, for the remaining batches, the results are pretty consistent with themselves. The coefficient of variation (COV) for all of them is within 2 and 5 %. The average modulus of elasticity for batch 200 is larger than for batch 400. However, the compressive strength for batch 200 is lower than for batch 400. This is in agreement with what was

stated in Chapter 1 regarding the Young's modulus and f'c not having a unique relationship, but it depends on many factors.

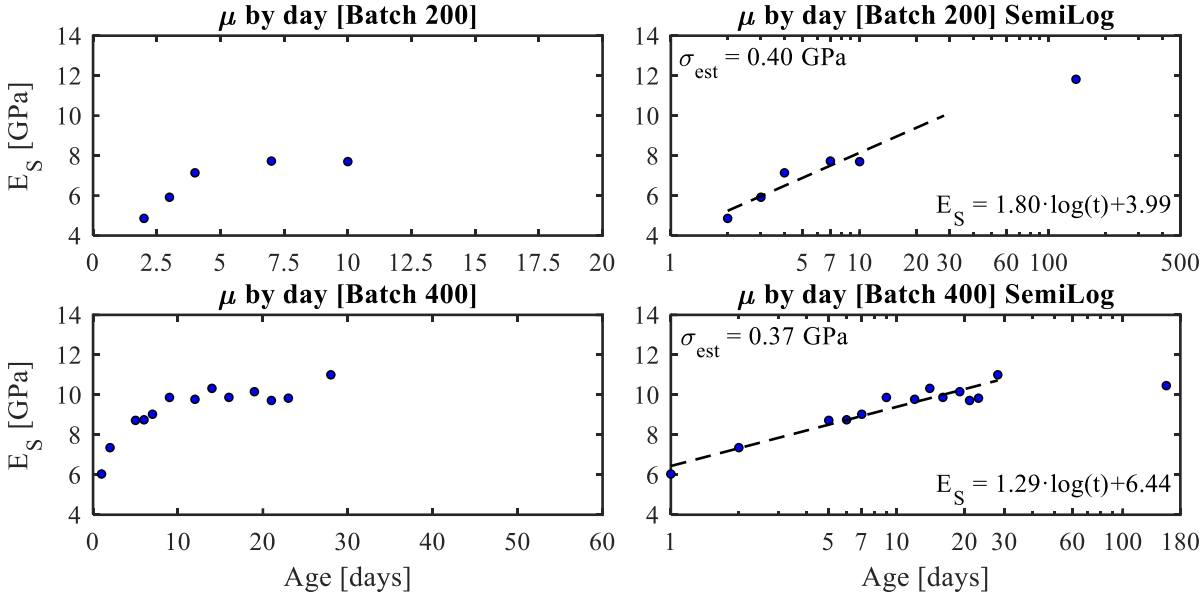

Figure 6.15 Average static elastic modulus *"Es"* development with age for batch 200 (top) and batch 400. Left plots have a linearly scaled axis, while the right plots have a semilogarithmic axis. Linear regressions with its standard error of the estimations are also shown.

The standard error of the estimation of the average static modulus as a function of the age, using the semilogarithmic axis is relatively low, 0.4 GPa for batch 200 and 0.37 for batch 400. These estimation errors are lower than for the linear regressions of the compressive strength. Although compared with the range of the obtained static modulus, they represent similar errors between 3 and 8% of the estimated values. Once again, the linear regressions were made considering only the data for tests at ages below the 28th day.

6.2.3 Concluding Remarks

After reviewing the results from the static test, the following conclusions can be made:

The modulus of elasticity computed has lower values than the expected ones due to the usage of the compression machine internal displacement gauges instead of gauges directly attached to the concrete specimens. But despite the lower values, the results are consistent with each other. This factor does not affect the final objectives of this work.

Both, the compressive strength and the Young's modulus follow a linear trend in a semilogarithmic axis. Therefore, a simple linear model can be used for forecasting their values.

However, it's a complicated task to use the dynamic values to estimate the ultimate compressive strength of concrete, due to higher variability in the latter due to factors that do not affect the dynamic properties as much as the compressive strength, such as cavities inside the cylinders or imperfections in the surfaces.

6.3 Results Comparisons

This section will correlate the results already shown individually with each other. Three correlations will be made: Static modulus of elasticity and the compressive strength, Static modulus with the dynamic modulus, and finally correlation of both to obtain a forecasting methodology using the linearity of both relationships to estimate the static modulus using only early ages dynamic measurements.

6.3.1 Static Moduli – Compressive Strength Comparison

First, the static modulus of elasticity will be compared with the compressive strength of each tested cylinder. The relationship between these two results for all batches is plotted in Figure 6.16, each batch with a different marker. Given that all data visually follows the same trend, all data points were used to curve fit the most used empirical equation used for relating the static modulus and compressive strength ($E_S = c_1 \cdot \sqrt{f'c}\ [MPa]$). Table 2.3 presents several different relationships proposed for the static modulus and the compressive strength. The resulting fitting coefficient is equal to *"1684"* and the standard error of the estimation is equal to 0.93 GPa. This error represents a relative error between 7 and 15% of the estimated values.

Although this estimation might be good enough for practical purposes, a fine-tuned relationship can be obtained by curve fitting for only specific concrete batches. Figure 6.16-Left shows the curve fitted equation plotted on a larger scale focusing on the data points. On the other hand, Figure 6.16-Right shows a zoom out of the same image, where four proposed relationships from Table 2.3 are plotted. These relationships correspond to the ones proposed by the ACI and CSA building codes for normal concrete and their equations that also depend on the concrete density. The density used for the plotted lines was the average density for all cylinders at the moment of the compressive test (2,284 kg/m3).

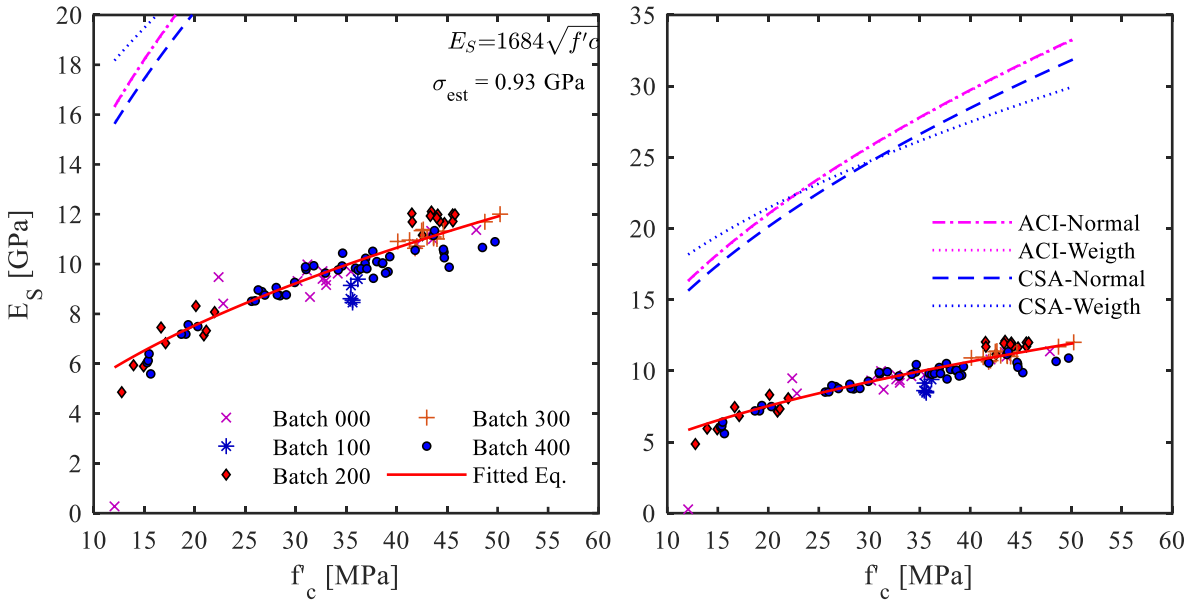

Figure 6.16 Static modulus compressive strength relationship. The left plot shows all the individual data gathered for each batch along with a fitting equation and it's standard error od the estimation. The right plot shows equations given by different building codes as standard

When the experimental results on this study are compared with the other four proposed E_S-$f'c$ relationship equations proposed by the ACI and CSA, it is when is evident that the Young's moduli obtained on this study are way below the expected values (between 1/3 and ½ the values from the building code relationships). As it was mentioned in a previous subsection (6.2.2), the low static elasticity moduli are due to the lack of direct measurement of the tests specimen strains and using the load frame built-in extensometers instead (5.3.1).

6.3.2 Static Moduli – Dynamic Moduli Comparison

Now the static modulus of elasticity will be compared with its dynamic counterpart. The relationship between these two parameters for each one of the tests has been plotted in Figure 6.17, using different markers for each batch. In Table 2.4 different relationships between the static and the dynamic moduli made by several researchers were presented. Among them, most of them follow a linear behaviour. Given this predominance, and how the data is distributed in Figure 6.17, all the data points were used to compute a linear regression with the form of $E_D = c_1 \cdot E_S - c_2$ *[GPa]* where the dynamic modulus is a function of the static modulus.

All data is distributed together, so all the data will be included for the linear regression. In Figure 6.17-Left the linear regression is plotted as a red continuous line. The resultant fitted equations is: E_D

$= 0.38 \cdot E_S - 3.35$. The standard error of the estimation is relatively high (1.07 GPa) representing between the 8 and 17 % of the estimated value. However, a better regression could be made by only using the data for the specific concrete mix for which the regression is intended for.

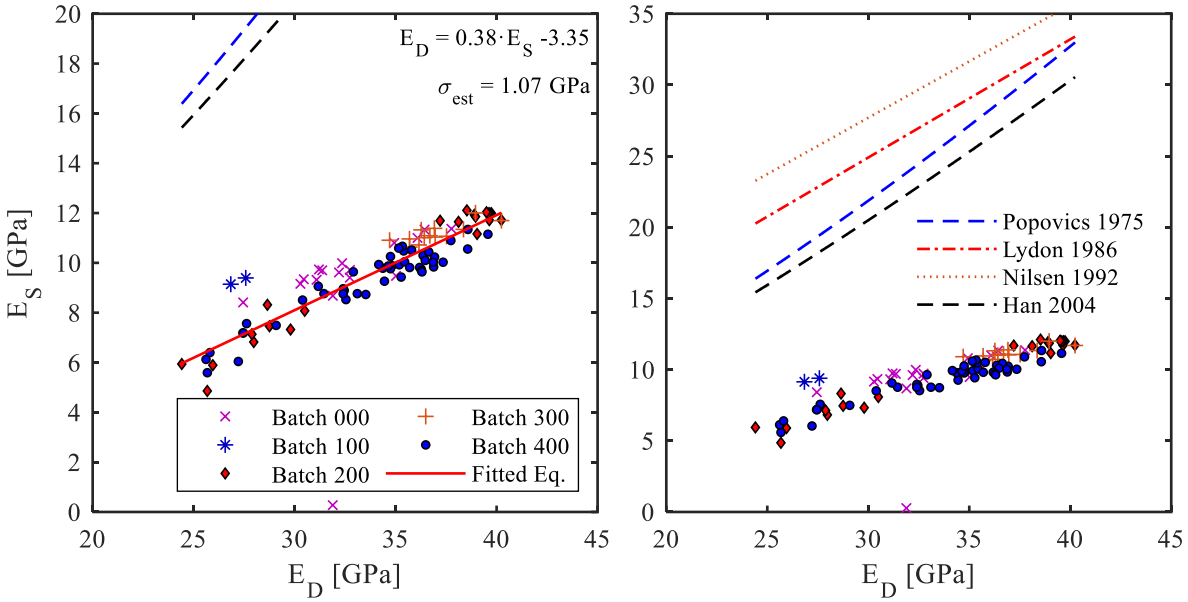

Figure 6.17 Static and dynamic moduli relationship. All individual tests for all batches are plotted. The left plot shows what data points correspond to which batch. And the right plot shows other *E_S-E_D* relationships proposed by other researchers.

Due to the low values of the obtained static modulus which were discussed in section 6.2.2, it is expected that the relationship between the static and dynamic moduli found in this study, has a lower ratio than the proposed by other researchers. In Figure 6.17-Right, the same data is plotted zoomed out, to show the other 4 proposed relationships from Table 2.4. From these other relationships, the ones proposed by (S. Popovics, 1975) and (Han & Kim, 2004) are not strictly linear, although when plotted they follow a linear-like behaviour within the range of interest. The equations proposed by (S. Popovics, 1975) are also a function of the density, and the equation from (Nilsen & Aitcin, 1992) depends on the Poisson's ratio. To plot these two relationships an average density of 2286.3 kg/m^3 and a Poisson's ratio of 0.3 were used.

From the data plotted in Figure 6.17, the relationships for the cylinder of batch 100 are the ones farther from the mean values. This is believed to be a direct consequence of testing batch 100 with another methodology, using at least twice the load rate during the static tests, as can be seen in Table 5.25.

6.3.3 Forecasting of Elastic Modulus

The forecasting methodology proposed is based on the linearity of both E_S-E_D relationship (6.2) and E_D-log*(Age)* (6.1). Fusing both equations together results in a static modulus equation (6.3) as a function of the dynamic modulus and the age "*t*". The dynamic modulus for a concrete cylinder batch is assumed to be normally distributed with mean "μ_{Ed_t}" and standard deviation "σ_{Ed_t}" at age "*t*". Similarly, the E_S-E_D relationship has a standard estimation error which is constant within the fitting range. This error represents an intrinsic model error or standard deviation "σ_{St}" of the relationship.

$$E_D(t) = a_1 \log(t) + a_2 \tag{6.1}$$

$$E_S(E_D) = b_1 E_D + b_2 \tag{6.2}$$

$$E_S(E_D, t) = b_1 E_D(t) + b_2 \tag{6.3}$$

The average and the standard deviation of the dynamic elastic moduli for the cylinders tested per day are meant to be used on the methodology proposed. The reasoning for this is that the end goal is to forecast the Young's modulus of the concrete batch rather than for a single cylinder. Performing a linear regression to the mean and standard deviation per day in agreement with the equation (6.1) yields two forecasting equations for the dynamic elastic modulus; One for their mean, and other for its standard deviation.

Using these two resulting equations, the expected mean "μ_{Ed_28}" and standard deviation "σ_{Ed_28}" for the dynamic modulus for the concrete batch on the 28th day can be estimated. These two dynamic parameters (μ_{Ed_28} , σ_{Ed_28}) can be translated into static values (μ_{s_28} , σ_{s_28}) using the E_S-E_D relationship equation (6.2). However, for converting the dynamic standard deviation into a static value, the coefficient b_2 is disregarded, (i.e. it is multiplied only by b_1). This follows the theory of functions of random variables.

Assuming the random variables (dynamic and static modulus) are normally distributed, then the equation (6.2) distribution is also normal. The confidence interval for the expected static modulus would be computed with the inverse cumulative normal distribution. For computing the confidence interval, the expected standard deviation needs to be ad up to the intrinsic model error of the E_S-E_D relationship "σ_{St}", i.e. σ_{St}+ σ_{s_28}.

For the practical application of the forecasting methodology presented, it is needed to know beforehand the E_S-E_D relationship. It is relatively easy for a concrete supplier company to developed

the relationship for the concrete mixes that they typically sell. Given that the relationship E_S-E_D is considered to be independent of concrete maturity and other factors, (BS_8110_2, 1985; Han & Kim, 2004; Lydon & Balendran, 1986; Nilsen & Aitcin, 1992; S. Popovics, 1975) depending mostly on the concrete mix proportions and the type of aggregates. Then, the relationship can be estimated by just taking measurements of their concrete mixes at the ages of 1 and age 28 days old to gather data with both low and high elastic moduli values.

Forecasting procedures for the concrete compressive strength using static early age measurements have been already standardized by the (ASTM_C918, 2013), however, there is no equivalent standard for the Young's modulus neither with the static or dynamic values. The ASTM C918-13 follows a similar procedure to the one proposed in this subsection with a linearized semilogarithmic equation, but instead of using just the concrete maturity, it uses an index to account for curing factors such as the temperature.

The methodology proposed in this research assumes that the relationship E_S-E_D is independent of environmental and curing factors, and it only depends on the concrete mix properties such as the aggregates or the water-cement ratio, etc.

6.3.3.1 Practical Example

To illustrate the methodology proposed and asses how good the estimation obtained is, the same data used for this research is going to be used, specifically the data from batch 200 and 400. The calibration of the E_S-E_D model will be done using only the data from both extreme testing dates. For the monitored data, only the data from the first 3 days of testing will be included for the static modulus forecasting. The estimated static modulus will be compared with the actual value from the measurements. The static modulus from batch 200 will be estimated for the 10^{th} day because there are only static results available for this age on this batch. The E_S for Batch 400 will be estimated for the 28^{th} day. And finally, the estimation error will be computed.

The first step is to obtain the relationship between the static modulus 'E_S' and the dynamic modulus 'E_D'. Given a linear relationship is expected, only the data from the first and last dates for each batch are going to be used for the linear regression. This is the first and the 10^{th} day for batch 200, and the first and the 28^{th} day for batch 400. The resulting linear regression equations for the E_S-E_D relationships are the following:

$E_S = 0.35\ E_D - 2.83$ for batch 200; And $E_S = 0.41\ E_D - 4.54$ for batch 400.

These relationships are plotted in Figure 6.18.

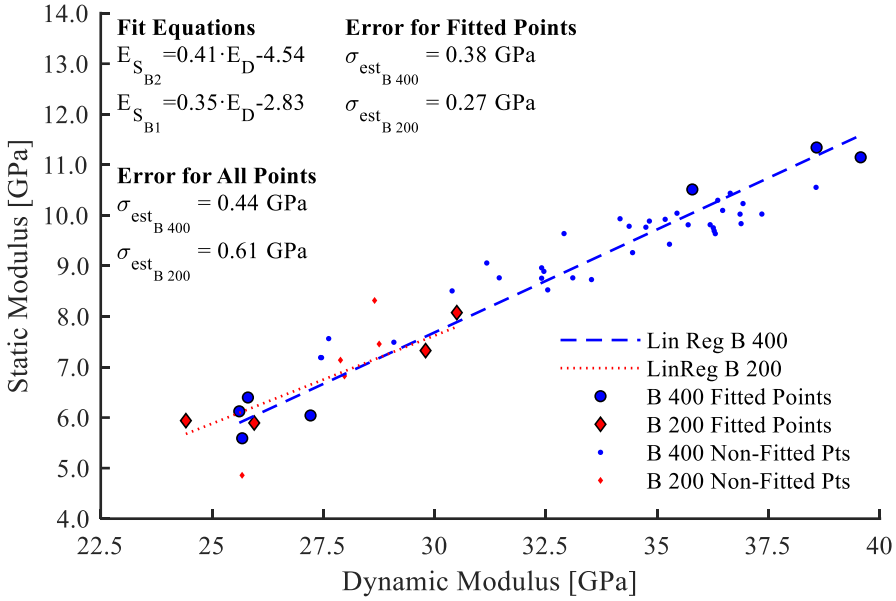

Figure 6.18 Calibration of the E_S-E_D relationship using data from batches 200 and bat400. For batch 200 data from 1st day and the 10th day was used. While for batch 400 data for the 1st day and 28th day.

The errors of the estimations for the fitted points for both batches are 0.27 and 0.38 GPa for each batch respectively. This error represents less than 5% of the estimated static values. This is errors are between ¼ and 1/3 of the linear regressions considering all the cylinder tested in this study (~1 GPa - Figure 6.17). The errors for the same linear regressions shown in Figure 6.18 but computed for all data in the batch 200 and 400 are 0.61 and 0.44 GPa respectively. These errors are still around half the errors for all batches. Therefore there is an improvement in the accuracy of the forecasting by calibrating the E_S-E_D relationship for a specific concrete mix.

The second step is to compute the linear regression for the mean and standard deviation for the dynamic modulus measurements per day, using the first 3 days of measurements (Figure 6.19). The results for fitting linear equations for the mean and standard deviations for both batches are listed below:

$E_{D\_200} = 3.95 \log(t) + 21.58$ and $\sigma_{D\_200} = 0.09 \log(t) + 0.95$ for batch 200; and

$E_{D\_400} = 3.32 \log(t) + 27.03$ and $\sigma_{D\_400} = 0.02 \log(t) + 1.04$ for batch 400.

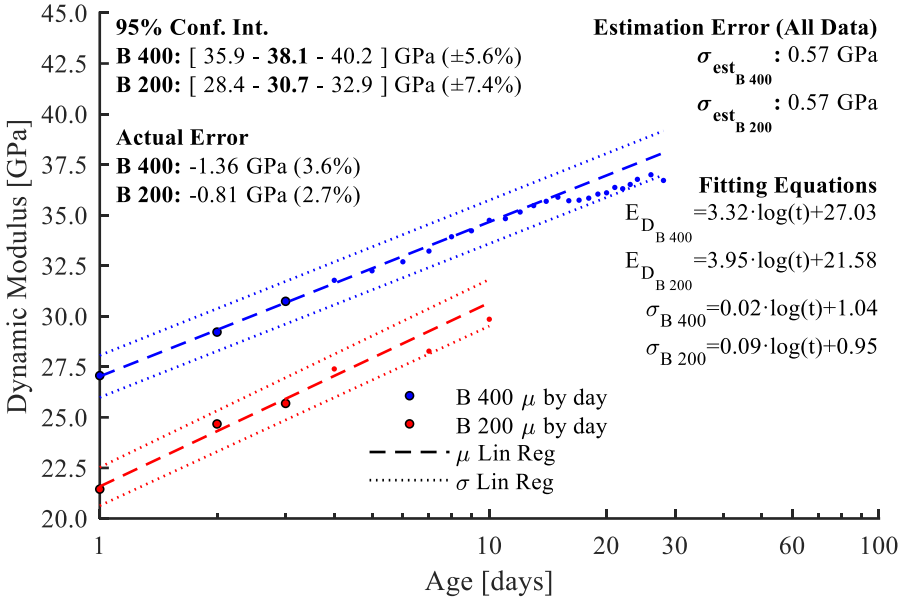

Figure 6.19 Forecasting of the dynamic modulus for the 10th day and the 28th day for batch 200 and 400 respectively. Only the average dynamic modulus for the first 3 days of monitoring was used for computing the linear regression

As expected the estimation errors for the whole data set using these linear regressions, are higher than when the fitting is done considering all the data. In the mean linear regressions from Figure 6.19, the error s were 0.57 GPa for both batches, while in Figure 6.15 the errors were 0.4 and 0.37 GPa for batch 200 and 400 respectively.

Based on the expected standard deviation and mean values for the dynamic modulus of each batch at the forecasting date, a 95% confidence interval for the dynamic modulus expected on the 28th day is computed. The confidence intervals for batch 200 and 400 are ±7.4% and 5.6% (Figure 6.19). Both of them are narrow enough for practical purposes with an expected value of 30.7 and 38.1 GPa for batch 200 and 400 respectively. The actual error computed by comparing with the actual measurements is within the confidence interval with an error of 2.7 and 3.6% respectively.

The third and final step is to translate the forecasted mean and standard deviation for the dynamic modulus into static values (Figure 6.20), using the E_S-E_D relationship from the calibration (Figure 6.18). The resulting mean and standard deviation for the static modulus on the 10th day for batch 200 are 7.85 and 0.40 GPa respectively. Similarly, for batch 400 but on the 28th day are 10.97 and 0.44 GPa.

The 95% confidence interval for the expected static Young's modulus is computed using the expected mean values (7.9 and 11 GPa for each batch respectively). However the standard deviation to be used in the calculation of the confidence interval is the sum of the E_S-E_D model error and the expected standard deviation of the measurements. This means that for batch 200, 0.4 and 0.27 GPa need to be added, summing 0.68 GPa. On the other hand, for batch 400, 0.44 and 0.38 GPa are added, resulting in 0.83 GPa.

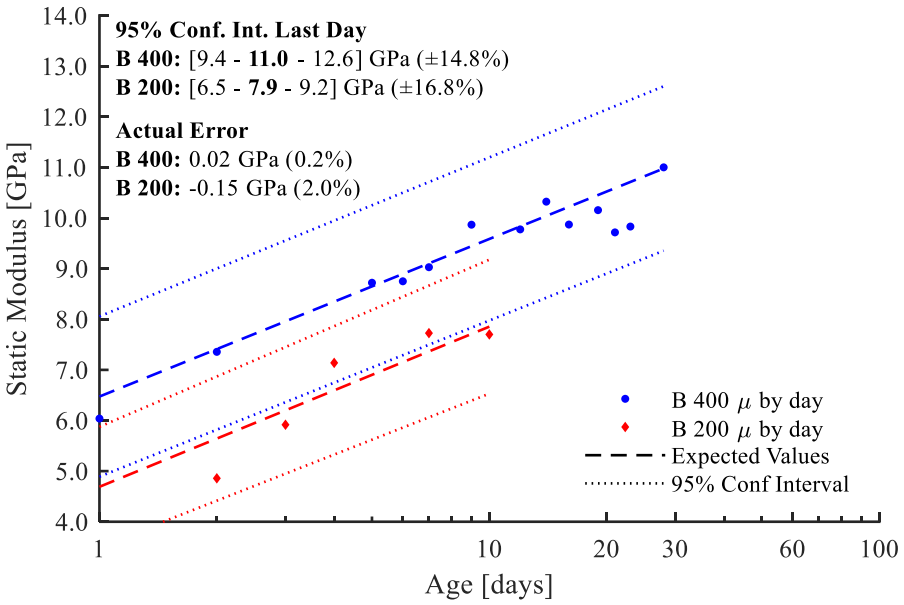

Figure 6.20 Forecasting of the static modulus of elasticity at the 10th and the 28th day for batch 200 and 400 respectively. The forecasting used the linear regression from Figure 6.19 and the E_S-E_D relationship from Figure 6.20

Finally, the 95% confidence interval for the static modulus at the age of 10th days and 28th days for batch 200 and 400 respectively, is computed. Resulting in the expected value of 7.9 and 11 GPa for each one of the batches, with a confidence interval of ± 16.8% and 14.8% respectively. Although the confidence interval is relatively large is good enough for practical purposes (ACI_301, 2010; ACI_311.4R, 2000; ACI_363.2R, 1998; Mostofinejad & Nozhati, 2005). However, the actual error of the estimated static value compared with the measured static modulus of elasticity is only 2% and 0.2% for batch 200 and 400 respectively. These errors are within the expected lab variability for concrete specimens (ASTM_C469, 2014).

Chapter 7
Summary & Conclusions

7.1 Summary

The objective of this research is to develop and validate a simple, more affordable, faster and reliable methodology for testing standard concrete cylinders, by measuring their resonant frequencies using the microphone of a smartphone. This work also develops a reliable forecasting methodology for the static modulus of elasticity on the 28th day, using early age monitoring of concrete cylinders with the aforementioned test methodology.

There is extensive research regarding the main two components of this research, the resonant test method in concrete cylinders, and the relationship between the static and dynamic modulus. The extensiveness emphasizes the advantages of using NDT over traditional tests, due to its affordability and portability. Nevertheless, most of the research done involves the usage of specialized sensors such as accelerometers or transducers for these tests. Although they are still cheaper and more portable than the machines used for the static tests, there is still room for improvement. There is little research done with resonant tests using microphones, and all of them use professional audio recording equipment with flat responses over a large frequency bandwidth (over 100 kHz).

The test setup and methodology developed has the advantage of not requiring complicated or specialized equipment. Due to the popularity, affordability and portability of smartphones nowadays, almost every person carries one in their pockets. An app can be then developed using the signal processing and postprocessing algorithm used in this research. The other instruments required for the test methodology presented, besides a smartphone, are a foam block, a small hammer with a steel sphere and a scale.

Using this test methodology, monitoring concrete cylinders on-site could be done instantly obtaining an estimation for the static modulus on the 28th day. This estimation could be updated with time by performing continuous monitoring. However, this methodology, as most of the non-destructive evaluations of concrete strength requires certain prior calibration. For the methodology proposed such calibration is the static-dynamic modulus relationship for the specific concrete mix intended to validate.

To validate the methodology, different microphones were tested in a frequency band from 1 to 20 kHz to investigate if they had a flat response in the range of interest and define what microphone would be best to use. Similarly, different impulse hammers, impact locations, and supports for the cylinder were tested. The results from the different test setups were compared with each other to provide advice on how to perform the test to obtain the best results.

Besides performing the resonant test, some cylinders were subject to other non-destructive tests, such as UPV and MASW. The results obtained from these other techniques were combined with the resonant test results, to reach additional conclusions about the validity of the methodology and asses the Poisson's ratio assumed.

The theoretical background behind the resonant test method and the other testing methods discussed were also included in this research. Likewise, the theoretical background for the main signal processing techniques was also presented.

7.2 Conclusions

7.2.1 General Conclusions

The methodology developed for testing with the resonant test using a smartphone's microphone has been proved to provide good results, with around ±3% variability from the accelerometer results. And the resonant frequencies obtained with the microphone showed better consistency with themselves than the accelerometer results. The frequencies from the accelerometer signals were shifting to lower values on some testing dates.

When the optimal impulse hammer was used, the resonant frequencies of the cylinder were accurately detected in all cases using the microphone signals. To achieve this the signals were processed as was described in this work.

Both, the static and dynamic moduli, increase linearly with the logarithm of time. And the relationship between static and dynamic modulus is also linear. The E_S-E_D relationship is typically reported as independent of other factors such as temperature, curing conditions, or age. It is considered to just be dependent on the concrete admixtures and the static test setup used.

These features described above can be used to forecast accurately the static modulus, using early measurements of the dynamic modulus.

The 95% confidence interval for the forecasted static modulus on the 28th day using the first 3 days of dynamic measurements was ≈±15%. This confidence interval includes the variability of the batch of cylinders tested and the estimated error for the static-dynamic moduli relationship. Nevertheless, the actual error of the estimated values with the measured static modulus of elasticity on the 28th day was 0.2% for batch 400.

7.2.2 Specimen Recommendations

The test methodology presented can be used for testing other cylindrical samples, not only for concrete. As long as the expected longitudinal frequency is within the flat response of the microphone used and also lower than 20 kHz. This maximum resonant frequency is due to the typical sampling rate for audio is either 44.1 or 48 kHz and the Nyquist sampling theorem.

The expected maximum frequency of a cylinder can be estimated with the equation (7.1). For this, an approximation of the expected Young's modulus and density or the P-wave velocity in the material would be needed.

$$f_{l_{\max}} = \frac{1}{2L}\sqrt{\frac{E}{\rho}} = \frac{V_P}{2L} \tag{7.1}.$$

For concrete cylinders or core samples, the minimum cylinder length on which conventional microphones could be used for measuring the dynamic modulus is around 11 cm. The maximum length depends on obtaining a flexural resonant frequency above typical noise frequencies. If most of the noise is assumed to be below 2.5 kHz, and the cylinders maintain a length-diameter ratio of 2, the maximum cylinder length is 50 cm.

7.2.3 Smartphone's Microphone Recommendations

The microphone from the smartphone used for this research (Moto G4 Plus®) showed a relatively flat response over the frequency bandwidth tested (1-20 kHz). However, the other microphones tested seem to have low pass filters with a cut-off frequency of around 11 kHz. These other microphones were built into a laptop computer. It is believed that the laptop sound card includes filtering features for voice enhancing.

The best results were obtained when placing the microphone very close from the top surface of the cylinder, around 2-4 cm. It's not critical the exact spot where the microphone is located as long as it is on the opposite side of where the impact is made.

If the methodology suggested were to be used in other smartphones it would be needed to validate it has a flat response over the frequency range of interest. This could be verified quite easily. If an app is coded, a tool for verifying the flat response could be included, along with instructions about how to perform the test. The procedure for doing so would be similar to the one used in this research, so only a computer with speakers and a quiet space would be required.

The tests done in this research were done in a normal level noise environment, and not under heavy noises. Additional tests under a noisier environment such as the inside of a construction office trailer would need to be performed in order to test the signal processing algorithm for the detection of the resonant frequencies.

7.2.4 Impulse Hammer Recommendations

The impulse hammer used for the test is of great importance to properly excite the concrete cylinders in the resonant frequency range. The simpler the better, trying to avoid heavy handles. The optimal approach is to use a steel bearing with a thin handle like a nail, or as it was used in this research a handle made of magnets piled up over each other.

For the concrete cylinders used on this research with dimensions around 10x20 cm diameter and length, the optimal diameter for the steel bearing is ¾" or 19 mm. However, the optimal diameter depends on the frequencies desired to be excited (i.e. the maximum resonant frequency to be excited). So, if the specimen dimensions or the material to be tested change, the optimal steel bearing diameter can be estimated by equation (7.2). If the material tested is concrete, the optimal diameter can be roughly estimated by dividing the length of the cylinder by 10.

$$d_s \approx \frac{2L}{0.0043\sqrt{E/\rho}} = \frac{2L}{0.0043 \cdot V_P} \tag{7.2}$$

The impact point does not need to be very precise, as long as it is done between the center of the cylinder and the edge and the recording device (i.e. the microphone) is located on the opposite side of the impact.

During the dynamic testing is advice to record at least 10 seconds and impacting the cylinder with the hammer as many times as possible but not faster than 4 times per second. On this test, the average recording time for the dynamic test was 15 seconds, with impacts approximately every half a second.

7.2.5 Cylinder Support Recommendations

It was found that the support used for placing the cylinder does not have interference with the frequencies found. As long as the resonant frequencies of the object used as support do not match the ones from the concrete cylinder tested, and the material had a different impedance than concrete.

However, using a foam block is still advisable. It helps to dampen the wave transmission into other objects and therefore the test becomes quieter. This way most of the sound waves produced by the test would be coming from the cylinder and not from other undesired sources.

7.2.6 Practice Recommendations

Given that the dynamic modulus on its own is not useful in the practice due to the strain levels at which it is measured. In order to use the testing and forecasting methodologies in practice, the static-dynamic moduli relationship is required to be known a priori.

For the application of this methodology is advised for the concrete supplier companies to develop the relationships for the concrete mixes they sell. This would be beneficial for their clients and for them to have a way to quickly calibrate their own mixes.

The linearity of the relationship between the static and dynamic moduli allows estimating the relationship with a relatively low number of tests. An idea that would simplify the calibration process would be to test a batch of cylinders on the 1^{st} day after casting and a second test after the 28^{th} day after casting. Using the results at these two ages, it is possible to establish the relationship.

7.3 Suggestions for Future Work

For further improvement of the current work, the following work could be done:

- Investigate if the ES-ED relationship is truly independent of the curing conditions. To do this it would be required to cast a new and larger batch of concrete cylinders using the same concrete mix proportion as the batch 400 from this work. Divide those cylinders into different groups and cure each group differently. Test the cylinders in the same way and same machine as the one followed in this work. Ideally, increase the number of concrete cylinders tested statically each day for each group.

- Test the methodology with the microphones under a noisy environment to evaluate how robust is the signal processing algorithm used in this work. And try to improve them using other techniques such as the Hilbert transform or a wavelet synchro-squeezed transformed.
- Develop the mobile app with the procedure described.

Bibliography

ACI_301. (2010). *Specifications for structural concrete.* Tech. rep., ACI.

ACI_311.4R. (2000). *Guide for concrete inspection.* Tech. rep., ACI.

ACI_318. (2014). *Building code requirements for structural concrete.* Tech. rep., ACI.

ACI_363.2R. (1998). *Guide to quality control and testing of high-strength concrete.* Tech. rep., ACI.

ACI_363R. (1992). *Report on high-strength concrete.* Tech. rep., ACI.

AIJ. (1985). *Standard for structural calculation of reinforced concrete structures.* Tech. rep., Architectural Institute of Japan.

Allen, J. (1977, 6). Short term spectral analysis, synthesis, and modification by discrete Fourier transform. *Acoustics, Speech and Signal Processing, IEEE Transactions on, 25*, 235-238. Retrieved from http://resolver.scholarsportal.info/resolve/00963518/v25i0003/235_stsasambdft

ASTM_C192. (2018). *Standard practice for making and curing concrete test specimens in the laboratory.* Tech. rep., ASTM. doi:10.1520/C0192_C0192M-18

ASTM_C215. (2014). *Standard test method for fundamental transverse, longitudinal, and torsional resonant frequencies of concrete specimens.* Tech. rep., ASTM. doi:10.1520/C0215-14

ASTM_C39. (2018). *Standard test method for compressive strength of cylindrical concrete specimens.* Tech. rep., ASTM. doi:10.1520/C0039_C0039M-18

ASTM_C469. (2014). *Standard test method for static modulus of elasticity and Poisson's ratio of concrete in compression.* Tech. rep., ASTM. doi:10.1520/C0469_C0469M-14

ASTM_C597. (2016). *Standard test method for pulse velocity through concrete.* Tech. rep., ASTM. doi:10.1520/C0597-16

ASTM_C670. (2015). *Standard practice for preparing precision and bias statements for test methods for construction materials.* Tech. rep., ASTM. doi:10.1520/C0670-15

ASTM_C918. (2013). *Standard test method for measuring early-age compressive strength and projecting later-age strength.* Tech. rep., ASTM. doi:10.1520/C0918_C0918M-13

ASTM_D2845. (2008). *Standard test method for laboratory determination of pulse velocities and ultrasonic elastic constants of rock.* Tech. rep., ASTM.

ASTM_D5777. (2018). *Standard guide for using the seismic refraction method for subsurface investigation.* Tech. rep., ASTM. doi:10.1520/D5777-18

ASTM_D7128. (2018). *Standard guide for using the seismic-reflection method for shallow subsurface investigation.* Tech. rep., ASTM. doi:10.1520/D7128-18

ASTM_E1875. (2013). *Standard test method for dynamic Young's modulus, shear modulus, and Poisson's ratio by sonic resonance.* Tech. rep., ASTM. doi:10.1520/E1875-13

ASTM_E1876. (2015). *Standard test method for dynamic Young's modulus, shear modulus, and Poisson's ratio by impulse excitation of vibration.* Tech. rep., ASTM. doi:10.1520/E1876-15

Bancroft, D. (1941, 4). The velocity of longitudinal waves in cylindrical bars. *Phys. Rev., 59*(7), 588-593. doi:10.1103/PhysRev.59.588

Bay, J. A., & Stokoe, H. (1992). Field and laboratory determination of elastic properties of portland cement concrete using seismic techniques. *Transportation Research Record*.

Behnood, A., Olek, J., & Glinicki, M. A. (2015). Predicting modulus elasticity of recycled aggregate concrete using M5′ model tree algorithm. *Construction and Building Materials, 94*, 137-147. Retrieved from http://resolver.scholarsportal.info/resolve/09500618/v94icomplete/137_pmeoracummta

Bjurstrom, H., Gudmarsson, A., Ryden, N., & Starkhammar, J. (2016, 2). Field and laboratory stress-wave measurements of asphalt concrete. *Construction and Building Materials, 126*, 508+. doi:https://doi.org/10.1016/j.conbuildmat.2016.09.067

Bjurstrom, H., Ryden, N., & Birgisson, B. (2016, 1). Non-contact surface wave testing of pavements: comparing a rolling microphone array with accelerometer measurements. *Smart Structures and Systems, 17*, 1-15. doi:http://doi.org/10.12989/SSS.2016.17.1.001

Boileau, P. E., Greiner, M., & Leach, M. F. (1981, 4). A modified resonance method for determining elastic moduli. *NDT International, 14*, 43-48. Retrieved from http://www.sciencedirect.com/science/article/pii/0308912681900419

Boone, S. D. (2005). *A comparison between the compressive strength and the dynamic properties of concrete as a function of time.* Master's thesis, University of Tennessee, Knoxville.

Brzev, S., & Pao, J. (2009). *Reinforced concrete design: A practical approach* (Updated ed.). Pearson Custom Publishing.

BS_8110_2. (1985). *BS 8110-2 Structural use of concrete Part 2: Code of practice for special circumstances.* Tech. rep., British Standards Board.

Carette, J., & Staquet, S. (2016). Monitoring and modelling the early age and hardening behaviour of eco-concrete through continuous non-destructive measurements: Part II. Mechanical

behaviour. *Cement and Concrete Composites, 73*, 1-9. Retrieved from http://resolver.scholarsportal.info/resolve/09589465/v73icomplete/1_mamteanmpimb

Carino, N. J., & Sansalone, N. N. (1986). Flaw detection in concrete by frequency spectrum analysis of impact-echo waveforms. *International Advances in Nondestructive Testing, 12*, 117-146. Retrieved from https://books.google.ca/books?hl=en&lr=&id=8f-vOXqLOMYC&oi=fnd&pg=PA117&dq=Flaw+Detection+in+Concrete+by+Frequency+Spectrmn+Analysis+of+Impact-Echo+Waveforms&ots=YdFOE3iztI&sig=QgmAJ3Fw5Qs0LwDxSKPFw3ApFT8#v=onepage&q=Flaw%20Detection%20in%20Concrete%20by%20Frequency%20Spectrmn%20Analysis%20of%20Impact-Echo%20Waveforms&f=false

Carreira, D. J., & Chu, K. H. (1985). Stress-strain relationship for plain concrete in compression. *ACI*, 797-804.

Christaras, B., Auger, F., & Mosse, E. (1994). Determination of the moduli of elasticity of rocks. comparison of the ultrasonic velocity and mechanical resonance frequency methods with direct static methods. *Materials and Structures, 27*, 222-228. Retrieved from http://resolver.scholarsportal.info/resolve/13595997/v27i0004/222_dotmoefmwdsm

CSA_A23.3. (2014). *CSA A23.3-14 Design of concrete structures.* Tech. rep., Canadian Standards Association.

Davis, T. J., & Opat, G. I. (1983). Elastic vibrations of rods and Poisson's ratio. *American Journal of Physics, 51*. doi:10.1119/1.13315

Dikmen, Ü., Arısoy, M. Ö., & Akkaya, İ. (2010, 5). Offset and linear spread geometry in the MASW method. *Journal of Geophysics and Engineering, 7*. doi:10.1088/1742-2132/7/2/S07

Diógenes, H. J., Cossolino, L. C., Pereira, A. H., El Debs, M. K., & El Debs, A. L. (2011). Determinação do módulo de elasticidade do concreto a partir da resposta acústica. *Revista IBRACON de Estruturas e Materiais, 4*, 803-813.

Dytran. (1995). *Impulse hammer model 5850B specifications.* Dytran Instruments, Inc. Dytran Instruments Inc.

Dytran. (2004). *Accelerometer model 3055B Datasheet.* Tech. rep., Dytran Instruments, Inc.

EN. (1992). *Design of concrete structures.* Tech. rep., European Committee for Standardization.

Erickson, K. (1952). *Dynamic modulus of elasticity and Poisson's ratio of concrete.* University of Wyoming. Ann Arbor: University of Wyoming. Retrieved 07 31, 2017, from

https://search.proquest.com/docview/302075681/citation/1E31AFE3412645F9PQ/1?accountid=14906

Fartosy, S. (2018). *Non-destructive evaluation of damage in concrete with applications in shallow foundations.* University of Waterloo. UWSpace. Retrieved from http://hdl.handle.net/10012/13926

Fowler, C. M. (2005). *The Solid Earth: An Introduction to Global Geophysics* (Second ed.). Cambridge University Press. Retrieved from http://gen.lib.rus.ec/book/index.php?md5=eca2ce14ebf3adbe31692974569fd85d

Gaidis, J. M., & Rosenberg, A. M. (1986). New test for determining fundamental frequencies of concrete. *Cement, Concrete and Aggregates, 8*(2), 117-119. doi:10.1520/CCA10065J

Gibson, A., & Popovics, S. (2005, 5). Lamb wave basis for impact-echo method analysis. *Journal of Engineering Mechanics, 131*, 438-443. doi:10.1061/(asce)0733-9399(2005)131:4(438)

Graff, K. F. (1975). *Wave motion in elastic solids.* Dover Publications. Retrieved from https://books.google.ca/books?id=jorRAgAAQBAJ

Groschup, R., & Grosse, C. U. (2015). MEMS microphone array sensor for air-coupled impact-echo. *Sensors (Basel, Switzerland), 15*, 14932-14945. Retrieved from http://resolver.scholarsportal.info/resolve/14248220/v15i0007/14932_mmasfai

Gross, D., Hauger, W., Schröder, J., Wall, A., & Bonet, J. (2011). *Engineering Mechanics 2.* Springer. doi:10.1007/978-3-642-12886-8

Guthrie, W. S., Larsen, J. L., Baxter, J. S., & Mazzeo, B. A. (2019, 3). Automated air-coupled impact-echo testing of a concrete bridge deck from a continuously moving platform. *Journal of Nondestructive Evaluation, 38*, 32. Retrieved from https://doi.org/10.1007/s10921-019-0566-9

Han, S.-H., & Kim, J.-K. (2004, 7). Effect of temperature and age on the relationship between dynamic and static elastic modulus of concrete. *Cement and Concrete Research, 34*, 1219-1227. Retrieved from http://www.sciencedirect.com/science/article/pii/S0008884603004344

Harter, L. H. (1970). *Order Statistics and their use in testing and estimation. Vol 1: Tests based on range and studentized range of samples from a normal population.* Tech. rep., Applied Mathematics research Laboratory. Aerospace Research Laboratories, Wright-Patterson Air Force Base, Ohio. US.

Hassoun, M. N., & Al-Manaseer, A. (2008). *Structural concrete: theory and design* (Fourth ed.). John Wiley & Sons, Inc.

IS. (2000). *IS 456 Indian Standard Plain and Reinforced Concrete Code of Practice.* Tech. rep., Bureau of Indian Standards.

Ito, Y., & Uomoto, T. (1997, 8). Nondestructive testing method of concrete using impact acoustics. *NDT & E International, 30*, 217-222. Retrieved from http://www.sciencedirect.com/science/article/pii/S096386959600059X

Jinying, Z., & Popovics John, S. (2007, 8). Imaging concrete structures using air-coupled impact-echo. *Journal of Engineering Mechanics, 133*, 628-640. doi:10.1061/(asce)0733-9399(2007)133:6(628)

Johnson, N. L., Kotz, S., & Balakrishnan, N. (1995). *Continuous univariate distributions* (Second ed., Vol. 2). John Wiley & Sons, Inc.

Jones, R. (1949). The non-destructive testing of concrete. *Magazine of Concrete Research, 1*, 67-78. doi:10.1680/macr.1949.1.2.67

Jones, R. (1962, 1). Surface wave technique for measuring the elastic properties and thickness of roads: Theoretical development. *British Journal of Applied Physics, 13*, 21-29. doi:10.1088/0508-3443/13/1/306

Kang, F., & Zhong-Ci, S. (1996). *Mathematical theory of elastic structures* (First ed.). Springer-Verlag Berlin Heidelberg. Retrieved from http://gen.lib.rus.ec/book/index.php?md5=490d3aa3d428ef21084c55bd495ea8e8

Karu, Z. (2001). *Signals and systems made ridiculously simple.* Zizi Press. Retrieved from http://gen.lib.rus.ec/book/index.php?md5=94325442dcc8d5c7e7f044a1461b3fd7

Kolias, S., & Williams, R. I. (1980). Relationships between the static and the dynamic moduli of elasticity in cement stabilised materials. *Matériaux et Construction, 13*, 99-107.

Kolluru, S., Popovics, J., & Shah, S. (2000). *Determining elastic properties of concrete using vibrational resonance frequencies of standard test cylinders.* Tech. rep., ASTM.

Lakes, R. (1987, 2). Foam structures with a negative Poisson's ratio. *Science, 235*, 1038+. Retrieved from http://link.galegroup.com/apps/doc/A4776404/AONE?u=uniwater&sid=AONE&xid=2d5fda25

Lalanne, C. (2014). *Mechanical vibration and shock analysis - Sinusoidal vibration* (Third ed., Vol. 1). John Wiley & Sons. Retrieved from https://app.knovel.com/hotlink/khtml/id:kt011BTSG1/mechanical-vibration/swept-sine-swept-sine

Lara, C. A. (2015). Relationship between the static and dynamic elastic moduli of concrete experimentally measured.

Lee, B. J., Kee, S.-H., Oh, T., & Kim, Y.-Y. (2015). Effect of cylinder size on the modulus of elasticity and compressive strength of concrete from static and dynamic tests. *Advances in Materials Science and Engineering, 2015*, 12. doi:10.1155/2015/580638

Lee, K.-M., Kim, D.-S., & Kim, J.-S. (1997, 12). Determination of dynamic Young's modulus of concrete at early ages by impact resonance test. *KSCE Journal of Civil Engineering, 1*, 11-18. Retrieved from https://doi.org/10.1007/BF02830459

Lemmens, J. (1990). Impulse excitation: a technique for dynamic modulus measurement. In A. Wolfenden (Ed.), *Dynamic Elastic Modulus Measurements in Materials* (pp. 90-99). ASTM International. doi:10.1520/STP24617S

Lin, C.-C., Liu, P.-L., & Yeh, P.-L. (2009, 10). Application of empirical mode decomposition in the impact-echo test. *NDT & E International, 42*, 589-598. Retrieved from http://www.sciencedirect.com/science/article/pii/S0963869509000589

Lin, Y., Sansalone, M., & Carino, N. (1991). Impact-echo response of concrete shafts. *Geotechnical Testing Journal, 14*, 121-137.

Love, A. E. (1944). *A Treatise on the Mathematical Theory of Elasticity.* Cambridge University Press Warehouse.

Lydon, F. D., & Balendran, R. V. (1986). Some observations on elastic properties of plain concrete. *Cement and Concrete Research, 16*, 314-324. doi:10.1016/0008-8846(86)90106-7

Malhotra, V. M. (1974). Evaluation of the Windsor probe test for estimating compressive strength of concrete. *Matériaux et Constructions, 7*. doi:10.1007/BF02482675

Medina, R., & Bayón, A. (2010). Elastic constants of a plate from impact-echo resonance and Rayleigh wave velocity. *Journal of Sound and Vibration, 329*, 2114-2126. Retrieved from http://resolver.scholarsportal.info/resolve/0022460x/v329i0011/2114_ecoapfirarwv

Mehta, P. K., & Monteiro, P. J. (2005). *Concrete: Microstructure, properties and materials* (Third ed.). McGraw-Hill. doi:10.1036/0071462899

Mostofinejad, D., & Nozhati, M. (2005). Prediction of the modulus of elasticity of high strength concrete. *Iranian Journal of Science & Technology, 29*.

Neville, A. M. (1996). *Properties of concrete.* Pearson.

Ni, S.-H., & Li, J.-L. (2019). HHT-based CEEMD to improve an impact echo test. *Journal of Testing and Evaluation, 47*. Retrieved from http://resolver.scholarsportal.info/resolve/00903973/v47i0004/nfp_hctiaiet

Nilsen, A., & Aitcin, P. (1992). Static modulus of elasticity of high-strength concrete from pulse velocity tests. *Cement, Concrete and Aggregates, 14*, 64-66. doi:10.1520/CCA10577J

Nilson, A. H., Darwin, D., & Dolan, W. (2004). *Design of concrete structures* (Fourteenth ed.). (B. Hash, & K. Buczek, Eds.) McGraw-Hill Higher Education.

Noguchi, T., Tomosawa, F., & Nemati, K. M. (1993). Relationship between compressive strength and modulus of elasticity of high-strength concrete. *Proceedings of the Third International Symposium on Utilization of High-Strength Concrete*, *2*, pp. 1247-1254.

Noguchi, T., Tomosawa, F., Nemati, K. M., Chiaia, B. M., & Fantilli, A. P. (2009). A practical equation for elastic modulus of concrete. *ACI Structural Journal, 106*, 690.

Ohtsu, M. (2016). Basics and applications of nde based on elastodynamics toward infra-dock for concrete structures. *Proc. emerging technologies in non-destructive testing VI*, 3-11.

Oppenheim, V., Willsky, S., & Hamid, S. (1996). *Signals and systems* (Second ed.). (M. Horton, Ed.) Prentice-Hall. Retrieved from http://gen.lib.rus.ec/book/index.php?md5=8169478eeb6b45dc63f1165f8cb90681

Pain, H. J. (2005). *The physics of vibrations and waves* (Sixth ed.). Wiley. Retrieved from http://gen.lib.rus.ec/book/index.php?md5=AC06E0FF962F3662EC5743725248015A

Papoulis, A. (1962). *The Fourier integral and its applications* (First Edition ed.). McGraw-Hill. Retrieved from http://gen.lib.rus.ec/book/index.php?md5=195303AB4E33EC7B8A93CDF71EA0A181

Physclips. (2019, 3). Travelling sine wave. Retrieved from http://www.animations.physics.unsw.edu.au/jw/travelling_sine_wave.htm

Pickett, G. (1945). Equations for computing elastic constants from flexural and torsional resonant frequencies of vibration of prism and cylinders. *ASTM Proceedings, 45*, 846-863. Retrieved from https://compass-astm-org.proxy.lib.uwaterloo.ca/DIGITAL_LIBRARY/PROCEEDINGS/PAGES/PRO1945-45.htm

Polytec. (2014). *CLV-2534 Compact laser vibrometer.* Tech. rep., Polytec. Retrieved from https://www.polytec.com/int/vibrometry-polytec/vibrometry-products-polytec/single-point-vibrometers/clv-2534-compact-laser-vibrometer/

Popovics, J. S., Zemajtis, J., & Shkolnik, I. (2008). A study of static and dynamic modulus of elasticity of concrete. *ACI-CRC Final Report*.

Popovics, S. (1975). Verification of relationships between mechanical properties of concrete-like materials. *Matériaux et Construction, 8*, 183-191. Retrieved from http://resolver.scholarsportal.info/resolve/00255432/v08i0003/183_vorbmpocm

Powers, T. C. (1938). Measuring Young's modulus of elasticity by means of sonic vibrations. *ASTM Proceeding*, *38*, pp. 460-469.

Pujol, J. (2003). *Elastic wave propagation and generation in seismology* (CUP ed.). Cambridge University Press. Retrieved from http://gen.lib.rus.ec/book/index.php?md5=E0D009E2A3EB80859FB18676DDEF1AC3

Qasrawi, H. Y. (2000). Concrete strength by combined nondestructive methods simply and reliably predicted. *Cement and Concrete Research*, 739-746. doi:10.1016/S0008-8846(00)00226-X

Rayleigh, B., & Strutt, J. W. (1877). *The theory of sound, vol. 1.* Macmillan, London.

Richart, F. E., Hall, J. R., & Woods, R. D. (1970). *Vibrations of soils and foundations.* (N. M. Newmark, Ed.) Prentice-Hall.

Ryden, N., Park Choon, B., Ulriksen, P., & Miller Richard, D. (2004, 5). Multimodal approach to seismic pavement testing. *Journal of Geotechnical and Geoenvironmental Engineering, 130*, 636-645. doi:10.1061/(ASCE)1090-0241(2004)130:6(636)

Shin, S. W., Popovics, J. S., & Oh, T. (2019, 8). Cost effective air-coupled impact-echo sensing for rapid detection of delamination damage in concrete structures. *Advances in Structural Engineering, 15*, 887-895. doi:10.1260/1369-4332.15.6.887

Shkolnik, I. E. (2005). Effect of nonlinear response of concrete on its elastic modulus and strength. *Cement and Concrete Composites, 27*, 747-757. doi:10.1016/j.cemconcomp.2004.12.006

Simmons, J. C. (1955, 4). Poisson's ratio of concrete: a comparison of dynamic and static measurements. *Magazine of Concrete Research, 7*, 61-68. doi:10.1680/macr.1955.7.20.61

Sleiman, N. (2017). *Tests on gfrp reinforced concrete knee-joints subjected to negative moments.* Master's thesis, University of Waterloo. Retrieved from http://hdl.handle.net/10012/12174

Sokolowski, J., Obuchowski, J., Zimroz, R., Wylomanska, A., & Koziarz, E. (2016). Algorithm indicating moment of p-wave arrival based on second-moment characteristic. *Hindawi Publishing Corporation Shock and Vibration, 2016*. doi:http://dx.doi.org/10.1155/2016/4051701

Szynalski, T. P. (2018, 3). Online tone generator. Retrieved from https://www.szynalski.com/tone-generator/

Tefft, W. E., & Spinner, S. (1962). Cross-sectional correction for computing young's modulus from longitudinal resonance vibrations of square and cylindrical rods. *Journal of Research of the National Bureau of Standards A, 66*, 193-197.

The MathWorks, Inc. (2019, 04 15). *Cross-correlation*. Retrieved from MathWorks Documentation: https://www.mathworks.com/help/matlab/ref/xcorr.html

Trtnik, G., Kavčič, F., & Turk, G. (2009). Prediction of concrete strength using ultrasonic pulse velocity and artificial neural networks. *Ultrasonics, 49*(1), 53-60. doi:10.1016/j.ultras.2008.05.001

TSE. (2000). *TS 500 Requirements for design and construction of reinforced concrete structures.* Tech. rep., TSE.

Wang, J.-J., Chang, T.-P., Chen, B.-T., & Wang, H. (2012). Determination of Poisson's ratio of solid circular rods by impact-echo method. *Journal of Sound and Vibration, 331*, 1059-1067. doi:https://doi.org/10.1016/j.jsv.2011.10.030

Wiciak, P., Cascante, G., & Polak, M. A. (2019). Frequency and geometry effects on ultrasonic pulse velocity measurements of concrete specimens. *ACI Journal submitted*.

Wight, K., & MacGregor, G. (2012). *Reinforced concrete mechanics and design* (Sixth ed.). (H. Stark, Ed.) Pearson.

Ye, J., Kobayashi, T., Iwata, M., Tsuda, H., & Murakawa, M. (2018). Computerized hammer sounding interpretation for concrete assessment with online machine learning. *Sensors (Basel, Switzerland), 18*. Retrieved from http://resolver.scholarsportal.info/resolve/14248220/v18i0003/nfp_chsifcawoml

Yeh, P.-L., & Liu, P.-L. (2008). Application of the wavelet transform and the enhanced Fourier spectrum in the impact echo test. *NDT and E International, 41*, 382-394. Retrieved from http://resolver.scholarsportal.info/resolve/09638695/v41i0005/382_aotwtasitiet

Zhang, S. X., Chan, L. S., & Xia, J. (2004, 1 01). The selection of field acquisition parameters for dispersion images from multichannel surface wave data. *Pure and Applied Geophysics, 161*, 185-201. doi:10.1007/s00024-003-2428-7

Zhang, Y., & Xie, Z. (2012, 10). Ensemble empirical mode decomposition of impact-echo data for testing concrete structures. *NDT & E International, 51*, 74-84. Retrieved from http://www.sciencedirect.com/science/article/pii/S0963869512000801

Zonst, E. (2005). *Understanding the FFT: A tutorial on the algorithm & software for laymen, students, technicians & working engineers.* Citrus Press. Retrieved from http://gen.lib.rus.ec/book/index.php?md5=71D520CD868C6FAAD28C136BCE2724C9

Appendix A

Complete Specimen Data

Table A1.1 Complete weight measurement for cylinders in batch 200. Average, standard deviation and coefficient of variation per day are included.

Specimen Number	Weight (gm) at Age (days)					
	1	**2**	**3**	**4**	**7**	**10**
201	3,653.9	3,667.7				
202	3,699.5	3,710.6	3,713.6			
203	3,664.5	3,643.2	3,650.8			
204	3,687.5	3,649.6	3,654.5	3,659.9		
205	3,723.5	3,725.0	3,736.4	3,700.3		
206	3,680.4	3,693.8	3,697.5	3,629.9	3,639.1	
207	3,747.1	3,745.4	3,748.3	3,705.8	3,728.2	
208	3,690.4	3,687.2	3,688.8	3,693.2	3,697.6	3,642.7
209	3,684.0	3,689.3	3,689.4	3,692.0	3,700.4	3,666.1
210	3,750.6	3,765.2	3,764.1	3,767.4	3,771.4	3,684.9
211	3,730.7	3,753.1	3,754.5	3,751.7	3,755.2	3,759.6
212	3,689.9	3,716.7	3,715.5	3,712.0	3,718.9	3,722.4
213	3,691.6	3,703.2	3,702.5	3,704.8	3,719.4	3,721.2
214	3,707.0	3,706.1	3,704.3	3,701.1	3,726.6	3,737.7
215	3,707.0	3,703.7	3,706.9	3,705.8	3,723.6	3,734.0
216	3,673.1	3,683.6	3,686.4	3,687.0	3,695.1	3,703.9
217	3,730.4	3,742.4	3,742.8	3,745.9	3,758.7	3,764.0
218	3,747.9	3,751.6	3,754.5	3,754.4	3,776.8	3,785.1
219	3,714.6	3,713.2	3,713.2	3,710.6	3,747.8	3,753.6
220	3,705.1	3,699.9	3,698.0	3,696.5	3,743.3	3,746.0
221	3,675.4	3,672.3	3,668.5	3,666.8	3,707.2	3,712.7
Average:	3,702.6	3,705.8	3,709.5	3,704.7	3,725.6	3,723.9
Std dev:	27.14	32.58	31.87	33.45	33.32	38.06
COV:	0.7%	0.9%	0.9%	0.9%	0.9%	1.0%

Table A1.2 Complete density computation for cylinders in batch 200. Average, standard deviation and coefficient of variation per day are included.

Specimen Number	Density (kg/m^3) at Age (days)					
	1	2	3	4	7	10
201	2,255.1	2,263.6				
202	2,238.4	2,245.1	2,246.9			
203	2,209.5	2,242.7	2,151.3			
204	2,234.1	2,289.2	2,292.2	2,295.6		
205	2,244.8	2,245.7	2,252.6	2,272.1		
206	2,240.8	2,248.9	2,251.2	2,243.6	2,249.3	
207	2,259.0	2,258.0	2,259.8	2,273.5	2,287.2	
208	2,246.9	2,245.0	2,245.9	2,248.6	2,251.3	2,249.6
209	2,259.7	2,262.9	2,263.0	2,264.6	2,269.8	2,254.0
210	2,278.1	2,286.9	2,286.3	2,288.3	2,290.7	2,307.9
211	2,249.2	2,262.7	2,263.6	2,261.9	2,264.0	2,266.6
212	2,235.6	2,251.8	2,251.1	2,249.0	2,253.1	2,255.3
213	2,247.6	2,254.7	2,254.2	2,255.6	2,264.5	2,265.6
214	2,251.4	2,250.9	2,249.8	2,247.9	2,263.3	2,270.1
215	2,229.4	2,227.4	2,229.3	2,228.7	2,239.4	2,245.6
216	2,230.9	2,237.3	2,239.0	2,239.4	2,244.3	2,249.6
217	2,260.1	2,267.3	2,267.6	2,269.4	2,277.2	2,280.4
218	2,259.6	2,261.8	2,263.6	2,263.5	2,277.0	2,282.0
219	2,250.5	2,249.6	2,249.6	2,248.0	2,270.6	2,274.1
220	2,206.6	2,203.5	2,202.3	2,201.4	2,229.3	2,230.9
221	2,204.9	2,203.1	2,200.8	2,199.8	2,224.0	2,227.3
Average:	2,242.5	2,250.4	2,246.0	2,252.8	2,259.7	2,261.4
Std dev:	18.35	20.82	30.63	24.60	18.82	20.60
COV:	0.8%	0.9%	1.4%	1.1%	0.8%	0.9%

Table A1.3 Diameter and length dimensions for batch 400 cylinders at the ages of 128 and 156 days old. Average, standard deviation and coefficient of variation per day included.

Age (days):	128			156		
Specimen Number	Diameter (cm)	Length (cm)	Area (cm^2)	Diameter (cm)	Length (cm)	Area (cm^2)
443	10.16	19.77	81.10	10.15	19.87	80.91
444	10.17	19.94	81.24	10.16	20.03	81.09
445	10.19	19.88	81.54	10.05	19.94	79.29
446	10.14	19.83	80.77	10.17	19.86	81.25
447	10.19	19.78	81.61	10.18	19.76	81.44
448	10.15	20.05	80.93	10.18	19.93	81.35
Average:	10.2	19.9	19.9	10.1	19.9	19.9
Std dev:	0.019	0.097	0.097	0.046	0.081	0.097
COV:	0.2%	0.5%	0.5%	0.5%	0.4%	0.5%

Table A1.4 Weight measurement for Batch 400. Part I (Cylinders 401-435 Ages 1-9)

Specimen Number	Weight (grams) at Age (days)								
	1	2	3	4	5	6	7	8	9
401	3720.0								
402	3686.6								
403	3678.7								
404	3663.9								
405	3708.0	3708.0							
406	3676.0	3676.0							
407	3676.3	3676.3							
408	3818.8	3818.8							
409	3665.5	3673.9	3675.6	3673.4	3674.5				
410	3743.7	3750.0	3755.5	3753.3	3753.9				
411	3777.1	3784.4	3790.7	3793.7	3796.1				
412	3751.3	3756.6	3761.9	3765.2	3768.0				
413	3757.3	3764.4	3764.8	3768.1	3768.2	3770.9			
414	3685.1	3689.8	3691.9	3702.4	3701.6	3703.8			
415	3665.9	3663.4	3674.9	3679.3	3677.6	3678.9			
416	3703.0	3702.4	3710.7	3714.1	3712.6	3716.7	3716.0		
417	3712.7	3712.4	3718.0	3721.4	3719.2	3723.9	3724.1		
418	3644.9	3651.0	3657.2	3657.0	3654.2	3660.1	3658.2		
419	3728.7	3740.3	3741.3	3741.5	3739.3	3744.7	3745.1	3747.0	3746.2
420	3709.0	3724.8	3724.7	3727.1	3725.6	3729.8	3732.4	3733.9	3733.7
421	3734.4	3747.5	3749.6	3751.0	3748.8	3753.5	3752.4	3754.6	3753.6
422	3668.9	3679.9	3683.2	3683.9	3681.9	3686.6	3685.4	3688.6	3688.0
423	3723.0	3731.6	3734.2	3734.1	3732.5	3738.0	3737.5	3741.9	3740.4
424	3703.9	3703.9	3712.2	3713.7	3710.6	3718.6	3717.9	3720.8	3720.1
425	3789.6	3798.0	3802.4	3804.9	3802.5	3807.9	3807.7	3810.1	3809.5
426	3681.1	3691.7	3694.3	3695.7	3699.1	3695.8	3699.8	3702.6	3702.2
427	3734.3	3748.0	3754.9	3753.3	3751.3	3755.5	3759.8	3763.2	3762.9
428	3768.8	3780.7	3788.5	3786.1	3784.0	3790.4	3793.2	3795.4	3795.0
429	3767.8	3777.1	3785.2	3784.0	3781.3	3786.6	3787.8	3790.8	3788.9
430	3840.0	3850.1	3852.0	3854.5	3850.8	3855.0	3856.2	3858.8	3858.7
431	3714.3	3720.1	3725.1	3727.7	3726.5	3727.6	3730.1	3732.2	3733.2
432	3756.0	3767.5	3771.1	3772.8	3772.1	3772.1	3776.1	3778.5	3779.4
433	3744.0	3753.0	3757.5	3756.4	3755.9	3761.0	3762.5	3763.2	3763.8
434	3676.1	3690.1	3697.1	3697.5	3696.0	3701.5	3701.5	3702.4	3701.8
435	3705.8	3717.5	3723.7	3725.6	3723.5	3729.5	3728.0	3729.7	3728.8

Table A1.5 Weight measurement for Batch 400. Part II (Cylinders 436-448 Ages 1-9)

Specimen Number	Weight (grams) at Age (days)								
	1	2	3	4	5	6	7	8	9
436	3799.8	3812.2	3819.4	3819.9	3815.8	3820.3	3820.1	3821.7	3821.9
437	3647.1	3658.3	3665.7	3665.9	3665.1	3667.8	3668.4	3670.3	3670.0
438	3691.2	3696.6	3703.7	3704.7	3706.3	3707.5	3710.2	3712.7	3713.3
439	3728.0	3729.8	3739.6	3741.1	3740.2	3742.2	3746.6	3750.9	3750.5
440	3657.6	3660.9	3667.4	3667.7	3666.5	3668.3	3674.7	3675.4	3676.8
441	3787.2	3791.9	3797.6	3800.1	3799.7	3807.6	3808.4	3808.8	3810.2
442	3751.4	3757.5	3766.0	3767.9	3766.8	3772.6	3771.5	3773.8	3774.3
443	3625.7	3634.4	3639.2	3641.5	3640.9	3646.9	3645.9	3649.4	3648.4
444	3758.7	3764.9	3764.4	3766.8	3765.9	3774.3	3775.9	3779.0	3778.0
445	3665.1	3674.1	3675.8	3676.8	3675.3	3681.3	3683.6	3686.2	3686.0
446	3645.1	3650.9	3655.6	3656.5	3655.9	3662.1	3663.5	3664.8	3664.9
447	3639.6	3646.0	3649.2	3650.0	3698.4	3657.9	3658.9	3661.7	3662.1
448	3700.5	3703.1	3706.4	3707.5	3706.4	3717.7	3720.6	3723.9	3724.5
Average:	3,714.1	3,723.4	3,728.7	3,730.1	3,730.3	3,731.5	3,733.9	3,739.7	3,739.6
Std dev:	49.61	51.56	50.64	50.62	48.99	50.63	51.43	51.85	51.84
COV:	1.3%	1.4%	1.4%	1.4%	1.3%	1.4%	1.4%	1.4%	1.4%

Table A1.6 Weight measurement for Batch 400. Part III (Ages 10-18)

Specimen Number	Weight (grams) at Age (days)								
	10	11	12	13	14	15	16	17	18
420									
421									
422	3687.3	3690.7	3691.1						
423	3740.5	3743.9	3745.3						
424	3720.6	3724.0	3725.1						
425	3810.6	3812.1	3808.5	3811.4	3812.9				
426	3703.6	3704.6	3700.3	3703.4	3704.4				
427	3764.1	3764.3	3759.8	3764.1	3764.9				
428	3795.9	3797.8	3794.2	3797.7	3793.8	3797.5	3797.4		
429	3790.1	3793.8	3790.6	3792.0	3788.7	3793.1	3793.7		
430	3860.4	3865.3	3863.5	3865.4	3861.5	3865.5	3866.1		
431	3735.9	3737.9	3734.2	3737.5	3734.7	3738.7	3736.0	3738.1	3738.1
432	3782.1	3783.9	3780.5	3784.1	3780.7	3784.2	3780.8	3783.7	3784.5
433	3765.4	3767.3	3766.0	3768.1	3764.8	3769.0	3766.8	3768.7	3764.0
434	3702.5	3705.5	3704.3	3705.8	3702.5	3707.7	3706.7	3708.0	3708.6
435	3729.5	3731.8	3730.8	3733.3	3728.8	3733.4	3732.9	3733.0	3732.9
436	3822.9	3824.8	3821.9	3826.9	3822.0	3827.7	3826.2	3827.6	3827.6
437	3671.1	3673.5	3669.8	3674.5	3670.3	3674.6	3671.6	3675.0	3675.0
438	3714.2	3716.4	3713.9	3717.6	3713.1	3717.7	3714.8	3717.4	3718.6
439	3751.2	3753.8	3751.1	3755.1	3750.5	3755.5	3755.0	3756.2	3758.2
440	3679.1	3681.5	3678.5	3681.1	3677.9	3681.8	3681.8	3682.5	3683.6
441	3811.0	3814.2	3808.4	3812.9	3809.4	3814.1	3812.6	3814.9	3814.6
442	3774.8	3778.0	3773.6	3771.0	3774.3	3779.2	3776.3	3780.1	3779.8
443	3649.4	3652.8	3649.6	3654.3	3649.4	3654.7	3650.6	3653.8	3655.4
444	3778.7	3781.2	3777.8	3781.2	3776.5	3782.1	3780.0	3781.8	3782.7
445	3687.2	3689.6	3684.6	3689.9	3684.7	3690.2	3688.7	3690.8	3691.0
446	3665.6	3668.0	3662.4	3668.0	3663.1	3668.7	3666.1	3669.3	3668.7
447	3663.0	3664.6	3658.1	3664.5	3659.7	3663.9	3661.6	3666.3	3664.8
448	3725.4	3726.1	3720.1	3726.3	3721.7	3726.8	3723.2	3728.0	3727.4
Average:	3,740.1	3,742.5	3,739.4	3,745.3	3,742.1	3,744.1	3,742.3	3,732.0	3,732.0
Std dev:	54.66	54.80	54.97	56.65	57.20	58.19	58.79	51.65	51.50
COV:	1.5%	1.5%	1.5%	1.5%	1.5%	1.6%	1.6%	1.4%	1.4%

Table A1.7 Weight measurement for Batch 400. Part IV (Ages 19-43)

Specimen Number	Weight (grams) at Age (days)								
	19	20	21	22	23	24	26	28	43
429									
430									
431	3739.0								
432	3785.3								
433	3769.4								
434	3705.5	3707.7	3703.8						
435	3730.6	3733.5	3729.9						
436	3825.8	3827.1	3823.6						
437	3673.7	3675.0	3675.5	3674.9	3669.9				
438	3716.7	3716.9	3718.6	3718.2	3712.7				
439	3753.4	3756.6	3756.7	3756.9	3750.0				
440	3679.1	3682.7	3683.3	3682.4	3683.5	3683.0	3683.2	3679.7	
441	3810.6	3814.0	3814.7	3814.1	3815.3	3814.6	3815.0	3811.3	
442	3776.7	3779.7	3780.6	3779.8	3781.1	3780.3	3780.0	3776.7	
443	3650.3	3653.9	3654.5	3654.8	3655.9	3654.3	3655.0	3649.4	3616.6
444	3778.4	3782.5	3782.2	3782.4	3783.2	3782.9	3782.4	3777.7	3744.9
445	3686.8	3690.8	3686.2	3689.3	3690.6	3691.2	3690.8	3685.7	3651.9
446	3665.0	3669.3	3669.2	3668.9	3670.3	3670.3	3669.4	3665.0	3632.7
447	3660.6	3665.6	3666.6	3666.3	3667.2	3666.2	3665.8	3660.9	3628.1
448	3722.9	3727.5	3729.1	3729.1	3729.8	3728.9	3728.5	3722.8	3687.3
Average:	3,729.4	3,725.5	3,725.0	3,718.1	3,717.5	3,719.1	3,718.9	3,714.4	3,660.3
Std dev:	52.32	53.68	53.45	51.53	51.52	56.27	56.28	56.67	44.09
COV:	1.4%	1.4%	1.4%	1.4%	1.4%	1.5%	1.5%	1.5%	1.2%

Table A1.8 Weight measurement for Batch 400. Part V (Ages 47-156)

Specimen Number	Weight (grams) at Age (days)				
	47	57	65	128	156
441					
442					
443	3613.0	3604.2	3599.4	3569.7	3561.4
444	3741.3	3732.4	3727.0	3698.6	3690.7
445	3648.1	3638.9	3634.9	3605.3	3597.7
446	3629.1	3620.5	3616.6	3587.1	3579.3
447	3624.4	3615.5	3611.1	3582.3	3574.4
448	3683.7	3674.6	3670.3	3642.0	3634.2
Average:	3,656.6	3,647.7	3,643.2	3,614.2	3,606.3
Std dev:	44.11	44.05	43.75	44.17	44.23
COV:	1.2%	1.2%	1.2%	1.2%	1.2%

Table A1.9 Density measurement for Batch 400. Part I (Cylinders 401-435 Ages 1-9)

Specimen Number	Density (kg/m^3) at Age (days)								
	1	2	3	4	5	6	7	8	9
401	2,301.1								
402	2,281.3								
403	2,271.1								
404	2,270.6								
405	2,275.3	2,275.3							
406	2,276.1	2,276.1							
407	2,277.2	2,277.2							
408	2,254.6	2,254.6							
409	2,265.3	2,270.5	2,271.6	2,270.2	2,270.9				
410	2,296.9	2,300.8	2,304.2	2,302.8	2,303.2				
411	2,300.4	2,304.8	2,308.7	2,310.5	2,312.0				
412	2,287.1	2,290.3	2,293.6	2,295.6	2,297.3				
413	2,287.8	2,292.1	2,292.4	2,294.4	2,294.4	2,296.1			
414	2,288.1	2,291.1	2,292.4	2,298.9	2,298.4	2,299.8			
415	2,274.1	2,272.5	2,279.7	2,282.4	2,281.3	2,282.1			
416	2,278.2	2,277.9	2,283.0	2,285.1	2,284.1	2,286.7	2,286.2		
417	2,292.4	2,292.2	2,295.7	2,297.8	2,296.4	2,299.3	2,299.4		
418	2,241.0	2,244.8	2,248.6	2,248.5	2,246.7	2,250.4	2,249.2		
419	2,291.6	2,298.7	2,299.3	2,299.5	2,298.1	2,301.4	2,301.7		
420	2,250.8	2,260.4	2,260.3	2,261.8	2,260.9	2,263.4	2,265.0	2,265.9	2,265.8
421	2,265.6	2,273.6	2,274.8	2,275.7	2,274.3	2,277.2	2,276.5	2,277.9	2,277.3
422	2,230.9	2,237.6	2,239.6	2,240.0	2,238.8	2,241.7	2,241.0	2,242.9	2,242.5
423	2,250.9	2,256.1	2,257.6	2,257.6	2,256.6	2,259.9	2,259.6	2,262.3	2,261.4
424	2,252.7	2,252.7	2,257.8	2,258.7	2,256.8	2,261.6	2,261.2	2,263.0	2,262.6
425	2,280.3	2,285.3	2,288.0	2,289.5	2,288.1	2,291.3	2,291.2	2,292.6	2,292.3
426	2,287.2	2,293.7	2,295.4	2,296.2	2,298.3	2,296.3	2,298.8	2,300.5	2,300.3
427	2,256.5	2,264.8	2,269.0	2,268.0	2,266.8	2,269.3	2,271.9	2,274.0	2,273.8
428	2,275.6	2,282.7	2,287.5	2,286.0	2,284.7	2,288.6	2,290.3	2,291.6	2,291.4
429	2,296.5	2,302.2	2,307.1	2,306.4	2,304.8	2,308.0	2,308.7	2,310.5	2,309.4
430	2,302.9	2,308.9	2,310.0	2,311.5	2,309.3	2,311.8	2,312.6	2,314.1	2,314.1
431	2,259.0	2,262.5	2,265.6	2,267.2	2,266.4	2,267.1	2,268.6	2,269.9	2,270.5
432	2,258.3	2,265.2	2,267.4	2,268.4	2,268.0	2,268.0	2,270.4	2,271.8	2,272.4
433	2,315.0	2,320.6	2,323.4	2,322.7	2,322.4	2,325.5	2,326.4	2,326.9	2,327.3
434	2,247.3	2,255.9	2,260.2	2,260.4	2,259.5	2,262.9	2,262.9	2,263.4	2,263.0
435	2,264.6	2,271.8	2,275.6	2,276.7	2,275.4	2,279.1	2,278.2	2,279.2	2,278.7

⋮

Table A1.10 Density measurement for Batch 400. Part II (Cylinders 436-448 Ages 1-9)

Specimen Number	Density (kg/m^3) at Age (days)								
	1	**2**	**3**	**4**	**5**	**6**	**7**	**8**	**9**
436	2,271.8	2,279.2	2,283.5	2,283.8	2,281.4	2,284.0	2,283.9	2,284.9	2,285.0
437	2,234.6	2,241.5	2,246.0	2,246.1	2,245.6	2,247.3	2,247.6	2,248.8	2,248.6
438	2,231.8	2,235.1	2,239.4	2,240.0	2,240.9	2,241.7	2,243.3	2,244.8	2,245.2
439	2,252.3	2,253.4	2,259.3	2,260.2	2,259.6	2,260.8	2,263.5	2,266.1	2,265.9
440	2,228.9	2,230.9	2,234.9	2,235.1	2,234.3	2,235.4	2,239.3	2,239.8	2,240.6
441	2,266.7	2,269.6	2,273.0	2,274.5	2,274.2	2,279.0	2,279.4	2,279.7	2,280.5
442	2,295.3	2,299.0	2,304.2	2,305.4	2,304.7	2,308.3	2,307.6	2,309.0	2,309.3
443	2,231.9	2,237.3	2,240.2	2,241.6	2,241.3	2,244.9	2,244.3	2,246.5	2,245.9
444	2,303.8	2,307.6	2,307.3	2,308.7	2,308.2	2,313.3	2,314.3	2,316.2	2,315.6
445	2,210.4	2,215.8	2,216.8	2,217.4	2,216.5	2,220.1	2,221.5	2,223.1	2,223.0
446	2,252.6	2,256.2	2,259.1	2,259.6	2,259.3	2,263.1	2,263.9	2,264.8	2,264.8
447	2,233.0	2,236.9	2,238.9	2,239.4	2,269.1	2,244.2	2,244.8	2,246.6	2,246.8
448	2,248.7	2,250.3	2,252.3	2,252.9	2,252.3	2,259.1	2,260.9	2,262.9	2,263.3
Average:	2,268.0	2,271.0	2,274.1	2,274.9	2,275.0	2,274.7	2,273.8	2,273.8	2,273.7
Std dev:	23.81	24.18	25.06	25.28	24.77	25.04	25.30	25.43	25.37
COV:	1.0%	1.1%	1.1%	1.1%	1.1%	1.1%	1.1%	1.1%	1.1%

Table A1.11 Density measurement for Batch 400. Part III (Ages 10-18)

Specimen Number	Density (kg/m^3) at Age (days)								
	10	**11**	**12**	**13**	**14**	**15**	**16**	**17**	**18**
420									
421									
422	2,242.1	2,244.2	2,244.4						
423	2,261.4	2,263.5	2,264.3						
424	2,262.9	2,264.9	2,265.6						
425	2,292.9	2,293.8	2,291.7	2,293.4	2,294.3				
426	2,301.1	2,301.8	2,299.1	2,301.0	2,301.6				
427	2,274.5	2,274.6	2,271.9	2,274.5	2,275.0				
428	2,291.9	2,293.1	2,290.9	2,293.0	2,290.7	2,292.9	2,292.8		
429	2,310.1	2,312.4	2,310.4	2,311.3	2,309.3	2,311.9	2,312.3		
430	2,315.1	2,318.0	2,316.9	2,318.1	2,315.7	2,318.1	2,318.5		
431	2,272.1	2,273.4	2,271.1	2,273.1	2,271.4	2,273.8	2,272.2	2,273.5	2,273.5
432	2,274.0	2,275.1	2,273.0	2,275.2	2,273.2	2,275.3	2,273.2	2,275.0	2,275.4
433	2,328.2	2,329.4	2,328.6	2,329.9	2,327.9	2,330.5	2,329.1	2,330.3	2,327.4
434	2,263.5	2,265.3	2,264.6	2,265.5	2,263.5	2,266.6	2,266.0	2,266.8	2,267.2
435	2,279.1	2,280.5	2,279.9	2,281.4	2,278.7	2,281.5	2,281.2	2,281.2	2,281.2
436	2,285.6	2,286.7	2,285.0	2,288.0	2,285.1	2,288.5	2,287.6	2,288.4	2,288.4
437	2,249.3	2,250.8	2,248.5	2,251.4	2,248.8	2,251.4	2,249.6	2,251.7	2,251.7
438	2,245.7	2,247.0	2,245.5	2,247.8	2,245.0	2,247.8	2,246.1	2,247.6	2,248.4
439	2,266.3	2,267.9	2,266.2	2,268.6	2,265.9	2,268.9	2,268.6	2,269.3	2,270.5
440	2,242.0	2,243.5	2,241.6	2,243.2	2,241.3	2,243.7	2,243.7	2,244.1	2,244.8
441	2,281.0	2,282.9	2,279.4	2,282.1	2,280.0	2,282.8	2,282.0	2,283.3	2,283.1
442	2,309.6	2,311.6	2,308.9	2,307.3	2,309.3	2,312.3	2,310.5	2,312.9	2,312.7
443	2,246.5	2,248.6	2,246.6	2,249.5	2,246.5	2,249.7	2,247.2	2,249.2	2,250.2
444	2,316.0	2,317.6	2,315.5	2,317.6	2,314.7	2,318.1	2,316.8	2,317.9	2,318.5
445	2,223.7	2,225.1	2,222.1	2,225.3	2,222.2	2,225.5	2,224.6	2,225.9	2,226.0
446	2,265.2	2,266.7	2,263.3	2,266.7	2,263.7	2,267.2	2,265.6	2,267.5	2,267.2
447	2,247.4	2,248.3	2,244.4	2,248.3	2,245.3	2,247.9	2,246.5	2,249.4	2,248.5
448	2,263.8	2,264.2	2,260.6	2,264.4	2,261.6	2,264.7	2,262.5	2,265.4	2,265.0
Average:	2,274.5	2,276.0	2,274.1	2,278.2	2,276.3	2,277.1	2,276.0	2,272.2	2,272.2
Std dev:	26.30	26.34	26.41	26.50	27.05	27.98	28.23	26.58	26.17
COV:	1.2%	1.2%	1.2%	1.2%	1.2%	1.2%	1.2%	1.2%	1.2%

Table A1.12 Density measurement for Batch 400. Part IV (Ages 19-43)

Specimen Number	Density (kg/m^3) at Age (days)								
	19	20	21	22	23	24	26	28	43
429									
430									
431	2,274.0								
432	2,275.9								
433	2,330.7								
434	2,265.3	2,266.6	2,264.3						
435	2,279.8	2,281.5	2,279.3						
436	2,287.3	2,288.1	2,286.0						
437	2,250.9	2,251.7	2,252.0	2,251.6	2,248.6				
438	2,247.2	2,247.3	2,248.4	2,248.1	2,244.8				
439	2,267.6	2,269.5	2,269.6	2,269.7	2,265.6				
440	2,242.0	2,244.2	2,244.6	2,244.0	2,244.7	2,244.4	2,244.5	2,242.4	
441	2,280.8	2,282.8	2,283.2	2,282.8	2,283.6	2,283.1	2,283.4	2,281.2	
442	2,310.8	2,312.6	2,313.2	2,312.7	2,313.5	2,313.0	2,312.8	2,310.8	
443	2,247.0	2,249.3	2,249.6	2,249.8	2,250.5	2,249.5	2,249.9	2,246.5	2,226.3
444	2,315.9	2,318.4	2,318.2	2,318.3	2,318.8	2,318.6	2,318.3	2,315.4	2,295.3
445	2,223.5	2,225.9	2,223.1	2,225.0	2,225.7	2,226.1	2,225.9	2,222.8	2,202.4
446	2,264.9	2,267.5	2,267.5	2,267.3	2,268.2	2,268.2	2,267.6	2,264.9	2,244.9
447	2,245.9	2,249.0	2,249.6	2,249.4	2,249.9	2,249.3	2,249.1	2,246.1	2,226.0
448	2,262.3	2,265.1	2,266.1	2,266.1	2,266.5	2,265.9	2,265.7	2,262.2	2,240.7
Average:	2,270.7	2,268.0	2,267.6	2,265.4	2,265.0	2,268.7	2,268.6	2,265.8	2,239.3
Std dev:	26.94	24.63	24.69	26.52	26.88	29.48	29.42	29.62	28.52
COV:	1.2%	1.1%	1.1%	1.2%	1.2%	1.3%	1.3%	1.3%	1.3%

Table A1.13 Density measurement for Batch 400. Part IV (Ages 47-156)

Specimen Number	Density (kg/m^3) at Age (days)				
	47	57	65	128	156
441					
442					
443	2,224.1	2,218.7	2,215.7	2,226.4	2,215.2
444	2,293.1	2,287.7	2,284.3	2,283.2	2,272.3
445	2,200.1	2,194.6	2,192.2	2,224.1	2,275.5
446	2,242.7	2,237.4	2,235.0	2,239.6	2,218.2
447	2,223.7	2,218.2	2,215.5	2,219.2	2,221.2
448	2,238.5	2,232.9	2,230.3	2,244.5	2,241.5
Average:	2,237.0	2,231.6	2,228.8	2,239.5	2,240.6
Std dev:	28.54	28.57	28.33	21.43	24.99
COV:	1.3%	1.3%	1.3%	1.0%	1.1%